Light-Matter Interaction on the Attosecond Timescale

Dahlström, Marcus

2011

Light–matter interaction on the attosecond timescale

J. Marcus Dahlström

Doctoral Thesis
2011

Lund University

Light–matter interaction
on the attosecond timescale

Printed in Sweden by Media-Tryck, Lund, 2011

Division of Atomic Physics
Department of Physics
Faculty of Engineering, LTH
Lund University
P.O. Box 118
SE–221 00 Lund
Sweden

http://www.atomic.physics.lu.se

ISSN 0281-2762
Lund Reports on Atomic Physics, LRAP-438

ISBN: 978-91-7473-140-8

"There is great pleasure in recognizing old things from a new point of view."
R. P. Feynman

Space–Time Approach to Non-Relativistic Quantum Mechanics

Abstract

Attosecond science refers to physical processes that occur on the natural timescale of electron motion in atomic and molecular systems. Attosecond time resolution can be obtained experimentally through a process called high-order harmonic generation where sharp attosecond pulses are formed in the time domain.

Attosecond pulse trains contain many attosecond pulses with a constant pulse-to-pulse separation. The attosecond pulse trains provide a unique combination of temporal and spectral properties, since they correspond to coherent odd harmonics in the spectral domain. It is possible to use these temporal properties to ionize an atom at specific times, but it is also possible to use the spectral properties and tune a harmonic at a specific atomic resonance. In either case, the emitted photoelectrons can be probed with a coherent infrared field, and attosecond temporal information can be obtained. The work presented in this thesis shows that attosecond pulse trains can be used to study the phase variation of various two-photon ionization processes and, thus, the temporal properties of emitted photoelectrons. The delay in photoemission, the so-called Wigner delay, is discussed from a theoretical stand-point, and it is explained how it relates to the experimental method.

The generation of attosecond pulses can be controlled using two-color laser fields for the high-order harmonic process. Experimental and theoretical results are presented, where the two-color field consists of a fundamental laser field, with an intensity of $\sim 10^{14}\,\mathrm{W/cm^2}$, and a second harmonic field with a relative intensity of $\sim 10\%$. The delay between the two fields can be used to smoothly alter the spectral content, the divergence and the temporal properties of the attosecond pulses. Alternatively, when the second harmonic field is weak, $\sim 0.1\%$ relative intensity, it can be used to probe the one-color high-order harmonic generation process by considering the phase offset of the weak even-order harmonics. The established RABITT method is compared experimentally to the two-color probing technique and inconsistencies are reported close to the cutoff. Theoretical work presented in this thesis, shows that the inconsistencies can be explained using a quantum mechanical model for the two-color high-order harmonic generation. Finally, the transition from many attosecond pulses to few attosecond pulses using a second harmonic field in combination with a few-cycle fundamental laser field is reported.

Populärvetenskaplig sammanfattning

När ljus belyser ett material kan elektroner frigöras via en process som kallas den fotoelektriska effekten. Experiment utförda under slutet av 1800-talet visade att det inte är styrkan på ljuset som avgör om elektroner kan frigöras, det är istället ljusets färg. Rött ljus har en låg frekvens och blått ljus har en hög frekvens, men hur kan denna frekvens spela en så avgörande roll för frigörandet av elektronerna? Einstein förklarade den fotoelektriska effekten 1905 genom att *kvantisera* ljuset: Han antog att ljuset bestod av små partiklar, fotoner, som alla har en exakt energi. En fotons energi antogs vara proportionell mot ljusets frekvens. Elektronerna i materialet kan endast absorbera *en* foton och de kan endast friges om denna foton har tillräckligt med energi för att övervinna bindingsenergin i materialet. Den bindningsenergi som krävs för att frigöra en elektron varierar kraftigt mellan olika material. I denna avhandling frigörs elektroner från gaser som kräver ultraviolett strålning, en frekvens så hög att den inte kan ses av våra ögon. Einsteins arbete blev startskottet för den moderna fysiken och för kvantmekaniken. Experimenten som först påvisade den fotoelektriska effekten är idag mer än hundra år gamla och sedan dess har en enorm teknisk utveckling skett. Lasern uppfanns på 1960-talet och den gjorde experiment möjliga där ljusets styrka kunde ökas dramatiskt. Dessa nya experiment visade att en elektron i ett material kan absorbera två eller fler fotoner om styrkan på ljuset är tillräckligt hög. Lasern, med sin höga intensitet, gjorde det möjligt att studerna icke-linjär optik. Till exempel kan en intensiv röd laserstråle förvandlas till en blå. I denna fundamentala process sammanfogas två röda fotoner till en blå foton. Allt eftersom laserns intensitet ökat har nya fysikaliska effekter kunnat undersökas och förklaras. Under 1990-talet upptäcktes att en hel rad av nya färger, så kallade "övertoner", kan genereras om laserns hela effekt fokuseras på en gas av atomer. Det banbrytande med övertonerna, var att alla ingående färger vara ungefär lika starka. Tidigare experiment hade visat att färgerna med hög frekvens alltid var mycket svagare än de färger med låg frekvens. Övertonernas fotonenergi visade sig vara upp till hundra gånger så stor som den ursprungliga fotonenergin från lasern. En elektron har alltså först absorberat hundra laserfotoner och sedan emitterat en väldigt energirik foton. Övertonsgenerering av detta slag har använts i alla experiment i denna avhandling. Vi har kontrollerat produktionen av övertoner genom att använda två intenstiva laserfält, ett rött och ett blått. En av de många intressanta tillämpningarna av övertonerna är att skapa världens kortaste ljusblixtar. Ljusblixtarna kallas för *attosekundspulser*, eftersom de

varar i ungefär hundra attosekunder. En attosekund förhåller sig till en sekund, så som en sekund förhåller sig till två gånger hela universums ålder (en attosekund är 10^{-18} sekunder). Blixtarna är så korta att all atomär rörelse är fryst i jämförelse. I denna avhandling har vi använt attosekundspulser för att undersöka tidsaspekter hos den fotoelektriska effekten: Hur lång tid tar det för en elektron att lämna sin atom? Går det att mäta denna extremt korta tid med hjälp av attosekundspulser? Kan vi kontrollera elektronens bana på dess väg bort från atomen? Attosekundspulserna öppnar upp dörrarna för tidsupplösta mätningar av kemiska reaktioner och för kontroll av dess kvantmekaniska processer. Att studera den fotoelektriska effekten, det är bara början.

List of Publications

This thesis is based on the following papers, which will be referred to by their roman numerals in the text.

I **Phase Measurement of Resonant Two-Photon Ionization in Helium**
M. Swoboda, T. Fordell, K. Klünder, J. M. Dahlström, M. Miranda, C. Buth, K. J. Schafer, J. Mauritsson, A. L'Huillier, and M. Gisselbrecht.
Phys. Rev. Lett. **104**, 103003 (2010).

II **Probing Single-Photon Ionization on the Attosecond Time Scale**
K. Klünder, J. M. Dahlström, M. Gisselbrecht, T. Fordell, M. Swoboda, D. Guénot, P. Johnsson, J. Caillat, J. Mauritsson, A. Maquet, R. Taïeb, and A. L'Huillier.
Phys. Rev. Lett. **106**, 143002 (2011).

III **Spectral Shaping of Attosecond Pulses using Two-Color Laser Fields**
E. Mansten, J. M. Dahlström, P. Johnsson, M. Swoboda, A. L'Huillier and J. Mauritsson.
New J. Phys. **10**, 083041 (2008).

IV **Interference Effects in Two-Color High-Order Harmonic Generation**
X. He, J. M. Dahlström, R. Rakowski, C. M. Heyl, A. Persson, J. Mauritsson, and A. L'Huillier.
Phys. Rev. A **82**, 033410 (2010).

V **Atomic and Macroscopic Measurements of Attosecond Pulse Trains**
J. M. Dahlström, T. Fordell, E. Mansten, T. Ruchon, M. Swoboda, K. Klünder, M. Gisselbrecht, A. L'Huillier, and J. Mauritsson.
Phys. Rev. A **80**, 033836 (2009).

VI **Quantum Mechanical Approach to Probing the Birth of Attosecond Pulses using a Two-Color Field**
J. M. Dahlström, A. L'Huillier and J. Mauritsson.
J. Phys. B: At. Mol. Opt. Phys. **44**, 095602 (2011).

VII **Intensity Dependence of Laser-Assisted Attosecond Photoionization Spectra**
M. Swoboda, J. M. Dahlström, T. Ruchon, P. Johnsson, J. Mauritsson, A. L'Huillier and K. J. Schafer.
Laser Physics **19**, 1591 (2009).

VIII **Sub-cycle Control of Attosecond Pulse Generation using Two-Colour Laser Fields**
J. Mauritsson, J. M. Dahlström, E. Mansten and T. Fordell.
J. Phys. B: At. Mol. Opt. Phys. **42**, 134003 (2009).

IX **Spectral Signature of Short Attosecond Pulse Trains**
E. Mansten, J. M. Dahlström, J. Mauritsson, T. Ruchon, A. L'Huillier, J. Tate, M. B. Gaarde, P. Eckle, A. Guandalini, M. Holler, F. Schapper, L. Gallmann, and U. Keller.
Phys. Rev. Lett. **102**, 083002 (2009).

Abbreviations

APT	Attosecond Pulse Train
ATI	Above-Threshold Ionization
CC	Continuum–Continuum
CEP	Carrier–Envelope Phase
CPA	Chirped Pulse Amplification
CRAB	Complete Reconstruction of Attosecond Burst
DOG	Double Optical Gate
FEL	Free-Electron Laser
FTPT	First-order Time-dependent Perturbation Theory
FWHM	Full-Width at Half-Maximum
FROG	Frequency-Resolved Optical Gating
GD	Group Delay
HHG	High-order Harmonic Generation
IR	Infrared ($0.004 < \hbar\omega < 1.7$ eV)
MBES	Magnetic Bottle Electron Spectrometer
MCP	Microchannel Plate
RABITT	Reconstruction of Attosecond Beating by Interfering Two-photon Transitions
SAP	Single Attosecond Pulse
SFA	Strong-Field approximation
SPA	Stationary Phase Approximation
STPT	Second-order Time-dependent Perturbation Theory
STS	Simple Trajectory Selection
TDSE	Time-Dependent Schrödinger Equation
TOF	Time Of Flight
VMIS	Velocity Map Imaging Spectrometer
XUV	Extreme Ultraviolet ($10 < \hbar\omega < 124$ eV)
WKB	Wentzel–Kramers–Brillouin

Contents

Papers

Chapter 1

Introduction

1.1 Prologue

When I first entered the Attolab in the basement at the Lund Laser Center, it was as if I had stepped into another world. Huge metal tables were covered with intricate optical devices on which invisible laser beams were bouncing at the speed of light.

"Are we ready to shoot?" There was a steady, rhythmic thunder from the cryo-coolers for the regenerative amplifiers.

"Is the probe beam activated?' It was difficult to see because the room was lit only by the stray light from monitors, and we were all wearing dark laser goggles.

"The gas pressure must be kept steady at three times ten to the minus three microbars." I tried to turn the knob for the gas pressure, but it did not respond. Fog was forming on the inside of my goggles.

"The flow of cooling water must be increased." Another scientist flew out of his chair and started adjusting the level of cooling water.

"That's it, we have nice harmonics in the magnetic bottle!" We began to record the attosecond pulse train and the corresponding RABITT scan started to form on the monitor, pixel by pixel.

Running an attosecond experiment is almost like standing on the command deck of an intergalactic spaceship, I thought.

Work on generating attosecond light pulses was already in progress when I started as a PhD student in the summer of 2007. The shortest pulses ever produced had already been generated and measured in the laboratory where I was starting work. The group was moving towards the control and application of the attosecond pulses. During my PhD studies I have become familiar with the experimental methods required to generate attosecond pulses, but I have mostly worked as a theorist, interpreting the experimental results. In Section 1.2, the fundamental concepts of attophysics are reviewed, and in Section. 1.3, I motivate and provide an outline of the work presented in this thesis.

1.2 Overview of attophysics

This section provides a short historical overview of attophysics. Key components of the work presented in this thesis, such as high-order harmonic generation and attosecond pulse trains, are introduced.

1.2.1 High-order harmonic generation

The work on attosecond light pulses stems from a process discovered in the late 1980s called high-order harmonic generation (HHG) [1, 2]. It was found that a broad comb of equally strong harmonics in the extreme ultraviolet regime (XUV) could be produced by focusing an intense ultrashort infrared (IR) laser pulse into a gas of noble atoms, see Figure 1.1. The typical laser intensity used for HHG is $\sim 10^{14}\,\mathrm{W/cm^2}$ with a wavelength $\sim 800\,\mathrm{nm}$. Harmonic conversion efficiencies as high as one in a million and photon energies in the soft x-ray regime have been obtained [3–8].

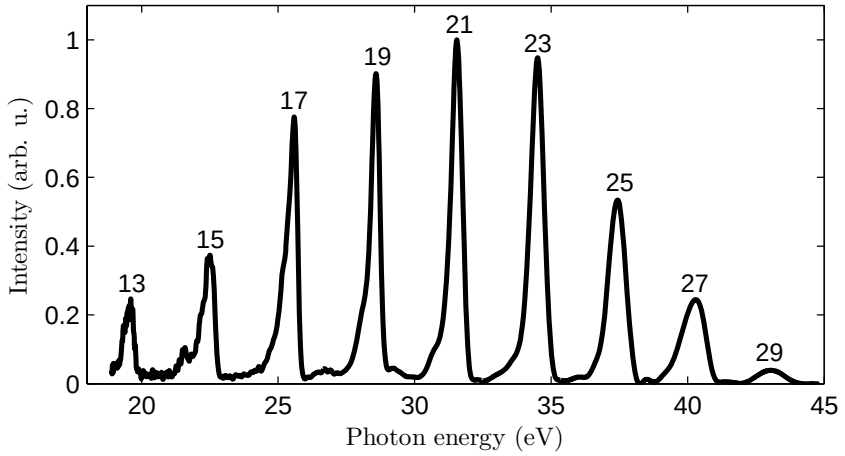

Figure 1.1. *High-order harmonics generated in argon gas and detected using an electron spectrometer. The range of harmonics with comparable intensity (from 13 to 27 in this case) is called the harmonic plateau. After harmonic 29, there is an exponential decrease in the harmonic yield, which is known as the harmonic cutoff. The data were collected for Paper* **V**. *The intensity of the harmonics in the plateau depends on the macroscopic phase matching conditions.*

The cut-off law

Neither the broad comb of high-order harmonics nor their high conversion efficiency can be explained using traditional nonlinear optics, where the laser field is treated as a perturbation [9]. In the perturbative formalism, an increase in harmonic order is always accompanied by a reduction in conversion efficiency; while in HHG, the harmonic plateau contains several harmonic orders of comparable intensity. An empirical *cut-off*

law for the maximal photon energy in the HHG plateau was found to be [10, 11]

$$\hbar\Omega_{co} \approx I_p + 3U_p, \tag{1.1}$$

where I_p is the ionization potential of the atom, and

$$U_p = \frac{e^2 E_0^2}{4m\omega^2} = \frac{e^2\lambda^2 I}{8\pi^2\epsilon_0 c^3 m}, \tag{1.2}$$

is the ponderomotive (wiggle) energy of the electron in the laser field [12]. Using Eqs. 1.1 and 1.2 in the limit $U_p \gg I_p$, the cut-off increases quadratically for longer laser wavelengths, $\hbar\Omega_{co} \propto \lambda^2$, and linearly with the laser intensity, $\hbar\Omega_{co} \propto I$. This scaling has been used to increase the harmonic photon energies into the keV regime using laser fields with longer wavelengths (mid-IR wavelengths) [13–16]. The generation of high-order harmonics was initially explained in three quasiclassical steps, known as the *three-step model*. The three steps are illustrated in Figure 1.2. A more detailed

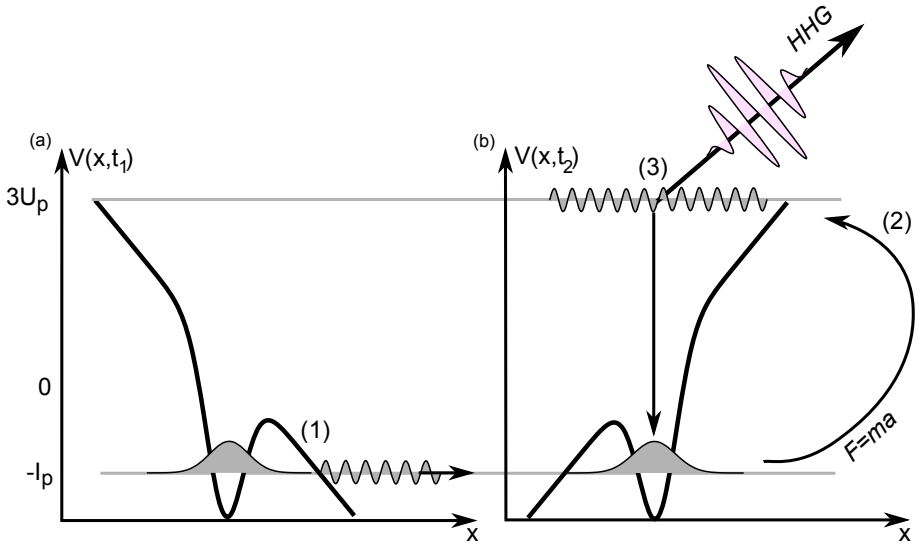

Figure 1.2. *The three-step model for HHG: (1) When the electric field of the laser is large, the electron can tunnel under the Coulomb barrier into the continuum (a). (2) The electron will then accelerate on almost classical trajectories in the laser field (b). (3) Finally, the electron may be driven back to the atom and recombine, emitting a high-order harmonic photon.*

quantum mechanical theory for HHG was published in 1994 [17], showing that the quasiclassical trajectories could be obtained from the Schrödinger equation using the strong field approximation (SFA). The theory explained why the harmonics were of comparable strength, but it also revealed that there are several possible ways in which the electron can return to the atom. These lead to quantum interference and to a

complicated pulse structure with several bursts being emitted from each atom. The problem of multiple bursts could be circumvented experimentally through macroscopic phase matching, where the emission from the shortest of the electron trajectories could be selected and enhanced.

It was soon understood that such high-order harmonics could support light with pulse durations on the attosecond timescale, *i.e.* shorter than any light pulses ever produced [18, 19]. Creating these attosecond pulses would, however, not be easy because it required control of the complex harmonic phase over a large spectral bandwidth [20]. Another considerable challenge was to devise a scheme to measure the duration of the pulses. Existing methods used in traditional ultrafast optics could not be directly applied due to the short wavelength and relatively low intensity of the harmonics.

1.2.2 Attosecond pulse trains

In 2001, more than a decade after the first HHG, the first attosecond pulse train (APT) was observed using a scheme called RABITT (Reconstruction of Attosecond Beating by Interfering Two-photon Transitions) [21, 22]. The attosecond pulse duration was 250 as $= 250\times10^{-18}$ s, corresponding to $\sim 1/10$ of the laser period, and to $\sim 1/100$ of the laser pulse duration used for HHG. Two attosecond pulses were produced per oscillation of the laser field, resulting in a train of ~ 30 pulses in the total APT.

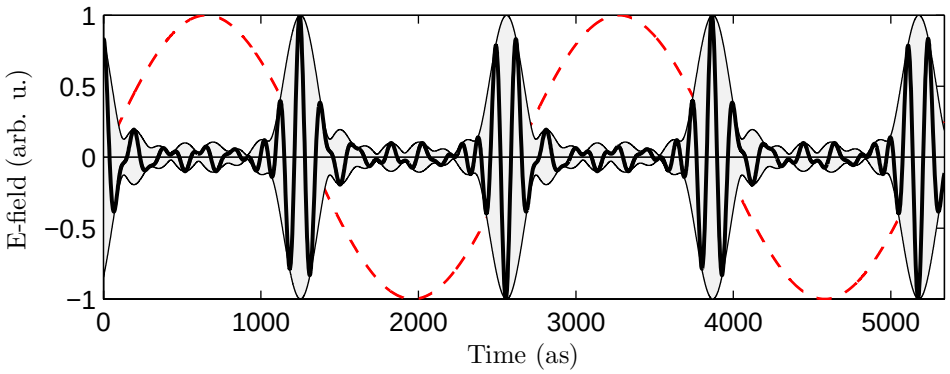

Figure 1.3. *A train of attosecond pulses (gray area). The attosecond pulse duration is a fraction of the fundamental laser period (red dashed curve). The pulse separation is half an IR laser period and the sign of the attosecond electric field (heavy black curve) changes from pulse to pulse. The absolute phase of the electric field is arbitrary relative to both the IR and the attosecond envelope (light black curve). The data was collected for Paper* **V** *using the RABITT scheme.*

1.2.3 Single attosecond pulses

Making the IR pulse shorter naturally leads to fewer attosecond pulses. It was soon demonstrated that a single attosecond pulse (SAP) could be generated using a few-

cycle IR pulse, $\sim 5\,\text{fs}$ [23]. The basic properties of the SAP can be determined using the attosecond streak camera method [24], while complete characterization requires the used of the FROG–CRAB scheme (Frequency Resolved Optical Gating – Complete Reconstruction of Attosecond Bursts) [25]. For such short IR pulses, the carrier envelope phase (CEP), is an important parameter that must be controlled. The generation of a SAP can be changed into the generation of two attosecond pulses by carefully tuning the CEP of the laser field [26]. The shortest SAP to date is 80 as [27].

A SAP can also be generated using slightly longer few-cycle laser pulses if an optical gating method is applied [28, 29]. Combining the two-color optical gate with a polarization gate leads to double optical gating (DOG), which relaxes the pulse duration requirements further [30, 31], but introduces more optical elements in the beam path.

Why attosecond pulses?

From a technical standpoint, attosecond pulses are interesting because they are shorter than any pulses created by conventional optical lasers. Physically, we understand this because the duration of a light pulse can not be shorter than its own period. Optical and IR lasers have a period that is longer than a femtosecond, leading to the so-called *femtosecond barrier* for ultrashort pulses. The power needed to drive a laser scales strongly with the photon energy, $P \propto \omega^5$, which effectively prevents the conventional laser scheme from going beyond optical wavelengths [14].

Mathematically, we can show that a pulse intensity envelope has a minimal duration proportional to the inverse of the supporting coherent bandwidth,

$$\tau > \frac{C}{\Delta\omega} \approx \frac{C}{2\pi}\frac{\lambda^2}{c\Delta\lambda}, \tag{1.3}$$

where $\Delta\omega$ (and $\Delta\lambda \ll \lambda$) is the intensity bandwidth of the light. C is a numerical constant equal to $4\ln 2$ for the full-width at half-maximum (FWHM) of Gaussian intensity envelopes. The minimal pulse duration, called the *Fourier-limited* pulse duration, occurs when all the spectral components are compressed. The propagation of a short pulse in a medium leads to dispersion of the pulse and an increase in duration. The attosecond pulses produced through HHG can overcome the femtosecond barrier not only because they have a much shorter wavelength than optical light, but also because they have a broad coherent bandwidth. Using Equation 1.3 we find that a pulse of $\tau \approx 80\,\text{as}$ duration must be supported by a bandwidth of $\hbar\Delta\omega > 20\,\text{eV}$. It is interesting to compare the coherent bandwidth of the laser used for HHG with the bandwidth of the attosecond pulses being generated. The IR laser pulses used in this work for HHG have a duration of 30 fs and a bandwidth of 60 meV; while typical attosecond pulses are 100 as with a bandwidth of 15 eV, corresponding to ten harmonic orders. During the HHG process the coherent bandwidth is increased by a factor of 250 from laser to high-order harmonics.

Why are subfemtosecond pulses not generated at large accelerator facilities, such as synchrotrons, where an extremely short wavelength (XUV or X-ray) is easily achievable? Accelerators provide short-wavelength light, but the light emitted is normally not coherent and the light pulse duration is then limited by the incoherent electron bunches, so-called "buckets", in the accelerator. Intense coherent radiation can, however, be produced at accelerator facilities if the relativistic electron beam is propagated

into an undulator, an arrangement consisting of magnets with alternating polarity. This setup is called a free electron laser (FEL), and it can produce extremely intense, tunable and coherent light pulses. A problem associated with current FELs is the difficulty in synchronizing them to external probes. An important advantage of XUV-attosecond pulses from HHG is that they are are naturally synchronized to the fundamental laser pulse, making it easier to perform time-dependent experiments, such as cross-correlations or pump–probe experiments. Schemes where HHG is used to seed the FEL are being investigated at many facilities and may lead to a similar natural synchronization between the IR and the XUV light [32, 33].

Attosecond XUV pulses from HHG are more than a new table-top method of obtaining coherent light for traditional spectroscopy in the water window,[1] because the attosecond pulses have a duration that approaches the atomic unit of time, 24 as. This corresponds to the timescale of electronic motion in atomic systems. Being able to study atoms and molecules and control chemical reactions on the electronic timescale has signaled the start of a new scientific era called *attoscience* [34–36].

[1] Light in the XUV water window (43-80 eV) is of interest in the study of biological systems because the light is more absorbed by carbon than by water.

1.3 Motivation and outline of this thesis

The work presented in this thesis is based on nine papers (Papers **I**–**IX**), and three theoretical chapters (Chapters 2–4). The papers contain both experimental and theoretical results, while the chapters detail the more theoretical aspects of the work.

The aim of this scientific work is three-fold: first, to probe various atomic processes on the attosecond timescale using the temporal resolution provided by attosecond pulses; second, to investigate how the generation of attosecond XUV pulses can be controlled using 2-color laser fields for HHG; third, to compare established characterization methods for attosecond pulses with more recently developed methods. In all three of these, the experimental efforts have been strongly complemented with theoretical work.

The theoretical work was focused on finding *interpretations* of the experimental results, rather than laborious numerical simulations. This is especially clear in Papers **I** and **II**, where the analytical work led to a better understanding of the photoionization process in the attosecond timedomain. The appropriate theory to describe these experiments is rooted in a combination of optics and atomic scattering theory, which is bridged in Chapters 2 and 3. The aim of the work in Chapter 2 is to derive the propagation of attosecond light pulses and ultrafast nonrelativistic electron pulses in a common formalism, where the similarities and differences between the two kinds of pulses are identified. The aim of the work in Chapter 3 is to theoretically treat the photoionization process, and to account for attosecond delays of the emitted photoelectrons.

Control of attosecond pulse generation is demonstrated in Papers **III** and **IV**, where a strong second-harmonic laser field is used in addition to the strong fundamental laser field. The experimental results are well reproduced with the strong field approximation (SFA) using a simple trajectory selection method, which is described in Chapter 4.

Experimental work on the characterization of attosecond pulses is presented in Paper **V**, where the RABITT method is compared to a two-color *in situ* method [37]. The theoretical work presented in Paper **VI** further examines the reliability of the two-color *in situ* method. In Paper **VII**, a new version of the RABITT method is experimentally demonstrated, where higher-order IR transitions are employed to gain information about the attosecond pulses.

Finally, the work presented in Papers **VIII** and **IX** deals with the transition from APT to SAP using the control aspects of two-color HHG. Being able to control the temporal properties of the attosecond pulses and the number of attosecond pulses is important for the versatility of the generation process and for future applications. A common summary and outlook of all the papers and theoretical chapters is given in Chapter 5.

The experimental setup used to produce attosecond pulses at the Lund Laser Center is reviewed in Section 1.4. In the following chapters, the focus is on the theoretical aspects of attosecond experiments and the generation of attosecond pulses.

1.4 Setup

A schematic diagram of the setup used for the experimental work presented in this thesis, is shown in Figure 1.4. The "boxes" in the setup are briefly explained below.[2]

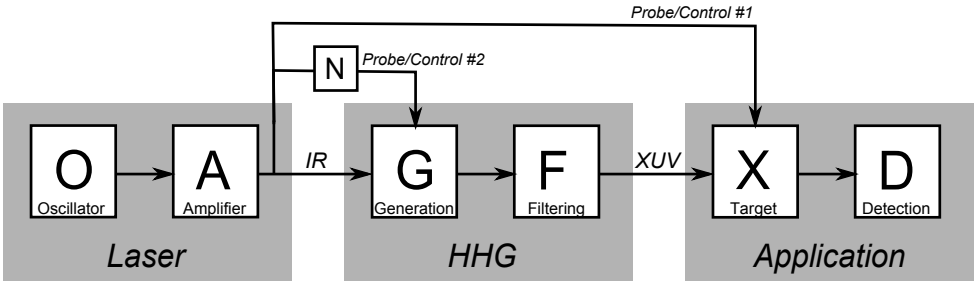

Figure 1.4. *A schematic block diagram over the setup used for generation and application of attosecond pulses.*

1.4.1 Laser system

The laser system is a titanium sapphire chirped pulse amplification (CPA) system [38]. The first box in the laser system is the oscillator, [**O**]. It is currently a *Rainbow* system from Femtolasers, which uses chirped mirrors for dispersion management [39, 40]. The oscillator can be mode locked, and can produce 2.5 nJ pulses at a repetition rate of 80 MHz. The central photon energy is 1.5 eV and the laser bandwidth is 500 meV. The laser pulses from the oscillator are approximately 7 fs with a CEP that can be stabilized using an integrated feedback loop [41, 42]. After the oscillator there is a so-called *Dazzler* from Fastlite, which is an acousto-optic programmable dispersive filter, that allows for control of the phase and amplitude of the oscillator output. The bandwidth of the laser pulses used after the Dazzler is reduced to 150 meV.

The second box in the laser system is the amplification stage, [**A**]. The pulses are stretched using gratings to a duration of 200 ps, and the repetition rate is reduced to 1 kHz using a Pockels cell. Amplification is done in two stages. The pulses pass through a regenerative amplifier, which is pumped by a frequency-doubled 30 W diode-pumped neodymium-doped yttrium lithium fluoride laser. The pulses typically make 12 passes in this regenerative amplifier gaining a pulse energy of 0.5 mJ before continuing to the next amplification step. Here, the pulse energy is increased to 8 mJ using a cryogenically-cooled 5-pass amplifier. Finally, the pulse is compressed using gratings to a duration of 35 fs.

[2] This is the setup used in the Attolab at Lund Laser Center for the work presented in Papers **I**, **II**, **III**, **V**, **VII**, and **VIII**. The experimental work presented in Papers **IV** and **VI** was carried out at the 10 Hz beam line from the TW laser at the Lund Laser Center, while, the experimental work presented in Paper **IX** was carried out at ETH in Zürich.

1.4.2 High-order harmonic chamber

Next, the beam is split into two parts: the main part (80%) is used for HHG in the generation chamber [**G**], while the smaller fraction (20%) can be used for probing and/or controlling the HHG process or the target atoms in the application chamber. The beam is reduced using a solid aperture with a diameter ranging from 10 mm to 15 mm depending on the intensity requirements of the gas used for HHG. Noble atoms have a high binding potential and require intensities on the order of 10^{14} W/cm^2 for HHG. To reach these high intensities, the main beam is focused by a mirror with a focal length ranging from 30 cm to 75 cm (50 cm is most often used). The focused beam passes through a 1-kHz pulsed valve gas target [43] where HHG occurs. The most common geometry of the gas target is a narrow cylinder 6 mm in length. Choosing the best length of the gas target and the best position relative to the focus of the laser beam is important to obtain the highest conversion efficiency through macroscopic phase matching of the HHG process. The pressure in the gas target is ~ 10 mbar, while the backing pressure in the generation chamber is kept as low as possible, typically 3×10^{-3} mbar.

The XUV and IR fields now co-propagate and the IR field must be removed in order to reveal the XUV-attosecond pulse structure. This is achieved by spatial and spectral filtering, [**F**]. First, the pulses pass through a differential pump hole with a diameter of 2 mm, which removes the more divergent parts of the XUV and the IR beams. This reduces the total IR energy and "cleans" the phase of the XUV pulse (which may vary spatially due to contributions from longer quantum trajectories). After the differential pumping hole, the backing pressure is reduced to $\sim 10^{-5}$ mbar. Second, the pulses pass through a thin metallic foil which transmits the XUV while the remaining IR is blocked. It is important to choose a suitable metal for the desired spectral region. Most metals work as band pass filters in the XUV, and some metals allow a broad spectral range of harmonics to pass through. A beneficial side effect of the metallic foils is that they can simultaneously compress the attosecond pulses [44]. The low-energy part of the band pass yields "anomalous" dispersion while the high-energy part of the transmission window yields normal dispersion. By choosing an appropriate thickness of the foil, the attosecond pulses can be compressed down to the Fourier limit, as demonstrated in Paper **V**. The standard choice of atom–foil combination used in the Attolab in Lund is Ar–Al (argon gas and aluminum foil), because the good conversion efficiency of Ar and the high transmission of Al lead to a reliable output. The low pass of the Al filter is at 20 eV while the high pass is at 72 eV [45]. This atom–foil combination typically leads to a comb of harmonics ranging from order 13 to 27, as shown in Figure 1.1. In this case, the lower onset is due to the Al filter while the upper cut-off is set by the HHG process. Other atom–foil combinations are used when higher harmonic orders are needed or a specific spectral range is required, as in the work presented in Paper **II**, where a 200 nm chromium foil was used.

1.4.3 Applications

The XUV beam is focused into the application chamber using a grazing incidence toroidal mirror, where it photoionizes a target gas, [**X**]. The ejected electrons are detected, [**D**], using a magnetic bottle electron spectrometer (MBES) [46] or a velocity

map imaging spectrometer (VMIS) [47]. The MBES is a time-of-flight (TOF) spectrometer, which collects half of the photoelectrons (2π solid angle) using a magnetic parallelization mechanism. The electrons are photoionized in the presence of a strong magnetic field (~ 1 T) which is directed along of the flight tube. As the field strength is adiabatically reduced to a constant value ($\sim 1\,\mathrm{mT}$), all electrons with a velocity component in the direction of the flight tube will gradually turn and propagate along the flight tube. The arrival time of the electrons at the end of the tube depends on their initial velocity. A typical photoelectron energy of 20 eV leads to a velocity of 2.7×10^6 m/s. For a flight tube of 60 cm, this implies a time of flight of 220 ns. The TOF signal is recorded using the integrated signal from a microchannel plate (MCP). The backing pressure in the MBES is $\sim 10^{-4}$ mbar. The MBES was used in Papers **I**, **II**, **V** and **VIII**.

Unlike the MBES, the VMIS is *not* a TOF system. The VMIS measures the transverse momentum (p_x, p_y) of the photoelectrons. In the VMIS the focused XUV beam is crossed with a pulsed atomic beam in a strong electric field ($\sim 1\,\mathrm{kV}$, along $\hat{z}$). Once liberated, the photoelectrons are accelerated in the electric field towards the imaging MCP detector coupled to a phosphor screen, which is read out by a CCD camera. The accelerating electric field is set by two electrodes: the repeller and the extractor, $V_R < V_E < 0$. The signal on the MCP is a 2D projection of the 3D momentum distribution. Assuming azimuthal symmetry, the 3D momentum distribution of the photoelectrons can be retrieved using an iterative inversion algorithm [48]. The VMIS was used in Paper **III** and as a complement in the other papers. Both the MBES and the VMIS can be used for cross-correlation experiments where a probe/control field is simultaneously present in the ionization process, [**X**]. The probe/control field can be used to extract temporal information about the XUV pulses.

Alternatively, the XUV pulses can be directly detected using a XUV photon spectrometer at [**D**] without any interaction in [**X**]. This has the advantage of resolving the spatial profile of the XUV beam, but lacks the possibility of obtaining any temporal information about the XUV pulse using on-target cross-correlation techniques. XUV spectrometers were used in the work presented in Papers **IV**, **VI** and **IX**.

Chapter 2

Ultrafast wave packets

This thesis presents experimental measurements of short delays, either for XUV pulses as they propagate through dispersive media [Paper **V**], or for nonrelativistic photoelectrons as they escape from the atomic potential [Paper **II**]. This Chapter provides a common theoretical background to these extremely short time delays. In brief, we will compare the dispersion relations of XUV light and nonrelativistic electrons.

Starting from the Maxwell equations, a one-dimensional wave equation for XUV attosecond light pulses is derived in Section 2.1. Short light pulses can be described as a superposition of monochromatic light waves [Sec. 2.1.1] and the propagation of the pulse can be understood in terms of the phase of these monochromatic waves. The attosecond pulses can be strongly stretched in time by a dispersive medium, but conversely, it is also possible to compress a stretched pulse using a medium with negative (anomalous) dispersion [Sec. 2.1.2]. The stationary phase approximation (SPA) is introduced and applied to the propagation of attosecond pulses in Section 2.1.3.

The attosecond pulses can be used to ionize atoms at extremely well-defined times, but how do the resulting photoelectron pulses behave after the ionization event? In Section 2.2, we perform a wave packet analysis of the emitted photoelectrons. The electron wave packets consist of superpositions of time-independent electron states. These states are studied using a semiclassical approximation in Section 2.2.1. Finally, the transition of a quantum mechanical photoelectron wave packet into a classical momentum distribution is derived using the SPA [Secs. 2.2.2 & 2.2.3].

2.1 Attosecond wave packets of light

The propagation of an attosecond XUV light pulse in a dielectric medium is described by the Maxwell equations [9, 49]

$$\nabla \cdot \vec{\tilde{E}} = -\frac{1}{\epsilon_0}\nabla \cdot \vec{\tilde{P}} \equiv \frac{\rho}{\epsilon_0} \tag{2.1}$$

$$\nabla \cdot \vec{\tilde{B}} = 0 \tag{2.2}$$

$$\nabla \times \vec{\tilde{E}} = -\frac{\partial \vec{\tilde{B}}}{\partial t} \tag{2.3}$$

$$\nabla \times \vec{\tilde{B}} = \frac{1}{\epsilon_0 c^2}\frac{\partial}{\partial t}\left\{\vec{\tilde{P}} + \epsilon_0 \vec{\tilde{E}}\right\}, \tag{2.4}$$

where $\vec{\tilde{E}}$ and $\vec{\tilde{B}}$ are the electric and magnetic fields in space–time, and where the electric permittivity, ϵ_0, and the magnetic permeability, μ_0, are related to the speed of light by $c = 1/\sqrt{\epsilon_0\mu_0}$. The polarization is described by $\vec{\tilde{P}}$, and the magnetization of the material has been neglected. Taking the curl of the Maxwell-Faraday equation (Eq. 2.3) leads to the famous wave equation for the electric field

$$\nabla^2 \vec{\tilde{E}} - \frac{1}{c^2}\frac{\partial \vec{\tilde{E}}}{\partial t} = \mu_0 \frac{\partial^2 \vec{\tilde{P}}}{\partial t^2} - \frac{1}{\epsilon_0}\nabla(\nabla \cdot \vec{\tilde{P}}). \tag{2.5}$$

A similar equation can be derived for the magnetic field yielding the magnetic contribution to the electromagnetic field, but the magnetic field will not be considered in following. In free space, $\vec{\tilde{P}} = 0$, and the wave equation [Eq. 2.5] yields waves traveling at the speed of light, c. In a dielectric material, the right-hand-side is non-zero and it can be understood as a polarization source term for the wave equation. The last term in Equation 2.5 can often be neglected because it vanishes for isotropic media and for plane waves.

The wave equation can be recast into a *time-independent form* using the orthogonality of the Fourier integral expansions of the time-dependent fields

$$\nabla^2 \vec{E} + \frac{\omega^2}{c^2}\vec{E} = -\frac{1}{\epsilon_0}\frac{\omega^2}{c^2}\vec{P} - \frac{1}{\epsilon_0}\nabla(\nabla \cdot \vec{P}), \tag{2.6}$$

where the electric field is expanded as a superposition of monochromatic waves

$$\vec{\tilde{E}}(t, \vec{r}) = \frac{1}{2\pi}\int d\omega\ \vec{E}(\omega, \vec{r})e^{-i\omega t}, \tag{2.7}$$

and the polarization is given by

$$\vec{\tilde{P}}(t, \vec{r}) = \frac{1}{2\pi}\int d\omega\ \vec{P}(\omega, \vec{r})e^{-i\omega t}. \tag{2.8}$$

where the monochromatic fields in space–frequency are written without a tilde, *e.g.* $E(\omega)$. Finding solutions to Equation 2.6 may be easy or difficult depending on the polarization term. The polarization induced by a weak attosecond pulse in an isotropic medium is given by the linear response

$$\vec{P}(\omega, \vec{r}) = \epsilon_0 \chi^{(L)}(\omega, \vec{r})\vec{E}(\omega, \vec{r}), \tag{2.9}$$

where the linear susceptibility, $\chi^{(L)} \equiv \chi^{(1)}$, may depend on space due to changing density or composition of the medium. Nonlinear polarization can be neglected if it is assumed that the intensity of the attosecond pulse is low and that there are no other fields that coherently alter the polarization. Nonlinear polarization must be taken into account in the case of an XUV beam co-propagating with an intense IR field, as in the HHG process. The IR field will induce an extreme nonlinear polarization, $\chi^{(NL)}$, which can either enhance of reduce the intensity of the XUV beam depending on phase matching conditions. The origin of this extreme nonlinear polarization is discussed in Chapter 4.

2.1.1 Wave propagation of XUV light

The propagation of attosecond light pulses is governed by the frequency-dependent phase variation of the monochromatic waves. The following ansatz, $\vec{E}(\omega, \vec{r}) \propto \exp\left[i\phi(\omega, x)\right] \hat{z}$, is used to obtain a differential equation for the phase of monochromatic waves

$$i\frac{\partial^2 \phi}{\partial x^2} - \left(\frac{\partial \phi}{\partial x}\right)^2 + \frac{\omega^2}{c^2} = -\frac{\omega^2}{c^2}\chi^{(1)}. \tag{2.10}$$

For slow variations of the material, we expect $|\partial^2\phi/\partial x^2| \ll |\partial\phi/\partial x|^2$, which leads to a simpler differential equation,

$$\frac{\partial \phi}{\partial x} = \frac{\omega}{c}\sqrt{1+\chi^{(1)}}. \tag{2.11}$$

The phase of the electric field can be directly integrated as

$$\phi(\omega, x) = \frac{\omega}{c}\int_{-\infty}^{x} dx' \ \sqrt{1+\chi^{(1)}(x')} \equiv \frac{\omega}{c}\int_{-\infty}^{x} dx' \ n(x'), \tag{2.12}$$

where $n(x)$ is the *local refractive index* of the material. This is an excellent approximation for the phase of a monochromatic field passing through a dilute gas cloud. The asymptotic phase difference between propagation through a finite material and free propagation can be written as

$$\delta(\omega) = \lim_{x\to\infty} \frac{\omega}{c}\int_{-\infty}^{x} dx' \ \left[n(x') - 1\right]. \tag{2.13}$$

A frequency-independent refractive index leads to a linear phase shift in frequency. This linear phase shift causes a time delay, $\tau = \delta/\omega$, of the attosecond pulse [Eq. 2.7],

$$\tilde{E}(t-\tau, x) = \frac{1}{2\pi}\int d\omega \ E(\omega, x)e^{-i\omega[t-\tau]}, \tag{2.14}$$

compared to free-space propagation. Equation 2.14 is a direct application of the well-known *shift theorem* of Fourier transforms.

Example: A constant refractive index

The asymptotic phase acquired by an attosecond pulse passing through a material of length, L, with a constant refractive index, $n = \sqrt{1+\chi^{(1)}}$, is

$$\delta \ = \ \frac{\omega}{c}\left[n-1\right]L \ = \ \frac{2\pi}{\lambda}\left[n-1\right]L \ \approx \ \frac{\omega}{2c}\,\chi^{(1)}L, \tag{2.15}$$

where $\lambda = 2\pi c/\omega$ is the wavelength of the light wave in vacuum. The corresponding delay of the pulse is $\tau = [n-1]L/c$.

Dispersion

So far we have assumed that the linear response is frequency-independent. This is an adequate approximation for narrow-bandwidth laser pulses, but it is not a good approximation for attosecond pulses which have a large spectral bandwidth. In a more realistic model, the material will be dispersive, *i.e.* the refractive index will be *frequency-dependent*, $n(\omega, x)$ [45, 50, 51]. This leads to a *nonlinear* frequency dependence of the asymptotic phase [Eq. 2.13] and to deformations of the attosecond pulse in the time domain. It is common to develop the asymptotic (spectral) phase in a Taylor series,

$$\delta(\omega) = \delta(\omega_0) + \sum_{n=1}^{\infty} \frac{1}{n!} \frac{\partial \delta}{\partial \omega}\bigg|_{\omega_0} (\omega - \omega_0)^n, \tag{2.16}$$

around the central frequency of the pulse, ω_0. We will use the following short-hand notation, $\partial\delta/\partial\omega|_{\omega_0} = \delta'(\omega_0) = \delta'_0$, for the spectral derivatives. In most practical cases it is sufficient to consider the first few terms in this expansion. We have already seen that the zero-order term determines the overall phase of the pulse, and that the first order term determines the delay of the pulse. In the optical regime, most materials have a positive (normal) dispersion, which means that the refractive index increases as a function of frequency. This implies longer delays for higher frequency pulses passing through the same medium. Close to resonances the refractive index has a negative (anomalous) dispersion. The refractive index of argon gas at XUV frequencies is reviewed in Figure 2.1.

The *group delay* (GD) is defined as

$$\tau_{GD}(\omega) = \frac{\partial \delta}{\partial \omega}, \tag{2.17}$$

and it represents the delay of a certain spectral region of the attosecond pulse centered at ω. The nonlinear variation of δ over ω causes different spectral parts of the pulse to be delayed by different amounts, thus leading to an increase in pulse duration.

Example: Dispersion through a plasma

Consider an XUV wave after traveling through a plasma, where

$$n_p(\omega) \;=\; \sqrt{1 - \left(\frac{\omega_p}{\omega}\right)^2} \;\approx\; 1 - \frac{1}{2}\left(\frac{\omega_p}{\omega}\right)^2, \tag{2.18}$$

is the refractive index of the plasma, $\omega_p = \sqrt{Ne^2/\epsilon_0 m}$, is the plasma frequency, and N the concentration of free electrons in the plasma [54]. Using Equation 2.15, the asymptotic phase becomes negative

$$\delta_p(\omega) \;=\; \frac{\omega}{c}\left[n_p(\omega) - 1\right] L \;\approx\; -\frac{1}{2}\frac{\omega_p^2}{c}\frac{L}{\omega}, \tag{2.19}$$

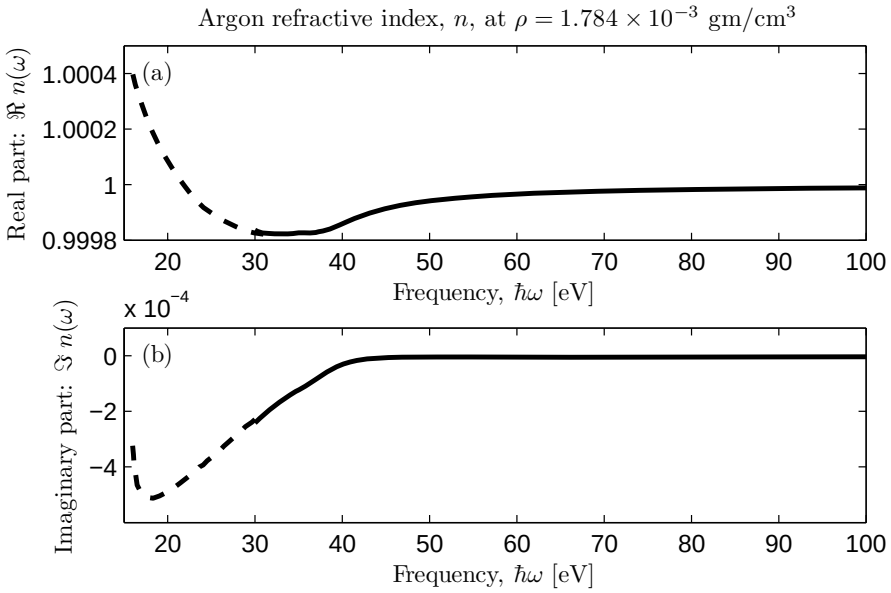

Figure 2.1. *Real part (a) and imaginary part (b) of the refractive index for argon gas (Ar) at XUV frequencies. Above ∼38 eV, the dispersion of Argon is normal with a refractive index that increases with frequency, while below ∼30 eV the argon gas has negative (anomalous) dispersion. Argon absorbs (has a negative imaginary refractive index) below ∼42 eV. Above ∼20 eV, the real part of the refractive index is less than one, which results in a superluminal phase velocity, and the refractive index approaches one as the frequency is increased further. The data above 30 eV is experimental [line] [52], while the data close to threshold is theoretical [dashed] [53]. The refractive index of Argon at optical wavelengths is larger than one.*

which implies that the phase velocity of the monochromatic field is *faster* than c (superluminal). The corresponding group delay is, however, positive

$$\tau_{GD} = \frac{\partial \delta_p}{\partial \omega} \approx \frac{1}{2}\frac{\omega_p^2}{c}\frac{L}{\omega^2}, \tag{2.20}$$

which reassures us that any light pulse is delayed by the plasma, and that it travels at a speed less than c. The superluminal phase velocity can be controlled by increasing or decreasing the density of the plasma.

In a neutral medium of argon the refractive index of the laser, $n_0(\omega)$, and the XUV, $n_0(\Omega)$, are different, $n_0(\omega) > 1 > n_0(\Omega)$ [Fig. 2.1]. This implies that the phase of the fields travel at different speeds. In the HHG process, it is possible to balance the effective refractive indices by ionizing the medium and creating the right amount of plasma to achieve phase matching, $n(\omega) = n(\Omega)$, where the effective refractive of the laser field is $n(\omega) \approx n_0(\omega) + n_p(\omega)$ and the effective refractive index of the XUV light is $n(\Omega) \approx n_0(\Omega)$, where n_0 denotes the neutral refractive index. Increasing the laser intensity further will result in more plasma and an overcompensation of the refractive index, $n(\omega) < n(\Omega)$.

2.1.2 Attosecond pulse propagation

In the following, we will assume that the pulse has passed through a medium and acquired a spectral phase, $\delta(\omega)$. The time domain electric field [Eq. 2.7] is

$$\tilde{E}(t) = \frac{E_0}{2\pi} \int d\omega \ \exp\left[i(\delta(\omega) - \omega t) - g(\omega - \omega_0)^2\right], \tag{2.21}$$

where a Gaussian spectral envelope is assumed: $\vec{E}(\omega) \propto \exp\left[-g(\omega - \omega_0)^2\right] \hat{z}$, where $g = 2\ln(2)/\Delta\omega^2$, corresponding to a FWHM bandwidth $\Delta\omega$, centered at ω_0. The time domain electric field can be integrated analytically, using the expansion in Equation 2.16 up to second order

$$\tilde{E}(t) = \frac{E_0}{2\pi}\sqrt{\frac{\pi}{\gamma}} \exp\left[i(\delta_0 - \omega_0 t) - \frac{(\delta_0' - t)^2}{4\gamma}\right], \tag{2.22}$$

where $\gamma = g - i\delta_0''/2$ is a complex number. The intensity envelope of the pulse is calculated as the square of the electric field,

$$\tilde{I}(t) = \frac{cn\epsilon_0}{2} \ |\tilde{E}(t)|^2 \propto \frac{1}{|\Delta t|} \exp\left[-\frac{(\delta_0' - t)^2}{\Delta t^2}\right]. \tag{2.23}$$

The attosecond pulse is a Gaussian with a duration (intensity FWHM) equal to

$$\begin{aligned} \tau &= 2\sqrt{\ln(2)}\ \Delta t \\ &= 2\sqrt{2\ln(2)}\ \sqrt{\frac{g^2 + \delta''(\omega_0)^2/4}{g}} \\ &= 2\sqrt{2\ln(2)}\ \sqrt{\frac{2\ln(2)}{\Delta\omega^2} + \frac{\Delta\omega^2}{2\ln(2)}\frac{\delta_0''}{4}}, \end{aligned} \tag{2.24}$$

which depends on both the bandwidth, $\Delta\omega$, and the spectral chirp, δ_0'', of the pulse. The shortest attosecond pulse duration, $\tau = 4\ln(2)/\Delta\omega$, occurs for $\delta_0'' = 0$, which is referred to as the *Fourier limit*. Increasing the spectral bandwidth reduces the pulse duration. In the case of a large spectral chirp, the pulse duration is $\tau \approx \Delta\omega\sqrt{\delta_0''}$, we see that the pulse duration grows linearly with the bandwidth of the pulse. In the case of attosecond pulses, which have a *very* large spectral bandwidth, this means that extreme care must be taken to remove or compensate for all dispersive material. Paper **V** describes an experimental study in which the GD of attosecond pulses can be controlled by simply changing the density of the gas where they are produced. A higher gas pressure implies more dispersion, but in the present case, phase matching and absorption also play important roles. When present, higher order dispersive terms will deform the pulse in a more complicated way, leading to further broadening and an asymmetric intensity envelope.

Temporal chirp

The temporal phase of the electric field is defined as

$$\tilde{\phi}(t) = \arg\left[\tilde{E}(t)\right]. \tag{2.25}$$

Using Equation 2.22 for the case of a Gaussian pulse we find a constant temporal chirp

$$\tilde{\phi}''(t) \equiv \frac{\partial^2}{\partial t^2} \arg\left[\tilde{E}(t)\right] = \frac{1}{4}\frac{\delta_0''}{|\gamma|^2} = \frac{\delta_0''}{{\delta_0''}^2 + (2g)^2}, \tag{2.26}$$

which is related to both the spectral chirp and the bandwidth of the pulse. A constant temporal chirp implies a linear variation of the instantaneous frequency of the pulse, but there is not necessarily one-to-one mapping between the instantaneous frequency and the GD. In the case of a Fourier-limited pulse, $\delta_0'' = 0$, the instantaneous frequency is constant. In the limit of large spectral chirp, ${\delta_0''}^2 \gg (2g)^2$, we find $\tilde{\phi}''(t) = 1/\delta_0''$, *i.e.* that the temporal chirp is the inverted spectral chirp.

Attosecond pulse trains

So far, we have considered the propagation of a SAP, but the experimental work presented in this thesis [Papers **I**, **II**, **V** and **VII**] employed APTs, *i.e.* periodic sequences of attosecond pulses. APTs arise naturally from the HHG process when the driving laser field is many periods long. The train contains two pulses per period of the fundamental field. These two attosecond pulses are identical, except that their electric fields have opposite sign. Dispersion modifies the attosecond pulses in the APT as if they were SAPs. Uncompensated dispersion can lead to a temporal overlap between adjacent attosecond pulses in the APT, when the pulse duration increases beyond a half-period of the fundamental laser field. An *ideal* APT can be written as a Fourier sum, *i.e.* as a discrete version of Equation 2.7, over all high-order harmonics

$$\tilde{E}(t) = \sum_{q:odd} |E_q| \exp\left[i\delta_q - iq\omega t\right], \tag{2.27}$$

where q is odd because only odd harmonics are generated from HHG due to parity reasons. *Ideal* indicates that Equation 2.27 leads to an APT that extends to infinity, while an actual APT will have a duration comparable to that of the fundamental laser field [55, 56]. The subcycle behavior of the ideal APT can, however, be understood as an average subcycle pulse structure in the actual APT. Papers **III**, **IV**, **VIII** and **IX** present experiments carried out using APT with one pulse per period of the fundamental field. The generation of these APTs is discussed further in Chapter 4.

Example: Compression of attosecond pulses using metallic foils

Attosecond pulses can be compressed in time using thin metallic foils [44, 57, 58]. In Figure 2.2, we present experimental data from Paper **V**, where attosecond pulses are compressed after propagating through a 400 nm thin aluminum foil. The foil provides negative dispersion in the low-energy part of the metallic transmission window. The high-energy part of the transmission window provides positive dispersion. Attosecond pulses are generated with a positive intrinsic chirp from the HHG process. Fourier-limited attosecond pulses were generated in the experiment by compensating for the intrinsic positive chirp of the HHG process by the negative dispersion provided by the low-energy part of the metallic transmission window. Notice the structure of the APT, with two pulses per period of the fundamental laser field. Note also, that the electric field of the two adjacent pulses have different signs.

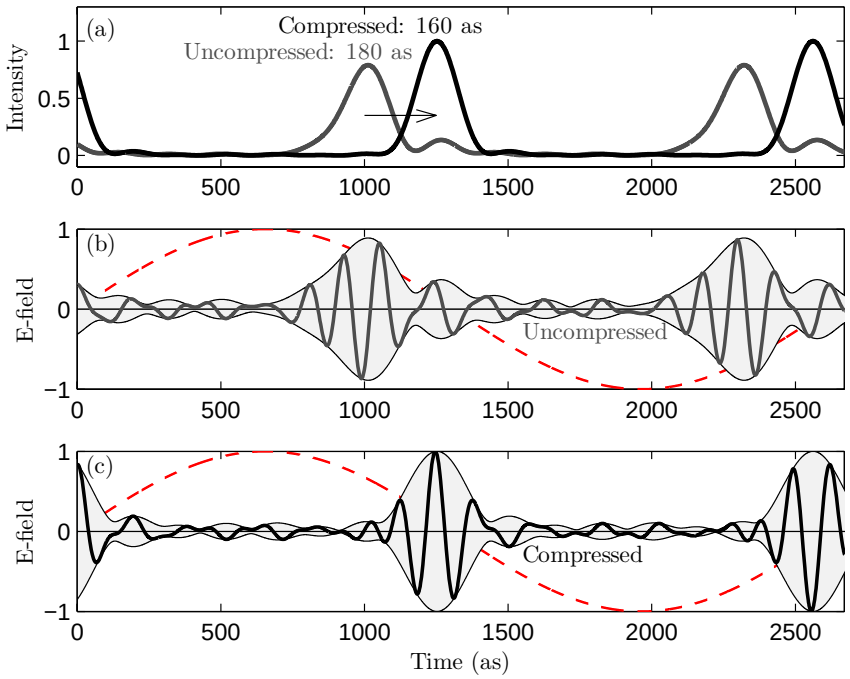

Figure 2.2. *(a) Attosecond pulses generated in Ar before (gray curve) and after (black curve) passing through a 400 nm Al foil. In addition to a delay of the pulse of* ~ 250 *as, the pulse shape changes due to the Al foil. The attosecond pulses before the foil have a positive chirp, which is intrinsic to the HHG process. (b) The uncompressed pulse is 180 as and it is asymmetric with a small post pulse. (c) After the foil, the compressed pulse is 160 as and symmetric. The CEP was set arbitrarily. The IR laser field (dashed curve) is plotted for comparison. Experimental phase data from Paper* ***V*** *was used. The amplitude effects from the foil are neglected for simplicity.*

2.1.3 Applications of the stationary phase approximation

Complex Gaussian integrals and the SPA are reviewed in this section. The SPA is a popular approximation in attophysics because it can be used to evaluate complex integrals, such as Fourier transforms. The SPA is frequently used in the quantum mechanical treatment of HHG, and we have applied the SPA to calculate HHG from two-color laser fields, in the work presented in Papers **III**–**IX**. For pedagogical reasons, the SPA is introduced already in this chapter and it is applied to some elementary examples concerning the propagation of attosecond light pulses. In the next section, the SPA will be applied to ultrashort pulses of electrons; and then finally to HHG in Chapter 4.

Complex Gaussian integrals

Complex Gaussian integrals are important in many applications in attophysics because they are closely related to the SPA which is discussed below. Consider the following integral,

$$\int_{-\infty}^{\infty} dx \;\; \exp\left[-\beta \; x^2\right] \;\; = \;\; \sqrt{\frac{\pi}{\beta}}, \tag{2.28}$$

where β may be complex. The integral is regular (vanishes in the limits) if $\Re(\beta) > 0$. In the special case of $\Re(\beta) = 0$, the integral is not regular in the common sense, but the equality still holds if $\Im(\beta) \neq 0$ due to rapid complex oscillations in the asymptotic regions, $|x| \to \infty$. The endpoints of the integral can be moved in the complex plane using Cauchy's integral theorem, provided that the asymptotic arc integrals vanish. We do not provide a rigorous mathematical proof of Equation 2.28, we simply illustrate the basic properties of the Gaussian integrals numerically in Figure 2.3.

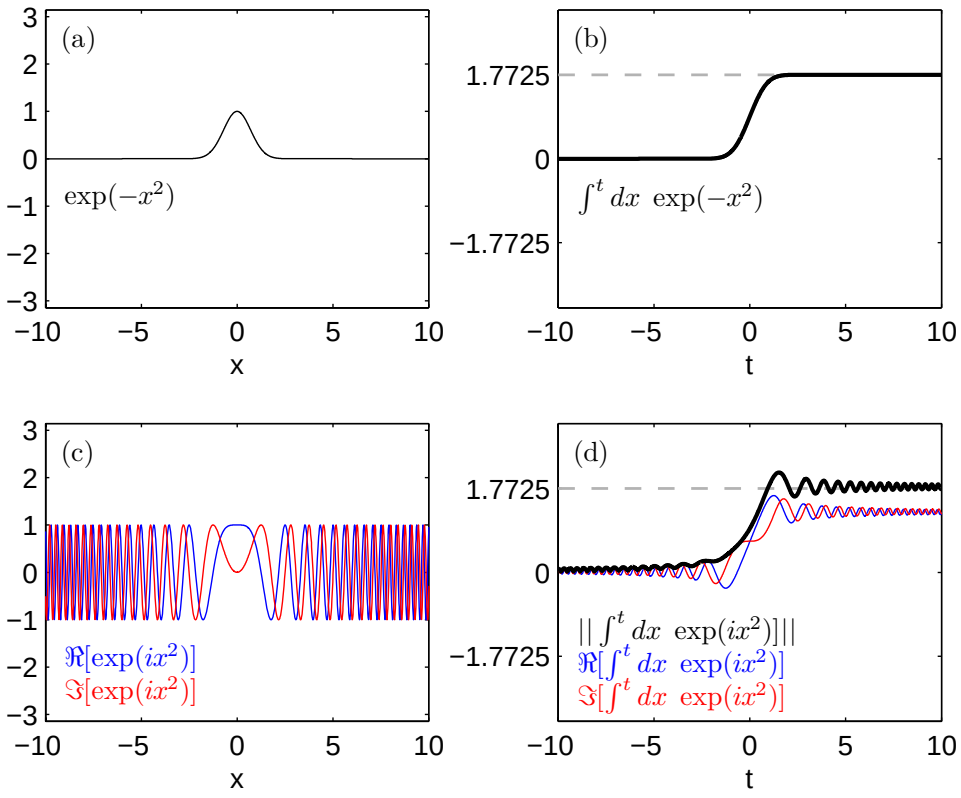

Figure 2.3. *(a) A real Gaussian function ($\beta = 1$). (b) The real Gaussian integral equals $\sqrt{\pi} \approx 1.7725$. (c) A complex Gaussian function ($\beta = -i$). Notice the fast complex oscillations for large values of $|x|$. (d) The complex Gaussian integral equals $\sqrt{\pi}\exp[i\pi/4]$.*

Stationary phase approximation

The SPA reads

$$\int_{-\infty}^{\infty} dx\ F(x) \exp\left[if(x)\right] \ \approx \ \sum_s F(x_s) \sqrt{\frac{2\pi i}{f''(x_s)}} \exp\left[if(x_s)\right], \tag{2.29}$$

where $f''(x_s) = \partial^2 f/\partial x^2\big|_{x_s}$. The sum runs over all solutions to the stationary phase equation

$$\frac{\partial}{\partial x}\left[f(x)\right] \ = \ 0, \tag{2.30}$$

where the stationary phase solutions, $x = x_s$, are labeled by the index s. The number of solutions depends on the properties of the phase factor, f. In the simplest cases, there is only one solution. F is a slow amplitude factor. The SPA can be derived by Taylor expanding the phase factor to second order around the stationary points and applying the complex Gaussian integral [Eq. 2.28]. The SPA does *not* replace the residue theorems, one should always be careful with poles [59].

Example I: A stretched "attosecond" pulse

In this example, an attosecond pulse [Eq. 2.21] with a large spectral chirp, $g \ll |\delta_0''|$, is reconstructed using the SPA. Let us assume that the variation of the spectral (Gaussian) amplitude can be considered slow. The SPA then implies that the amplitude factor will only contribute a local value, $F(\omega_s) = \exp[-g(\omega_s - \omega_0)^2]$, occurring at the stationary frequency, ω_s. This is quite similar to the way in which a delta function operates, selecting a specific value of a function, and it arises from a small constructive window in the complex integral around the stationary frequency. The next task is to find the stationary frequency, ω_s, using Equation 2.30. The phase factor is identified as $f(\omega) = \delta(\omega) - \omega t$. The stationary phase equation reads, $f'(\omega_s) = \delta_0' + \delta_0''(\omega_s - \omega_0) - t = 0$, with the solution

$$\omega_s(t) = \omega_0 + \frac{1}{\delta_0''}\ (t - \delta_0'), \tag{2.31}$$

which is a function of time. The stationary frequency can be seen as the frequency that makes the dominant contribution at a given time, t. At the center of the pulse, $t = \delta_0'$, the stationary frequency equals the central frequency, $\omega_s = \omega_0$. More generally, the stationary frequency varies as $\omega_s'(t) = 1/\delta_0'' \equiv \tilde{\phi}''$, which is the same as the way in which the instantaneous frequency varies in the limit of a large spectral chirp [Eq. 2.26]. The SPA is not only useful for making approximations, it can also be used to physically interpret the results. In the current case, identifying the stationary frequency as the instantaneous frequency yields an intuitive, physical understanding of stretched light pulses. In some sense, the complicated wave packet is simplified to a number.

In this derivation of the stretched pulse, it is only required that the spectral envelope is slow compared to the spectral chirp, it is *not* necessary to specify the exact shape of the envelope. Any other slow envelope, $F(\omega)$, will work, resulting in a pulse envelope that varies in the *same* way in the time domain as it does in the spectraldo-

main,

$$\underbrace{|\tilde{F}(t)|}_{\text{Temporal}} \;=\; \Big|\frac{1}{2\pi}\int d\omega\; F(\omega)\exp[i\delta(\omega)-i\omega t]\Big| \;\approx\; \frac{1}{2\pi}\;\underbrace{|F(\omega_s(t))|}_{\text{Spectral}}\;\underbrace{\sqrt{\frac{2\pi}{|\delta_0''|}}}_{\text{Constant}}, \qquad (2.32)$$

because the stationary frequency increases linearly in time [Eq. 2.31]. Mapping from the spectral envelope to the temporal envelope is scaled by the inverse spectral chirp, $1/\delta_0'' \equiv \tilde{\phi}''$. At the end of the next section, we will see that the properties of these super-stretched light pulses are similar to the way in which nonrelativistic electrons are dispersed through propagation in vacuum.

Example II: A compressed attosecond pulse

In this example, we consider a general Gaussian attosecond pulse [Eq. 2.21] with *any* ratio of bandwidth, $\Delta\omega$, and spectral chirp, δ_0''. In this case, it can not be assumed that the spectral envelope is slow. The Gaussian envelope must instead be *included* in the fast phase factor, $f(\omega) = \delta(\omega) - \omega t + ig(\omega-\omega_0)^2$. The stationary phase equation is $f'(\omega_s) = \delta_0' + \delta_0''(\omega_s-\omega_0) - t + i2g(\omega_s-\omega_0) = 0$, with the solution

$$\omega_s(t) = \omega_0 + \frac{\delta_0'' - i2g}{\delta_0'' + (2g)^2}\;(t-\delta_0'), \qquad (2.33)$$

which is complex and depends on time. When including *fast* amplitude effects, it is common to obtain complex stationary points in the SPA. The real part is identified as the instantaneous frequency using Equation 2.26. The imaginary part of the stationary frequency determines the duration of the attosecond pulse. The intensity of the attosecond pulse will only be large close to the center of the pulse, $t = \delta_0'$, where the imaginary part of the stationary frequency vanishes. Inserting the complex stationary frequency into the right-hand-side of Equation 2.29 yields the exact solution found in Equation 2.22.

In the special case of a Fourier-limited pulse, $\delta_0'' = 0$, the stationary frequency becomes the central frequency of the pulse plus a purely imaginary term, $\omega_s(t) = \omega_0 + i[\delta'(\omega_0) - t]/2g$. This is closely related to the Fourier-limited pulse shape, which has a constant carrier frequency equal to the central frequency. The imaginary part of the stationary frequency leads to the finite duration of the pulse in time. The SPA is based on approximating the actual integral by a complex Gaussian integral at each stationary point of the phase. In the current case, the pulse was a complex Gaussian, so the SPA was exact.

2.1.4 Summary of attosecond pulse propagation

In this section, we have reviewed the basic properties of light pulses which propagate through a medium in one dimension. Attosecond XUV light pulses are a special kind of light pulse with a large spectral bandwidth. The larger the bandwidth, the more sensitive the pulses are to the dispersion induced by the medium. Using an appropriate medium, it is possible to correct for small spectral chirps and reduce the attosecond pulses to their shortest possible duration. Once the attosecond pulses are

adjusted, they can be used to ionize atoms at extremely well-defined times [60]. The photoionization process will be discussed in Chapter 3, but before that we will review the properties of nonrelativistic photoelectron pulses, in order to understand how the photoelectrons evolve after such a well-defined ionization event.

2.2 Wave packets of photoelectrons

A fundamental application of attosecond pulses is to photoionize atoms and then study the temporal properties of the emitted photoelectrons. In this section, we perform a wave packet analysis of photoelectrons similar to that in the previous section. The propagation of a nonrelativistic photoelectron is described by the time-dependent Schrödinger equation (TDSE) [61]

$$H_0\big|\Psi(t)\big\rangle \;=\; [T+V_0]\big|\Psi(t)\big\rangle \;=\; i\hbar\frac{\partial}{\partial t}\big|\Psi(t)\big\rangle, \tag{2.34}$$

where H_0 is a time-independent Hamiltonian, and $\Psi = \Psi(t,\vec{r}) = \big\langle\vec{r}\big|\Psi(t)\big\rangle$ is the time-dependent wavefunction. The Hamiltonian consists of two parts, T and V_0, with $T = -\hbar^2\nabla^2/2m$ being the kinetic energy operator, and $V_0 = V_0(\vec{r})$ being the time-independent atomic potential. We here assume that the ionizing attosecond pulse disappears immediately, so that the emitted photoelectron only interacts with the field-free potential. A common approach to solving the TDSE [Eq. 2.34] is to first find the solutions to the time-independent Schrödinger equation,

$$H_0\psi(E,\vec{r}) = E\psi(E,\vec{r}), \tag{2.35}$$

where $E = \hbar\omega$ is the energy (eigenvalue) of the solution (eigenstate), $\psi(E,\vec{r})$. In the following, these time-independent solutions are referred to as *states*. The states form the basis that spans the complete space in which the electron moves. Photoelectrons are in the continuum with positive energies, $E > 0$,

For a spherical potential, $V(r)$, the states can be written on a spherical basis, $\psi(E,\vec{r}) = R_\ell(E,r)Y_\ell^m(\theta,\phi)$, where R_ℓ is the radial wavefunction and Y_ℓ^m is a spherical harmonic [61]. It is possible to reduce the Schrödinger equation to separate radial equations, each corresponding to a specific angular momentum quantum number, ℓ.

To emphasize the similarities with and differences between the one-dimensional propagation of light pulses [Sec. 2.1], the *effective radial* electron states, $\psi_\ell(r) = rR_\ell(r)$, are used. These states represent the total electron probability density over the surface of a sphere of radius r. The states do not decrease as r is increased, since the total probability on the surface is independent of r. The effective radial states can be interpreted as an electron wave propagating in *one* dimension through an effective potential, $V_0 = V_0' + V_\ell$, where V_0' is the three-dimensional radial potential and V_ℓ is a centrifugal potential that depends on the angular momentum, ℓ, of the electron. The effective radial time-independent Schrödinger equation for atomic hydrogen is

$$\Big[-\frac{\hbar^2}{2m}\frac{\partial^2}{\partial x^2}\overbrace{\underbrace{-\frac{e^2}{4\pi\epsilon_0 x}}_{V_C}+\underbrace{\frac{\ell(\ell+1)\hbar^2}{2mx^2}}_{V_\ell}}^{V_0}\Big]\psi_\ell(E,x) = E\psi_\ell(E,x). \tag{2.36}$$

Starting with Equation 2.36, the radial variable r is relabeled x to ease the comparison of one-dimensional light propagation with the propagation of photoelectrons. The boundary condition for all states is $\psi_\ell(E,0) = 0$. The effective radial time-dependent wavefunction of a photoelectron (in angular subspace ℓ) can be written as a superposition

$$\Psi_\ell(t,x) = \int_0^\infty dE\; a(E,t)\psi_\ell(E,x)\exp\left[-iEt/\hbar\right], \tag{2.37}$$

where $a(E,t)$ is the complex amplitude at energy E. Alternatively, the photoelectron can be written in terms of the wavevector states

$$\Psi_\ell(t,x) = \int dk\ a(k,t)\psi_\ell(k,x)\exp\left[-i\hbar k^2 t/2m\right], \tag{2.38}$$

where $k = \sqrt{2mE}/\hbar$ is the wavevector (number). Much like the attosecond light pulses [Eq. 2.7], the photoelectron pulse is written as a superposition of "monochromatic" continuum states. More information about the normalization of the continuum states can found be found at the end of this chapter, in Section 2.2.2.

2.2.1 Wave propagation of continuum electrons

The propagation of photoelectron pulses is governed by the way in which the phases of the continuum states vary as a function of energy. The Wentzel–Kramers–Brillouin (WKB) approximation is well suited for studying continuum states within a quasiclassical framework [61]. The WKB approximation relies on a similar ansatz as in Section 2.1.1 for XUV light. The effective radial wavefunction is taken to be $\psi_\ell(E,x) \propto \exp[i\phi(E,x)]$. The ansatz is expected to be adequate when the potential energy is varying slowly compared to the de Broglie wavelength of the electron, $\lambda_{dB} \equiv h/\sqrt{2mE} = 2\pi/k$. Inserting the WKB ansatz into the Schrödinger equation [Eq. 2.36], leads to a differential equation for the phase of the state,

$$-i\frac{\hbar^2}{2m}\frac{\partial^2\phi}{\partial^2 x} + \frac{\hbar^2}{2m}\left(\frac{\partial\phi}{\partial x}\right)^2 = E - V_0(x). \tag{2.39}$$

Assuming that the rate of change is small compared to the local de Broglie wavelength, $|\partial^2\phi/\partial x^2| \ll |\partial\phi/\partial x|^2$, the above equation can be simplified

$$\frac{\partial\phi}{\partial x} = \frac{1}{\hbar}\sqrt{2m[E - V_0(x)]}, \tag{2.40}$$

which can be integrated

$$\phi(E,x) = \frac{1}{\hbar}\int_{-\infty}^{x} dx'\ \sqrt{2m[E - V_0(x')]} = \frac{1}{\hbar}\int_{-\infty}^{x} dx'\ p(x'), \tag{2.41}$$

where $p(x)$ is the *local momentum* of the electron. The local momentum corresponds to the local kinetic energy, which is the total energy minus the local potential energy. The phase of the electron varies faster as the local momentum is increased. Equations 2.12 and 2.41 are now compared to highlight the differences between the propagation of XUV light and photoelectrons. In a medium with negligible dispersion, the phase of light is approximately proportional to ω, leading to a simple shift of the pulse in time. In a negligible potential, the phase of the electron is proportional to the square root of the energy, $\sqrt{E} \propto \sqrt{\omega}$. This implies that an electron pulse will broaden, even when propagating in free space. This broadening effect is referred to as "quantum diffusion" and it can be understood physically from the fact that electrons of different energies travel at different speeds, $v(E) = \sqrt{2E/m}$; whereas light always travels at the speed of light, c. Quantum diffusion is a fundamental limiting factor for the efficiency of HHG, as will be discussed further in Section 2.2.2 and in Chapter 4. When writing

the WKB solution, it is common to include the first order of $|\partial^2\phi/\partial x^2|$. This leads to the famous form for the WKB state

$$\psi_{wkb}^{(\pm)}(E,x) \propto \frac{1}{\sqrt{p(x)}} \exp\left[\pm\frac{i}{\hbar}\int_{-\infty}^{x} dx'\ p(x')\right], \tag{2.42}$$

where the two solutions, $(\pm)$, describe an electron moving in the positive and negative direction, respectively. The probability density, $\rho(x) = |\psi_{wkb}^{(\pm)}(E,x)|^2 \propto 1/|p(x)|$, is smaller where the electron moves rapidly. Physically, we understand this because the electron will spend a shorter time in a place when moving with a greater velocity.

Alternatively, we can form a real WKB solution,

$$\psi_{wkb}(E,x) \propto \frac{1}{\sqrt{p(x)}} \sin\left[\frac{1}{\hbar}\int_{a}^{x} dx'\ p(x') + \phi_a\right], \tag{2.43}$$

where a classical reflection point is assumed at $x = a$, *i.e.* $V_0(a) = E$. The determination of the absolute phase (reflection phase), ϕ_a, requires a theory beyond the WKB approximation [61]. The basic properties of the real WKB states are illustrated in Figure 2.4, where electrons are passing through an attractive potential.

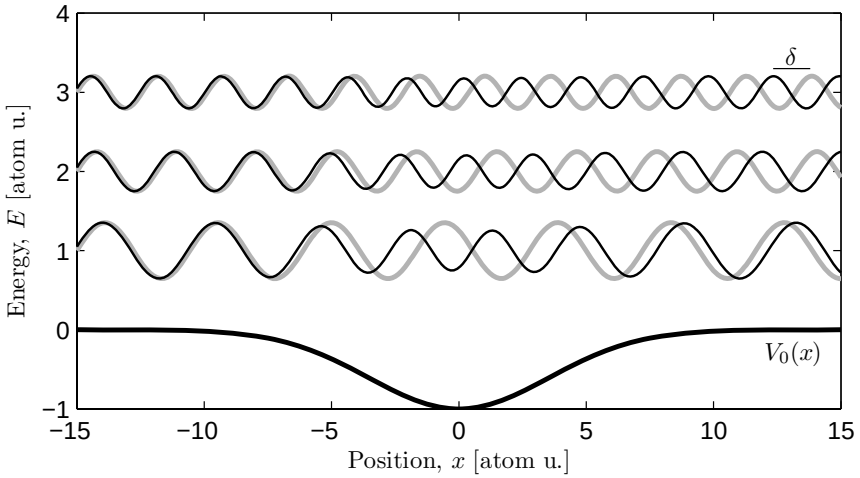

Figure 2.4. *Electrons passing through an attractive potential, $V_0(x)$. The real WKB solutions [Eq. 2.43, thin black curves] are compared to the real free electron states [thick gray curve] at three different energies: $E = 1, 2, 3$ a.u.. The phase of the electron wavefunction varies more quickly over the potential, which leads to an accumulated phase difference, δ, compared to the free case. This phase difference can be related to an electron pulse structure. Note that the modulations of the wavefunctions should be interpreted in the third dimension of the graph, and not as an energy modulation.*

Wigner delay

Consider the situation illustrated in Figure 2.4, where an electron passes through a short-range attractive potential. The electron is classically allowed to pass through

the potential, but as it does so, it will acquire a quantum phase. The asymptotic phase difference, between an electron wave propagating through a short-range potential [Eq. 2.41] and free wave propagation, is defined in analogy with Equation 2.13

$$\delta(E) = \frac{1}{\hbar} \lim_{x\to\infty} \int_{-\infty}^{x} dx' \ [p(x) - p_0] \,, \tag{2.44}$$

where $p_0 = \sqrt{2mE}$ is the free (asymptotic) momentum of the electron. The GD concept [Eq. 2.17] can also be applied to electrons using Equation 2.44

$$\tau_W(E) = \frac{\partial \delta}{\partial \omega} = \hbar \frac{\partial \delta}{\partial E}. \tag{2.45}$$

The electron GD is then only the result of the interaction with the potential, since the intrinsic delay due to different final velocities has been subtracted. Using the asymptotic phase to calculate the delay of electron wave packets was first done by Eisenbud, Wigner and Smith [62–64], hence the name Eisenbud–Wigner–Smith delay, (or Wigner delay for short). Photoionization is referred to as a *half-collision* because the electron only moves out of the atom (and not into it). The delay in photoemission is, therefore, the derivative of the radial asymptotic phase. Paper **II** presents an experiment where a time delay between photoelectrons from the $3p$ and $3s$ states in argon is measured using an APT. Our experiment is complementary to the experiment of Schultze *et al.*, where a time delay was observed between photoelectrons from the $2p$ and $2s$ states in neon using a SAP [65]. Another related time delay has been measured between the $4f$ state and the *conduction band* in condensed matter, single-crystal tungsten using a SAP [66]. The interpretation of our experimental time delay is discussed further in Chapter 3, where it is explained in detail, *how* it relates to the Wigner delay of the photoelectrons.

Example: Wigner delay from a weak potential

For a weak potential, $|V_0| \ll E$, the local momentum is $p(x) \approx p_0 \, [1 - V_0(x)/2E]$, which leads to an asymptotic phase

$$\delta(E) \approx -\frac{1}{\hbar}\sqrt{\frac{m}{2E}} \int_{-\infty}^{\infty} dx' \ V_0(x') \equiv -\frac{1}{\hbar}\sqrt{\frac{m}{2E}} \ I_V \,, \tag{2.46}$$

where the potential integral, I_V, is independent of the energy. The Wigner delay is

$$\tau_W = \sqrt{\frac{m}{8}} \frac{I_V}{E^{3/2}}. \tag{2.47}$$

It takes a shorter time, $\tau_W < 0$, for an electron to pass a weak attractive potential, $I_V < 0$, than through free space. Physically, this is due to the higher local velocity of the electron in the potential valley. The opposite is true for a weak repulsive potential, where the electron is slowed down on the potential hill. Furthermore, the timing of slow electrons is affected more than the timing of fast electrons, due to the longer total time that the slow electrons spend in the potential.

Coulomb–WKB states

So far, we have only discussed the phase properties of electrons passing through *short-range* potentials. Photoelectrons created from neutral atoms will pass through the Coulomb potential, $V_C = -C/x$, which has a *long range*. Far away from the atom, the WKB approximation [Eq. 2.43] can be applied, $E \gg |C/x|$, for $x \to \infty$. The local momentum can then be expanded as $p(x) \approx p_0[1 + C/2Ex]$, where $p_0 = \sqrt{2mE}$. The phase of the WKB state [Eq. 2.41] must, therefore, vary asymptotically as

$$\phi(E,x) \approx \frac{p_0}{\hbar}\int^x dx' \left[1 + \frac{C}{2Ex'}\right] = kx + \frac{\ln(kx)}{ka_0} + \eta, \tag{2.48}$$

where $k = p_0/\hbar$ is the wavevector, and a_0 is the Bohr radius. The absolute phase, $\eta = \eta(E)$, is undetermined. The *Coulomb–WKB* state varies as

$$\psi_C(E,x) \propto \sin\left[kx + \frac{\ln(kx)}{ka_0} + \eta\right] \equiv \sin\left[kx + \Phi(x)\right], \tag{2.49}$$

for $x \to \infty$. Interestingly, the phase, $\Phi(x)$, does not settle into free particle behavior, instead the phase diverges logarithmically. What does this divergent phase mean for the Wigner delay? The logarithmic term leads to a *Wigner–Coulomb delay*,

$$\tau_{WC}(x) \;\equiv\; \hbar\frac{\partial}{\partial E}\left[\frac{\ln(kx)}{ka_0}\right] \;=\; \frac{m}{\hbar a_0 k^3}\left[1 - \ln(kx)\right], \tag{2.50}$$

which depends on how far away the electron is from the ion. The Wigner–Coulomb delay can be neglected if the electron has high enough energy, $k \gg [1-\ln(kx)]^{1/3}$ a.u., where $x \approx vt = p_0 t/m$ is the approximate position of the photoelectron pulse. In cases when τ_{WC} is not negligible, it is necessary to consider the Wigner delay, $\tau_W = \hbar\partial\eta/\partial E$, relation to τ_{WC}.

The absolute determination of the asymptotic phase, η, is difficult for atoms in general, because it depends on the detailed nature of the atomic potential at short range. In the special case of hydrogen, the phase is known analytically [61],

$$\eta_\ell^{(H)} = -\ell\pi/2 + \sigma_\ell, \tag{2.51}$$

where

$$\sigma_\ell = \arg[\Gamma(\ell + 1 - i/ka_0)] \tag{2.52}$$

with Γ being the complex gamma function. This result can be generalized for any spherical atom,

$$\eta_\ell = -\ell\pi/2 + \sigma_\ell + \delta_\ell, \tag{2.53}$$

where δ_ℓ is the phase difference compared to hydrogen. We will return to the Coulomb–WKB states in Chapter 3, where we study the continuum–continuum transitions occurring in the RABITT method [Paper **II**]. The long-range behavior of the Coulomb potential leads to an additional time delay in the RABITT signal, which must be accounted for theoretically before the photoelectron Wigner time can be extracted from the experimental data.

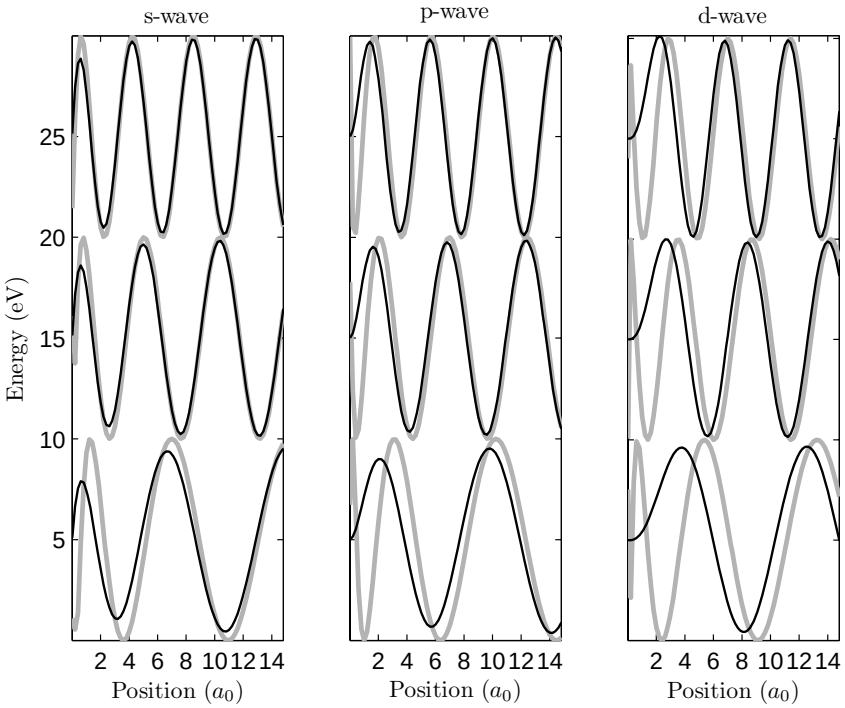

Figure 2.5. *Exact hydrogen wavefunctions (thin black curve) for $\ell = 0$, 1 and 2, corresponding to s-, p- and d-waves in the continuum. The Coulomb–WKB approximation (grey thick curve) is shown for comparison. The agreement between the Coulomb waves and the WKB solution is excellent far away from the core. At high energies agreement is reached faster. The WKB approximation is better for $\ell = 0$ than for $\ell > 0$ because of the increasing influence of the centrifugal potential, V_ℓ, which is neglected in the Coulomb–WKB approximation.*

Exact Coulomb states

The Coulomb–WKB states are compared with the *exact* Coulomb states for hydrogen in Figure 2.5. The exact analytical states of the hydrogen atom are called the regular Coulomb functions of the first kind [67],

$$F_\ell(\eta, \rho) = C_\ell(\eta)\ \rho^{\ell+1}\ \exp[-i\rho]\ {}_1F_1(\ell + 1 - i\eta; 2l + 2; 2i\rho), \tag{2.54}$$

where $\eta = -1/ka_0$ and $\rho = kx$. The prefactor is

$$C_\ell(\eta) = \frac{2^\ell \exp[-\pi\eta/2]\ \ |\Gamma(\ell + 1 + i\eta)|}{\Gamma(2\ell + 2)}, \tag{2.55}$$

and the integral form of the confluent hypergeometric function of the first kind is

$${}_1F_1(a; b; z) = \frac{\Gamma(b)}{\Gamma(b-a)\Gamma(a)} \int_0^1 dt\ \exp[zt] t^{a-1}(1-t)^{b-a-1}, \tag{2.56}$$

which is integrated numerically to produce the exact wavefunctions in Figure 2.5.

2.2.2 Photoelectron pulse propagation

In this subsection, we discuss the propagation of a photoelectron pulse in time using the continuum states derived in the previous section. It is convenient to expand the electron pulse [Eq. 2.38] on wavevector continuum states,[1]

$$\psi(k,x) = \frac{1}{\sqrt{2\pi}} \exp[ikx]. \tag{2.57}$$

The explicit electron pulse expansion is

$$\Psi(x,t) = \frac{1}{\sqrt{2\pi}} \int dk\ a(k) \exp\left[i \left(kx - \frac{\hbar k^2}{2m} t + \delta(k) \right) \right]. \tag{2.58}$$

The asymptotic phase, $\delta(k)$, describes the phase of the electron state after passing through a short-range potential.[2] The wave packet is normalized over k-space, $\int_{-\infty}^{\infty} dk\ |a(k)|^2 = 1$, which also implies that the wavefunction is normalized in space at any time, $\int_{-\infty}^{\infty} dx\ |\Psi(x,t)|^2 = 1$.[3] The complex amplitude is assumed to be a real normalized Gaussian function,

$$a(k) = \left(\frac{2g}{\pi} \right)^{1/4} \times \exp\left[-g(k-k_0)^2 \right], \tag{2.59}$$

where $k_0 = \sqrt{2mE_0}/\hbar$ and $g = 8\ln(2)\hbar^2 E_0/\Delta E^2 m$, E_0 being the central energy and ΔE the FWHM energy bandwidth of probability for the photoelectron. Free propagation, $\delta(k) = 0$, is considered for simplicity. The integral in Equation 2.58 can be evaluated using the SPA [Eq. 2.29]. The phase factor is identified as $f(k) = kx - \hbar t k^2/2m + ig(k-k_0)^2$. The stationary phase equation, $f'(k) = 0$, yields the stationary wavevector,

$$k_s(x,t) = \frac{2gk_0 + ix}{2g + i\hbar t/m}, \tag{2.60}$$

which is complex and dependent on the observation point, (x,t). The corresponding electron pulse is

$$\Psi(x,t) = \frac{1}{\sqrt{2\pi}} \left(\frac{2g}{\pi} \right)^{1/4} \sqrt{\frac{2\pi i}{f''(k_s)}} \exp\left[i f(k_s) \right] =$$

$$= \left(\frac{g}{2\pi\gamma^2(t)} \right)^{1/4} \exp\left[\frac{(2gk_0 + ix)^2}{4\gamma(t)} - gk_0^2 \right], \tag{2.61}$$

where $\gamma(t) = g + i\hbar t/2m$. The probability density of the electron takes a more intuitive form,

$$\rho(x,t) = |\Psi(x,t)|^2 = \frac{1}{\sqrt{\pi}|\Delta x(t)|} \exp\left[-\frac{(x - v_0 t)^2}{\Delta x(t)^2} \right], \tag{2.62}$$

[1] In Chapter 4, we will need the three-dimensional wavevector states: $\psi(\vec{k},\vec{r}) = (2\pi)^{-3/2} \exp[i\vec{k}\cdot\vec{r}]$.
[2] δ is also a function of x if the electron is still in the potential, or if the potential is long-range.
[3] Follows from Parseval's theorem and proper normalization, $\int_{-\infty}^{\infty} dx\ \psi(k,x)^* \psi(k',x) = \delta(k,k')$.

where the electron is moving with a constant velocity, $v_0 = \hbar k_0/m$, related to the central wavevector. Furthermore, the size of the electron wave packet is determined by the real factor $1/\Delta x^2 = g/2|\gamma(t)|^2$. The FWHM electron pulse duration can be estimated as

$$\tau \approx 2\sqrt{\ln(2)}\frac{\Delta x(t)}{v_0} = \frac{2\sqrt{2\ln(2)}}{v_0}\sqrt{\frac{g^2 + (\hbar t/2m)^2}{g}}, \tag{2.63}$$

which is very similar to Equation 2.24 for the duration of an attosecond light pulse. The duration of the electron wave packet is minimal at $t = 0$. At later times, $t > 0$, the electron will start to diffuse. In the limit of large times, the electron pulse duration will increase linearly with time. It is important to note that the electron pulse duration depends on time explicitly due to quantum diffusion. This makes "dispersion management" more difficult for nonrelativistic electron pulses than for light pulses and relativistic electron pulses. Finally, there is a velocity dependence, which implies that high-velocity electrons have shorter pulse durations.

In the following, we consider a more complicated electron wave packet [Eq. 2.58], *e.g.* the photoelectrons from an APT, in the limit of time going to infinity [64]. The phase factor will be fast compared to *any* initial complex amplitude, $a(k)$, which means that the SPA [Eq. 2.29] can be applied as

$$\Psi(x,t) \;\approx\; a(k_s)\,\sqrt{\frac{i}{f''(k_s)}}\;\exp[if(k_s)], \tag{2.64}$$

where the phase is $f(k) = kx - \hbar k^2 t/2m + \delta(k)$. The stationary phase equation, $f'(k_s) = 0$, yields the stationary wavevector, k_s. It is interesting to note that Equation 2.64 provides a direct link between the complex amplitudes of the wavevector states and the electron wavefunction in space–time. To understand this link better, we write the corresponding stationary electron velocity,

$$v_s(x,t) \;\equiv\; \frac{\hbar k_s}{m} \;=\; \frac{1}{t}\,\left(x + \frac{\partial\delta}{\partial k}\right). \tag{2.65}$$

This implies that the dominant contribution to the electron pulse at a given point in space–time (x,t), arises from the part of the wave packet that fulfills $v_s t = x + \delta'(k) \approx x$, where the Wigner shift is extremely small compared to the final position. The complex amplitude is mapped linearly from wavevector to space at any given large time [68]. The probability density is

$$\rho(x,t) \;=\; |\Psi(x,t)|^2 \;\approx\; |a(k_s)|^2\,\frac{m}{\hbar t}, \tag{2.66}$$

where the dependence of t is due to spreading of the wave packet, *i.e.* quantum diffusion. The photoelectron wavevector-to-space mapping, described above, is similar to the frequency-to-time mapping for super-chirped light pulses, which was discussed in Section. 2.1.3. For photoelectrons, the mapping occurs automatically after long enough times, and there is no need for a dispersive material. Classically, the electron mapping is *obvious* since electrons in a classical distribution are moving at different speeds. If we know that they all started at a distinct point in space–time, then we know that the fast electrons will reach the detector (at x) first. This mapping of complex amplitudes into space and time is the basic principle of the TOF detection scheme, which was used in most experiments presented in this thesis.

Renormalization

It is important to distinguish between bound states ($E < 0$), and continuum states ($E > 0$). Bound states have a finite extent in space because they are trapped by the potential, V_0. Bound states are normalized as $\int_{-\infty}^{\infty} dx\ |\psi(E,x)|^2 = 1$. Continuum states have an energy large enough for them to escape the potential and extend to infinity. Continuum states are normalized using the following trick. First, consider an infinite box potential of length L. The corresponding states are $\psi(E_N, x) = C\sin(\pi N x/L)$, with energy $E_N = \hbar^2\pi^2N^2/2mL^2$, where N is a positive integer, and $C = \sqrt{2/L}$ is the normalization factor for states in the box. At high energy, the states will become very close, and we can calculate the number of states, ΔN, in a small energy region, ΔE,

$$\Delta N = \frac{L}{2\pi}\sqrt{\frac{2m}{\hbar^2 E}}\Delta E \equiv \rho(E)\Delta E, \tag{2.67}$$

where $\rho(E)$ is the density of states. The continuum states are normalized to energy (and *not* to quantum number),

$$C_{[E]}^2 \equiv \rho(E)C^2 = \frac{1}{\pi}\sqrt{\frac{2m}{\hbar^2 E}}, \tag{2.68}$$

which is independent of the length of the box. Using the energy normalization convention, $C \to C_{[E]}$, the interpretation of $|a(E,t)|^2\Delta E$ is the probability of the electron being in a region bounded by $E \pm \Delta E/2$. Energy normalization also yields consistency between the radial bound and continuum states in atoms and the highly excited renormalized Rydberg states will connect smoothly to the continuum states at the ionization threshold ($E = 0$). Finally, energy normalization leads to $\int_0^{\infty} dx\ \psi(E',x)^*\psi(E,x) = \delta(E'-E)$. A free-electron wave packet can be written

$$\Psi^{(free)}(t,x) = \int_0^{\infty} dE\ a(E,t)\psi(E,x)\exp\left[-iEt/\hbar\right]. \tag{2.69}$$

In this derivation it is assumed that the electron is located at $x > 0$, with $\Psi_{free}(t,0) = 0$ as required for the effective radial atomic states used in the next chapter.

2.2.3 Summary of attosecond photoionization

Using attosecond pulses, electrons can be ionized at distinct times. The uncertainty principle (or the time–bandwidth product) then dictates that the energy content must be very broad. How long do the photoelectrons remain well-localized in time under typical experimental conditions? The central energy of the photoelectron is calculated using Einstein's law for the photoelectric effect, and the bandwidth of the attosecond pulse is simply transferred to the electron. Consider a photoelectron with $E_0 = 20\,\text{eV}$ and $\Delta E = 20\,\text{eV}$, which leads to an initial electron duration of $\sim 200\,\text{as}$. In attosecond experiments using trains of attosecond pulses, photoelectrons are created twice per laser period, *e.g.* a temporal separation of 1.35 fs for a titanium sapphire laser system. Coincidentally, we find that the electron pulse duration is $\sim 1.3\,\text{fs}$ after 2.7 fs, *i.e.* the electron occupies half of the laser period already after a single laser period of propagation. At later times, the photoelectron pulse duration scales as $\tau \approx 0.5t$. We should, therefore, *not* think of the electron pulses as attosecond pulses. After one

second of free propagation the electron pulse duration is half a second, and the size of the electron pulse would be roughly a fifth of the radius of the Earth. Photoelectron wave packets from attosecond light pulses grow large very fast.

Chapter 3

Attosecond photoionization

In this chapter, we provide a theoretical background for attosecond photoionization, which was studied experimentally using APTs, presented in Papers **I**, **II**, **V** and **VII**. The attosecond pulse structure in the APT is faster than any detector or electronic device can record. It is possible, however, to obtain temporal information about attosecond photoionization indirectly by investigating coherent cross-correlation photoelectron spectrograms between the attosecond pulses and a weak IR laser probe. The XUV attosecond pulse ionizes the atom and creates a photoelectron [Sec. 3.1], while the IR probe acts as a phase gate, modulates the emitted electron, and provides insight into the temporal structure of the attosecond pulse [Sec. 3.2]. Tunneling ionization is a different kind of ionization mechanism [69], which is important in intense, low-frequeny laser fields, and plays a major role in the generation of high-order harmonics [Sec. 3.3]. Finally, the detection of photoelectrons is examined from a scattering theory viewpoint [Sec. 3.4], with the aim of bridging the gap between the quantum mechanical photoelectron wave packets calculated in this chapter, and the different electron spectrometers used in the experimental work.

3.1 First-order time-dependent perturbation theory

The interaction of an attosecond pulse with an atom can often be approximated using first-order time-dependent perturbation theory (FTPT) [70]. The field-free states of the atom satisfy

$$[T + V(r)]\big|\tilde{n}\big\rangle \;=\; E_n\big|\tilde{n}\big\rangle \;=\; i\hbar\frac{\partial}{\partial t}\big|\tilde{n}\big\rangle, \tag{3.1}$$

where T is the kinetic energy operator, and $V(r)$ is the atomic binding potential. Using FTPT, we can assume that the electron remains mostly in the initial field-free state at all times, and that only a small fraction of the electron is promoted to the excited field-free states by the attosecond pulse. The electron wave packet can be expanded on the field-free states as

$$\begin{aligned}\big|\Psi(t)\big\rangle \;&\approx\; \big|\Psi^{(0)}(t)\big\rangle \;+\; \big|\Psi^{(1)}(t)\big\rangle \\ &=\; \big|\tilde{i}(t)\big\rangle \;+\; \sum\!\!\!\!\!\!\int_n a_n^{(1)}(t)\;\big|\tilde{n}(t)\big\rangle,\end{aligned} \tag{3.2}$$

where the zero-order part, $\big|\Psi^{(0)}(t)\big\rangle$, is the *initial* state,

$$\big|\tilde{i}(t)\big\rangle \;\equiv\; \big|\tilde{i}\big\rangle \;\equiv\; \big|i\big\rangle\;\exp[-i\omega_i t]; \tag{3.3}$$

and the first-order part, $\big|\Psi^{(1)}(t)\big\rangle$, is a superposition of *excited* states,

$$\big|\tilde{n}(t)\big\rangle \;\equiv\; \big|\tilde{n}\big\rangle \;\equiv\; \big|n\big\rangle\;\exp[-i\omega_n t]. \tag{3.4}$$

The integral–sum in Equation 3.2 runs over all excited bound and continuum states. The complex amplitudes of the excited states, $\big|\tilde{n}\big\rangle$, are approximated using FTPT [70]

$$a(E_n, t) \;\equiv\; a_n(t) \;\approx\; a_n^{(1)}(t) = \frac{1}{i\hbar}\int_{-\infty}^{t} dt'\;\big\langle\tilde{n}(t')\big|V_I(t')\big|\tilde{i}(t')\big\rangle, \tag{3.5}$$

where $V_I(t)$ is the interaction potential of the attosecond pulse. We describe the interaction between the atom and the attosecond pulse using the dipole approximation in the length gauge

$$V_I(t) \;=\; ez\;\tilde{E}_I(t) \;=\; ez\;\tilde{\Lambda}_I(t)\;\exp[-i\Omega t], \tag{3.6}$$

where $\tilde{E}_I(t)$ is the electric field of the attosecond pulse; Ω and $\tilde{\Lambda}_I(t)$ being the central frequency and the temporal envelope, respectively. The attosecond pulse is linearly polarized along the $\hat{z}$ direction. We define $-e = -|e|$ to be the charge of the electron. After a long time, when the attosecond pulse has passed, the first-order complex amplitude is proportional to the dipole matrix element, $z_{ni} = \big\langle n\big|z\big|i\big\rangle$, and to the Fourier transform of the electric field,

$$S_{n/i}^{(1)} \;\equiv\; \lim_{t\to\infty} a_n^{(1)}(t) \;=\; \frac{e}{i\hbar}\,z_{ni}\int dt\;\tilde{E}_I(t)\exp\left[i(\omega_n-\omega_i)t\right] \;=\; \frac{e}{i\hbar}\,z_{ni}\;\Lambda_I(\Delta\omega), \tag{3.7}$$

where $\Lambda_I(\Delta\omega)$ is the spectral envelope of the attosecond pulse at

$$\Delta\omega \;=\; \omega_n - \omega_i - \Omega \;\equiv\; \omega_n - \omega_c, \tag{3.8}$$

which describes the difference in frequency between the state, $\left|n\right\rangle$, with energy E_n, and the *central* state, $\left|c\right\rangle$, with energy $E_c = E_i + \hbar\Omega$. For photoelectrons, $\hbar\Omega > I_p \equiv -E_i$ and $\left|n\right\rangle$ are continuum states, this implies that the *spectral envelope* of the attosecond pulse is continuously mapped on the *complex amplitude* of the electron, but note that the photoelectron is *not* an exact spectral replica of the attosecond pulse since the amplitude and phase of the dipole matrix element may change over the broad spectral bandwidth of the attosecond pulse [71]. In Equation 2.66, we showed that the *probability* for an electron to be at the position x, on the detector, is proportional to the complex amplitude squared, $|a(E_s,t)|^2$, where $v_s = \sqrt{2E_s/m} = x/t$ is the stationary classical velocity. The spectral intensity distribution of attosecond pulses can, therefore, be determined using an electron TOF spectrometer by counting the number of photoelectrons reaching the detector as a function of time, and then correcting for the dipole matrix element, z_{ni}. The same information can, of course, be obtained directly by measuring the spectral intensity of the attosecond pulses with an XUV spectrometer. Information about the temporal structure of the XUV light is not accessible in either case.

3.1.1 Photoelectron wave packet

In this section properties and formation of photoelectron wave packets are discussed. First, finite-duration XUV pulses are considered, and then the limit of XUV fields with infinite duration.

Photoelectron wave packets from the box

In this subsection we study photoelectron wave packets, created by a weak box-shaped attosecond pulse, $\tilde{E}(t) = iE_I^{(0)}\ [\Theta(t) - \Theta(t - T_{dur})]\ \exp[-i\Omega t]$, of duration T_{dur} and with $\hbar\Omega > I_p$.[1] The attosecond pulse is turned on at $t = 0$ and turned off at $t = T_{dur}$ using the Heaviside stepfunctions. Direct application of Equation 3.5 leads to

$$\begin{aligned} a_n^{(1)}(t = T_{dur}) &= \frac{ez_{ni}E_I^{(0)}}{\hbar}\left[\frac{\exp[i\Delta\omega t']}{i\Delta\omega}\right]_0^{T_{dur}} \\ &= \frac{ez_{ni}E_I^{(0)}}{\hbar}\left(\frac{\sin[\Delta\omega T_{dur}]}{\Delta\omega} + i\ \frac{1-\cos[\Delta\omega T_{dur}]}{\Delta\omega}\right), \end{aligned} \tag{3.9}$$

where $\Delta\omega$ is the frequency offset from the central state [Eq. 3.8]. Figure 3.1 illustrates the evolution of the complex amplitudes and the corresponding reconstructed photoelectron wave packets, $\left|\Psi^{(1)}(t)\right\rangle$, for increasing interaction durations, T_{dur}.

Fermi's golden rule for photoionization states that the total probability of excitation increases linearly with time, $P = \int dE\ |a(E,t)|^2 \propto T_{dur}$. The photoelectron wave packet, in Figure 3.1, behaves indeed as predicted by Fermi's golden rule since the wave packet extends linearly in time. The size of the wave packet is approximately $x \approx v_c T_{dur}$, where $v_c = \sqrt{2E_c/m}$ is the central velocity of the photoelectron after ionization and T_{dur} is the duration of the interaction. Inside this "classical" extent of the

[1] We implement the rotating wave approximation, $2E_I^{(0)}\sin[\Omega t] \rightarrow iE_I^{(0)}\exp[-i\Omega t]$. The CEP can be introduced as $\exp[-i\Omega t + i\varphi(\Omega)]$, corresponding to a delayed real field, $\sin[\Omega(t-\tau)]$, where $\tau = \varphi/\Omega$.

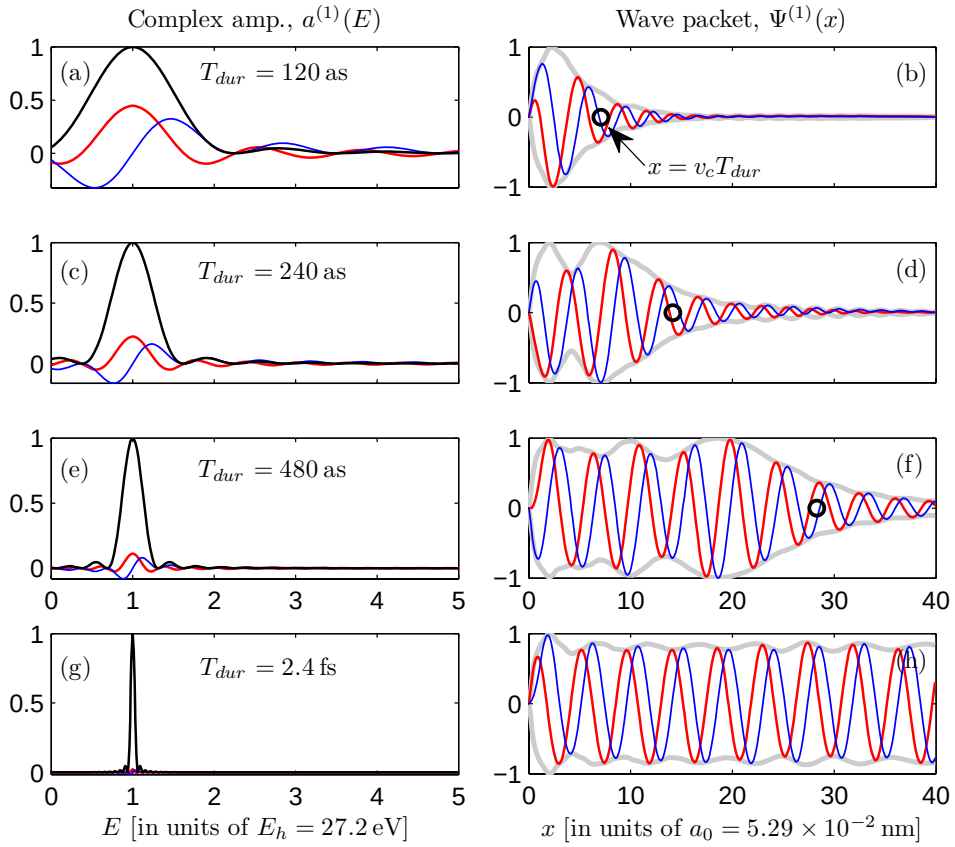

Figure 3.1. *Complex amplitudes (left) and "snapshots" of the corresponding photoelectron wave packets (right) after photoionization of increasing duration, T_{dur}: (a,b) 120, (c,d) 240, (e,f) 480 and (g,h) 2400 as. (a,c,e,g) The probability distribution over energy (black line) becomes narrower as the interaction duration increases. (b,d,f,h) In space, this corresponds to an expanding electron wave packet. The size of the photoelectron wave packet is well estimated by the classical distance $x = v_c t$ (black circle). This is a one-dimensional model calculation where the continuum states are plane waves and the dipole transition matrix element approximated as constant. The carrier frequency of the light is $\hbar\Omega = 41$ eV and the binding energy is $I_p = 13.6$ eV, resulting in a central energy, $E_c = \hbar\Omega - I_p = 27.1$ eV $= 1$ atomic unit, of the photoelectron. The photoelectron wave packet is complex; the real and imaginary parts being shown in red and blue, respectively.*

wave packet, the probability density is roughly constant, After the attosecond pulse is over, the photoelectron will continue to propagate freely and diffuse as described in Section 2.2.2.

Exponential turn-on of ionization

Rather than turning on the ionizing field instantaneously, as was done above, the electric field can be smoothly increased from minus infinity using an exponential slow turn-on [70]. The electric field is written $\tilde{E}(t) = iE_I^{(0)} \exp[-i\Omega t + \alpha t]$, including an attenuation factor, $\alpha > 0$, that reduces the field strength as $t \to -\infty$. Inserting the field into Equation 3.5 yields

$$a_n^{(1)}(t) = \frac{e}{\hbar} z_{ni} E_I^{(0)} \left(\frac{1}{\alpha + i\Delta\omega} \right) e^{i\Delta\omega t + \alpha t} \to \frac{e}{\hbar} z_{ni} E_I^{(0)} \left(\pi\delta(\Delta\omega) - i\wp \frac{1}{\Delta\omega} \right) e^{i\Delta\omega t}. \tag{3.10}$$

The arrow represents taking the limit, $\alpha \to 0^+$, using the *Sokhatsky–Weierstrass* theorem. The notation used requires some explanation: We write δ for the Dirac delta function, and $\wp$ is written to indicate that the discontinuity of $1/\Delta\omega$ has been removed, so that when integrated the result is Cauchy's principal value.[2]

Similarly, we can calculate the slow turn-off using $\exp[-i\Omega t - \alpha t]$ from $t = 0$ to $t \to \infty$, giving the same result as in Equation. 3.10, but with the opposite sign of the principal value part. Combining the slow turn-on and the slow turn-off, therefore, leads to symmetric cancelation of the principal value contribution. The resulting complex amplitude, corresponding to an interaction with the field from minus infinity to plus infinity, shows that energy must be conserved,

$$S_{n/i}^{(1)} = \frac{e}{\hbar} z_{ni} E_I^{(0)} \left[\frac{2\alpha}{\alpha^2 + \Delta\omega^2} \right] \to e z_{ni} E_I^{(0)} \; 2\pi\delta(E_n - E_i - \hbar\Omega), \tag{3.11}$$

and that only the central energy state $\left|c\right\rangle$, with $E_c = \hbar\Omega + E_i$, will be populated. This result correponds to a Fourier transform of a continuously oscillating electric field [Eq. 3.7]. We stress that it is valid as $t \to \infty$, which we interpret as the electric field being turned *off*.

The interesting aspect of the exponential turn-on method, is that it allows us to reconstruct a photoelectron wave packet at *any* time, t, while ionization is ongoing and the electric field is *on*

$$\begin{aligned} \left|\Psi^{(1)}(t)\right\rangle &= \sum\!\!\!\!\!\!\int_n a_n^{(1)}(t) \; \left|\tilde{n}(t)\right\rangle \\ &= eE_I^{(0)} \left[\pi z_{ci} \left|c\right\rangle - i \underbrace{\wp \sum\!\!\!\!\!\!\int_n \frac{z_{ni}}{E_n - E_c} \left|n\right\rangle}_{|\rho>} \right] \exp[-i\omega_c t], \end{aligned} \tag{3.12}$$

where the total phase of the wave packet is evolving at the angular frequency, $\omega_c = \omega_i + \Omega$, corresponding to the energy E_c of the central state $|c\rangle$. The wave packet consists of two terms: first a central part, $\propto |c\rangle$, corresponding to the field-free central state; and second a superposition of non-central (non-resonant) field-free states, $\propto |\rho\rangle$. The latter states are either under or over the laser-induced resonance at E_c, and are out of phase by $\pm\pi/2$ compared to the central state. This phase offset can be understood

[2] The Sokhatsky-Weierstrass theorem can be verified by multiplying the denominator of Eq. 3.10 by its complex conjugate and then identifying the limits of the delta function, $\alpha/(\alpha^2 + x^2) \to \pi\delta(x)$, and the principal value, $x/(\alpha^2 + x^2) \to \wp(1/x)$.

in analogy with a classical pendulum which is either overdriven or underdriven by an external oscillating force. In Paper **I** we report on similar phase changes of a bound state, the $1s3p$ state in He, using tunable, coherent high-order harmonics. In this chapter, however, we concentrate on the properties of photoelectron wave packet, and neglect the discrete nature of the bound states.

3.1.2 Asymptotic form of the photoelectron wave packet

It may be difficult to directly envisage what the reconstructed wave packet looks like in space by considering Equation 3.12. Note that the central part is real and that the non-central part is imaginary, at $t = 0$. From Figure 3.1, we expect that the photoelectron wave packet will be some kind of an outgoing wave,

$$\sim \frac{1}{i}\exp[i(kx - \omega_c t)] \;=\; \{\sin[ikx] - i\cos[ikx]\}\exp[-i\omega_c t]. \tag{3.13}$$

To verify this guess, consider the asymptotic form of the central radial atomic wavefunctions [Eq. 2.49],

$$\langle x|c\rangle \;\equiv\; \psi(E_c, x) \;\approx\; C\sin\left[k_c x + \Phi_c(x)\right], \tag{3.14}$$

and the non-central wavefunctions

$$\langle x|n\rangle \;\equiv\; \psi(E_n, x) \;\approx\; C\sin\left[k_n x + \Phi_n(x)\right], \tag{3.15}$$

where $\Phi(x) \equiv \Phi(E, x) = \ln(kx)/ka_0 + \eta$, and $\eta = \eta(E)$ is the total asymptotic (scattering) phase. $C = C(E)$ is the energy renormalization coeffient. We remind the reader that x is the radial dimension r of the atom to maintain the same notation as in the previous chapter for the one-dimensional, effective, radial wavefunctions. The integral–sum is approximated by a smooth integral from minus infinity to plus infinity, $\sum_n \to \int_{-\infty}^{\infty} dE$, and the discrete nature of the bound states will be neglected. This approximation is adequate if $\hbar\Omega > I_p$ and it is expected to reproduce the main features of the close-to-threshold Rydberg states. The behavior of the non-central part of the wave packet can be found by evaluating the smoothed principal value integral in Equation 3.12 using *contour integration*[3]

$$\langle x|\rho\rangle \;\equiv\; \rho \;\approx\; \pi\; ez_{ci}C(E_c)\;\cos\left[k_c x + \Phi(E_c, x)\right], \tag{3.16}$$

for $x \to \infty$. The total photoelectron wave packet is, indeed, an outgoing wave

$$\Psi^{(1)}(t, x) \;\approx\; \frac{\pi}{i}\; ez_{ci}E_I^{(0)}\; C(E_c)\; \underbrace{\exp\left[i\left(k_c x + \Phi(E_c, x) - \omega_c t\right)\right]}_{\text{Outgoing Coulomb wave}}, \tag{3.17}$$

which includes the effect of the atomic potential through $\Phi(E_c, x)$. We stress that this intuitive form of the first-order wave packet is only valid asymptotically. The real part of the wave packet is proportional to the regular solution of the field-free problem for all x [Eq. 3.1], while the imaginary part is proportional to the irregular solution in the asymptotic regime, $x \to \infty$. Close to the core, the imaginary part of the wave packet will go to zero and *not* diverge like the irregular solution. The asymptotic form of the wave packet can be related to the Coulomb Green's function [72, 73].

[3] The sum–integral is approximated as a smooth integral and it is performed by changing the integrand from energy to wavevector, $\wp\sum_n \approx \;\wp\int_{-\infty}^{\infty} dE \;=\; \wp\int_{-\infty}^{\infty} dk\; \partial E/\partial k$, and by evaluating the two complex Euler terms independently.

Angular subshells

So far, we have not emphasized the role of the different angular subshells. We have worked with the atom as if it were one-dimensional, and we have labeled the spatial dimension, x. In reality, in three dimensions, each dipole transition leads to an adjacent angular subspace, $\ell' = \ell \pm 1$. This implies that the photoelectron has a different angular momentum from the initial state. Transitions to higher angular momentum are more probable as a rule of thumb, but Cooper minima can easily lead to a local violation of this rule of thumb [74]. In argon there is a relevant Cooper minimum for $\hbar\Omega \approx 47$ eV, where the radial dipole integral of the initial p-state and the resonant d-wave vanishes [75]. We will, however, continue to suppress the angular dimensions of the atom, since the attosecond delays, which we wish to study, arise in the radial dimension.

3.1.3 Summary of first-order photoelectron wave packets

In this section, we have found that a sinusoidal (monochromatic) ionizing electric field leads to an outgoing photoelecton wave packet. The phase of the outgoing electron is equal to the scattering phase of the real, regular, time-independent states. Any attosecond XUV *pulse* can be written as a linear superposition of monochromatic waves, and the corresponding photoelectron pulse will display a delay equal to $\tau_{pe} = \tau_{GD} + \tau_W$, where τ_{GD} is the group delay of the attosecond pulse [Eq. 2.17] and τ_W is the Wigner delay of the electron [Eq. 2.45]. These delays are on the attosecond timescale, and they can not be resolved in photoelectron TOF spectrometers.

3.2 Second-order time-dependent perturbation theory

Papers **I**, **II**, **VII**, and **V** presents experimental studies in which the temporal structure of attosecond pulses and photoelectrons were studied by perturbing the attosecond ionization event with a weak IR probe. As the photoelectron is released into the IR-dressed continuum it may absorb and emit IR photons, thereby changing its energy. Provided that the IR field is weak, the energy of the electron will only change by *one* IR photon. Temporal information about the ionization event can then be obtained using the RABITT method. In this section, we give a theoretical background to this method, with special emphasis on stimulated continuum–continuum photoelectron transitions using second-order time-dependent perturbation theory (STPT) [70]. The second-order complex amplitude from the interaction with $V_I \propto E_I^{(0)} \exp[-i\Omega t]$ and the subsequent interaction with $V_{II} \propto E_{II}^{(0)} \exp[\mp i\omega t]$ is given by

$$\begin{aligned} a_f^{(2)}(t) &= \frac{1}{i\hbar}\int_{-\infty}^{t} dt' \sum_n \left\langle \tilde{f}(t')\middle|V_{II}(t')\middle|\tilde{n}(t')\right\rangle a_n^{(1)}(t') \\ &= \frac{1}{i\hbar}\int_{-\infty}^{t} dt' \left\langle \tilde{f}(t')\middle|V_{II}(t')\middle|\Psi^{(1)}(t')\right\rangle, \end{aligned} \tag{3.18}$$

where we can identify the first-order wave packet [Eq. 3.12]. It is meaningful to compare the second-order perturbation complex amplitude [Eq. 3.18] with the first-order amplitudes [Eq. 3.5]. In the first-order, the electron makes a transition from the

initial field-free state into the field-free continuum, creating a first-order wave packet. In the second order, the first-order wave packet can be seen as the initial state for the second interaction, and the second-order transition will occur from a complex wave into a different, regular, continuum state. We can write the second-order wave packet formally as

$$\left|\Psi^{(2)}(t)\right\rangle \equiv \sum_n a_n^{(2)}(t) \left|\tilde{n}(t)\right\rangle, \tag{3.19}$$

in analogy with Equation 3.2.

3.2.1 RABITT method

In the RABITT method the delay between the two fields is scanned and a photoelectron cross-correlation spectrogram between the XUV and IR is recorded. Information

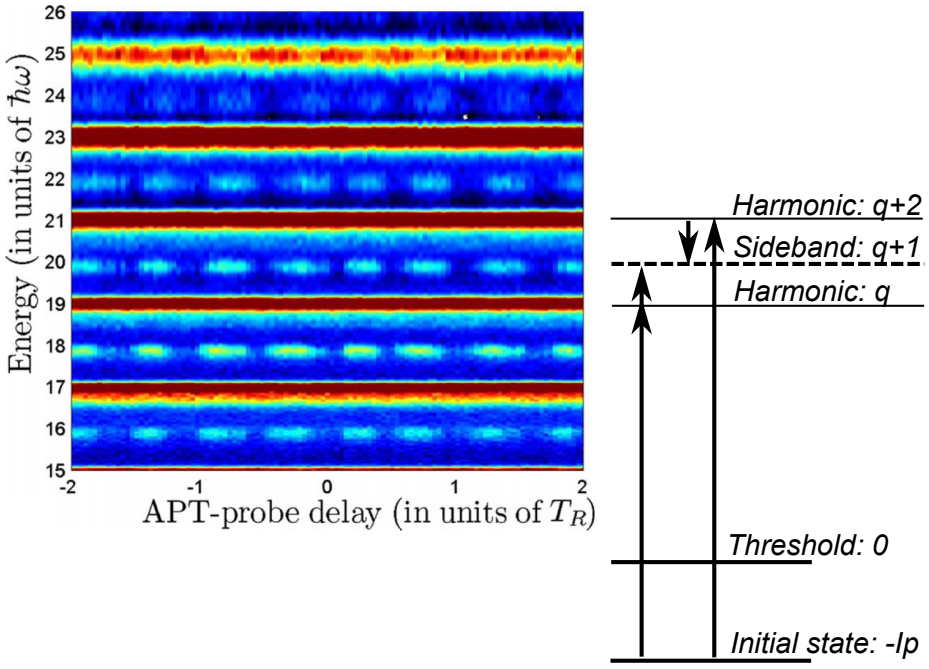

Figure 3.2. *Left: RABITT spectrogram over photon energy and delay between the APT and the IR field. The offset in the modulation of the sidebands contains information about the attosecond pulses and the ionization process. Right: Schematic energy diagram over the quantum paths leading to the same final energy in sideband $q+1$. Experimental data is taken from Paper* **V**.

about the timing of the photoionization process is found in the modulated sidebands, which are reached by two interfering quantum paths, see Figure 3.2. The first quantum path is absorption of a harmonic field, $V_I^{(q)} \propto \exp[-iq\omega t + i\varphi_q]$, and then the absorption of an IR photon, $V_{II}^{(1)} \propto \exp[-i\omega t + i\varphi_1]$, resulting in a photoelectron

with energy $E_f = (q+1)\hbar\omega - I_p$. The second quantum path is absorption of a harmonic, $V_I^{(q+2)} \propto \exp[-i(q+2)\omega t + i\varphi_{q+2}]$, followed by the emission of an IR photon, $V_{II}^{(-1)} \propto \exp[i\omega t - i\varphi_1]$, resulting a photoelectron with the *same* final energy, $E_f = (q+1)\hbar\omega - I_p$. The second-order complex amplitude for each quantum path is

$$a_f^{(2,\pm)}(t) \;=\; \frac{e}{i\hbar}\, E_{II}^{(0,\pm)}\; z_{f\Psi}^{(\pm)} \int_{-\infty}^{t} dt'\; \exp\left[i(\omega_f \mp \omega - \omega_c)t'\right], \tag{3.20}$$

with the corresponding limit for $t \to \infty$

$$S_{f/i}^{(2,\pm)} \;=\; \frac{e}{i}\, E_{II}^{(0)}\; z_{f\Psi}^{(\pm)} \;\times\; 2\pi\delta(E_f \mp \hbar\omega - E_c) \tag{3.21}$$

$$\equiv\; M_{f/i}^{(2,\pm)} \;\times\; 2\pi\delta(E_f \mp \hbar\omega - E_c), \tag{3.22}$$

where $(+)$ refers to absorption of an IR photon and $(-)$ refers to emission of an IR photon. The central energy is $E_c = E_f \mp \hbar\omega$ of the corresponding intermediate first-order wave packet. The complex dipole matrix element between the first-order wave packet and the final state is

$$z_{f\Psi}^{(\pm)} \;\equiv\; \left\langle f\middle|z\middle|\Psi^{(1,\pm)}\right\rangle \;=\; eE_I^{(0)}\Big[\pi z_{fc}z_{ci} - i\wp\sum_n{}'\frac{z_{fn}z_{ni}}{E_n - E_c}\Big], \tag{3.23}$$

and the second-order transition matrix element,

$$M_{f/i}^{(2,\pm)} \;=\; \frac{e^2}{i}E_{II}^{(0,\pm)}E_I^{(0)}\Big[\pi z_{fc}z_{ci} - i\wp\sum_n{}'\frac{z_{fn}z_{ni}}{E_n - E_c}\Big], \tag{3.24}$$

is a complex quantity that contains information about the timing of the ionization process. It is important to consider both the real, central part and the imaginary, non-central part of the first-order wave packet [Eq. 3.12]. If we were to apply the so-called *pole approximation* for multiphoton transitions [76], which consists of neglecting the non-central contribution, all attosecond timing would be lost.

The probability to generate sideband $q+1$ is proportional to the square of a sum over all quantum paths, Q, reaching the final state,

$$P_{q+1}^{(2)} \propto \Big|\sum_Q M_{f/i}^{(2,Q)}\Big|^2 \;\approx\; \left|M_{f/i}^{(2,+)} + M_{f/i}^{(2,-)}\right|^2, \tag{3.25}$$

where the quantum paths of first absorbing/emitting an IR photon and *then* absorbing an XUV photon are neglected. The exact first-order wave packet can be found through numerical integration [77], but we will instead develop an approximation for the complex transition matrix elements, which retains approximate phase and time information of the photoionization process analytically.

Asymptotic approximation

In this section we develop an *asymptotic approximation* for the RABITT method using the asymptotic form of the wavefunctions in the complex transition matrix element, $M_{f/i}^{(2)}$. We assume that the harmonic photon energy is larger than the ionization

potential, $\hbar\Omega \equiv \hbar q\omega > I_p$, so that the concept of an outgoing first-order wave packet can be applied. The exact form of the first-order wave packet is replaced by

$$\left|\Psi^{(1)}\right\rangle \;\sim\; \exp[i\{k_c x + \Phi_c(x)\}], \tag{3.26}$$

and the final state is replaced by

$$\left|f\right\rangle \;\sim\; \sin[k_f x + \Phi_f(x)]. \tag{3.27}$$

The asymptotic approximation does *not* take into account the full short-range interaction between the electron and the core, but it does allow us to account for the long-range Coulomb potential. The complex dipole matrix element, in atomic units, becomes

$$\begin{aligned}
z_{f\Psi}^{(\pm)} &\approx \left\langle f\middle|x\middle|\Psi^{(1)}\right\rangle^{(asymp.)} \\
&\propto \int_0^\infty dx\ \sin[k_f x + \Phi_f(x)]\ x\ \exp[i(k_c x + \Phi_c(x))] \\
&\approx -\frac{1}{2i}\int_0^\infty dx\ x \exp[i\{(k_c - k_f)x + \Phi_c(x) - \Phi_f(x)\}] \qquad (3.28) \\
&= -\frac{e^{i(\eta_c-\eta_f)}}{2i}\ \frac{(2k_c)^{i/k_c}}{(2k_f)^{i/k_f}}\ \left(\frac{i}{k_c - k_f}\right)^{2+i\xi}\Gamma(2+i\xi) \qquad (3.29)
\end{aligned}$$

where Γ is the complex gamma function and $\xi = 1/k_c - 1/k_f$. We drop the Euler term with fast oscillations, $k_f + k_c$ in Equation 3.28. The logarithmic phases in $\Phi(x) = \ln(kx)/k + \eta$, are brought down from the exponent and the integral is evaluated in Equation 3.29.[4]

Phase of two-photon matrix elements

The asymptotic approximation for the complex transition matrix element is

$$M_{f/i}^{(2,\pm)} \propto \underbrace{E_{II}^{(0)} E_I^{(0)}}_{(A)}\ \underbrace{\exp\left[i\{\eta_c - \eta_f\}\right]}_{(B)}\ \underbrace{\frac{(2k_c)^{i/k_c}}{(2k_f)^{i/k_f}}\left(\frac{i}{k_c - k_f}\right)^{2+i\xi}\Gamma(2+i\xi)}_{(C)}. \tag{3.31}$$

The phase can be separated into three parts. Factor (A) contains the phase of the light fields: $E_I^{(0)} \equiv |E_q|\exp[i\varphi_q]$, corresponds to absorption of an the qth harmonic photon; and $E_{II}^{(0)} \equiv |E_1|\exp[\pm i\varphi_1]$, corresponds to absorption $(+)$ or emission $(-)$ of an IR photon. The spectral derivative of the harmonic phase is the GD of the attosecond pulse [Eq. 2.17]. Factor (B) contains the difference in scattering phase between the central state, $\left|c\right\rangle$, and the final state, $\left|f\right\rangle$. These phases are related to

[4] The remaining integral was solved using complex contour integration [59]

$$\int_0^\infty dx\ x^{1+i\{1/k_c - 1/k_f\}}\exp[i(k_c - k_f)x] = \left(\frac{i}{k_c - k_f}\right)^{2+i\xi}\Gamma(2+i\xi). \tag{3.30}$$

the Wigner delay of the electron [Eq. 2.45]. Factor (C) contains an additional phase, the *continuum–continuum* (CC) phase

$$\phi_{cc}^{(\pm)} = \arg\left[\frac{(2k_c)^{i/k_c}}{(2k_f)^{i/k_f}}\left(\frac{i}{k_c - k_f}\right)^{2+i\xi}\Gamma(2+i\xi)\right], \tag{3.32}$$

where $k_c^2/2 \pm \omega = k_f^2/2$. The CC phase depends on the motion of the electron in the Coulomb potential and the frequency of the laser, ω. The approximate CC phase has been verified using the asymptotic Coulomb Green's function [A. Maquet, private communication (December 1, 2010)]. We will discuss the physical significance of the CC phase further below.

Sideband modulation in RABITT

The phases of the second-order transition matrix element lead to an offset in the modulated sideband

$$P_{q+1} \propto |M^{(+)}|^2 + |M^{(-)}|^2 + |M^{(+)^*}M^{(-)}|\cos[2\omega(\tau - \tau_{GD} - \tau_W - \tau_{cc})], \tag{3.33}$$

where $\tau = \varphi_1/\omega_1$ is the IR delay, $\tau_{GD} \approx (\varphi_{q+2} - \varphi_q)/2\omega$ is the GD of the attosecond pulses, $\tau_W \approx (\eta_{c,q+2} - \eta_{c,q})/2\omega$ is the Wigner delay with $\eta_{c,q} = \eta_c(E_q)$, and $\tau_{cc} \approx (\phi_{cc}^{(-)} - \phi_{cc}^{(+)})/2\omega$ is the corresponding CC delay, which is the phase difference between the emission ($-$) and absorption ($+$) processes that reach the final state. Note that the dependence on the final state asymptotic phase, η_f, has cancelled out. In fact, the asymptotic approximation leads to the same sideband offset for any allowed final state.

Intrinsic delay of the RABITT method

It is common to assume that the Wigner delay and the CC delay vary slowly compared to the GD of the attosecond pulses. The RABITT method will then directly map out the GD of the attosecond pulses in the sidebands, $\tau \sim \tau_{GD}$. This assumption is valid only at high photon energies, and it is closely related to the strong-field approximation, where the continuum states are replaced by plane waves. At lower photon energies the Wigner delay and the CC delay will contribute significantly to the modulation of the sidebands and they must be properly accounted for in order to obtain the attosecond pulse structure. If we assume that the GD of the attosecond pulses, τ_{GD}, is known [Eq. 3.33], then the RABITT method can yield information about the *intrinsic* two-photon ionization process, $\tau_W + \tau_{cc}$. Figure 3.3 compares the asymptotic approximation for the intrinsic delay in the RABITT method, $\tau_W + \tau_{cc}$, with the corresponding exact analytical result in hydrogen. The agreement between them is not perfect, but the general trend is reproduced. The intrinsic RABITT delay is negative, and it vanishes with increasing photoelectron energy. The discrepancy is due to the asymptotic approximation of the wavefunctions which neglects the close-to-the-core centrifugal barrier interaction [Fig. 2.5]. In more complicated atoms, there will be a short-range screening potential due to the remaining electrons in addition to the centrifugal barrier. The experimental data from the RABITT method can be used to test screening potentials if the GD of the attosecond pulses is known.

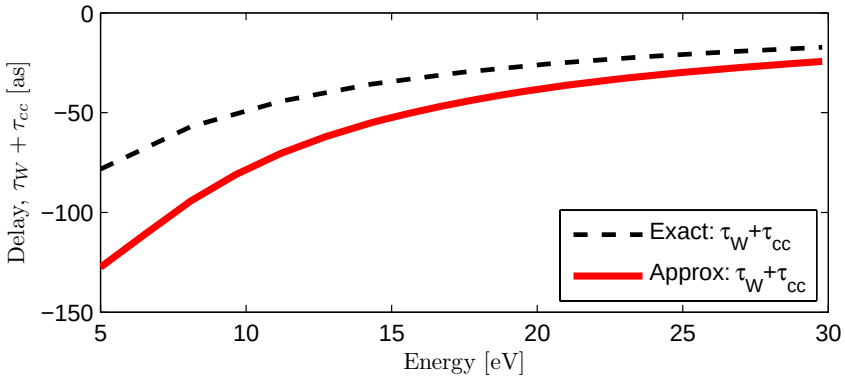

Figure 3.3. *Comparision of the intrinsic delay in RABITT for hydrogen, $\tau_W + \tau_{cc}$. The exact analytical result for the two possible final states: $\ell = 0$ and $\ell = 2$ are equal (black dashed curve). The asymptotic approximation leads to a similar trend for the delay (red curve). The theoretical data is taken from Paper **II**.*

Continuum–continuum delay

In this subsection we study the CC delay further. The CC delay for three different laser frequencies is shown in Figure 3.4. The behavior of the delay is similar at all

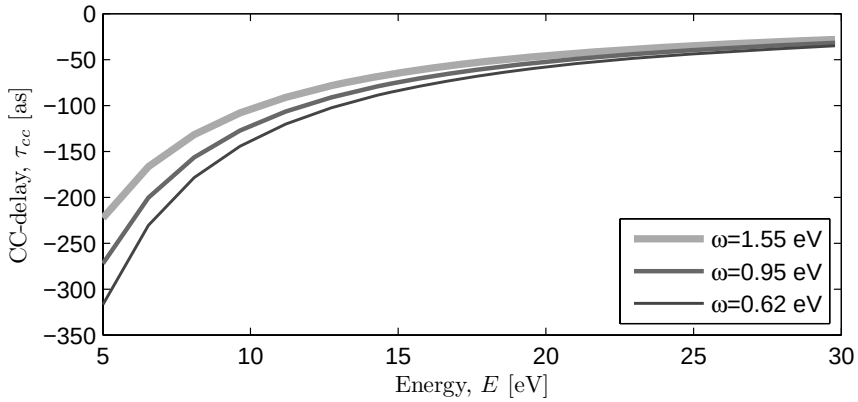

Figure 3.4. *Continuum–continuum (CC) delay for three different laser wavelengths: 800 nm (thick), 1.3 μm (medium) and 2 μm (thin). The delays were calculated using the asymptotic approximation.*

frequencies, but the absolute magnitude changes. A lower laser frequency leads to a

more negative delay. It is, perhaps, surprising that the delay increases in magnitude with decreasing laser photon energies, but this is physically resonable since the laser period increases.

Classical continuum–continuum phase

The behavior of the CC phase can be derived qualitatively by considering the classical dipole of an electron passing through a potential,

$$d(\omega) \equiv \int dt\ ex(t) \exp[i\omega t], \tag{3.34}$$

where $x(t)$ is the position of the electron. The integral can be transformed into an integral over space rather than time using

$$v(x) = \frac{dx}{dt} \ \rightarrow\ dt = \frac{dx}{v(x)} \ \rightarrow\ t(x) = \int^x \frac{dx'}{v(x')}, \tag{3.35}$$

where the velocity depends on the position of the electron in the potential, $V(x)$, in which the electron moves,

$$v(x) = \sqrt{\frac{2}{m}} \left[E - V(x)\right]^{1/2} \approx \sqrt{\frac{2E}{m}} \left[1 - \frac{1}{2}\frac{V(x)}{E}\right]. \tag{3.36}$$

The electron reaches its asymptotic energy, E, as $x \rightarrow \infty$. Time is an explicit function of space

$$t(x) = \int^x \frac{dx'}{v(x')} \approx \int^x dx' \sqrt{\frac{m}{2E}} \left[1 + \frac{1}{2}\frac{V(x')}{E}\right]. \tag{3.37}$$

The approximations in Equations 3.36 and 3.37 are valid only in the case of $|E| \gg |V(x)|$. We write the Fourier transform of the dipole as an integral over space

$$\begin{aligned} d(\Omega) &= \int_{-\infty}^{\infty} dx\ \frac{ex}{v(x)} \exp[i\omega t(x)] \\ &\approx \int_{-\infty}^{\infty} dx\ \sqrt{\frac{m}{2E}}\ ex\ \exp\left[i\omega \int^x dx'\ \sqrt{\frac{m}{2E}}\ \left\{1 + \frac{1}{2}\frac{V(x')}{E}\right\}\right], \end{aligned} \tag{3.38}$$

where the zero-order velocity is used for the amplitude and first-order time is used for the phase. The physical interpretation is that the electron passes over the potential and radiates as it is being accelerated. If $V(x)$ is small, the electron trajectory is only slightly distorted and the approximation is good. In the case of a Coulomb potential, $V(x) = -C/|x|$, there is a divergence at the origin, and the potential will be larger than the asymptotic energy for positions close to the core. This causes the approximation for the classical trajectories to break down, much like the way in which the WKB states break down close to the core. In the RABITT scheme the electron only leaves the atom (a half collision) and the lower limit in the integral should be zero rather than minus infinity. Inserting the Coulomb potential into Equation 3.38 and evaluating the integrals leads to the *classical* version of the asymptotic CC phase

$$\phi_{cc}^{(cl)}(\omega, E) = \arg\left[\left(\frac{i}{-\omega/\sqrt{2E}}\right)^{2+i\xi^{(cl)}} \Gamma(2 + i\xi^{(cl)})\right], \tag{3.39}$$

where $\xi^{(cl)} = \omega/(2E)^{3/2}$. This classical phase corresponds to the low-laser frequency limit, $E = E_c \approx E_f \gg \hbar\omega$, of the quantum mechanical phase, ϕ_{cc} [Eq. 3.32]. Assuming that the photon energy is small compared to the photoelectron energy is the essence of the so-called *soft-photon approximation* [78], which is used in the Volkov and Coulomb–Volkov approximations for XUV–IR ionization. Our approximation of the quantum mechanical CC phase [Eq. 3.32] goes beyond the soft-photon approximation and, thereby, beyond the classical picture. Armed with this classical picture we understand that $\tau_{IR}^{(cl)}(\omega, E) = \partial\phi_{cc}^{(cl)}/\partial\omega$ describes the delay in absorption or emission of an IR laser photon with frequency ω after photoionization by an XUV photon Ω. This is, however, *not* the delay which is present in RABITT, $\tau_{cc}^{(cl)}(E) \approx [\phi_{cc}^{(cl)}(-\omega, E) - \phi_{cc}^{(cl)}(\omega, E)]/2\omega$, for a given laser frequency, ω. The classical limit of RABITT is especially interesting in relation to the attosecond streaking method.

Intrinsic RABITT delays in neon

Figure 3.5 presents the relevant delays for the RABITT method in neon for $\hbar\omega = 1.55\,\text{eV}$. The Wigner delays, τ_W, for neon (red line) were computed using Hartree-Fock scattering phases [79], $\eta = \sigma + \delta$, where σ is the scattering phase of hydrogen and δ is the asymptotic phase shift of neon compared to hydrogen [Eq. 2.53]. We observe that the difference in Wigner delay, $\partial\delta/\partial\Omega$, between neon (red) and hydrogen (dashed) is barely visible in the energy range shown. The total Wigner delay increases slightly with angular momentum, ℓ, and decreases with energy for both neon and hydrogen. This is consistent with Equation 2.47 for an increasing repulsive potential, $0 < V_\ell \propto \ell(\ell+1)$. The Wigner delay increases dramatically close to threshold, below ~ 10 eV. The CC delay has the opposite sign compared to the Wigner delay. We have used the asymptotic approximation for the CC delay which is identical for all angular channels. The total intrinsic RABITT delay, $\tau_W + \tau_{cc}$, follows τ_{cc} to a good approximation because the Wigner delay is small compared to the CC delay.

Intrinsic RABITT delays in argon

Figure 3.6 presents same delays in argon for $\hbar\omega = 1.55$ eV. There is a considerable difference in Wigner delay, $\partial\delta/\partial\Omega$, between argon and hydrogen for the d-wave. This leads to a noticeable shift of the intrinsic RABITT delay, compared to the CC delay. The Wigner delays for s-waves and the p-waves are very small. The corresponding intrinsic delay is, therefore, caused mainly by the CC delay. The difference in intrinsic delay between p-waves and d-waves is ~ -50 as, in the energy region shown. The intrinsic delay from the $3s$ and $3p$ state in argon was studied experimentally [Paper **II**], where we demonstrated how the GD of the attosecond pulses can be cancelled from the RABITT measurements.

3.3 Higher-order processes

This section reviews higher-order photon processes, such as multiphoton ionization and tunneling ionization.

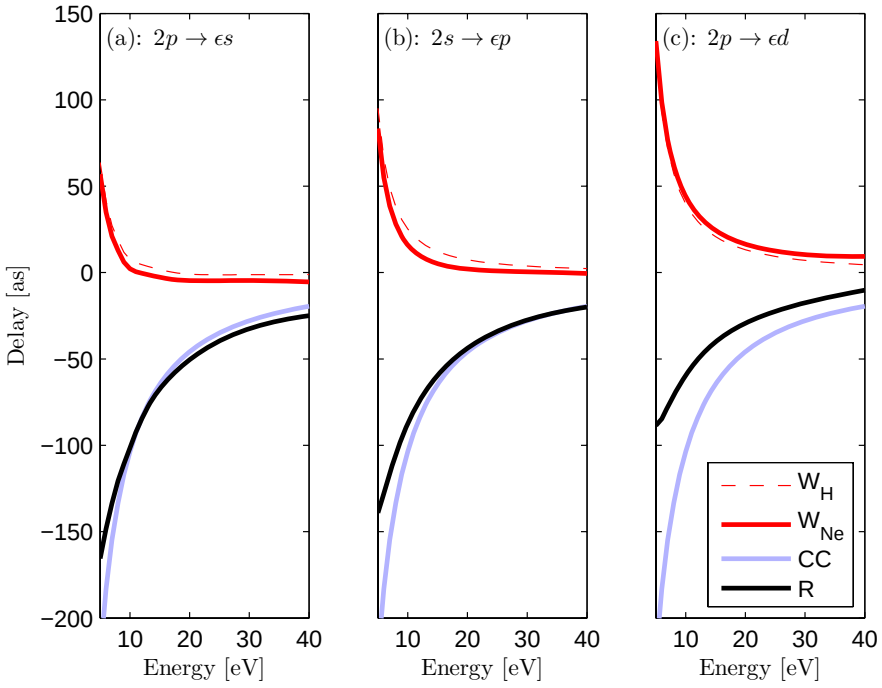

Figure 3.5. *Neon (Ne) delays for three different photoionization channels: (a) $2p \rightarrow \epsilon s$, (b) $2s \rightarrow \epsilon p$ and (c) $2p \rightarrow \epsilon d$. The Wigner delay of hydrogen [W_H] is a thin dashed curve, while the Wigner delay from neon [W_{Ne}] is a red curve. The asymptotic approximation for the CC delay is a blue curve which is insensitive of the short range interactions and, hence, independent of ℓ. The total intrinsic delay of RABITT [R] is the sum of Wigner and CC delays, $\tau_W + \tau_{cc}$, which is plotted as a black curve for neon.*

Multiphoton ionization

Multiphoton processes can be accounted for using higher-order pertubation theory if the interaction is weak [70, 76]. The complex amplitudes of order j can be computed as

$$\begin{aligned} a_f^{(j)}(t) &= \frac{1}{i\hbar}\int_{-\infty}^{t} dt' \sum_n \langle \tilde{f}(t')|V_I(t')|\tilde{n}(t')\rangle a_n^{(j-1)}(t') \\ &= \frac{1}{i\hbar}\int_{-\infty}^{t} dt' \langle \tilde{f}(t')|V_I(t')|\Psi^{(j-1)}(t')\rangle, \end{aligned} \tag{3.40}$$

where the sum runs over all relevant states $|n\rangle$ that are populated in the previous order, $j-1$, by the complex amplitude $a_n^{(j-1)}(t')$. The integral–sum is understood to include also the bound states and continuum states. The $j-1$ order wave packet can be identified in analogy with Equations 3.5 and 3.18. This perturbative approach is closely related to the photon picture, where the j^{th} order corresponds to a maximal absorption of j photons. The transition rate of an j-order process can be written in the spirit of Fermi's golden rule, where the probability increases linearly with time,

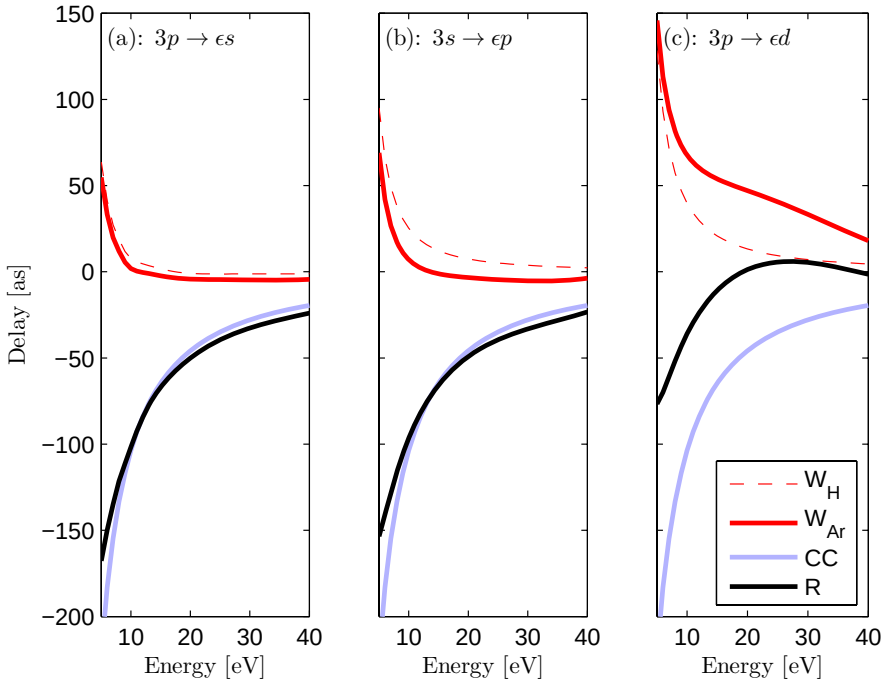

Figure 3.6. *Argon (Ar) delays for three different photoionization channels: (a) $3p \rightarrow \epsilon s$, (b) $3s \rightarrow \epsilon p$ and (c) $3p \rightarrow \epsilon d$. The Wigner delay of hydrogen [W_H] is a thin dashed curve, while the Wigner delay from argon [W_{Ar}] is a red curve. The asymptotic approximation for the CC delay is a blue curve which is insensitive of the short range interactions and, hence, independent of ℓ. The total intrinsic delay of RABITT [R] is the sum of the Wigner and CC delays, $\tau_W + \tau_{cc}$, which is plotted as a black curve for argon.*

provided that the interaction is weak. In Paper **VII**, we report on an extension of the RABITT method, where higher-order IR transitions lead to higher frequency components in the cross-correlation spectrogram. Given an appropriate experimental probe intensity, these higher frequency modulations can provide temporal information about the APT, when the IR field is too strong for the traditional RABITT method to be valid. The perturbative approach breaks down when the interaction is too strong. In Chapter 4, we review HHG, a process in which multiphoton processes occur as a result of strong interaction with a laser field.

ADK tunneling rate

The photoionization process can be separated into two distinct limits according to the theory of Keldysh [80]: the multiphoton ionization regime, for $\gamma \gg 1$; and the tunneling ionization regime, for $\gamma \ll 1$, where $\gamma = \sqrt{I_p/2U_p}$ is the Keldysh parameter, and $U_p = e^2E_0^2/4m\omega^2$ is the ponderomotive energy [Eq. 4.11]. In this section, the *static* tunneling process is reviewed. This may seem out-of-place, but the final result is useful for understanding the tunneling ionization mechanism of an atom in an intense, low-

frequency laser field.

Consider an electron, with wavefunction $\psi^{(+)}$, and energy E, moving in the positive direction through a large positive potential barrier that is classically forbidden to enter. The tunneling starts and ends when the electron energy equals the potential energy, $E = V_0(a) = V_0(b)$, and the potential is $0 < E < V_0(x)$ for $a < x < b$. The penetration coefficient [76] is defined as the ratio of the state amplitudes before, $x = a$, and after, $x = b$, passing the potential,

$$D = \frac{\psi^{(+)}(b)}{\psi^{(+)}(a)}. \tag{3.41}$$

The penetration coefficient can be estimated using the WKB states [Eq. 2.41] as

$$D = \exp\left[-\frac{\alpha_{BC}}{\hbar}\int_a^b dx'\ \sqrt{2m\left[V_0(x') - E\right]}\right], \tag{3.42}$$

where the WKB phase factor is turned into an exponential damping factor due to $E - V_0 < 0$, *i.e.* the WKB state turns into a *tunneling* wavefunction. The exponential coeffient, $\alpha_{BC} = 2$, arises from matching the boundary contitions at the entrance and at the exit of the potential.[5] The main features of static tunneling are captured in the following example.

Example: Tunneling ionization from a metal

The tunneling formula is applied to the Sommerfeld model for a metal in a static electric field, $V_0(x) = -I_p$ for $x < a = 0$, and $V(x) = -eE_0x$ for $x > 0$, where I_p is the binding potential in the metal, and E_0 is the electric field strength outside the metal. The second reflection point, b, is given by $I_p = eE_0b$, where the potential energy of the metal matches the potential outside the metal. We obtain a penetration coefficient of

$$D = \exp\left[-\frac{4}{3}\ \frac{\sqrt{2m}}{e\hbar}\ \frac{|I_p|^{3/2}}{E_0}\right]. \tag{3.43}$$

The probability of passing the classically forbidden barrier, $w = |D|^2$, is referred to as the *tunneling rate*. More generally, the same equation is valid for tunneling ionization from atoms in static fields and in slowly varying (quasistatic) fields, using slightly different numerical coefficients. This ADK tunneling theory was developed by Ammosov, Delone and Krainov (1986), and the potential, $|I_p|$, should be interpreted as the first ionization potential of the atom. Tunnel ionization from atoms is the dominant ionization process for ultra-short, intense, low-frequency laser pulses. Because the tunnel ionization rate depends exponentially on the electric field strength, the ionization can occur in very short bursts close to the peak of the electric field amplitude. This effect has recently been exploited for time-resolved tunneling spectroscopy on the attosecond timescale [81, 82]. Tunneling ionization arises naturally in the SFA for atoms in intense, low-frequency laser fields, which is the topic of Chapter 4.

[5] The determination of α_{BC} requires a more sophisticated theory, since the WKB solutions become invalid at the reflection points.

3.4 Measurement process

Photoelectron wave packets were derived in Section 3.1 using quantum mechanics and time-dependent perturbation theory. For each photon that the electron absorbs, its angular momentum quantum number, ℓ, changes by one. For an initial p-state, this implies that the first-order wave packet is a combination of s-waves and d-waves, while the second-order wave packet is a combination of p-waves and f-waves. At the end of Section 2.2.2, the SPA was used to relate the complex amplitudes of one-dimensional field-free continuum states to the photoelectron probability density at a distant detector. The situation similar in three dimensions, but there may be more than one way for the electron to reach the detector. If the initial state is a p-wave, then the first-order photoelectron can reach the detector as either an s-wave or as a d-wave. Will these two contributions interfere or are they independent? To answer this question, we need to specify more precisely how the detector works. In this thesis, experimental studies are presented in which two different schemes were used for measuring photoelectrons:

(i) angular integrated energy distributions, $\sim \big|E,\ell,m\big\rangle$,
(ii) angular resolved momentum distributions, $\sim \big|\vec{k}\big\rangle$.

One of the most fundamental postulates in quantum mechanics says that the measuring process can be seen as a projection of the total wavefunction, $\big|\Psi\big\rangle$, on an eigenstate, $\big|M\big\rangle$, of some observable M. The probability of the outcome M is [70]

$$P_M = \Big|\big\langle M\big|\Psi(t)\big\rangle\Big|^2. \tag{3.44}$$

Consider the three-dimensional, first-order photoelectron wave packet

$$\big|\Psi^{(1)}(t)\big\rangle \;=\; \sum_{\ell,m}\big|\Psi^{(1)}_{\ell,m}(t)\big\rangle \;=\; \sum_{n,\ell,m} a_{\ell,m}(E_n)\big|n,\ell,m\big\rangle\exp[-i\omega_c t], \tag{3.45}$$

which is a sum over all separate angular channels, ℓ, m. The complex amplitudes, $a_{\ell,m}(E)$, describe the coherent population of the degenerate angular waves. The theoretical aspect of the two detection schemes are discussed in more detail below.

3.4.1 Energy scheme

(i) If the detector collects photoelectrons over all angles, then the angular wave packets can be considered orthogonal and they will not interfere.

The energy scheme was used in most of the experiments presented in this thesis using the MBES. If the energy of the photoelectrons is measured over all angles (4π solid angle), then the MBES simultaneously observes all energy degenerate states, $\big|E,\ell,m\big\rangle$, where the angular momentum quantum number, ℓ, ranges from zero to infinity for photoelectrons, $E > 0$. The probability postulate [Eq. 3.44] should be applied *independently* to all degenerate final states,

$$P_E = \sum_{\ell=0}^{\infty}\sum_{m=-\ell}^{\ell}\Big|\big\langle E,\ell,m\big|\Psi^{(1)}(t)\big\rangle\Big|^2 = \sum_{\ell=0}^{\infty}\sum_{m=-\ell}^{\ell}|a^{(1)}_{\ell,m}(E)|^2, \tag{3.46}$$

so that they can have *any* relative phase. In practice, only a few of the angular states can be reached from the ground state due to the selection rules for linearly polarized light: $\Delta\ell = \pm 1$ and $\Delta m = 0$. The strength of the angular waves is related to the Clebsch-Gordan coefficients from the angular integration, and also to the radial integration, which depends on the exact shape of the overlap between the initial state and the final state close to the core. There are no selection rules for the radial integrations. There is no interference between the degenerate final states since they are orthogonal.

The MBES actually only collects photoelectrons in half of the unit sphere (2π solid angle). The alignment of the polarization is arbitrary in the simplest cases (one-photon transition) when the distribution of photoelectrons is symmetric (eigenstate of parity). The total number of electrons detected will thus be half the total number of photoelectrons ejected. In more advanced experiments, multiphoton processes can break the photoelectron symmetry and the alignment of polarization can lead to different results. In this case the wave packet must be integrated over the appropriate angles of detection.

3.4.2 Momentum scheme

(ii) The local photoelectron probability density will depend on the asymptotic phase difference, $\Delta\eta_c$, of the different angular waves. A detector at a specific position in space will, therefore, display interference between different angular waves.

The VMIS was used as a complement to the MBES in several experiments presented in this thesis. In this case, the photoelectron position is determined using an imaging MCP, which can be associated with an asymptotic momentum (wavevector) using the SPA in 3D.

`Short-range potential:` In the momentum scheme, the total wavefunction should be projected on a state with appropriate asymptotic momentum. For simplicity, we first consider a photoelectron traveling along the $\hat{z}$-axis with a wavevector $k\hat{z}$. The desired state is an eigenstate to the field-free Hamiltonian, and it contains both a *projectile* part and the modifications due to elastic *scattering* in the potential. For a short-range potential with spherical symmerty, the asymptotic form should consist of a plane wave and a spherical outgoing wave [61]

$$\psi_{k\hat{z}}(\vec{r}) \approx \exp[ikz] + f(\theta)\frac{\exp[ikr]}{r}, \tag{3.47}$$

where f is the scattering amplitude. After making an asymptotic partial wave expansion of Equation 3.47 using the regular solutions to the time-independent problem, $\psi_\ell(r) \approx \sin[kr - \ell\pi/2 + \delta_\ell]$, the scattering amplitude can be identified in terms of the asymptotic phases, δ_ℓ, as,

$$f(\theta) = \frac{1}{k}\sum_{\ell=0}^{\infty}\sqrt{4\pi(2\ell+1)}\ Y_\ell^0(\theta)\ \sin[\delta_\ell]\ \exp[i\delta_\ell], \tag{3.48}$$

where Y_ℓ^0 are the spherical harmonics with $m = 0$.[6] The scattering state can be

[6] A useful expansion of the plane wave on a spherical basis, $e^{ikz} = \sum_{\ell=0}^{\infty}(2\ell+1)i^\ell j_\ell(kr)P_\ell(\cos\theta)$, where the asymptotic form of the spherical Bessel function is $j_\ell(kr) \approx \sin[kr - \ell\pi/2]/kr$, and the Legendre polynomial is related to the spherical harmonic, $P_\ell(\cos[\theta])\sqrt{(2\ell+1)/4\pi}{=}Y_{\ell,0}$.

written as a complex superposition of partial waves,

$$\psi_{k\hat{z}}(\vec{r}) = \frac{1}{kr}\sum_{\ell=0}^{\infty}\sqrt{4\pi(2\ell+1)}\ Y_\ell^0(\theta)\ \psi_\ell(r)\ \exp[i\pi\ell/2 + i\delta_\ell], \tag{3.49}$$

where the complex phase of each term is related to the centrifugal phase, $\ell\pi/2$, and the asymptotic phase shift, δ_ℓ. Using this scattering state [Eq. 3.49] as $\big|M\big\rangle$ in the measurement postulate [Eq. 3.44], it is clearly seen that the outcome will depend on the interference between the different angular waves due to their different asymptotic phases. This derivation is only valid for short-range potentials, where the asymptotic form is given by Equation 3.47. In the case of the Coulomb potential, the asymptotic scattering wavefunction needs to be modified.

`Coulomb Potential:` When an electron scatters in the presence of a Coulomb potential, $V_C(r)$, and a short range potential, $V_S(r)$, Equation 3.47 must be modified due to the long-range nature of the Coulomb potential [61]. The projectile plane wave should be replaced by an *incoming Coulomb wave*, $\exp[ikz] \to \psi_C(\vec{r})$; and the outgoing spherical wave should include the logarithmic Coulomb phase term, $\exp[ikr]/r \to \exp[i(kr - \nu\ln(2kr))]/r$, where $\nu = -1/ka_0$, is the Coulomb parameter [Sec. 2.2.1]. We label the scattering factor f' in analogy with Equation 3.47 for the modified ansatz,

$$\psi_{k\hat{z}}(\vec{r}) \approx \psi_C(\vec{r}) + f'(\theta)\frac{\exp[i(kr - \nu\ln(2kr))]}{r}. \tag{3.50}$$

The analytical form of the incoming Coulomb projectile is known,

$$\psi_C(\vec{r}) = \underbrace{\exp[-\pi\nu/2]\ \Gamma(1+i\nu)\ F(-i\nu, 1; ik(r-z))}_{\text{Coulomb correction}}\ \underbrace{\exp[ikz]}_{\text{Plane wave}}, \tag{3.51}$$

in terms of the complex gamma function, Γ, and the confluent hypergeometric series, F. The behavior of the projectile can be identified as the plane wave factor in the right part of Equation 3.51; while the remaining prefactor contains the modifications due to the Coulomb potential. After making an asymptotic partial wave expansion using the regular Coulomb functions corresponding to the pure Coulomb potential: $V_0 = V_C$, $F_\ell(r) \approx \sin[kr - \nu\ln(2kr) + \sigma_\ell - \ell\pi/2]$; and the regular solutions to the combined potentials: $V_0 = V_C + V_S$, $\psi_\ell \approx \sin[kr - \nu\ln(2kr) + \sigma_\ell + \delta_\ell - \ell\pi/2]$, the scattering factor can be identified as,

$$f'(\theta) = \frac{1}{k}\sum_{\ell=0}^{\infty}\sqrt{4\pi(2\ell+1)}\ Y_\ell^0(\theta)\ \sin[\delta_\ell]\ \exp[i\delta_\ell + i2\sigma_\ell], \tag{3.52}$$

which is similar to the scattering factor in the short-range potential [Eq. 3.48], but with an additional phase factor of twice the asymptotic Coulomb phase. The scattering state in a Coulomb potential can be written as a complex superposition of partial waves,

$$\psi_{k\hat{z}}(\vec{r}) = \frac{1}{kr}\sum_{\ell=0}^{\infty}\sqrt{4\pi(2\ell+1)}\ Y_\ell^0(\theta)\ \psi_\ell(r)\ \exp[i\pi\ell/2 + \underbrace{i\delta_\ell + i\sigma_\ell}_{i\eta_\ell}]. \tag{3.53}$$

The scattering states in the Coulomb potential [Eq. 3.53] differ from the short-range case [Eq. 3.49] by an additional Coulomb phase factor, $\exp[i\sigma_\ell]$. Interestingly, when

measuring photoelectrons in a specific direction there will be interference between the different angular Coulomb waves. This interference is dictated by the total asymptotic phases, η_ℓ, of the radial functions. This is quite intuitive if we consider the angular channels separately. An electron in a given channel, ℓ, will reach the detector with the total asymptotic phase of that angular channel, η_ℓ. If the electron can also reach the detector through another angular channel, ℓ', with the opposite asymptotic phase, $\eta_{\ell'} = \eta_\ell + \pi$, then the electron will quantum mechanically avoid the detector. Attosecond physics and scattering theory are closely related.

So far, we have only considered photoelectrons with an asymptotic momentum along the $\hat{z}$-axis. A more general form of the scattering state can be obtained using the *addition theorem for spherical harmonics*,

$$\psi_{\vec{k}}(\vec{r}) = \frac{4\pi}{kr} \sum_{\ell=0}^{\infty} \sum_{m=-\ell}^{\ell} Y_\ell^{m*}(\hat{k})\ Y_\ell^m(\hat{r})\ \psi_\ell(r)\ \exp[i\pi\ell/2 + i\delta_\ell + i\sigma_\ell], \tag{3.54}$$

where the electron has an asymptotic momentum in the $\hat{k}$ direction and the position vector is in the $\hat{r}$ direction. It is common in attosecond physics to approximate the scattering states by plane waves. This approximation is equivalent to setting all the asymptotic (scattering) phases to zero, which implies that all the information about the attosecond electron dynamics is lost. It is cleary important to use proper scattering states in attosecond physics, especially close to the ionization threshold [83, 84].

Chapter 4

Extreme nonlinear optics

This chapter contains a theoretical derivation of the HHG process. In Section 4.1, we review the Volkov states that describe a nonrelativistic free electron in a laser field. These states are then used in Section 4.2 to model the interaction of an atom with an intense, low-frequency laser field. The electron will tunnel ionize from the atom and move on quasiclassical trajectories in the continuum. The HHG originates from a recombination process of such strongly driven electrons [Sec. 4.3]. The time–energy properties of the returning electrons are discussed for a one-color laser field [Sec. 4.3.1], and for a two-color laser field [Sec. 4.3.2]. This chapter serves as a theoretical background to the results presented in Papers **III**–**IX**, where both the *control* and *probe* aspects of the two-color HHG are closely examined, both experimentally and theoretically.

4.1 Volkov states

Consider a free electron in a laser field, $\vec{E}(t) = E(t)\hat{x}$. The intensity of the laser field may be large, but not so large that the electron motion becomes relativistic, or that the magnetic field bends the trajectories. The classical motion of the electron can then be described by the *Lorentz force*, $\vec{F} = -e[\vec{E} + \vec{v} \times \vec{B}] \approx -e\vec{E}$, where $-e$ is the charge of the electron. The corresponding quantum mechanical evolution of an electron in a laser field can be described using *Volkov states*. The following derivation of the Volkov states is detailed, because they are extremely useful for describing strong-field processes such as HHG and above-threshold ionization (ATI). The total Hamiltonian of an electron in a laser field is $H = T + V_I$, where T is the kinetic energy operator and $V_I = exE(t)$ is the dipole potential in the length gauge. The TDSE reads

$$[T + V_I(t)] \left|\tilde{k}\right\rangle = i\hbar \frac{\partial}{\partial t} \left|\tilde{k}\right\rangle, \tag{4.1}$$

where $\left|\tilde{k}\right\rangle$ is a Volkov state. Unlike most time-dependent problems in quantum mechanics, there is an exact analytical expression for the time-dependent Volkov state. Consider the corresponding one-dimensional TDSE

$$\left[-\frac{\hbar^2}{2m}\frac{\partial^2}{\partial x^2} + exE(t)\right] \tilde{\psi}_{[k]}(t,x) = i\hbar \frac{\partial}{\partial t} \tilde{\psi}_{[k]}(t,x). \tag{4.2}$$

A time-dependent ansatz for the Volkov state is written in terms of the wavevector states [Eq. 2.57], $\tilde{\psi}_{[k]}(t,x) = a(t,x)\psi(k,x)$, where the tilde indicates time dependence of the Volkov state. Notice that the prefactor, $a(t,x)$, depends on both time and space. Inserting the ansatz yields

$$-\frac{\hbar^2}{2m}\left[\frac{\partial^2 a}{\partial x^2} + 2ik\frac{\partial a}{\partial x} - k^2 a\right] + exEa = i\hbar\frac{\partial a}{\partial t}, \tag{4.3}$$

with the solution

$$a(t,x) = \exp\left[iexA(t)/\hbar - iS(k,t,t_0)/\hbar\right], \tag{4.4}$$

where

$$A(t) = -\int_{-\infty}^{t} dt' \; E(t'), \tag{4.5}$$

is the vector potential of the laser, and where

$$S(k,t,t_0) = \frac{\hbar^2}{2m}\int_{t_0}^{t} dt' \; [k + eA(t')/\hbar]^2, \tag{4.6}$$

is the electron *action* due to the laser field. There is an arbitrary reference time, t_0, in the definition of the action because the absolute phase of an electron state is arbitrary. Inserting the Volkov amplitude [Eq. 4.4] into the ansatz for the Volkov state yields

$$\tilde{\psi}_{[k]}(t,x) = a(t,x)\psi_{[k]}(x) = \frac{1}{\sqrt{2\pi}}\exp\left[i(k + eA(t)/\hbar)x - iS(k,t,t_0)/\hbar\right]. \tag{4.7}$$

The physics of the Volkov state is seen more clearly if it is written,

$$\tilde{\psi}_{[k]}(t,x) = \frac{1}{\sqrt{2\pi}}\exp\left[i\tilde{k}(t)x - i\frac{\hbar}{2m}\int_{t_0}^{t} dt' \; \tilde{k}(t')^2\right], \tag{4.8}$$

introducing the instantaneous wavevector, $\tilde{k}(t) = k + eA(t)/\hbar$. The overall phase of the state is given by the second term in the exponent, which is the integrated instantaneous kinetic energy of the state, $\propto \tilde{k}^2/2$. When the vector potential is positive, the wavevector and the energy of the Volkov state are increased. When the vector potential is negative, the wavevector and the energy of the Volkov state are decreased. In a monochromatic laser field, the vector potential will vary between positive and negative values, resulting in a "breathing" motion of the Volkov state. It is important to note that an electron initially in state $\left|k\right\rangle$ will smoothly deform according to the Volkov state, $\left|\tilde{k}\right\rangle$, as the laser pulse is developing. As the laser pulse ceases, the electron will return to $\left|k\right\rangle$. The electron can thus *not* change state, but it may acquire a quantum phase compared to the field-free case. The difference in quantum phase due to the laser interaction is

$$\delta_I = \frac{\hbar}{2m}\int_{-\infty}^{\infty} dt' \ \left[\tilde{k}(t')^2 - k^2\right] = \frac{\hbar}{2m}\int_{-\infty}^{\infty} dt' \ \left[2keA(t')/\hbar - (eA(t')/\hbar)^2\right]. \quad (4.9)$$

The first term in the integral, which is $\propto kA(t')$, vanishes because it is required that $\int_{-\infty}^{\infty} dt\ A(t) = 0$ for a physical laser pulse. The second term, $\delta_P \propto A(t')^2$, is called the *ponderomotive phase shift* and it describes the increase in total average energy of the electron in the laser field. The ponderomotive phase can modify the absolute phase of an electron wave packet, but it does not affect any other temporal properties of the wave packet, since it is independent of the electron wavevector. In the case of a long, constant laser interaction, $T_{dur} \gg T$, the ponderomotive phase is

$$\delta_P \ = \ \frac{e^2}{2m\hbar}\int_{-\infty}^{\infty} dt' A(t')^2 \ \approx \ \frac{e^2}{2m\hbar}\ \frac{A_0^2}{2}\ T_{dur} \ \equiv \ \frac{U_p T_{dur}}{\hbar}, \quad (4.10)$$

where the *ponderomotive energy* is identified as

$$U_p = \frac{e^2 A_0^2}{4m} = \frac{e^2 E_0^2}{4m\omega^2} = \frac{e^2\lambda^2 I}{8\pi^2\epsilon_0 m c^3}. \quad (4.11)$$

The ponderomotive energy increases with intensity, I, and the wavelength squared, λ^2, of the laser because the electron is forced to oscillate more violently in response to the laser. It is, perhaps, surprising that the ponderomotive energy increases with longer laser wavelengths, *i.e.* with decreasing laser photon energy. Physically, this effect arises from the fact that a slower variation in the electric field will lead to a longer time for the electron to accelerate before the electric field changes sign and decelerates the electron. A longer laser wavelength, therefore, leads to a higher average kinetic energy of the electron, *i.e.* a higher ponderomotive energy.

The three-dimensional Volkov state

In analogy with Equation 4.7, the three-dimensional Volkov state is

$$\tilde{\psi}_{[\vec{k}]}(t,\vec{r}) \ = \ \frac{1}{(2\pi)^{3/2}} \exp\left[i(\vec{k} + e\vec{A}(t)/\hbar)\cdot\vec{r} - iS(\vec{k},t,t_0)/\hbar\right], \quad (4.12)$$

where $\vec{k}$ is the wavevector, and where the laser polarization is determined by $\vec{E} \propto \vec{A}$. The action in the three-dimensional case is

$$S(\vec{k},t,t_0) = \frac{\hbar^2}{2m}\int_{t_0}^{t} dt' \ \left[\vec{k} + e\vec{A}(t')/\hbar\right]^2, \quad (4.13)$$

where t_0 is an arbitrary reference time. Using bracket notation we can write the Volkov state as

$$\left|\tilde{k}\right\rangle \;=\; \left|\tilde{k}(t)\right\rangle \;=\; \left|\vec{k}+e\vec{A}(t)/\hbar\right\rangle \;\exp[-iS(\vec{k},t,t_0)], \tag{4.14}$$

where $\left|\vec{k}+e\vec{A}(t)/\hbar\right\rangle$ is the instantaneous, normalized ket corresponding to the direction $\vec{k}' = \vec{k}+e\vec{A}(t)/\hbar$. Direct substitution of the dressed continuum states by the Volkov states is a common approximation in attosecond physics and the fundamental assumption in the SFA.

4.2 Strong-field approximation

The SFA [17], which deals with the interaction of atoms in intense, low-frequency laser fields, is derived in this section using the properties of the Volkov states. The TDSE of the combined atom and laser interaction is

$$[T+V(r)+V_I(t)]\left|\Psi(t)\right\rangle = i\hbar\frac{\partial}{\partial t}\left|\Psi(t)\right\rangle, \tag{4.15}$$

where T is the kinetic energy operator, $V(r) \propto -1/r$ is the atomic binding potential and $V_I = ezE(t)$ is the dipole operator in the length gauge for a laser field with linear polarization in the $\hat{z}$-direction.

4.2.1 Assumptions and approximations

Equation 4.15 can be solved using the SFA with three simplifying assumptions.

Assumption I: No depletion

The ground state is undepleted by the laser field.
A similar approximation is made in time-dependent perturbation theory, where it is assumed that the total population stays mostly in the initial state. The laser intensity must be lower than the saturation intensity of the atom. For argon this means that the intensity must be kept well below 4×10^{14} W/cm^2. Depletion can be accounted for quantitatively by using sophisticated ionization models [85].

Assumption II: No internal resonances

The atom is described by one bound state only, denoted $\left|i\right\rangle$.
The remaining bound states can be neglected if the photon energy is much smaller than the ionization potential of the atom $I_p \gg \hbar\omega$. For argon and a titanium sapphire laser, $I_p/\hbar\omega = 15.76/1.55 \approx 10$, which satisfies the requirement. The bound state is assumed to be a spherically symmetric hydrogen-like state,

$$\left|i\right\rangle \;\sim\; N\exp\left[-\frac{Zr}{a_0}\right], \tag{4.16}$$

where Z is the effective charge of the nucleus and $N = 2(Z/a_0)^{3/2}$ is the normalization factor. The energy of the state is

$$E_i = -I_p = -\frac{1}{2}\;\frac{e^2}{4\pi\epsilon_0 a_0}\;Z^2. \tag{4.17}$$

The effective charge of the nucleus, Z, can be tuned to fit the ionization potential of any atom. For argon, this implies a slightly higher nuclear charge than hydrogen, $Z_{Ar} = \sqrt{15.76/13.6} \approx 1.077$.

Assumption III: Free particle trajectories

The continuum states are not influenced by the atomic potential, $V(r)$.
For this to be valid, twice the ponderomotive energy must be greater than the ionization potential, $I_p < 2U_p$. The acceleration of the electron will then be mainly due to the laser field and not the atomic potential. The assumption justifies substitution of the proper continuum states of the atom [Eq. 3.54] by simple plane wave states [Eq. 4.14]. For argon, this implies an intensity of $I > 1.3 \times 10^{14}$ W/cm^2, but the SFA is also adequate below this intensity for some specific applications, such as HHG, where corrections due to scattering are not critical.

4.2.2 SFA ansatz and derivation

The electron wavefunction is written as the sum of a bound part and a continuum part

$$\big|\Psi(t)\big\rangle \;=\; \big|\Psi_B(t)\big\rangle \;+\; \big|\Psi_C(t)\big\rangle \;=\; \big|\tilde{i}\big\rangle \;+ \int dk^3 \; c_{\vec{k}}(t)\big|\tilde{k}\big\rangle. \tag{4.18}$$

The bound part, $\big|\Psi_B(t)\big\rangle$, consists of the initial state, which satisfies

$$[T + V(r)]\big|\tilde{i}\big\rangle \;=\; -\,I_p\big|\tilde{i}\big\rangle \;=\; i\hbar\frac{\partial}{\partial t}\big|\tilde{i}\big\rangle, \tag{4.19}$$

where $I_p = -\hbar\omega_i$ is the ionization potential of the atom, and the time-dependent bound state is $\big|\tilde{i}\big\rangle = \big|\tilde{i}(t)\big\rangle = \big|i\big\rangle \exp[iI_pt/\hbar]$. The complex amplitude of the bound state is set to one, according to Assumption I. All remaining bound states are neglected, according to Assumption II. The continuum part, $\big|\Psi_C(t)\big\rangle$, consists of Volkov states, which satisfy

$$[T + V_I(t)]\big|\tilde{k}\big\rangle = i\hbar\frac{\partial}{\partial t}\big|\tilde{k}\big\rangle, \tag{4.20}$$

where V_I is the laser field interaction. When using the Volkov states, the influence of the atomic potential is neglected, according to Assumption III. Inserting the ansatz [Eq. 4.18] into the Schrödinger equation [4.15] yields

$$i\hbar \int d^3k \; \dot{c}_{\vec{k}}(t) \; \big|\tilde{k}\big\rangle \;=\; V_I(t) \; \big|\tilde{i}\big\rangle \;+\; V(r) \int d^3k \; c_{\vec{k}}(t)\big|\tilde{k}\big\rangle, \tag{4.21}$$

where Equations 4.19 and 4.20 are used to cancel two terms on each side. A differential equation for the complex amplitude of the Volkov states is obtained by multiplying Equation 4.21 by $\big\langle\tilde{k}'\big|$ and applying the orthogonality of the Volkov states, $\big\langle\tilde{k}'\big|\tilde{k}\big\rangle = \delta_{k',k}$. The differential equation simplifies to

$$i\hbar \; \dot{c}_{\vec{k}'}(t) \;=\; \big\langle\tilde{k}'\big|V_I(t)\big|\tilde{i}\big\rangle \;+ \int d^3k \; c_{\vec{k}}(t) \; \big\langle\tilde{k}'\big|V(r)\big|\tilde{k}\big\rangle, \tag{4.22}$$

where the first term on the right-hand side describes the transition from the ground state to the Volkov state, and the second term describes continuum–continuum transitions between the Volkov states due to scattering in the atomic potential. The

scattering term can be neglected if either: the ponderomotive energy of the electron is very large due to the laser field [Assumption III]; or the ionization is weak so that the first term, with the undepleted bound state, is dominant [Assumption I]. Neglecting the continuum–continuum scattering term, the complex amplitude [Eq. 4.22] can be integrated directly

$$c_{\tilde{k}}(t) \;=\; \frac{1}{i\hbar}\int_{-\infty}^{t} dt' \,\langle \tilde{k}(t')\big|V_I(t')\big|\tilde{i}(t')\rangle. \tag{4.23}$$

Notice that the SFA complex amplitude has the same form as the complex amplitude derived from FTPT [Eq. 3.5]. While the expressions appear similar, it is important to note that the final state in SFA is dressed by the laser field and is not a field-free state. The transition rate depends on the instantaneous wavevector of the Volkov state [Eq. 4.8]. The instantaneous wavevector depends on the laser intensity, and it affects the exponential factor of the Volkov state. This implies that a small, linear increase in the intensity will lead to an *exponential* change in the overlap between the bound state and the continuum state in the dipole matrix element, and, thus, an exponential change in the transition rate. Strong field ionization, which arises naturally in SFA, is of *tunneling* type [69]. It is common to associate tunneling ionization with the Keldysh parameter, $\gamma = \sqrt{I_p/2U_p} < 1$ [80], which corresponds to a quasistatic limit, where the instantaneous tunneling rate reduces to the ADK tunneling theory [Eq. 3.43].

The total electron wave packet [Eq. 4.18] in the strong laser field becomes

$$\big|\Psi(t)\big\rangle \;=\; \big|\tilde{i}(t)\big\rangle \;+\; \frac{e}{i\hbar}\int d^3k\;\big|\tilde{k}(t)\big\rangle\int_{-\infty}^{t} dt'\; E(t')\langle\tilde{k}(t')\big|z\big|\tilde{i}(t')\big\rangle, \tag{4.24}$$

where the electron enters the continuum state $\big|\tilde{k}(t')\big\rangle$ at time t'. Once in the continuum, the electron will remain in the same Volkov state, $\big|\tilde{k}(t)\big\rangle$, as long as the atomic potential is neglected. Equation 4.24 is identical to the more explicit, famous form of the SFA wave packet [17]

$$\begin{aligned}\big|\Psi(t)\big\rangle \;=\;& \big|i\big\rangle\;\exp\left[iI_p t/\hbar\right] \;+\; \frac{e}{i\hbar}\int d^3k\;\big|\vec{k}+e\vec{A}(t)/\hbar\big\rangle\times & (4.25)\\ & \int_{-\infty}^{t} dt'\;\exp\Big[i\left\{I_p t' - S(\vec{k},t,t')\right\}/\hbar\Big]\times & (4.26)\\ & E(t')\;\langle\vec{k}+e\vec{A}(t')/\hbar\big|z\big|i\rangle, & (4.27)\end{aligned}$$

where the electron is tunnel ionized at time t' [Eq. 4.27]. It then propagates in the continuum until time t [Eq. 4.26], acquiring a phase, $\{I_p t' - S(\vec{k},t,t')\}/\hbar$, where the electron action is

$$S(\vec{k},t,t') = \frac{\hbar^2}{2m}\int_{t'}^{t} dt''\;\Big[\vec{k}+e\vec{A}(t'')/\hbar\Big]^2. \tag{4.28}$$

The total wave packet is identified as a bound state plus plane wave states [Eq. 4.25]. According to this quantum mechanical treatment, the electron may tunnel at *any* time, $t' < t$, with *any* velocity, $v(t') = [\hbar/m](\vec{k}+e\vec{A}(t')/\hbar)$. In practice, only a few of these "trajectories" will contribute constructively.

Scattering in the atomic potential

The effect of scattering in the atomic potential can be included in a Born series expansion of Equation 4.22, where $c_{\vec{k}}(t) \approx c_{\vec{k}}^{(0)}(t) + c_{\vec{k}}^{(1)}(t) + \ldots$, with the zero-order being Eq. 4.23. This results in qualitative agreement for the process of ATI. Corrections due to the atomic potential can be taken into account using the Eikonal–Volkov approximation through an iterative procedure [83, 85]. Quantitative rescattering of the photoelectrons in the atomic potential [86–88] requires the use of atomic scattering states [Eq. 3.54]. Making corrections for the atomic potential is less important for the HHG process, and the zero-order SFA wave packet [Eq. 4.22] will, therefore, be used below.

4.3 High-order harmonic generation

In this section, the electron wave packet described by Equation 4.24 is used to calculate the nonlinear polarization of an atom in an intense, low-frequency laser field. This nonlinear polarization will result in the emission of high-order harmonic photons. The polarization is proportional to the position expectation value of the electron

$$\tilde{P}(t) \;\propto\; ez(t) \;=\; e\big\langle \Psi(t)\big|z\big|\Psi(t)\big\rangle \;\approx\; e\big\langle \Psi_B(t)\big|z\big|\Psi_C(t)\big\rangle \;+\; c.c., \tag{4.29}$$

where we assume linear laser polarization along $\hat{z}$. The frequency domain, nonlinear polarization is

$$P(\Omega) \;=\; \int dt\; \tilde{P}(t)\exp[i\Omega t] \;\propto\; \int dt\; e[\big\langle \Psi_B(t)\big|z\big|\Psi_C(t)\big\rangle + c.c.]\;\exp[i\Omega t]. \tag{4.30}$$

From Equations 4.29 and 4.30, it is clear that the polarization occurs due to an interference effect between the bound state, $\big|\Psi_B(t)\big\rangle$, and the continuum wave packet, $\big|\Psi_C(t)\big\rangle$. The properties of this time-dependent dipole matrix element are

$$\big\langle \Psi_B(t)\big|z\big|\Psi_C(t)\big\rangle \;=\; \frac{e}{i\hbar}\int_{-\infty}^{t} dt' \int d^3k\; \big\langle i\big|z\big|\vec{k} + e\vec{A}(t)/\hbar\big\rangle \;\times \tag{4.31}$$

$$\exp\left[-i\left\{S(\vec{k},t,t') + I_p(t-t')\right\}/\hbar\right] \;\times \tag{4.32}$$

$$E(t')\;\big\langle \vec{k} + e\vec{A}(t')/\hbar\big|z\big|i\big\rangle, \tag{4.33}$$

where the electron first tunnels into the continuum at time, t' [Eq. 4.33]; it then propagates in the continuum and acquires a phase, or a *quasiclassical action* [Eq. 4.32]; finally it returns to the bound state [Eq. 4.31], emitting a high-order harmonic photon in the process. In this interpretation, the quantum mechanical electron can tunnel at *any* time, $t' < t$, with *any* wavevector and still return to the core at time, t. This is reminiscent of Feynman's path integral formulation of quantum mechanics [70, 89, 90], in which the electron is allowed to take *all* paths to reach the final destination. Each path that the electron takes is associated with a classical action. The most probable paths are the classical paths that *extremize* the classical action, $\delta S = 0$. Inspired by Feynman's path integrals, Lewenstein *et al.* used the SPA to find the quasiclassical trajectories in the SFA that gave the dominant contributions

to the high-order polarization [17]. The fast phase factor of the SFA is identified as $f(\vec{k}) = -\{S(\vec{k},t,t') + I_p(t-t')\}/\hbar$, and the approximate volume integral is

$$\begin{aligned}
\langle \Psi_B(t)|z|\Psi_C(t)\rangle \;\approx\; & \frac{e}{i\hbar}\left(\frac{m}{\hbar}\right)^{3/2}\int_{-\infty}^{t} dt' \left(\frac{2\pi i}{(t-t')}\right)^{3/2} \times && (4.34)\\
& \langle i|z|\vec{k}^{(st)} + e\vec{A}(t)/\hbar\rangle \times && (4.35)\\
& \exp\left[-i\left\{S^{(st)} + I_p(t-t')\right\}/\hbar\right] \times && (4.36)\\
& E(t')\,\langle \vec{k}^{(st)} + e\vec{A}(t')/\hbar|z|i\rangle, && (4.37)
\end{aligned}$$

where $S^{(st)} = S^{(st)}(t,t') = S(\vec{k}^{(st)},t,t')$ is the stationary action over the three-dimensional wavevectors.[1] The stationary wavevector,

$$\vec{k}^{(st)} \;=\; \vec{k}^{(st)}(t,t') \;=\; -\frac{1}{t-t'}\int_{t'}^{t} dt''\; e\vec{A}(t'')/\hbar, \tag{4.38}$$

fulfills the stationary phase equation,

$$\nabla_{\vec{k}} f = \nabla_{\vec{k}}\left\{S(\vec{k},t,t') + I_p(t-t')\right\}|_{\vec{k}=\vec{k}^{(st)}} = 0. \tag{4.39}$$

Using this three-dimensional stationary phase method (3D:SPA), it is clear that only the "classical trajectories" contribute to the polarization. The velocity of this classical trajectory is $\vec{v}^{(cl)}(t'') = (\hbar/m)[\vec{k}^{(st)}(t,t') + e\vec{A}(t'')/\hbar]$. The electron follows Newtonian motion and it returns to its original position, $\Delta\vec{x}^{(cl)} = \int_{t'}^{t} dt''\; \vec{v}^{(cl)}(t'',t') = 0$, at time, t. There is a one-to-one correspondence between tunneling times, t', and return times, t. In the language of Feynman path integrals, the trajectories with $\vec{k} \approx \vec{k}^{(st)}$, add constructively; while other trajectories, with $\vec{k} \neq \vec{k}^{(st)}$, destructively cancel due to the rapid variation in action [Eq. 4.32].

Using 3D:SPA, the *exact* cut-off law for the high-order harmonics can be found [17]

$$\hbar\Omega_{co} \;=\; 1.3I_p + 3.2U_p, \tag{4.40}$$

which is slightly higher than the empirical law presented in the first chapter [Eq. 1.1]. The 3D:SPA was used to calculate the generation of high-order harmonics in the theoretical work presented in Papers **III-IX**.

Quantum diffusion

The prefactor that arises in 3D:SPA, $1/\tau^{3/2}$, where $\tau \equiv t - t'$, can be understood physically. This dependence on the duration of the trajectory in the continuum accounts for the spreading of the electron wave packet due to quantum diffusion.[2] Longer trajectories will naturally diffuse more and recombine with lower probability to the well-localized bound state, $\left|\langle \Psi_B|z|\Psi_C\rangle\right|^2 \sim 1/\tau^3$.

[1] The one-dimensional SPA can be applied to each wavevector direction independently because the Hessian matrix is diagonal, $(\partial^2/\partial i\partial j)[S(\vec{k},t,t') + I_p(t-t')]/\hbar = (\hbar/m)(t-t')\delta_{i,j}$, where i and j are any of $[k_x,k_y,k_z]$. Note that all diagonal elements are equal and lead to three identical prefactors, $[\sqrt{2\pi i m/(\hbar(t-t'))}]^3 = [(m/\hbar)(2\pi i/(t-t'))]^{3/2}$.

[2] The analysis of an electron wave packet in one dimension [Sec. 2.2.2], shows that the size of the pulse increases linearly with time, $\Delta x \propto \tau$ [Eq. 2.63]. The probability of recombination should then vary as $\propto 1/\tau^3$ in three dimensions. This confirms the interpretation of the SPA prefactor [Eq. 4.34] as quantum diffusion.

Five-dimensional stationary phase approximation

It is possible to go further, and to use the SPA when integrating over the remaining two time integrals [17, 55, 91]. It is then necessary to solve the stationary equation over $\vec{k}$ [Eq. 4.38] in combination with two additional stationary phase equations. The second stationary equation is over tunneling times, t', and it describes the tunneling process

$$\frac{mv^{(cl)}(t')^2}{2} \sim \frac{\hbar^2}{2m}[\vec{k} + e\vec{A}(t')/\hbar]^2 = -I_p, \tag{4.41}$$

while the third stationary equation is over return times, t, and it imposes energy conservation for the high-order emission process

$$\frac{mv^{(cl)}(t)^2}{2} \sim \frac{\hbar^2}{2m}[\vec{k} + e\vec{A}(t)/\hbar]^2 = \hbar\Omega - I_p. \tag{4.42}$$

The five-dimensional stationary phase method (5D:SPA), has complex stationary points, $[\vec{k}^{(st)}, t^{(st)}, t'^{(st)}]$, due to the tunneling step [Eq. 4.41]. The spectral phase of the high-order harmonics can be approximated using 5D:SPA as

$$\phi(\Omega) \approx -S^{(st)}/\hbar - I_p\left[t^{(st)} - t'^{(st)}\right]/\hbar + \Omega t^{(st)}, \tag{4.43}$$

where $S^{(st)} = S(\vec{k}^{(st)}, t^{(st)}, t'^{(st)})$. The properties of the high-order harmonic phase is reviewed in Figure 4.1 for a monochromatic laser field. There are two sets of solutions to 5D:SPA for continuum times less than a period, $\tau < T$. The phase of these two contribution is roughly linear [Fig. 4.1 (a)], the first emission (called the short trajectory) is emitted first, since it has a smaller phase slope (group delay). The second emission (called the long trajectory) is emitted later, since it has a more steep phase slope (group delay). In the next subsection, we will see that these two contributions can be explained qualitatively using classical mechanics.

4.3.1 One-color HHG

Consider an atom in a monochromatic, intense, low-frequency laser field. The laser field is referred to as the *fundamental field*, and it corresponds to the output of a titanium sapphire laser system with a laser period of $T_1 = T = 2.66\,\text{fs}$ [Sec. 1.4]. For a periodic process, *i.e.* an infinite laser pulse duration, it is sufficient to consider the polarization from one period of the fundamental laser field, $0 < t < T$. The tunneling times, t', should, in principle, be integrated from minus infinity [Eqs. 4.34-4.37]. This is, of course, not possible numerically, and it is not necessary in practice. Quantum diffusion strongly suppresses the contribution from trajectories with durations longer than one period of the fundamental laser field. Reducing the tunneling time integral to $t - T < t' < t$, yields an adequate approximation for single-atom polarization. Interestingly, two different classical trajectories return with the same energy within this restricted time-window. These are called the *short trajectory* and the *long trajectory*. The time–energy properties of the two trajectories are shown in Figure 4.2. The short trajectory spends a shorter time, $0 < \tau^{(S)} < 0.65T$, than the long trajectory, $0.65T < \tau^{(L)} < T$, in the continuum. In a macroscopic sample, the short and the long branch will phase match with different efficiencies depending on the experimental conditions. It is common to phase match the short branch and, thereby,

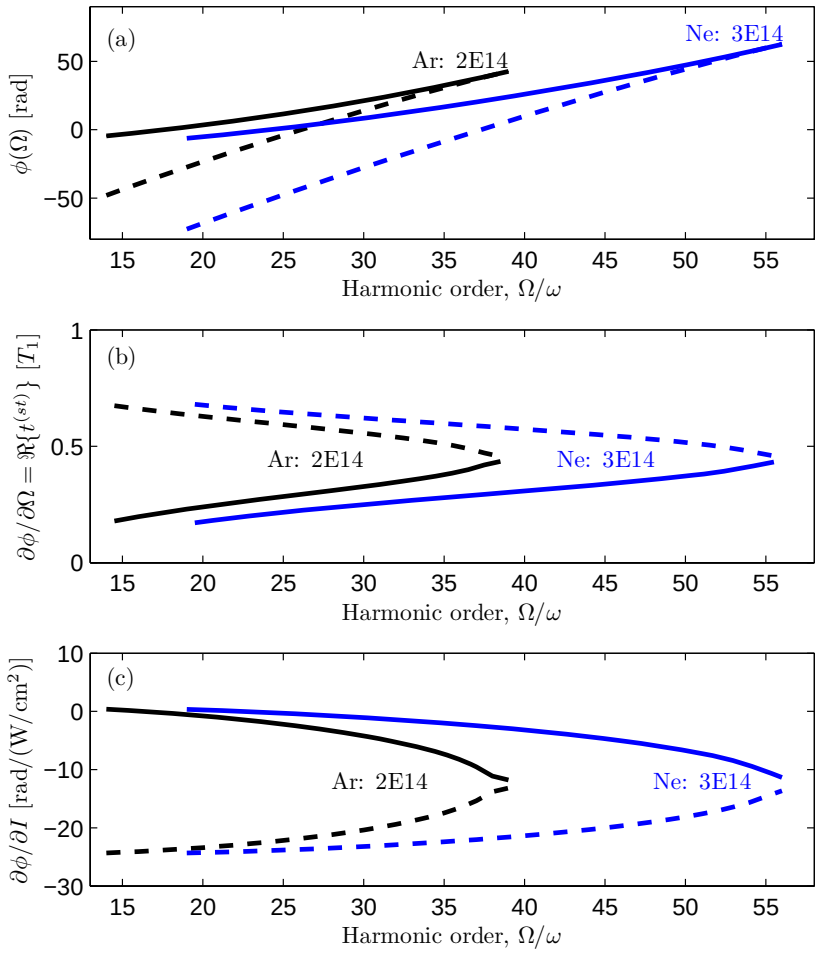

Figure 4.1. *(a) Spectral phase of high-order harmonics from argon at intensity* 2×10^{14} *W/cm*^{2} *[black curve] and for neon at intensity* 3×10^{14} *W/cm*^{2} *[blue curves]. (b) The emission time of harmonic* Ω *is* $\Re\{t^{(st)}(\Omega)\} = \partial\phi/\partial\Omega$*. The emission time is given in units of the fundamental field period,* $T = 2.66$ *fs. (c) The spectral phase derivatives with respect to intensity is an important quantity for macroscopic phase matching of the high-order harmonics (and it is often labeled as* $\partial\phi/\partial I = -\alpha$*). The short (long) trajectory is drawn with a full (dashed) line.*

select one of the two trajectories. Solving this problem numerically is a formidable task, which requires great computational power, involving the numerical evaluation the macroscopic Maxwell equations with the TDSE (or SFA) as a source term for the nonlinear polarization [92]. Rather than taking this rigorous numerical route, we directly select the short branch from the single-atom response. This simple trajectory selection (STS) method for the short branch consists of limiting the integral bounds

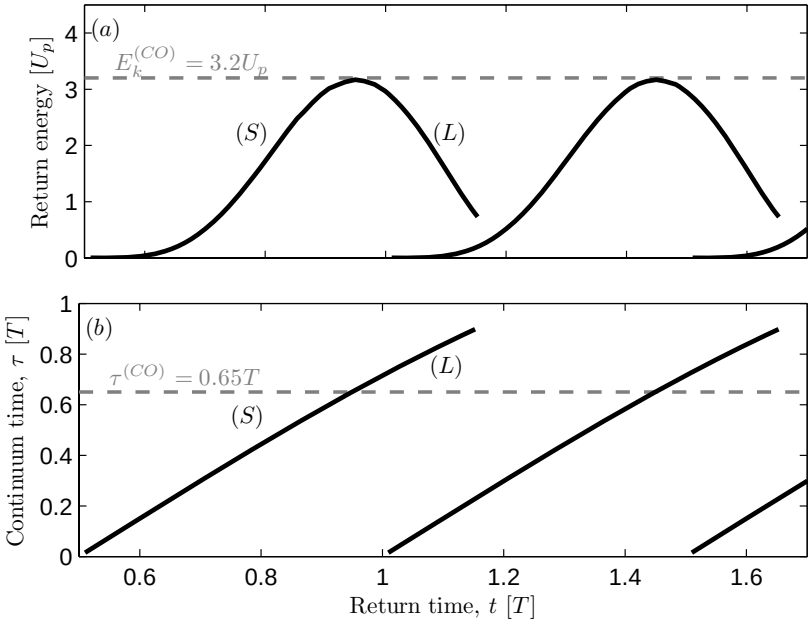

Figure 4.2. *(a) Kinetic return energy, $E_k(t) = (\hbar^2/2m)[k^{(st)}(t,t') + eA(t)/\hbar]^2$, for electrons that tunnel at time, t' into a monochromatic laser field. The short branch of trajectories (S) and the long branch of trajectories (L) merge at the cut-off with the maximal return energy, $E_k^{(CO)} = 3.2U_p$ [dashed line]. (b) Continuum times, $\tau = t - t'$, of the trajectories. The cut-off occurs for $\tau^{(CO)} = 0.65T$. The trajectories are repeated periodically over half a fundamental period, $T/2$.*

for the tunneling times $t - 0.65T < t' < t$, which is equivalent to $0 < \tau < 0.65T$. The nonlinear polarization will then only exhibit the features of the short branch. Harmonics calculated with the STS method are expected to be accurate for orders in the plateau; while the harmonic close to the cut-off may depend on how the cut in the tunneling time integral is made. To gauge the reliability of the STS method, the numerical integration has been ramped down smoothly and the position of the cut has been adjusted, while time–frequency window methods (Gabor transforms) have been used to visualize the trajectories in time–frequency space. Decreasing the tunnel time integral leads to a part of the high-energy, short trajectory being missing; while an increasing tunnel time integral leads to the inclusion of high-energy, long trajectory components.

4.3.2 Two-color HHG

So far, we have only considered the trajectories due to a monochromatic electric field with angular frequency, $\omega = 2\pi/T$. The experimental work presented in Papers **III**, **IV** and **VIII** shows that a strong second-harmonic field can be used to control the electron trajectories, and thereby alter the properties of the high-order harmonics

[93–97]. The total electric field driving the HHG process is

$$\tilde{E}(t) = E_1 \sin[\omega t] + E_2 \sin[2\omega t + \phi], \tag{4.44}$$

with an intensity ratio, $\mathcal{R} \equiv E_2^2/E_1^2 \gtrsim 10\%$.[3] The classical two-color trajectories in Figure 4.3 show how the second harmonic can be used to deform the trajectories

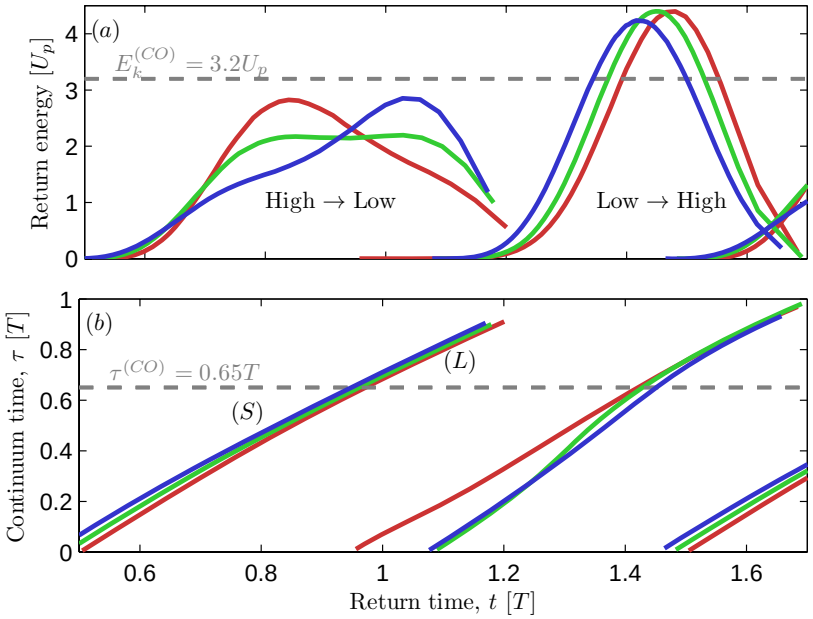

Figure 4.3. *(a) Kinetic return energy, $E_k(t) = (\hbar^2/2m)[k^{(st)}(t,t') + eA(t)/\hbar]^2$, for electrons that tunnel at time, t' into a two-color laser field. The intensity ratio between the second harmonic and the fundamental is $\mathcal{R} = 25\%$. The phase difference, ϕ, between the fields are: 0, 0.6 and 1.2 rad for the red, green and blue line respectively. The maximal return energy is lower than the one-color case [dashed line] in the first half-cycle. The maximal return energy is higher than the one-color case [dashed line] in the second half-cycle. (b) The continuum times, $\tau = t - t'$, of the trajectories are mostly constant in the first half-cycle; while the changes are more striking in the second half cycle. The trajectories are repeated periodically over a full fundamental period, T.*

compared to the one-color case [Fig. 4.2]. Note that the trajectories in adjacent half-cycles are deformed differently. This symmetry breaking originates from the following properties of the fields: $E_1(t) = -E_1(t+T/2)$ and $E_2(t) = +E_2(t+T/2)$. The second harmonic may, for instance, decelerate the electron in one half-cycle and accelerate the electron in the other.

[3] An efficient broadband second-harmonic field is generated using a *thin* doubling crystal. In Paper **III**, we used a 0.6 mm KDP (potassium dihydrogen phosphate) type I crystal and achieved an effective intensity ratio of $\mathcal{R} \approx 15\%$. Using a thicker crystal will increase the total conversion efficiency, but will also increase the pulse duration of the second harmonic field. Only the part of the second-harmonic field that overlaps the 30 fs fundamental laser pulse is useful for control of HHG.

The short trajectories have an approximate time in the continuum, $\tau^{(S)} \approx 0.5T$, corresponding to a full period of the second harmonic field. The second harmonic field can be synchronized to increase the total electric field at the tunneling time of the trajectories in one half-cycle. This *boosts* the tunneling rate, but at the expense of a weaker recombining force approximately half a period later, when the second harmonic field instead decreases the total electric field. The result is stronger harmonics but a lower maximal harmonic order, compared to the one-color case [Fig. 4.3: *High* $\rightarrow$ *Low*]. Conversely, the trajectories in the other half-cycle correspond to weaker tunnel ionization and stronger recombination [Fig. 4.3: *Low* $\rightarrow$ *High*]. As already mentioned, small changes in the instantaneous electric field lead to an exponential change in tunneling rate [Eq. 3.43]. This results in a negligible contribution from the second half-cycle compared to the first half-cycle and an attosecond pulse train of *one pulse per cycle* [98].

The long trajectories spend a longer time in the continuum, $\tau^{(L)} \approx 0.75T$, thus the boost in tunneling can be combined with an increase in the maximum kinetic energy. This scheme shows great promise for increasing the bandwidth of the HHG process, but it has not yet been successfully implemented due to the experimental difficulties in phase matching the long trajectories.

Figure 4.4 shows high-order harmonic intensities calculated using the STS method for two-color HHG with $\mathcal{R} = 10\%$. The maximal photon energy of the short trajectories [Fig. 4.4 (a)] can be controlled using the second harmonic control field, but, as expected from the classical analysis, it is only possible to decrease the maximal photon energy to values below the exact one-color cut-off, $1.3I_p + 3.2U_p$ [dashed line]. The maximal harmonic energy can also be controlled for the long trajectories [Fig. 4.4 (b)], and photon energies above the one-color cut-off can be produced at certain relative phases.

The detailed structure of the harmonic spectrogram [Fig. 4.4] can be better understood by considering the boost of tunneling in more detail. The even and odd harmonics behave in a similar way, both displaying a clear "tilt" over ϕ. This tilt is negative for the short trajectories, and positive for the long trajectories. The different signs of the tilt can be attributed to mapping from boosted tunneling time to the return energy of the electron trajectories. Together, these lead to a Λ-shaped spectrogram over ϕ. The same scenario is then repeated for every half-cycle, where the other half-cycle takes the role of *high*$\rightarrow$*low*. This control of the tunnel ionization leads to the spectral control of 2-color HHG presented in Paper **III**. Experimental and theoretical studies are presented in Paper **IV**, where weak interference between the deformed half-cycle trajectories is studied and showing how the phases of the electron trajectories are modified by the strong second harmonic. Changing the phase of the generation process using two-color laser fields provides an interesting approach to optimize macroscopic phase matching of high-order harmonics [93].

In the case of few-cycle laser pulses, the nonlinear polarization must be calculated at each time, t, of the pulse, and not just for one period. For ultra-short laser pulses, the electron trajectories will be modified in the rising (falling) part of the pulse due to the increasing (decreasing) overall field strength, compared to the trajectories in the stationary peak of the field. In Paper **VIII**, the similarities between two-color HHG and few-cycle HHG are stressed, where subcycle control and yield of the electron trajectories is imposed by the CEP [27].

In Paper **IX**, the combination of an APT with one pulse per period and a few-

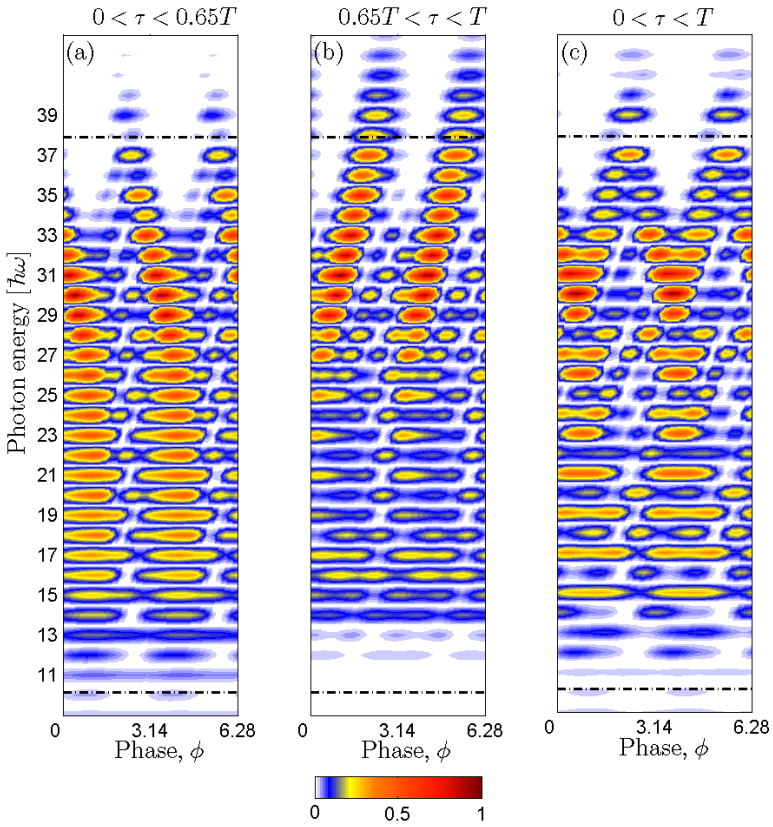

Figure 4.4. *Theoretical high-order harmonic intensity as a function of relative phase, ϕ, between fundamental and second-harmonic fields. The relative intensity is strong, $\mathcal{R} = 10\%$. The upper dot-dashed line indicates the exact one-color cut-off, $1.3I_p + 3.2U_p$, while the lower dot-dashed line indicates the atomic ionization potential, I_p, for argon. The three panels correspond to: (a) the short branch, $0 < \tau < 0.65T$, (b) the long branch, $0.65T < \tau < T$; and (c) both branches, $0 < \tau < T$. The data in false color were produced using the STS method developed in Paper **III**. The full-period integration (c) shows the "connection" between the short (left tilt) and long branches (right tilt) at the cut-off. The high→low half-cycle is completely dominant, which results in harmonics orders that are lower than the one-color cut-off at all delays for the short trajectories. The relative phase is related to the delay as $\phi = -2\omega_1\tau$.*

cycle fundamental field [99] was used to study the progression from a many attosecond pulses to fewer attosecond pulses experimentally. The experimental results show that a SAP could have been extracted if spectral filtering had been applied for a special combination of CEP and relative phase between the two fields. The rich interference structures observed were interpreted as pulse-to-pulse interference, in analogy with the interference structure from multiple slits in Fourier optics.

4.3.3 Probing high-order harmonic generation

In this section we will discuss the application of a weak, second-harmonic probe field to the HHG process. The total electric field is the same as in Equation 4.44, but with $\mathcal{R} \sim 0.1\%$. The main idea is to obtain information about the unperturbed process using the probe field. Figure 4.5 shows high-order harmonic intensities calculated using the STS method. The spectrogram consists of strong odd harmonics [red] and very

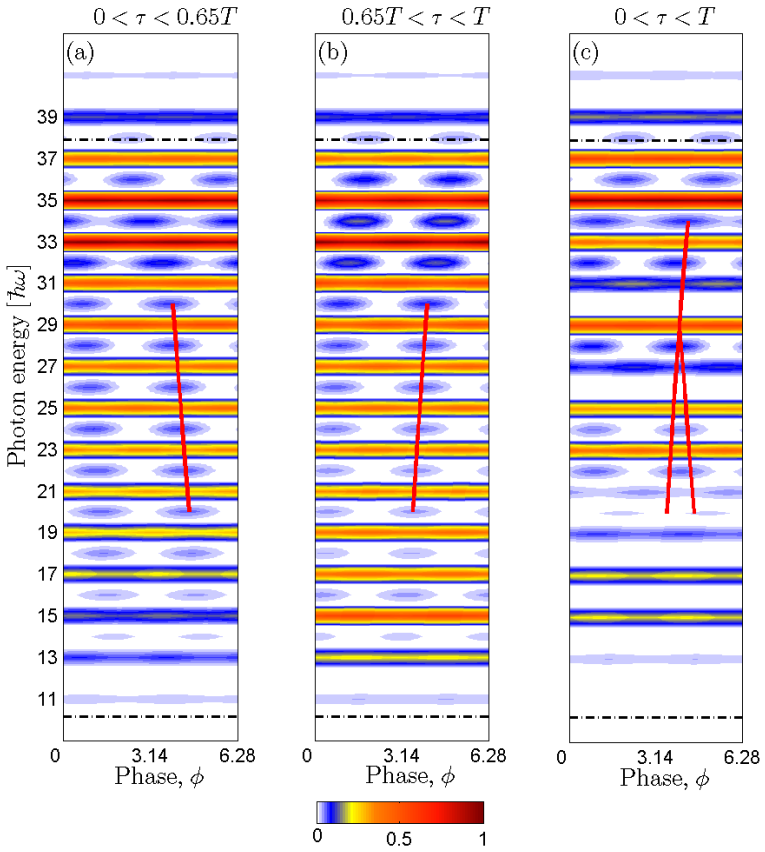

Figure 4.5. *Theoretical high-order harmonic intensity as a function of relative phase, ϕ, between fundamental and second-harmonic fields. The relative intensity is very low, $\mathcal{R} = 0.1\%$. The upper dot-dashed line indicates the cut-off; while the lower dot-dashed line indicates the ionization potential. The three panels correspond to: (a) the short branch, $0 < \tau < 0.65T$, (b) the long branch, $0.65T < \tau < T$; and (c) both branches, $0 < \tau < T$. The data in false color were produced using the STS method, while the red lines, which indicate the maximum of the even harmonics, were calculated using the 5D:SPA method developed in Paper* **VI**. *The agreement between the STS and the 5D:SPA is excellent in the center of the harmonic plateau for both the short and long trajectories. The full-period integration (c) agrees with the long branch 5D:SPA calculations close to the cut-off. The relative phase is related to the delay by $\phi = -2\omega_1\tau$.*

weak even harmonics [blue]. The odd harmonics arise from the fundamental process

with a monochromatic laser field; while the modulated even harmonics are induced by the second-harmonic probe field. The slope of the modulation is negative (positive) for the short (long) branch over ϕ. The modulation offset provides a robust, background-free experimental observable, which has been studied in depth in Papers **IV**, **V** and **VI**. The inspiration for this work originates from a study by Dudovich *et al.* [37], in which "the birth of attosecond pulses" was studied *in situ* using a second-harmonic probe field. Dudovich *et al.* used classical analysis to interpret the *in situ* phases, *i.e.* the offset in modulation of the even harmonics, as being proportional to the emission times of the harmonics from the atoms. This interpretation is appealing since the spectrograms [Fig. 4.5] are similar in appearance to the photoelectron spectrograms generated by the RABITT method [Fig. 3.2]. Paper **V** presents a side-by-side comparison of the RABITT method and the *in situ* method, where the slopes of the two methods are found to be similar in the lower part of the harmonic plateau. There is, however, a strong deviation, a "kink", close to the cut-off that can not be explained using classical theory. This kink was studied further experimentally using a different experimental setup, as reported in Paper **IV**. A quantum mechanical, perturbative approach to predict the maxima of the modulation in the even harmonics was developed and is presented in Paper **VI** [Fig. 4.5: red line]. The phase induced by the probe field is

$$\sigma(\vec{k}, t, t_0)/\hbar = \frac{e}{m}\int_{t_0}^{t} dt' \ \left[\vec{k} + e\vec{A}_1(t')/\hbar\right] \cdot \vec{A}_2(t', \phi), \tag{4.45}$$

where $[\vec{k}, t, t_0]$ are the five-dimensional stationary points of the one-color case. The induced action is a complex number because the probe field will influence both the tunneling probabilities of the electron trajectories and the phase of the electron trajectories in the continuum. The phase is odd over half-cycles and breaks the inversion symmetry, which causes even harmonics to appear. The kink was reproduced using both perturbative quantum mechanical theory and the STS method, and it is identified as a switch in dominance of the short and the long trajectories [Fig. 4.5]. The tunneling effects render the slope of phases that maximize the even harmonics mostly insensitive and to the intensity of the fundamental field. It would be interesting to study these phases further experimentally, since they provide a clean, background-free signal that can be compared with quantum mechanical single-atom calculations, but they are not suitable for temporal characterization of APTs.

In Papers **IV**-**V**, a simplified "classical" interpretation of Equation 4.45 was used, where the tunneling effects (the imaginary part) of the induced action [Eq. 4.45] is neglected. As the strength of the probe field, A_2, is increased, the induced phase increases. At a given probe intensity, the induced phase can be shifted between the two half-cycles by changing the relative phase between the two fields, and mapping out the interference between trajectories in adjacent half-cycles. The interference can be understood in analogy with Newton rings, where the number of "rings" that appear over a period of relative delay reveals the maximal phase difference between the adjacent half-cycles. Note that the interference observed experimentally, and described in Paper **IV**, is weak since the contrast between the adjacent cycles is low when tunnel ionization favors one half-cycle. The fast modulations can also be identified in the STS method for both the short and the long trajectories in between the main tilts [Fig. 4.4 (a), (b)]. The general signature of interference between adjacent subcycles is

that the odd and even harmonics behave in opposite ways: The odd harmonics peak when the even harmonic dip. Conversely, the signature of one pulse per period is that both odd and even harmonics behave in a similar way.

4.3.4 Summary of two-color HHG

The work presented in this thesis shows that a two-color HHG setup provides a versatile attosecond pulse source. By changing the relative phase between the control field and the fundamental field, the properties of the harmonics can be adjusted: the spectral bandwidth can be shifted; the spectral phase can be varied; the divergence of the harmonics can be controlled; and an APT with one pulse per period can be obtained.

Chapter 5

Summary and outlook

Attosecond science is attracting a great deal of attention because it promises accurate probing and control of electron processes in atomic and molecular systems. The work presented in this thesis shows that coherent high-order harmonics can indeed be used to probe atomic processes on the attosecond timescale. These high-order harmonics correspond to attosecond pulse trains in the time domain, but the duration of the actual pulses is not always critical. Depending on the application, the coherent nature of the harmonics and the broad bandwidth are sufficient to perform attosecond experiments using photoelectron interferometry. Paper **I** describes how high-order harmonics and a weak IR field can be used to study the phase of resonant two-photon ionization. The 15^{th} harmonic is resonant with the bound state (He: $1s3p\,^1P_1$), while the higher harmonics launch photoelectrons into the continuum. The role of the IR field is two-fold: to emit a near-threshold photoelectron from the resonant intermediate state, and to create an attosecond reference clock in the continuum. The phase of the resonant two-photon transition depends critically on the frequency offset between the lowest-order harmonic and the bound state. By tuning the frequency of the laser or by shifting the resonant level of the atom, we observe how the phase of the resonant transition changes compared to the reference clock. In this way, it is possible to map how the bound state is shifted due to the Stark shift from the IR field. Paper **II** describes the use of high-order harmonics and a weak IR field to probe the phase difference of two-photon ionization processes from different initial states. The fact that the same high-order harmonics (21, 23, 25 and 27) are used to photoionize both initial states (Ar: $3s^2$ and $3p^6$) makes it possible to subtract the phases of the harmonics and isolate the difference in phase between the electron transitions, corresponding to a delay of ~ -100 as. After a careful theoretical investigation, this delay was identified as the sum of the photoelectron Wigner delay and an additional delay, caused by the stimulated continuum transitions induced by the IR field. The total experimental delay observed in a RABITT scan is, therefore, composed of three parts: the group delay of the attosecond pulses; the Wigner delay of the photoelectrons; and the delay from continuum–continuum transitions induced by the IR field.

In Chapter 2, the temporal properties of attosecond XUV pulses were theoretically compared to the temporal properties of photoelectron wave packets. Photoelectrons are free particles with wavefunctions that are closely related to classical mechanics,

while the corresponding wave packet durations increase linearly in time due to strong quantum diffusion. The attosecond photoionization process was studied further in Chapter 3, where an asymptotic form for the photoelectron wavepacket was derived. Using this wave packet it was possible to estimate the extremely short delays that are present in laser-stimulated continuum–continuum transitions of photoelectrons. It would be interesting to study these delays further and to compare the corresponding quantum mechanical- and classical pictures in detail.

Coherent control experiments on the attosecond timescale can be carried out if the strength and phase of the individual high-order harmonics can be controlled. The different frequency components of the high-order harmonic bandwidth can then act on the target in a predetermined sequence causing a coherent reaction. In this work, the HHG process was coherently controlled using a second-harmonic control field. It is demonstrated that both the intensity and phase of HHG can be controlled using the control field. Paper **III** describes how the spectral content of the HHG process can be tuned using a strong second-harmonic control field. Using the STS method, it was concluded that the spectral shaping could be explained by the single-atom response. The second-harmonic field boosts the tunneling ionization of specific electron trajectories and alters their path in the continuum. In this way, it is possible to create APTs with one pulse per period, to increase the yield of the HHG process, and to control the spectral content of the APTs. Paper **IV** reports on faint, rapid modulations, observed experimentally, as a function of the delay between the fundamental and the second-harmonic field. These modulations were explained as interference between adjacent attosecond pulses. In analogy with Newton rings, it is possible to determine the phase difference of attosecond pulses induced by the second-harmonic control field by counting the number of modulations (rings) per period of relative delay. The induced phase difference influences the divergence of the harmonic beam and changes the temporal structure of the APT. The theoretical background for the SFA and the STS method was reviewed in Chapter 4. The phase properties of the HHG process has been studied using the 5D:SPA for both one-color and two-color laser fields. It would be interesting to apply the STS method to other atoms and laser field wavelengths, and to consider HHG from aligned molecules.

It is important to be able to characterize the phase of the high-order harmonics and the temporal structure of the attosecond pulses. Most existing methods of attosecond pulse characterization rely on making photoelectron replicas of the attosecond pulses, and then probing the photoelectrons using an IR field. A photoelectron cross-correlation spectrogram is obtained by recording the photoelectron energy distribution as a function of the delay between the attosecond pulses and the IR field. Understanding the ultrafast electron dynamics, and how it is related to the temporal structure of the attosecond pulses is critical for attosecond science. This thesis describes experimental studies in which the established RABITT method was compared with new alternative characterization schemes. Paper **V** presents an experiment where an APT is characterized using both the RABITT method and a novel two-color method which probes the HHG process *in situ*. The aim of these studies was to investigate the evolution of the attosecond pulses from single-atom emission to on-target detection. The experimental results indicate that the *in situ* method can provide complementary information to the RABITT method, but inconsistencies were found between the theory of the *in situ* method and the experimental data close to the harmonic cut-off. Paper **VI** presents an improved theory for the *in situ* method. This new theory is

capable of reproducing the main features of the two-color HHG close to the harmonic cut-off, but it also reveals that the *in situ* method cannot always be used for temporal characterization of APTs. It would be interesting to see more experiments using the *in situ* method, especially on different atoms and under conditions where both the short and the long trajectories are present. Paper **VII** presents experimental studies in which the RABITT method was investigated at increasing IR probe intensity. The transition from the photon picture to the so-called streaking regime occurs as the intensity of the probe is increased. It was found that the temporal information provided by the RABITT method was lost when the IR field intensity was increased beyond a perturbation, but that it was then possible to extract the temporal structure of the APTs from higher order components in the corresponding cross-correlation spectrograms.

An ideal source of attosecond pulses provides any number of attosecond pulses with any pulse spacing and any photon energy region. In practice, this is difficult to achieve, and the work described in this thesis has focused on applying the two-color control scheme to reduce the number of pulses in the APT and control the pulse properties. Paper **VIII** discusses the similarities between the control of HHG using a few-cycle IR field and using a two-color field. The advantage of the APT over the SAP is that the experiment is repeated coherently multiple times, which increases the signal. The disadvantage of APT is that the attosecond temporal information is given in modulus of a half fundamental period. In this sense, SAPs are better suited for studying absolute delays of a processes that are longer than a half fundamental period. An intrinsic attosecond delay of the photoelectrons is present also for SAP using the streaking method in analogy with the CC delay of the RABITT method. It would be interesting to compare these extremely short delays, which both contain information about the attosecond continuum–continuum transitions and the atomic screening potential. The use of a few-cycle two-color field is presented in Paper **IX**, where the number of pulses in the APT varies over the spectral bandwidth. The sequence of attosecond bursts was controlled using the CEP and the relative phase and strength between the two fields. The interference structure visible in the spectral domain was interpreted as the beating between a few distinct attosecond bursts in analogy with the diffraction pattern from a few slits in Fourier optics. This simple interpretation was verified using the STS method for the single-atom response and for full macroscopic simulations. Combining few-cycle pulses with a control field provides improved control of the generation of SAP. Two-color fields provide control of the single-atom response, and by changing the relative delay between the two fields, the amount of phase acquired by the quasiclassical trajectories can be controlled. It would, therefore, be extremely interesting to study the phase matching aspects of two-color HHG further.

In the work presented in this thesis, the two-color field consisted of a strong 800 nm fundamental field and a probe/control field at 400 nm. Going to longer wavelengths, such as 1.3 μm or 2 μm, implies longer trajectories, more quantum diffusion and more acquired phase. Here, a second harmonic control field could help to reduce quantum diffusion and to improve macroscopic phase matching. A fundamental field plus a third harmonic provides control of the trajectories without breaking the inversion symmetry. The tunneling ionization can be controlled, as well as the chirp of the attosecond pulses and the acquired phase. Using the third harmonic to flatten the intensity-dependent HHG phase could lead to improved phase matching conditions

and more intense two-pulse-per-cycle APTs. Another interesting field combination is a weak fundamental and a strong second harmonic. In this case, there will be four different short trajectories that will interfere in pairs. Depending on the fundamental wavelength, this setup could produce single-atom information complementary to the existing *in situ* method. It would also be interesting to study solid state media in intense, low-frequency fields and to apply the three-step model in a band structure. Being able to program a large, arbitrary coherent bandwidth into the HHG process will, most likely, require a long fundamental wavelength and many odd harmonic control fields that can be used to carefully alter the quasiclassical trajectories. As the photon energy increases, it will be possible to induce and probe deeper atomic dynamics, such as inner-shell ionization and multiple-electron excitations. Breaking a molecule coherently from the inside is a dream shared by many attosecond scientists. First, a high-frequency pulse from the coherent bandwidth initiates photoionization. Second, a lower-frequency part can be used to coherently control the dynamics of the excited states. Finally, a third, intermediate-frequency pulse can be used to probe the system. As the intensity of the attosecond pulses increase, it will be possible to perform nonlinear interactions with the attosecond pulses. This will enable exciting new possibilities for characterization and control on the attosecond timescale.

The link between classical mechanics and quantum mechanics in attoscience is fascinating, and I hope to encouter it again, many times, in different places.

Comments on the papers

I **Phase Measurement of Resonant Two-Photon Ionization in Helium**
In this paper we study the phase properties of two-photon resonant ionization of He. The phase information is gained by cross-correlating an IR field with a high-order harmonic comb, where the lowest harmonic is resonant with the bound $1s3p$ state in He. I took part in the execution of experimental work and I performed analytical calculations using second order perturbation theory to describe the observed phase shift and how it depends on the duration of the laser pulse. The calculations were transferred into a MATLAB program by M. Swoboda and compared to the TDSE calculations by K. J. Schafer in Figure 3. I took an active part in the writing of the manuscript.

II **Probing Single-Photon Ionization on the Attosecond Time Scale**
In this paper we study temporal properties of the photoionization process from two different initial states in Ar. Temporal information about the ionization process is gained by cross-correlating an IR probe with an APT and subtracting the chirp of the attosecond pulses. I was deeply involved in this experiment from idea to execution. I performed analytical calculations to describe the two-photon ionization process and I interpreted the observed delay as a sum of two contributions: the Wigner delay and the continuum-continuum delay, which depends on the laser wavelength. I wrote the theory part of the manuscript and I produced Figures 3 and 4.

III **Spectral Shaping of Attosecond Pulses using Two-Color Laser Fields**
In this paper we study spectral properties of two-color HHG with a strong second harmonic field. We obtain a tunable central energy of the attosecond pulses as a function of the relative phase between the fields. I performed calculations using SFA. I developed the STS method and I found good agreement with the experimental results by isolating the short trajectories. I wrote the theory part of the manuscript and I provided data for Figures 1, 3, 4 and 5.

IV **Interference Effects in Two-Color High-Order Harmonic Generation**
In this paper we studied the spectral modulation of two-color HHG with a strong second harmonic field as a function of the relative phase between the fields. I worked on the analysis of the experimental data and I interpreted the modulation as an interference effect between electron trajectories in adjacent half cycles. By comparing the experimental modulation with a simple interference model, I could estimate the amount of phase which was induced by the second harmonic field to the electron trajectories. I also explained that this induced phase leads to control of the high-order harmonic beam divergence. I wrote a large part of the manuscript and I worked on all figures.

V **Atomic and Macroscopic Measurements of Attosecond Pulse Trains**
In this paper we compare two characterization methods for attosecond pulses in trains. The well-established RABITT method measures the group delay dispersion of the attosecond pulses on target, while the in situ method yields information about the attosecond pulses as they are produced. I took part in the planning and execution of the experiment and I performed the analysis of the experimental data. I simulated the in situ method using SFA with the STS method. I wrote the manuscript and I produced all figures.

VI **Quantum Mechanical Approach to Probing the Birth of Attosecond Pulses using a Two-Color Field**
In this paper we perform a theoretical study the in situ method for characterization of attosecond pulses. I performed the theoretical investigation using a perturbative stationary phase analysis for two-color HHG. I wrote the manuscript and I produced all figures.

VII **Intensity Dependence of Laser-Assisted Attosecond Photoionization Spectra**
In this paper, we study the RABITT method at high probe field strengths. An extension to the method is proposed, based on higher-order perturbation theory, which I suggested: Higher-order RABITT signals at high probe intensities, where the fundamental RABITT signal at 2ϕ fails. I performed an analytical analysis. I contributed to the writing of the manuscript.

VIII **Sub-cycle Control of Attosecond Pulse Generation using Two-Colour Laser Fields**
I this paper we discuss the similarities between the generation of SAP and two-color HHG. I contributed to the manuscript and I provided the data for Figure 5 using SFA with the STS method.

IX **Spectral Signature of Short Attosecond Pulse Trains**
In this paper we use an ultrashort laser pulse mixed with its second harmonic to generate attosecond pulses. I took part in the execution of the experiment briefly at ETH. I performed SFA calculations and I interpreted the interference structures in the spectrum as pulse-to-pulse interferences in the generated APT. I contributed mostly to the theoretical part of the manuscript.

Acknowledgments

It has been a privilege to work as a PhD student at the Atomic Physics Division at Lund University. Professor Anne L'Huillier is the best supervisor that any PhD student could have as she radiates pure enthusiasm for physics, and stimulates everyone to do their best. I am also grateful to my co-supervisor University Lecturer Johan Mauritsson, who is an excellent role model for any young, aspiring researcher. I would also like to thank Professor Sune Svanberg and Professor Claes-Göran Wahlström, the former and present head of the division, for providing a friendly, creative and professional working atmosphere.

Sharing an office with Erik Mansten and Miguel Miranda has been fantastic in terms of scientific discussions and in terms of friendship. I also want to thank my friends and coworkers Marko Swoboda, Kathrin Klünder, Jörg Schwenke, Thomas Fordell, Cord Arnold, Thierry Ruchon, Xinkui He, Per Johnsson, Christian Erny, Esben Larsen, Piotr Rudawski, Rafal Rakowski, Anders Persson, Thomas Remetter, Mathieu Gisselbrecht, Franck Lépine, Christoph Heyl and Diego Guenot. Without your hard work I would not have come this far. I wish the best of luck to the new PhD students in the research group David Kroon, Eleonora Lorek and Linnea Rading.

Interesting ideas come at unexpected times, and I want to thank my fellow PhD students in other fields of physics Jonas Cremon, Mattias Borg, Guillaume Genoud, Pontus Svenmarker, Mikkel Brydegaard, Erik Alerstam and many more, for all the fun discussions.

I also want to thank some of the finest theorists in atomic physics, Alfred Maquet, Richard Taieb, Mette B. Gaarde and Kenneth J. Schafer, with whom I had the privilege to work. I thank Maciej Lewenstein for the discussions during my ultra-fast stay in Barcelona. I want to thank Ursula Keller for a fruitful collaboration and for the wonderful skiing trip in the Alps.

Teaching is one of my passions, and I would like to thank Nina Reistad and Lars Engström for allowing me to help with many laboratory exercises in diffraction and experimental methods, which I enjoyed very much, every time.

Finally, my thanks to Henrik Steen, Minna Ramkull, Camilla Nilsson, Harriet Lindahl and Bertil Hermansson for taking care of many of the technical and administrative things that were in the way of doing physics.

Jag vill också tacka mina föräldrar för deras ständiga stöd och jag önskar min syster all lycka i världen. Ett lite speciellt tack ger jag till Selma.

References

1. A. McPherson, G. Gibson, H. Jara, U. Johann, T. S. Luk, I. A. McIntyre, K. Boyer and C. K. Rhodes. *Studies of multiphoton production of vacuum-ultraviolet radiation in the rare gases.* J. Opt. Soc. Am. B **4**, 595 (1987).

2. M. Ferray, A. L'Huillier, X. F. Li, G. Mainfray and C. Manus. *Multiple-harmonic conversion of 1064 nm radiation in rare gases.* J. Phys. B **21**, L31 (1988).

3. Z. Chang, A. Rundquist, H. Wang, M. M. Murnane and H. C. Kapteyn. *Generation of Coherent Soft X Rays at 2.7 nm Using High Harmonics.* Phys. Rev. Lett. **79**, 2967 (1997).

4. Ch. Spielmann, N. H. Burnett, S. Sartania, R. Koppitsch, M. Schnürer, C. Kan, M. Lenzner, P. Wobrauschek and F. Krausz. *Generation of Coherent X-rays in the Water Window Using 5-Femtosecond Laser Pulses.* Science **278**, 661 (1997).

5. M. Schnürer, Z. Cheng, M. Hentschel, F. Krausz, T. Wilhein, D. Hambach, G. Schmahl, M. Drescher, Y. Lim and U. Heinzmann. *Few-cycle-driven XUV laser harmonics: generation and focusing.* Appl. Phys. B **70**, S227 (2000).

6. A. Paul, R. A. Bartels, R. Tobey, H. Green, S. Weiman, I. P. Christov, M. M. Murnane, H. C. Kapteyn and S. Backus. *Quasi-phase-matched generation of coherent extreme-ultraviolet light.* Nature **421**, 51 (2003).

7. E. A. Gibson, A. Paul, N. Wagner, R. Tobey, D. Gaudiosi, S. Backus, I. P. Christov, A. Aquila, E. M. Gullikson, D. T. Attwood, M. M. Murnane and H. C. Kapteyn. *Coherent Soft X-ray Generation in the Water Window with Quasi-Phase Matching.* Science **302**, 95 (2003).

8. E. Seres, J. Seres, F. Krausz and C. Spielmann. *Generation of Coherent Soft-X-Ray Radiation Extending Far Beyond the Titanium L Edge.* Phys. Rev. Lett. **92**, 163002 (2004).

9. R. W. Boyd. *Nonlinear Optics.* Academic Press (2003).

10. J. L. Krause, K. J. Schafer and K. C. Kulander. *High-order harmonic generation from atoms and ions in the high intensity regime.* Phys. Rev. Lett. **68**, 3535 (1992).

11. P. B. Corkum. *Plasma perspective on strong-field multiphoton ionization.* Phys. Rev. Lett. **71**, 1994 (1993).

12. P. H. Bucksbaum, R. R. Freeman, M. Bashkansky and T. J. McIlrath. *Role of the ponderomotive potential in above-threshold ionization.* J. Opt. Soc. Am. B **4**, 760 (1987).

13. J. Tate, T. Auguste, H. G. Muller, P. Salieres, P. Agostini and L. F. DiMauro. *Scaling of Wave-Packet Dynamics in an Intense Midinfrared Field.* Phys. Rev. Lett. **98**, 013901 (2007).

14. H. Kapteyn, O. Cohen, I. Christov and M. Murnane. *Harnessing Attosecond Science in the Quest for Coherent X-rays.* Science **317**, 775–778 (2007).

15. T. Popmintchev, M. C. Chen, O. Cohen, M. E. Grisham, J. J. Rocca, M. Murnane and H. C. Kapteyn. *Extended phase matching of high harmonics driven by mid-infrared light.* Opt. Lett. **33**, 2128–2130 (2008).

16. G. Doumy, J. Wheeler, C. Roedig, R. Chirla, P. Agostini and L. F. DiMauro. *Attosecond Synchronization of High-Order Harmonics from Midinfrared Drivers.* Phys. Rev. Lett. **102**, 093002 (2009).

17. M. Lewenstein, Ph. Balcou, M.Yu. Ivanov, A. L'Huillier and P. B. Corkum. *Theory of high-order harmonic generation by low-frequency laser fields.* Phys. Rev. A **49**, 2117 (1994).

18. G. Farkas and C. Tóth. *Proposal for attosecond light pulse generation using laser induced multiple-harmonic conversion processes in rare gases.* Phys. Lett. A **168**, 447 (1992).

19. S. E. Harris, J. J. Macklin and T. W. Hänsch. *Atomic scale temporal structure inherent to high-order harmonic generation.* Opt. Commun. **100**, 487 (1993).

20. Ph. Antoine, A. L'Huillier and M. Lewenstein. *Attosecond Pulse Trains Using High-Order Harmonicss.* Phys. Rev. Lett. **77**, 1234 (1996).

21. P. M. Paul, E. S. Toma, P. Breger, G. Mullot, F. Augé, Ph. Balcou, H. G. Muller and P. Agostini. *Observation of a train of tttosecond pulses from high harmonic generation.* Science **292**, 1689 (2001).

22. V. Véniard, R. Taïeb and A. Maquet. *Phase dependence of (N+1) - color (N>1) ir-uv photoionization of atoms with higher harmonics.* Phys. Rev. A **54**, 721 (1996).

23. M. Hentschel, R. Kienberger, Ch. Spielmann, G. A. Reider, N. Milosevic, T. Brabec, P. Corkum, U. Heinzmannß, M. Drescher and F. Krausz. *Attosecond metrology.* Nature **414**, 509 (2001).

24. J. Itatani, F. Quéré, G. L. Yudin, M. Yu. Ivanov, F. Krausz and P. B. Corkum. *Attosecond Streak Camera.* Phys. Rev. Lett. **88**, 173903 (2002).

25. Y. Mairesse and F. Quéré. *Frequency-resolved optical gating for complete reconstruction of attosecond bursts.* Phys. Rev. A **71**, 011401(R) (2005).

26. A. Baltuška, Th. Udem, M. Uiberacker, M. Hentschel, E. Goulielmakis, Ch. Gohle, R. Holzwarth, V. S. Yakovlev, A. Scrinzi, T. W. Hänsch and F. Krausz. *Attosecond control of electronic processes by intense light fields.* Nature **421**, 611 (2003).

27. E. Goulielmakis, M. Schultze, M. Hofstetter, V. S. Yakovlev, J. Gagnon, M. Uiberacker, A. L. Aquila, E. M. Gullikson, D. T. Attwood, R. Kienberger, F. Krausz and U. Kleineberg. *Single-Cycle Nonlinear Optics.* Science **320**, 1614 (2008).

28. I. J. Sola, E. Mével, L. Elouga, E. Constant, V. Strelkov, L. Poletto, P. Villoresi, E. Benedetti, J.-P. Caumes, S. Stagira, C. Vozzi, G. Sansone and M. Nisoli. *Controlling attosecond electron dynamics by phase-stabilized polarization gating.* Nature Phys. **2**, 319 (2006).

29. I. J. Sola, A. Zaïr, R. López-Martens, P. Johnsson, K. Varjú, E. Cormier, J. Mauritsson, A. L'Huillier, V. Strelkov, E. Mével and E. Constant. *Temporal and spectral studies of high-order harmonics generated by polarization-modulated infrared fields.* Phys. Rev. A **74**, 013810 (2006).

30. Zenghu Chang. *Controlling attosecond pulse generation with a double optical gating.* Phys. Rev. A **76**, 051403 (2007).

31. H. Mashiko, S. Gilbertson, C. Li, S. D. Khan, M. M. Shakya, E. Moon and Z. Chang. *Double optical gating of high-order harmonic generation with carrier-envelope phase stabilized lasers.* Phys. Rev. Lett. **100**, 103906 (2008).

32. L. H. Yu. *Generation of intense uv radiation by subharmonically seeded single-pass free-electron lasers.* Phys. Rev. A **44**, 5178–5193 (1991).

33. Juhao Wu, Paul R. Bolton, James B. Murphy and Xinming Zhong. *Free electron laser seeded by ir laser driven high-order harmonic generation.* Appl. Phys. Lett. **90**, 021109 (2007).

34. P. Agostini and L. F. DiMauro. *The physics of attosecond light pulses.* Rep. Prog. Phys **67**, 813 (2004).

35. P. B. Corkum and F. Krausz. *Attosecond Science.* Nature Physics **3**, 381 – 387 (2007).

36. Ferenc Krausz and Misha Ivanov. *Attosecond physics.* Rev. Mod. Phys. **81**, 163–234 (2009).

37. N. Dudovich, O. Smirnova, J. Levesque, Y. Mairesse, M. Yu. Ivanov, D. M. Villeneuve and P. B. Corkum. *Measuring and controlling the birth of attosecond XUV pulses.* Nature Phys. **2**, 781 (2006).

38. D. Strickland and G. Mourou. *Compression of amplified chirped optical pulses.* Opt. Commun. **56**, 219 (1985).

39. R. Szipöcs, K. Ferencz, Ch. Spielmann and F. Krausz. *Chirped multilayer coatings for broadband dispersion control in femtosecond lasers.* Opt. Lett. **19**, 201 (1994).

40. R. Szipöcs and A. Köházi-Kis. *Theory and design of chirped dielectric laser mirrors.* Appl. Phys. B **65**, 115 (1997).

41. Takao Fuji, Jens Rauschenberger, Alexander Apolonski, Vladislav S. Yakovlev, Gabriel Tempea, Thomas Udem, Christoph Gohle, Theodor W. Hänsch, Walter Lehnert, Michael Scherer and Ferenc Krausz. *Monolithic carrier-envelope phase-stabilization scheme.* Opt. Lett. **30**, 332–334 (2005).

42. T. Fordell, M. Miranda, A. Persson and A. L'Huillier. *Carrier-envelope phase stabilization of a multi-millijoule, regenerative-amplifier-based chirped-pulse smplifier system.* Opt. Express **17**, 21091–21097 (2009).

43. D. Proch and T. Tickle. *A high-intensity multi-purpose piezoelectric pulsed molecular beam source.* Rev. Sci. Instr. **60**, 713 (1988).

44. E. Gustafsson, T. Ruchon, M. Swoboda, R. López Martens, Ph. Balcou and A. L'Huillier. *Broadband attosecond pulse shaping.* Optics Letters **32**, 1353–1355 (2007).

45. B.L. Henke, J.C. Davis, E.M. Gullikson and R.C.C. Perera. A Preliminary Report on X-Ray Photoabsorption Coefficients and Atomic Scattering Factors for 92 Elements in the 10-10,000 eV Region. Lawrence Berkeley National Laboratory (1988).

46. P. Kruit and F. H. Read. *Magnetic field paralleliser for 2π electron-spectrometer and electron-image magnifier.* J. Phys. E **16**, 313 (1983).

47. A. T. J. B. Eppink and D. H. Parker. *Velocity map imaging of ions and electrons using electrostatic lenses: Application in photoelectron and photofragment ion imaging of molecular oxygen.* Rev. Sci. Instr. **68**, 3477 (1997).

48. M. J. J. Vrakking. *An iterative procedure for the inversion of two-dimensional ion/photoelectron imaging experiments.* Rev. Sci. Instr. **72**, 4084 (2001).

49. O. Svelto. *Principles of Lasers.* Plenum Press, New York (1998).

50. A. Dalgarno and A. E. Kingston. *The Refractive Indicies and Verdet Constants of the Inert Gases.* Proceedings of the Royal Society of London Series A-Mathematical and Physical Sciences **259**, 424 (1960).

51. *Laser Optics and Coatings.* CVI Laser Corporation (1997).

52. E. M. Gullikson B. L. Henke and J. C. Davis. *X-ray interactions: photoabsorption, scattering, transmission, and reflection at E=50-30000 eV, Z=1-92,.* Atomic Data and Nuclear Data Tables **54**(no.2), 181–342 (1993).

53. A. L'Huillier, X. F. Li and L. A. Lompré. *Propagation effects in high-order harmonic generation in rare gases.* JOSA B **7**, 527–536 (1990).

54. C. Kittel. *Introduction to Solid State Theory.* John Wiley and Sons (1996).

55. K. Varju, Y. Mairesse, B. Carre, M. B. Gaarde, P. Johnsson, S. Kazamias, R. Lopez-Martens, J. Mauritsson, K. J. Schafer, Ph. Balcou, A. L'Huillier and P. Saliéres. *Frequency chirp of harmonic and attosecond pulses.* J. Mod. Opt. **52**, 379 (2005).

56. K. Varjú, Y. Mairesse, P. Agostini, P. Breger, B. Carré, L. J. Frasinski, E. Gustafsson, P. Johnsson, J. Mauritsson, H. Merdji, P. Monchicourt, A. L'Huillier and P. Salières. *Reconstruction of Attosecond Pulse Trains Using an Adiabatic Phase Expansion.* Phys. Rev. Lett. **95**, 243901 (2005).

57. O. E. Martinez, J. P. Gordon and R. L. Fork. *Negative group-velocity dispersion using refraction.* J. Opt. Soc. Am. B **1**, 1003 (1984).

58. R. López-Martens, K. Varjú, P. Johnsson, J. Mauritsson, Y. Mairesse, P. Salières, M. B. Gaarde, K. J. Schafer, A. Persson, S. Svanberg, C.-G. Wahlström and A. L'Huillier. *Amplitude and phase control of attosecond light pulses.* Phys. Rev. Lett. **94**, 033001 (2005).

59. H. J. Weber and G. B. Arfken. *Essential Mathematical Methods for Physicists.* Elsevier Academic Press (2004).

60. J. Mauritsson, P. Johnsson, E. Mansten, M. Swoboda, T. Ruchon, A. L'Huillier and K. J. Schafer. *Coherent Electron Scattering Captured by an Attosecond Quantum Stroboscope.* Phys. Rev. Lett. **100**, 073003 (2008).

61. H. Friedrich. *Theoretical atomic physics.* Springer (1994).

62. E. P. Wigner. *Lower Limit for the Energy Derivative of the Scattering Phase Shift.* Phys. Rev. **98**, 145–147 (1955).

63. F. T. Smith. *Lifetime Matrix in Collision Theory.* Phys. Rev. **118**, 349–356 (1960).

64. C. A. A. de Carvalho and H. M. Nussenzveig. *Time delay.* Physics Reports **364**, 83 – 174 (2002).

65. M. Schultze, M. Fie, N. Karpowicz, J. Gagnon, M. Korbman, M. Hofstetter, S. Neppl, A. L. Cavalieri, Y. Komninos, Th. Mercouris, C. A. Nicolaides, R. Pazourek, S. Nagele, J. Feist, J. Burgdrfer, A. M. Azzeer, R. Ernstorfer, R. Kienberger, U. Kleineberg, E. Goulielmakis, F. Krausz and V. S. Yakovlev. *Delay in Photoemission.* Science **328**, 1658–1662 (2010).

66. A. L. Cavalieri, N. Müller, Th. Uphues, V. S. Yakovlev, A. Baltuška, B. Horvath, B. Schmidt, L. Blümel, R. Holzwarth, S. Hendel, M. Drescher, U. Kleineberg, P. M. Echenique, R. Kienberger, F. Krausz and U. Heinzmann. *Attosecond spectroscopy in condensed matter.* Nature **449**, 1029 (2007).

67. E. W. Weisstein. *MathWorld, http://mathworld.wolfram.com/.*

68. M. Wollenhaupt, A. Assion, D. Liese, Ch. Sarpe-Tudoran, T. Baumert, S. Zamith, M. A. Bouchene, B. Girard, A. Flettner, U.Weichmann and G. Gerber. *Interferences of Ultrashort Free ElectronWave Packets.* Phys. Rev. Lett. **89**, 173001 (2002).

69. M. Y. Ivanov, M. Spanner and O. Smirnova. *Anatomy of strong field ionization.* Journal of Modern Optics **52**, 165–184 (2005).

70. J. J. Sakurai. *Modern Quantum Mechanics.* Addison-Wesley Publishing Co. (1994).

71. V. S. Yakovlev, J. Gagnon, N. Karpowicz and F. Krausz. *Attosecond Streaking Enables the Measurement of Quantum Phase.* Phys. Rev. Lett. **105**, 073001 (2010).

72. A. Maquet. *Use of the Coulomb Green's function in atomic calculations.* Phys. Rev. A **15**, 1088–1108 (1977).

73. A. Maquet, V. Véniard and T. A. Marian. *The Coulomb Greens function and multiphoton calculations.* J. Phys. B **31**, 3743 (1998).

74. J. W. Cooper. *Photoionization from Outer Atomic Subshells. A Model Study.* Phys. Rev. **128**, 681 (1962).

75. J. P. Farrell, L. S. Spector, B. K. McFarland, P. H. Bucksbaum, M. Gühr, M. B. Gaarde and K. J. Schafer. *Influence of phase matching on the Cooper minimum in Ar high-order harmonic spectra.* Phys. Rev. A **83**, 023420 (2011).

76. M. V. Federov. *Atomic and Free Electrons In A Strong Light Field.* World Scientific (1997).

77. E. S. Toma and H. G. Muller. *Calculation of matrix elements for mixed extreme-ultraviolet-infrared two-photon above-threshold ionization of argon.* J. Phys. B **35**, 3435 (2002).

78. A. Maquet and R. Taïeb. *Two-colour IR + XUV spectroscopies: the 'soft-photon approximation'.* J. Mod. Opt. **54**, 1847–1857 (2007).

79. D. J. Kennedy and S. T. Manson. *Photoionization of the Noble Gases: Cross Sections and Angular Distributions.* Phys. Rev. A **5**, 227 (1972).

80. L .V. Keldysh. *Ionization in the Field of a Strong Electromagnetic Wave.* Sov. Phys. JETP **20**, 1307 (1965).

81. M. Uiberacker, Th. Uphues, M. Schultze, A. J. Verhoef, V. Yakovlev, M. F. Kling, Rauschenberger, N. M. Kabachnik, H. Schröder, M. Lezius, K. L. Kompa, H.-G. Muller, M. J. J. Vrakking, S. Hendel, U. Kleineberg, U. Heinzmann, M. Drescher and F. Krausz. *Attosecond real-time observation of electron tunnelling in atoms.* Nature **446**, 627 (2007).

82. P. Eckle, A. N. Pfeiffer, C. Cirelli, A. Staudte, R. Dörner, H. G. Muller, M. Büttiker and U. Keller. *Attosecond Ionization and Tunneling Delay Time Measurements in Helium.* Science **322**, 1525–1529 (2008).

83. O. Smirnova, M. Spanner and M. Ivanov. *Analytical solutions for strong field-driven atomic and molecular one- and two-electron continua and applications to strong-field problems.* Phys. Rev. A **77**, 033407 (2008).

84. D. G. Arbó, J. E. Miraglia, M. S. Gravielle, K. Schiessl, E. Persson and J. Burgdörfer. *Coulomb-Volkov approximation for near-threshold ionization by short laser pulses.* Phys. Rev. A **77**, 013401 (2008).

85. M. Y. Ivanov, T. Brabec and N. Burnett. *Coulomb corrections and polarization effects in high-intensity high-harmonic emission.* Phys. Rev. A **54**, 742–745 (1996).

86. Z. Chen, A. Le, T. Morishita and C. D. Lin. *Quantitative rescattering theory for laser-induced high-energy plateau photoelectron spectra.* Phys. Rev. A **79**, 033409 (2009).

87. A. Le, R. R. Lucchese, S. Tonzani, T. Morishita and C. D. Lin. *Quantitative rescattering theory for high-order harmonic generation from molecules.* Phys. Rev. A **80**, 013401 (2009).

88. Z. Chen, Y. Liang and C. D. Lin. *Quantitative rescattering theory of correlated two-electron momentum spectra for strong-field nonsequential double ionization of helium.* Phys. Rev. A **82**, 063417 (2010).

89. R. P. Feynman. *Space-Time Approach to Non-Relativistic Quantum Mechanics.* Rev. Mod. Phys. **20**, 367–387 (1948).

90. P. Salières, B. Carré, L. Le Déroff, F. Grasbon, G. G. Paulus, H. Walther, R. Kopold, W. Becker, D. B. Milošević, A. Sanpera and M. Lewenstein. *Feynman's Path-Integral Approach for Intense-Laser-Atom Interactions.* Science **292**, 902 (2001).

91. M. Lewenstein, P. Salières and A. L'Huillier. *Phase of the atomic polarization in high-order harmonic generation.* Phys. Rev. A **52**, 4747 (1995).

92. M. B. Gaarde, J. L. Tate and K. J. Schafer. *Macroscopic aspects of attosecond pulse generation.* J. Phys. B **41**, 132001 (2008).

93. M. Ivanov, P. B. Corkum, T. Zuo and A. Bandrauk. *Routes to control of intense-field atomic polarizability.* Phys. Rev. Lett. **74**, 2933 (1995).

94. S. Long, W. Becker and J. K. McIver. *Model calculations of polarization-dependent two-color high-harmonic generation.* Phys. Rev. A **52**, 2262–2278 (1995).

95. M. B. Gaarde, P. Antoine, A. Persson, A. L'Huillier B. Carré and and C.-G. Wahlström. *High-order tunable sum- and difference frequency mixing in the XUV region.* J. Phys. B **29**, L163 (1996).

96. L. E. Chipperfield, J. S. Robinson, J. W. G. Tisch and J. P. Marangos. *Ideal waveform to generate the maximum possible electron recollision energy for any given oscillation period.* Phys. Rev. Lett. **102**, 063003 (2009).

97. M. V. Frolov, N. L. Manakov, A. A. Silaev and N. V. Vvedenskii. *Analytic description of high-order harmonic generation by atoms in a two-color laser field.* Phys. Rev. A **81**, 063407 (2010).

98. J. Mauritsson, P. Johnsson, E. Gustafsson, A. L'Huillier, K. J. Schafer and M. B. Gaarde. *Attosecond Pulse Trains Generated Using Two Color Laser Fields.* Phys. Rev. Lett. **97**, 013001 (2006).

99. T. Pfeifer, L. Gallmann, M. J. Abel, D. M. Neumark and S. R. Leone. *Single attosecond pulse generation in the multicycle-driver regime by adding a weak second-harmonic field.* Opt. Lett. **31**, 975 (2006).

Papers

Paper I

Phase Measurement of Resonant Two-Photon Ionization in Helium

M. Swoboda, T. Fordell, K. Klünder, J. M. Dahlström, M. Miranda, C. Buth, K. J. Schafer, J. Mauritsson, A. L'Huillier, and M. Gisselbrecht.

Phys. Rev. Lett. **104**, 103003 (2010).

PRL 104, 103003 (2010) PHYSICAL REVIEW LETTERS week ending 12 MARCH 2010

Phase Measurement of Resonant Two-Photon Ionization in Helium

M. Swoboda,[1] T. Fordell,[1] K. Klünder,[1] J. M. Dahlström,[1] M. Miranda,[1,2] C. Buth,[3,4] K. J. Schafer,[3,4] J. Mauritsson,[1] A. L'Huillier,[1,*] and M. Gisselbrecht[1]

[1]*Department of Physics, Lund University, P.O. Box 118, 22100 Lund, Sweden*
[2]*Departamento de Física, Universidade do Porto, Rua do Campo Alegre 687, 4169-007 Porto, Portugal*
[3]*Department of Physics and Astronomy, Louisiana State University, Baton Rouge, Louisiana 70803, USA*
[4]*PULSE Institute, SLAC National Accelerator Laboratory, Menlo Park, California 94025, USA*

(Received 18 December 2009; published 12 March 2010)

We study resonant two-color two-photon ionization of helium via the $1s3p\ ^1P_1$ state. The first color is the 15th harmonic of a tunable Ti:sapphire laser, while the second color is the fundamental laser radiation. Our method uses phase-locked high-order harmonics to determine the *phase* of the two-photon process by interferometry. The measurement of the two-photon ionization phase variation as a function of detuning from the resonance and intensity of the dressing field allows us to determine the intensity dependence of the transition energy.

DOI: 10.1103/PhysRevLett.104.103003 PACS numbers: 32.80.Rm, 32.70.Jz, 32.80.Qk, 42.65.Ky

Multicolor resonant ionization is at the heart of numerous and diverse applications in fundamental and applied sciences. Examples are studies of very high Rydberg states [1], investigations of biomolecules [2] and specific selection of radioactive species [3]. In the simplest scheme, resonantly enhanced two-photon ionization (R2PI) occurs via the absorption of two photons, generally of different colors, one tunable (ω_1) used to scan across a resonant state (r), and the second (ω) ionizing from the excited state. In traditional R2PI, the *yield* of the produced ion species is recorded as a function of laser wavelength, and the position and shape of the observed resonance provides information on the underlying electronic and rovibrational structures. These studies rely on spectroscopic information using narrow-bandwidth lasers, which do not allow any temporal resolution. Here, we present an ultrafast time-resolved-technique to retrieve also the *phase* of R2PI when sweeping through the resonance. We demonstrate it by studying R2PI of He via the $1s3p\ ^1P_1$ state which lies 23.087 eV above the ground state.

The basic principle of our experiment is illustrated in Fig. 1. We study the interference between two pathways to the same ionized final state (f_1), one through the resonance with absorption of two photons with frequency ω_1 and ω, and the second through a continuum path, using a third color (ω_2), involving absorption of a photon with frequency ω_2 and emission of a photon with frequency ω. The phase of the R2PI is encoded in the modulation of the photoelectron signal S_{f_1} as a function of the delay τ between the (ω_1, ω_2) fields and the ω field [Fig. 1(b)]. When the energy of the exciting radiation ω_1, and thus the detuning from the resonance is changed, the phase variation of the resonant transition leads to a measurable shift of the S_{f_1} oscillation. This phase shift needs to be referenced against another modulation S_{f_2} that is independent of the resonance and thus providing a *clock* to our measurement. A process providing an independent modulation requires a fourth color (ω_3) and involves another final state (f_2) (see Fig. 1).

An essential requirement for our measurement is the use of phase-locked radiation fields with commensurate frequencies, and a temporal precision better than the periodicity of the interference signal, in our case 1.3 fs. Another requirement, is a high spectral resolution for the excitation of a narrow resonance. These requirements can be simultaneously fulfilled by using the high-order harmonic frequency combs produced when an intense laser field interacts with a gas of atoms or molecules [4]. As is now well understood [5,6], harmonics arise due to interferences

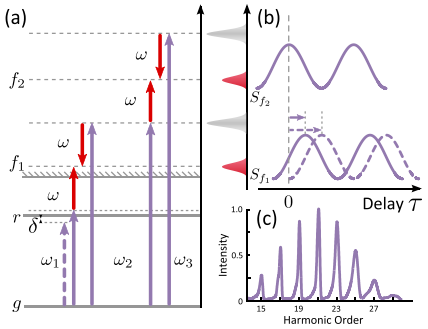

FIG. 1 (color online). (a) Schematic diagram illustrating the phase measurement of R2PI. The dashed and solid ω_1 lines represent two excitation energies on either side of the resonance. The photoelectron peaks used in the measurement are S_{f_1} and S_{f_2}. (b) Illustration of modulated sideband signals S_{f_1} and S_{f_2}. Two S_{f_1} modulations are indicated, corresponding to the two excitation energies in (a). (c) Experimental harmonic spectrum used in the measurements.

between attosecond pulses produced by tunnel ionization, acceleration of the created wave packet in the field and recombination back to the ground state at each half cycle of the laser field. The spectral width of the individual harmonics is thus related to the number of attosecond pulses, and decreases as the laser pulse duration increases [7]. In this process, a comb of phase-locked harmonics of odd order is generated.

In the present work, we use high-order harmonics to study two-color photoionization of He via the $1s3p\ ^1P_1$ state [8,9]. In contrast to the "reconstruction of attosecond bursts by interference of two-photon transition" (RABITT) technique, used to determine the pulse duration of attosecond pulses [10,11] and similarly to previous work performed in Ne [12] and N_2 [13], we eliminate the influence of the temporal characteristics of the attosecond pulses to concentrate on the influence of the atomic properties. We study the R2PI phase as a function of detuning from the resonance, by varying the fundamental wavelength (around 805 nm) or alternatively by increasing the fundamental intensity. We apply these measurements to determine the intensity-dependence of the energy of the $1s^2 \rightarrow 1s3p$ transition, and interpret the results using theoretical calculations consisting of solving the time-dependent Schrödinger equation (TDSE) in conditions close to the experimental ones [14].

Our experiments were performed with a 1-kHz 35-fs 4-mJ Ti:sapphire laser system. An acousto-optic programmable dispersive filter (DAZZLER) was used to change the central wavelength between 802.5 and 809.3 nm, while maintaining the spectral width of the amplified pulses approximately equal to 25 nm. High-order harmonics were generated in a pulsed Ar gas cell, filtered using a spatial aperture and a 200-nm thick Al thin film [15], and focused by a toroidal mirror into a vacuum chamber containing an effusive He gas jet. A magnetic bottle electron spectrometer (MBES) allowed us to record and analyze in energy the ejected electrons. Part of the laser field was extracted before the generation of harmonics, and recombined downstream collinearly with the harmonics, after a variable time delay that could be adjusted with sub-100-as precision [12].

A comb of about seven phase-locked harmonic fields [Fig. 1(c)], corresponding in the time domain to a train of attosecond pulses of 260 as duration, was thus sent into the interaction chamber together with the dressing field at frequency ω with an adjustable phase φ (or time $\tau = \varphi/\omega$) delay. In addition, a half-wave plate and polarizer in the dressing IR field arm allowed precise control of the pulse energy and therefore the intensity in the interaction region of the MBES. The detuning was determined from $\delta = 15hc/\lambda_0 - E_{3p}$, where E_{3p} is 23.087 eV and λ_0 is the barycenter of the fundamental frequency spectrum, shifted to the blue by $\delta\lambda \simeq 3.5$ nm to account for the blueshift from free electrons in the generation gas [16,17]. The dressing laser intensity was determined by measuring the energy shifts of the photoelectron peaks of harmonics 17 to 23 in the presence of the laser field, which is simply equal to the ponderomotive energy $U_p \approx 6.0I$ eV where the intensity I is in units of 10^{14} W cm^{-2} for a laser wavelength of 800 nm [18,19].

Figures 2(a) and 2(b) present electron spectra as a function of delay between the harmonics and the dressing field, obtained for two different detunings. Electrons are observed at energies corresponding to one-photon absorption of the harmonics (from the 17th) and at "sideband" energies due to two-photon ionization processes, which we label by the corresponding net number of infrared photons (16, 18, etc.). These sideband peaks strongly oscillate with the delay at a frequency equal to 2ω. The oscillations of sidebands 18, 20, 22, and 24 do not depend on the detuning, while sideband 16 is strongly affected by it. A Fourier transform of the sideband signal over about 10 fs (four cycles) allows us to determine the relative phases of the sideband oscillations with a precision of 0.1 rad. The phases are plotted in Fig. 2(c) for the two cases shown in (a),(b).

The relationship between the R2PI phase and the experimental results in Fig. 2 can be understood within second-order perturbation theory [10,12]. Using the notation from Fig. 1, the photoelectron signal S_{f_1} can be expressed as

$$S_{f_1} = |a_1^a + a_2^e|^2, \tag{1}$$

where a_1^a and a_2^e are the two-photon probability amplitudes with the superscript a or e referring to an absorption or emission of an ω photon and with the subscript 1 or 2 referring to absorption of an ω_1 or ω_2 photon. Introducing φ_1 and φ_2 as the phases of the radiation fields, as well as

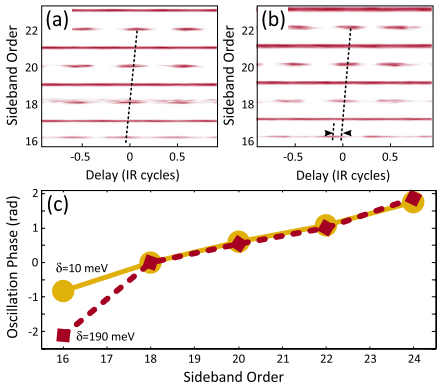

FIG. 2 (color online). Electron spectra as a function of delay for detunings $\delta = 10$ meV (a) and $\delta = 190$ meV (b). The oscillation of the 16th sideband depends on the detuning while the others do not (see dashed line) (c) Phase of the oscillations of the sideband peaks in light orange for (a) and dark red for (b). The two results have been superposed at sideband 18.

φ_1^a and φ_2^e as the phase terms involved in the two-photon transitions, Eq. (1) becomes

$$S_{f_1} = ||a_1^a|e^{i\varphi_1^a + i\varphi_1 + i\varphi} + |a_2^e|e^{i\varphi_2^e + i\varphi_2 - i\varphi}|^2$$
$$= |a_1^a|^2 + |a_2^e|^2 + 2|a_1^a a_2^e|\cos(\varphi_1^a - \varphi_2^e + 2\varphi + \varphi_1 - \varphi_2). \quad (2)$$

The cosine term leads to the modulation of the signal observed in the experiment. In general, the phase terms involved do not depend much on the photon energies. In two-photon ionization via a resonant state, however, the phase (φ_1^a) changes by π across the resonance. The study of the variation of φ_1^a as a function of detuning δ provides interesting information on the two-photon ionization process, e.g., on the relative importance of resonant and nonresonant contributions, ac Stark shift of the resonant state, depending on the spectral characteristics of the XUV and laser fields.

The variation of φ_1^a with the detuning can be experimentally obtained from $S_{f_1}(\varphi)$ provided the other phase terms φ_2^e, φ_1, φ_2 do not depend on δ and provided the phase delay φ is known in absolute value, which is generally not the case. $S_{f_1}(\varphi, \delta)$ is therefore referenced against $S_{f_2}(\varphi)$, assuming that the phase terms involved, φ_2^a and φ_3^e, are independent of the detuning and thus removing the need of knowledge of the absolute φ. When changing δ, the laser intensity used to generate the harmonics varies slightly, leading to a (small) variation of the group delay of the attosecond pulses and thus of $\varphi_1 - \varphi_2$. We take this effect into account by assuming a linear group delay [20], which we experimentally determine using higher-order sidebands. Its contribution is then subtracted from the measured phases and the phase of sideband 18 is set to zero for all detunings. The results are presented in Fig. 3(a). As expected, the phases corresponding to all sidebands except the 16th are almost superposed to each other and show no influence of detuning.

Figure 3(b) shows the variation of the R2PI phase as a function of detuning. We can tune only over half the resonance since for lower (negative detunings) sideband 16 moves progressively below the ionization threshold, thus making our phase measurement inaccurate. We also compare our measurements with the results of two different calculations (solid lines): The dark red line is obtained by a simple perturbative model [21], only considering the resonant state. Gaussian envelopes were used for the ir and XUV pulses with FWHMs of 30 and 10 fs, respectively. The light orange curve shows the result of calculations performed by numerically integrating the TDSE in the single active electron approximation [14] in conditions close to the experiment. We use a He pseudopotential with the energy of the $1s3p$ state equal to 23.039 eV. The result is therefore shifted by 40 meV for comparison with the experiment. The result shown in Fig. 3(b) agrees very well with the experiment, thus confirming our detuning calibration.

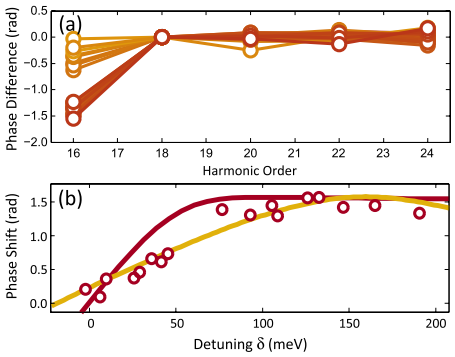

FIG. 3 (color online). (a) Measured sideband phases corrected for the attosecond group delay and normalized at zero for sideband 18. Different detunings are indicated by the color code [going from 11 meV below the resonance (dark red, lower points in order 16) to 190 meV above the resonance (light orange, upper in order 16)]. (b) Measurements (circles) of the R2PI phase as a function of detuning. The dark red line indicates results of a simple perturbative model while the light orange line shows results of simulations based on solving the TDSE.

In order to investigate how the $1s3p$ resonance behaves in a laser field, we measured the dependence of the R2PI phase on the dressing laser intensity. Figure 4(a) shows the R2PI phase determined similarly to Fig. 3(a) but keeping the wavelength constant at 805.5 nm and gradually increasing the dressing intensity. We verified that even at the highest intensity, higher-order multiphoton transitions were still negligible [22], thus not affecting our phase determination. Increasing the intensity from 0.1 to 1.8×10^{12} W/cm^2, the R2PI phase varies from -0.7 to 0.9 radians. Figure 4(b) presents the intensity dependence of all of the measured phases (circles). We find an almost linear increase of the phase with intensity, as indicated by the dark red curve obtained by averaging, with a saturation at around 1.3×10^{12} W/cm^2, due to the suppression of R2PI when part of the two-photon excitation bandwidth moves partly below the ionization threshold. The light orange line obtained by TDSE calculations agrees well with our measurements.

Combining our previous phase measurements as a function of detuning for a fixed (low) intensity and as a function of intensity (for a fixed detuning) allows us to determine the intensity dependence of the $1s^2 \rightarrow 1s3p$ transition energy. Both experimental (dark red solid) and TDSE (light orange solid) results are shown in Fig. 5(a). The dashed line is equal to $\Delta E_{1s^2} + U_p$, representing the variation of the transition energy if the $1s3p$ state was moving as a high-lying Rydberg state, following U_p [19]. The ac Stark shift of the fundamental state ΔE_{1s^2} is very small, equal to $-0.3I$ eV where the intensity I is in units of 10^{14} W cm^{-2} [23,24] so that $\Delta E_{1s^2} + U_p \approx U_p$. We find that the measured transition energy increases about 40%

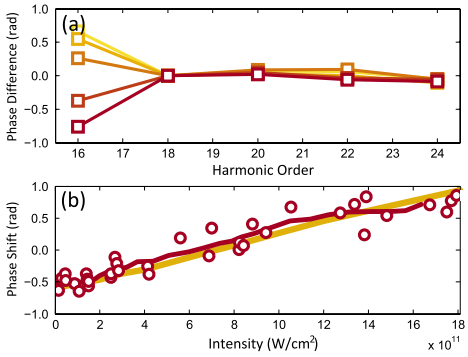

FIG. 4 (color online). Intensity dependence of the R2PI phase. (a) Harmonic phase differences at dressing intensities from 0.1 (dark red) to 2.2×10^{12} W cm^{-2} (light orange), with attosecond chirp correction and normalization at sideband 18. (b) R2PI phase (circles) as a function of intensity, with a six-point moving average (dark red line) and TDSE (light orange).

more rapidly with the laser intensity than U_p, up to the saturation at 1.3×10^{12} W cm^{-2}.

To better understand this faster than ponderomotive shift, we have calculated the XUV absorption cross section for helium in the presence of an 800 nm field by numerically solving the TDSE as a function of both XUV wavelength and laser intensity [Fig. 5(b)]. Using an XUV bandwidth of 50 meV or smaller we find that beyond 1×10^{11} W cm^{-2}, the $3p$ resonance has at least two components the higher of which shifts significantly faster than the ponderomotive energy. With the experimental XUV bandwidth (150 meV), however, the different components cannot be resolved. As a result, we observe shifts exceeding $E_{1s^2} + U_p$. Experimentally, the predicted structure in the $3p$ resonance could be observed using longer fundamental laser pulses, leading to spectrally narrower harmonic peaks.

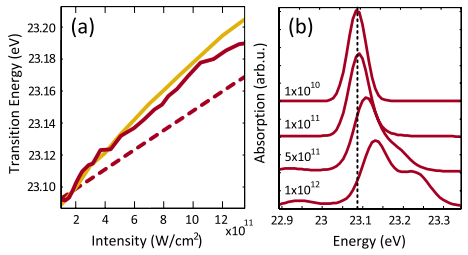

FIG. 5 (color online). (a) Measured transition energy of the $1s3p$ state. Experimental results (solid dark red), compared with $\Delta E_{1s^2} + U_p$ (dashed) and TDSE calculation (solid light orange). (b) TDSE calculation of XUV absorption for three different intensities with 50 meV resolution. The position of the $1s3p$ state is indicated by the dashed line.

In conclusion, we have shown how well-characterized phase-locked high-order harmonics can be used to measure the phase of R2PI and we have applied it to the determination of the ac Stark shift of the $1s3p\ ^1P_1$ state. Although our resolution was unsufficient to detect the splitting of the excited state, we observed a nontrivial, faster than ponderomotive, ac Stark shift. Our method, here demonstrated in He, could be applied to the study of numerous resonant or quasiresonant processes in atoms and molecules.

We thank A. Maquet and R. Taïeb for fruitful suggestions at the beginning of this work. This research was supported by the Marie Curie Intra-European Fellowship ATTOCO, the Marie Curie Early Stage Training Site (MAXLAS), the European Research Council (ALMA), the Knut and Alice Wallenberg Foundation and the Swedish Research Council. Funding at LSU is provided by the National Science Foundation through grant numbers PHY-0449235 and PHY-0701372.

*anne.lhuillier@fysik.lth.se
URL: http://www.atto.fysik.lth.se

[1] A. Osterwalder and F. Merkt, Phys. Rev. Lett. **82**, 1831 (1999).
[2] E. G. Robertson and J. P. Simons, Phys. Chem. Chem. Phys. **3**, 1 (2001).
[3] U. Koster, V. Fedoseyev, and V. Mishin, Spectrochim. Acta, Part B: At. Spectrosc. **58**, 1047 (2003).
[4] M. Ferray *et al.*, J. Phys. B **21**, L31 (1988).
[5] J. L. Krause, K. J. Schafer, and K. C. Kulander, Phys. Rev. Lett. **68**, 3535 (1992).
[6] P. B. Corkum, Phys. Rev. Lett. **71**, 1994 (1993).
[7] F. Brandi, D. Neshev, and W. Ubachs, Phys. Rev. Lett. **91**, 163901 (2003).
[8] P. Ranitovic *et al.*, New J. Phys. **12**, 013008 (2010).
[9] L. H. Haber, B. Doughty, and S. R. Leone, Phys. Rev. A **79**, 031401(R) (2009).
[10] V. Véniard, R. Taïeb, and A. Maquet, Phys. Rev. A **54**, 721 (1996).
[11] P. M. Paul *et al.*, Science **292**, 1689 (2001).
[12] K. Varjú *et al.*, Laser Phys. **15**, 888 (2005).
[13] S. Haessler *et al.*, Phys. Rev. A **80**, 011404(R) (2009).
[14] K. J. Schafer and K. C. Kulander, Phys. Rev. Lett. **78**, 638 (1997).
[15] R. López-Martens *et al.*, Phys. Rev. Lett. **94**, 033001 (2005).
[16] C. G. Wahlström *et al.*, Phys. Rev. A **48**, 4709 (1993).
[17] M. B. Gaarde, M. Murakami, and R. Kienberger, Phys. Rev. A **74**, 053401 (2006).
[18] R. K. Freeman *et al.*, Phys. Rev. Lett. **59**, 1092 (1987).
[19] K. Burnett, V. Reed, and P. Knight, J. Phys. B **26**, 561 (1993).
[20] Y. Mairesse *et al.*, Science **302**, 1540 (2003).
[21] N. Dudovich, D. Oron, and Y. Silberberg, Phys. Rev. Lett. **88**, 123004 (2002).
[22] M. Swoboda *et al.*, Laser Phys. **19**, 1591 (2009).
[23] M. D. Perry, A. Szoke, and K. C. Kulander, Phys. Rev. Lett. **63**, 1058 (1989).
[24] H. Rudolph *et al.*, Phys. Rev. Lett. **66**, 3241 (1991).

Paper II

Probing Single-Photon Ionization on the Attosecond Time Scale

K. Klünder, J. M. Dahlström, M. Gisselbrecht, T. Fordell, M. Swoboda, D. Guénot, P. Johnsson, J. Caillat, J. Mauritsson, A. Maquet, R. Taïeb, and A. L'Huillier.

Phys. Rev. Lett. **106**, 143002 (2011).

PRL **106,** 143002 (2011) PHYSICAL REVIEW LETTERS week ending 8 APRIL 2011

Probing Single-Photon Ionization on the Attosecond Time Scale

K. Klünder,[1] J. M. Dahlström,[1] M. Gisselbrecht,[1] T. Fordell,[1] M. Swoboda,[1] D. Guénot,[1] P. Johnsson,[1] J. Caillat,[2] J. Mauritsson,[1] A. Maquet,[2] R. Taïeb,[2] and A. L'Huillier[1,*]

[1]*Department of Physics, Lund University, P.O. Box 118, 22100 Lund, Sweden*

[2]*Laboratoire de Chimie Physique-Matière et Rayonnement, Université Pierre et Marie Curie, 11, Rue Pierre et Marie Curie, 75231 Paris Cedex, 05, France*

(Received 15 December 2010; published 5 April 2011; publisher error corrected 14 April 2011)

We study photoionization of argon atoms excited by attosecond pulses using an interferometric measurement technique. We measure the difference in time delays between electrons emitted from the $3s^2$ and from the $3p^6$ shell, at different excitation energies ranging from 32 to 42 eV. The determination of photoemission time delays requires taking into account the measurement process, involving the interaction with a probing infrared field. This contribution can be estimated using a universal formula and is found to account for a substantial fraction of the measured delay.

DOI: 10.1103/PhysRevLett.106.143002 PACS numbers: 32.80.Rm, 32.80.Qk, 42.65.Ky

The interaction of light with matter is an essential process in nature and, in particular, the photoelectric effect has been studied during decades using synchrotron radiation [1]. The development of ultrashort light pulses in the attosecond range allows scientists to tackle temporal aspects of electron transitions in atoms, molecules, and more complex systems. Cavalieri *et al.* [2] investigated photoemission from the valence and the conduction band in tungsten crystals using single attosecond pulses and an infrared (ir) probing field through the streaking technique [3]. Recently, Schultze *et al.* [4] implemented the same technique to study photoemission from the $2s^2$ and $2p^6$ shells in neon at a pulse energy of 100 eV. They measured a difference in photoemission time delays equal to 21 as, a value which is significantly larger than the expected theoretical value, as further discussed in a series of theoretical articles [5–8].

In this Letter, we examine photoemission of electrons from the $3s^2$ and $3p^6$ shells in argon. Our method uses a frequency comb of high-order harmonics with photon energies varying from 32 to 42 eV for the photoionization and a weak ir field for probing the outgoing electrons. It is based on interferometry and presents analogies with coherent control schemes used for phase measurements close to resonant states [9–11]. Here we explore single photoionization in the threshold region for the $3s^2$ shell, where one expects large variation in photoemission times. The measurement shows a delay between the ionization from the $3s^2$ and $3p^6$ shells which varies with photon energy. We investigate the influence of the interaction with the weak ir field, which is needed to do the interferometric measurement and get the temporal information. Probing the outgoing electron wave packet (EWP), even with a weak ir field, affects electron motion and therefore the measured delay. Fortunately, this effect can be analytically calculated and takes a universal form, that allows us to disentangle the different effects and gives us access to the single-photon ionization time, also called Wigner time [12,13].

The basic principle of our experiment is shown in Fig. 1. We ionize argon using a comb of high-order harmonics. With a central frequency of the harmonic comb above the binding energy of the $3s$ shell we simultaneously create two independent EWPs, one originating from the $3s^2$ and one from the $3p^6$ shell. The presence of a fraction of the fundamental laser field with frequency ω induces the formation of sideband peaks due to two-photon transitions including absorption or emission of an ir photon [14,15]. Two different and interfering quantum paths involving consecutive harmonics lead to the same sideband (see Fig. 1). When changing the delay τ between the harmonic comb and the laser field, the sideband signal from a given shell is modulated as [16]

$$S(\tau) = \alpha + \beta \cos[2\omega(\tau - \tau_A - \tau_I)], \quad (1)$$

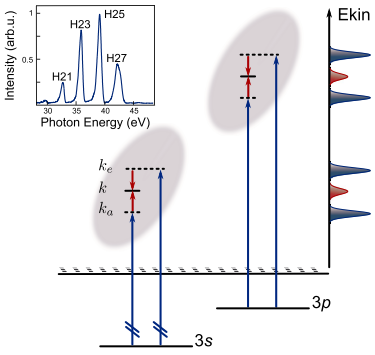

FIG. 1 (color online). Principle of the measurement. Two EWPs originating from different shells are simultaneously created using the same comb of high-order harmonics. The outgoing EWPs are further probed with a weak ir field. For simplicity only two harmonics are indicated. Also shown is the experimental harmonic spectrum used.

where α, β are two constants independent of τ. The term τ_A is proportional to the difference in phase between consecutive harmonics and describes the group delay of the attosecond pulses, while τ_I represents the atomic delay due to the two-photon ionization process [17]. As we will show below τ_I can be connected to the Wigner time delay τ_W for the single-photon ionization. The knowledge of τ_A as well as of the absolute value of the delay τ would enable us to determine τ_I directly. However, these variables are difficult to obtain separately. The simultaneous measurement of the two EWPs allows us to cancel the influence of the attosecond group delay τ_A and to determine $\tau_I(3s) - \tau_I(3p)$ at the same photon energy, i.e., at kinetic energies separated by the difference in binding energy between the two shells (13.5 eV).

Our experiments were performed with a 800 nm, 30 fs titanium-sapphire laser system [18]. High-order harmonics were generated in a pulsed Ar gas cell and spatially filtered using a small aperture [19]. We used a 0.2 μm thick chromium thin film to select a 10 eV-broad spectral window corresponding to harmonic 21 to 27 at 38 eV central energy (see Fig. 1). This filter was chosen to separate the wave packets emitted from the $3s$ and $3p$ shells in energy. The comb of four phase-locked harmonics, corresponding to a train of attosecond pulses with a 450 as duration, was focused by a toroidal mirror into the sensitive region of a magnetic bottle electron spectrometer containing a diffusive Ar gas jet. Part of the laser field was extracted prior to the high-order harmonic generation and recombined collinearly with the harmonics with a variable time delay τ. The precision of our measurement does not depend on the duration of the attosecond extreme-ultraviolet (xuv) pulses but on the interferometric stability of our experiment, estimated to be 50 as.

Figures 2(a) and 2(b) present electron spectra as a function of the delay τ between the xuv and the ir pulses. The low-energy spectrum in Fig. 2(a) shows electron peaks at energies corresponding to single-photon ionization from the $3s$ shell by the harmonics and additional sideband peaks due to two-photon transitions. The high-energy part of the spectrum shown in Fig. 2(b) presents the corresponding photoelectron spectra for $3p$ ionization. Although simultaneously recorded the results are presented separately due to the unequal signal strength caused by the difference in cross section and detector sensitivity (note the different color scales). For both channels the sideband signal oscillates, allowing us to extract the delay by Fourier transform along the time axis for a weak ir field [20]. The ir intensity was estimated to be well below 10^{12} W cm^{-2}. Figure 2(c) presents the delays obtained for the scan shown in (a) and (b), corrected for the influence of the Cr filter, which is positively dispersive in this region [21]. The variation in delay reflects mainly the positive chirp of the attosecond pulses. The main experimental result of the present work is the significant offset

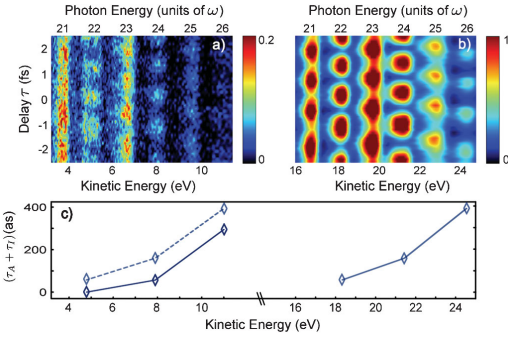

FIG. 2 (color). Energy spectra as a function of delay from electrons liberated from the $3s$ shell (a) and the $3p$ shell (b), respectively. (c) Retrieved delays corrected for the Cr group delay. Also shown are the $3p$ delays shifted down in energy for comparison with the $3s$ delays (dashed line).

between the delays measured for the two wave packets. To emphasize this result, we show as a dashed line the $3p$ delays shifted down in energy by 13.5 eV. Taking the difference between the measured delays at the same excitation energy allows us to eliminate the attosecond chirp and to reduce the effect of temporal drifts in the interferometer. Averaging over five independent measurements, we determine a difference in delays $\tau_I(3s) - \tau_I(3p)$ equal to -40 ± 10 as for sideband 22, -110 ± 10 as for sideband 24, and -80 ± 30 as for sideband 26.

To understand the meaning of these time delays, we need to establish the connection between single-photon ionization and the two-photon ionization process used in the measurement. The phase of the transition matrix element describing a single ionization process towards a final state with angular momentum ℓ is the scattering phase η_ℓ, i.e., the phase accumulated by the photoelectron when escaping from the atom. Its energy derivative $\tau_W = \hbar \partial \eta_\ell(\epsilon)/\partial \epsilon$ represents the "photoionization time delay" also called Wigner time delay [12,13]. Clearly, both η_ℓ and τ_W depend on the details of the atomic potential and their computation remains a challenge for theory. Using second-order perturbation theory, the transition matrix element for two-photon ionization involving absorption of a harmonic photon ω_H and an ir photon ω from an initial state φ_i to a continuum state $\varphi_{\vec{k}}$ with asymptotic momentum $\vec{k}$ can, using atomic units, be written as

$$M_a^{(2)}(\vec{k}) = -iE_L E_H \lim_{\varepsilon \to 0^+} \sum_n \frac{\langle \varphi_{\vec{k}} | \vec{\epsilon} \cdot \vec{r} | \varphi_n \rangle \langle \varphi_n | \vec{\epsilon} \cdot \vec{r} | \varphi_i \rangle}{\epsilon_i + \omega_H - \epsilon_n + i\varepsilon}. \quad (2)$$

The complex amplitudes of the laser and harmonic fields are denoted E_L and E_H and $\vec{\epsilon}$ is their common polarization vector. The energies of the initial and intermediate states are denoted ϵ_i and ϵ_n, respectively. The integral sum is performed over all possible intermediate states φ_n.

The index a indicates that we first discuss a two-photon process with absorption of the ir photon.

We consider the channels $s \rightarrow p \rightarrow \ell$ with $\ell = s, d$. Using spherical coordinates, separating radial and angular parts, and expanding the final wave function into partial waves, the transition matrix element becomes

$$M_a^{(2)}(\vec{k}) = -iE_L E_H \sum_{\ell=0,2} C_{\ell 0} Y_{\ell 0}(\hat{k}) e^{i\eta_\ell(k)} T_a^{(2)}(k), \quad (3)$$

where $Y_{\ell 0}$ is a spherical harmonic, $C_{\ell 0}$ is the corresponding angular coefficient, and η_ℓ is the scattering phase of the final state. The radial two-photon transition matrix element $T_a^{(2)}(k)$ can be expressed as [15,17]

$$T_a^{(2)}(k) = \sum\!\!\!\!\!\!\int_n \frac{\langle R_{k\ell}|r|R_{n1}\rangle\langle R_{n1}|r|R_{i0}\rangle}{\epsilon_i + \omega_H - \epsilon_n + i\varepsilon} = \langle R_{k\ell}|r|\rho_{k_a 1}\rangle. \quad (4)$$

In the right part of Eq. (4) we introduce the perturbed wave function $\rho_{k_a 1}$ with the wave number k_a such that $k_a^2/2 = \epsilon_i + \omega_H = k^2/2 - \omega$ (see Fig. 1) [22]. To get an estimate of the phase of $T_a^{(2)}$, we consider the asymptotic behavior of the wave functions involved in Eq. (4). The perturbed wave function $\rho_{k_a 1}$ is an outgoing wave [23,24]

$$\lim_{r\rightarrow\infty} \rho_{k_a 1}(r) \propto e^{i[k_a r - 1/2\pi + 1/(k_a)\ln(2k_a r) + \eta_1(k_a)]}, \quad (5)$$

while $R_{k\ell}$ is real with an asymptotic behavior:

$$\lim_{r\rightarrow\infty} R_{k\ell}(r) \propto \sin\left[kr - \frac{\ell}{2}\pi + \frac{1}{k}\ln(2kr) + \eta_\ell(k)\right]. \quad (6)$$

The factor $\ell\pi/2$ arises from the centrifugal potential, while $\ln(2kr)/k$ is a correction due to the long-range Coulomb potential. Using Eqs. (3)–(6) we find an approximate expression for $M_a^{(2)}(k)$

$$M_a^{(2)}(k) \propto \underbrace{e^{i\eta_1(k_a)}}_{\text{(I)}} \times \underbrace{\left(\frac{i}{k_a - k}\right)^{iz} \frac{(2k)^{i/k}}{(2k_a)^{i/(k_a)}} \Gamma(2 + iz)}_{\text{(II)}}, \quad (7)$$

where $z = 1/k_a - 1/k$ and $\Gamma(z)$ is the complex gamma function. The first phase term (I) is the scattering phase of the intermediate state and identical to the phase of the corresponding one-photon ionization. The phase of term (II) can be assigned to the laser-driven transition connecting the two continuum states in the presence of the long-range Coulomb potential, φ_a^{cc}. It is independent of the short-range behavior of the atomic potential and therefore universal. Corrections to this approximation due to the core are expected to become important only at energies close to threshold.

The phase of the two-photon matrix element $M_e^{(2)}$ for the second pathway, i.e., absorption of an harmonic photon ω_H followed by emission of an ir photon ω via an intermediate state with wave number $k_e^2/2 = k^2/2 + \omega$ (see Fig. 1), can be derived in a similar manner. The total interference signal is obtained by angular integration of $|M_a^{(2)} + M_e^{(2)}|^2$. It can be written as Eq. (1), with

$$\tau_I = \underbrace{\frac{\eta_1(k_e) - \eta_1(k_a)}{2\omega}}_{\tau_W} + \underbrace{\frac{\varphi_e^{cc}(k) - \varphi_a^{cc}(k)}{2\omega}}_{\tau_{cc}}. \quad (8)$$

This result gives an intuitive understanding of the ionization time $\tau_I(3s)$. It can be expressed as the sum of the Wigner time delay τ_W for one-photon ionization $3s \rightarrow \epsilon p$ and an additional continuum-continuum delay τ_{cc} inherent to the measuring process. This analytical derivation can be easily generalized to other ionization channels.

Figure 3 shows the delays involved in the three ionization channels $3p \rightarrow \epsilon s$ (a), $3p \rightarrow \epsilon d$ (b), and $3s \rightarrow \epsilon p$ (c) in Ar as a function of kinetic energy. The Wigner time delay τ_W (dashed) is obtained by taking the derivative of the scattering phase (Coulomb phase plus phase shift taken from [25]). For comparison, we also show in (d) the delays for the pathway $1s \rightarrow \epsilon p$ in hydrogen in the same energy region, using the Coulomb phase. The continuum-continuum delay τ_{cc} (dash-dotted) is calculated for a 800 nm laser wavelength and identical for all the channels and atoms. The solid line indicates τ_I as the sum of the two contributions. The Wigner time delay variation can be nicely and intuitively interpreted. Low-energy electrons take a longer time to escape from a given shell than high-energy electrons. Furthermore, electrons escaping to a channel with higher angular momentum take a longer time than those escaping to a channel with low angular momentum because of the centrifugal barrier. The continuum-continuum delay has the opposite behavior

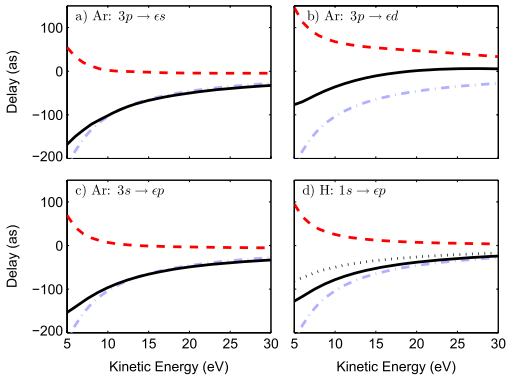

FIG. 3 (color online). Computed delays associated with the following ionization channels: (a) $3p \rightarrow \epsilon s$, (b) $3p \rightarrow \epsilon d$, (c) $3s \rightarrow \epsilon p$ in Ar, and (d) $1s \rightarrow \epsilon p$ in H. The dashed lines (red) are the one-photon Wigner time delays. The dash-dotted lines (blue) represent the estimated delays induced by the measurement τ_{cc}. The sum of the two delays is shown as a solid line (black). The dotted line (black) in (d) is the result of an exact calculation in H.

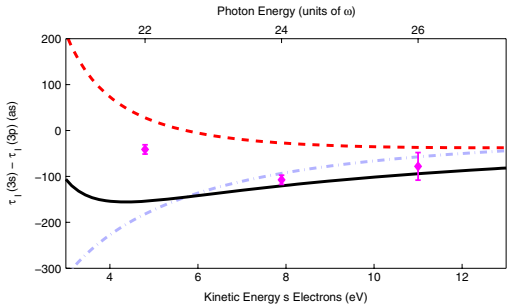

FIG. 4 (color online). Comparison between the measured delay differences for ionization of Ar from the $3s$ and $3p$ shells (diamonds) with calculations performed according to the approximate theory developed in this work (solid black line). Also shown is the delay expected for one-photon ionization (dashed red line) and the laser-driven continuum-continuum transition (dash-dotted blue line).

and leads to an apparent quicker escape for the low-energy electrons. Finally, we also indicate in Fig. 3(d) results from exact calculations in H (dotted line). The comparison between the solid and dotted lines gives an estimation of the error made in considering only the asymptotic behaviors of the perturbed and final wave functions. For the energy range considered in the present work the asymmetry parameter remains close to 2 [26], which indicates that the ionization channel $3p \rightarrow \epsilon d$ dominates over $3p \rightarrow \epsilon s$. Neglecting the $3p \rightarrow \epsilon s$ channel, we calculate $\tau_1(3s) - \tau_1(3p)$ at the same excitation energy [Eq. (8)]. Figure 4 presents the approximated delays (solid line), together with the experimental results (◆). The experimental results at the two highest energies agree well with the results of our calculation, indicating that the scattering phases [25] and our approximated continuum-continuum transition are reliable in this region. The lowest energy point, however, lies several standard deviations away from the calculated value. In this region the core may play a more important role for the continuum-continuum transition, and the Wigner time delays may differ from those calculated in [25]. In addition, the finite difference approximation to the Wigner time delay in Eq. (8) might break down in the presence of sharp resonances [27]. Using our experimental measurements combined with our estimated continuum-continuum delays, we can tentatively deduce the difference in single photoemission delays to be equal to 140 as at 34 eV and −20 as at 37 and 40 eV.

In conclusion, we have performed experimental measurements of photoemission from the $3s^2$ and $3p^6$ shells in Ar, using interferometry with a weak ir field to probe the created EWPs. We identify two contributions to the measured delays: the Wigner time delay and a delay inherent to the measurement process. Both contributions are most important near threshold and vanish as the energy increases. We believe that the work presented here will stimulate further experiments, aiming at measuring photoemission delays in a variety of systems, and providing data that could be compared to advanced theoretical calculations.

We thank Stefan Haessler, Franck Lépine, and Kenneth J. Schafer for stimulating discussions. This research was supported by the Marie Curie programs ATTOCO (IEF) and ATTOFEL (ITN), the European Research Council (ALMA), the Joint Research Programme ALADIN of Laserlab-Europe II, the Swedish Foundation for Strategic Research, the Swedish Research Council, the Knut and Alice Wallenberg Foundation, and the French ANR ATTO-WAVE.

*anne.lhuillier@fysik.lth.se
http://www.atto.fysik.lth.se

[1] V. Schmidt, Rep. Prog. Phys. **55**, 1483 (1992).
[2] A. L. Cavalieri *et al.*, Nature (London) **449**, 1029 (2007).
[3] J. Itatani *et al.*, Phys. Rev. Lett. **88**, 173903 (2002).
[4] M. Schultze *et al.*, Science **328**, 1658 (2010).
[5] V. S. Yakovlev, J. Gagnon, N. Karpowicz, and F. Krausz, Phys. Rev. Lett. **105**, 073001 (2010).
[6] J. C. Baggesen and L. B. Madsen, Phys. Rev. Lett. **104**, 043602 (2010).
[7] C.-H. Zhang and U. Thumm, Phys. Rev. A **82**, 043405 (2010).
[8] A. S. Kheifets and I. A. Ivanov, Phys. Rev. Lett. **105**, 233002 (2010).
[9] R. Yamazaki and D. S. Elliott, Phys. Rev. Lett. **98**, 053001 (2007).
[10] S. Haessler *et al.*, Phys. Rev. A **80**, 011404 (2009).
[11] M. Swoboda *et al.*, Phys. Rev. Lett. **104**, 103003 (2010).
[12] E. P. Wigner, Phys. Rev. **98**, 145 (1955).
[13] F. T. Smith, Phys. Rev. **118**, 349 (1960).
[14] J. M. Schins *et al.*, J. Opt. Soc. Am. B **13**, 197 (1996).
[15] V. Véniard, R. Taïeb, and A. Maquet, Phys. Rev. A **54**, 721 (1996).
[16] P. M. Paul *et al.*, Science **292**, 1689 (2001).
[17] E. S. Toma and H. G. Muller, J. Phys. B **35**, 3435 (2002).
[18] T. Fordell, M. Miranda, A. Persson, and A. L'Huillier, Opt. Express **17**, 21 091 (2009).
[19] R. López-Martens *et al.*, Phys. Rev. Lett. **94**, 033001 (2005).
[20] M. Swoboda *et al.*, Laser Phys. **19**, 1591 (2009).
[21] http://www.cxro.lbl.gov.
[22] A. Dalgarno and J. T. Lewis, Proc. R. Soc. A **233**, 70 (1955).
[23] M. Aymar and M. Crance, J. Phys. B **13**, L287 (1980).
[24] M. Edwards, X. Tang, and R. Shakeshaft, Phys. Rev. A **35**, 3758 (1987).
[25] D. J. Kennedy and S. T. Manson, Phys. Rev. A **5**, 227 (1972).
[26] R. G. Houlgate, J. B. West, K. Codling, and G. V. Marr, J. Electron Spectrosc. Relat. Phenom. **9**, 205 (1976).
[27] R. P. Madden, D. L. Ederer, and K. Codling, Phys. Rev. **177**, 136 (1969).

Paper III

Spectral Shaping of Attosecond Pulses using Two-Color Laser Fields

E. Mansten, J. M. Dahlström, P. Johnsson, M. Swoboda, A. L'Huillier and J. Mauritsson.

New J. Phys. **10**, 083041 (2008).

New Journal of Physics
The open-access journal for physics

Spectral shaping of attosecond pulses using two-colour laser fields

E Mansten[1,3], J M Dahlström[1], P Johnsson[1,2], M Swoboda[1], A L'Huillier[1] and J Mauritsson[1]

[1] Department of Physics, Lund University, P O Box 118, SE-221 00 Lund, Sweden
[2] FOM Institute for Atomic and Molecular Physics (AMOLF), Kruislaan 407, 1098 SJ Amsterdam, The Netherlands
E-mail: erik.mansten@fysik.lth.se and johan.mauritsson@fysik.lth.se

New Journal of Physics **10** (2008) 083041 (10pp)
Received 14 May 2008
Published 28 August 2008
Online at http://www.njp.org/
doi:10.1088/1367-2630/10/8/083041

Abstract. We use a strong two-colour laser field composed of the fundamental (800 nm) and the second harmonic (400 nm) of an infrared (IR) laser field to generate attosecond pulses with controlled spectral and temporal properties. With a second-harmonic intensity equal to 15% of the IR intensity the second-harmonic field is strong enough to significantly alter and control the electron trajectories in the generation process. This enables us to tune the central photon energy of the attosecond pulses by changing the phase difference between the IR and the second-harmonic fields. In the time domain the radiation is emitted as a sequence of pulses separated by a full IR cycle. We also perform calculations showing that the effect of even stronger second-harmonic fields leads to an extended tunable range under conditions that are experimentally feasible.

[3] Author to whom any correspondence should be addressed.

Contents

1. Introduction

Attosecond pulses represent the sharpest instruments available to study ultrafast dynamics [1]. These pulses are formed when a strong laser field interacts with a gaseous medium and the underlying physics is well described by the three step model. In this model the electron tunnels through the atomic potential, which is distorted by the strong laser field (I); gets accelerated by the field in the continuum (II); and may recombine with its parent ion (III) emitting the accumulated excess energy as a burst of extreme ultra-violet (XUV) light [2, 3]. For multi-cycle pulses, the repetition of the process, combined with the inversion symmetry of the atomic potential, leads in the time domain to a train of attosecond pulses separated by half a laser cycle and in the spectral domain to odd harmonics of the laser frequency. Spectral and temporal control of the attosecond pulse generation requires shaping of the generating laser field on a sub-cycle level. One example of such sub-cycle control is the use of phase stabilized few-cycle laser pulses [4], where the short pulse duration leads to a change in the field amplitude between consecutive half-cycles. Another, more elaborate, method is to use pulses with a time-varying polarization [5]–[7]. These methods allow control to be exerted by changing the carrier envelope phase of the laser pulse, in particular leading to the generation of single attosecond pulses [7, 8]. The technique with time-varying polarization also gives control of the photon energy of the pulses [9].

An alternative approach to control the sub-cycle field structure and thereby the electron dynamics is to mix the fundamental infrared (IR) field with its second harmonic [10]–[12]. The combined field can be written as: $E(t) = E_\omega[\sin(\omega t) + \sqrt{\mathcal{R}}\sin(2\omega t + \varphi)]$, where $\sqrt{\mathcal{R}} = E_{2\omega}/E_\omega$ is the ratio between the two field amplitudes $E_{2\omega}$ and E_ω, ω is the IR frequency, and φ a controllable phase difference between the fields, see figure 1(a). The shape and strength of the combined field in consecutive IR half-cycles differ beyond the simple sign change that occurs in a one colour field. The electron trajectories are also altered and instead of the normal two trajectories with excursion times (τ) shorter than one IR period (T), we now get four [12], as illustrated in figure 1(b). Two of these trajectories (a short and a long) come from ionization during the half-cycle when the electric field is strong and recombination during the weaker half-cycle, we will refer to these as high → low trajectories. The other two trajectories start when the field is weak and return during the stronger half-cycle (low → high) with the result that the harmonic emission from these trajectories reaches high photon energies but the yield can be orders of magnitude weaker than the emission from the high → low trajectories due to the difference in ionization probability. Schemes to use the low → high trajectories for isolated attosecond pulse generation have been proposed [13, 14]. We instead use the high → low trajectories which give much higher conversion efficiencies. In previous work, we

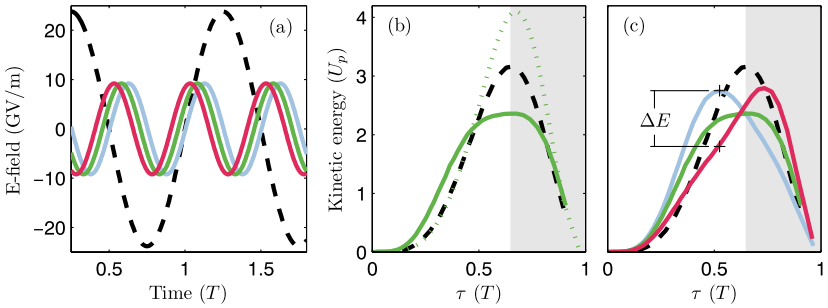

Figure 1. (a) IR field (dashed black) ($I = 7.5 \times 10^{13}\,\mathrm{W\,cm^{-2}}$) and second-harmonic fields with $\mathcal{R} = 15\%$. The phase differences for the three second-harmonic fields are $\varphi = 0$ rad (ice-blue), $\varphi = 0.6$ rad (green) and $\varphi = 1.2$ rad (red). The resulting E field is the sum of the IR and one of the 2ω fields. The timescale units are IR periods (T). (b) Return energy for the high $\rightarrow$ low and low $\rightarrow$ high trajectories calculated using classical mechanics for $\varphi = 0.6$ in solid and dotted green, respectively. Long trajectories are in the shaded regions, $\tau > 0.65T$. (c) High $\rightarrow$ low return for the three phases shown in (a). The dashed black curves in (b) and (c) show the return energy for a one-colour IR field. The kinetic energy of the electrons is given in units of the ponderomotive energy U_p for the IR field. τ is the time the electron spends in the continuum from ionization to recombination and ΔE is the tunable energy range.

have demonstrated that adding a second harmonic with a relative intensity of $\mathcal{R} = 10\%$ will induce a sufficiently strong variation between consecutive IR-half-cycles to efficiently cancel the generation every second half-cycle, which results in the generation of an attosecond pulse train (APT) with only one pulse per IR cycle [12]. In combination with the polarization gating technique mentioned above this can lead to the generation of isolated attosecond pulses [15].

In this paper we show that the field structure *within* each half-cycle can be controlled by using an even stronger blue field. The generated APT still consists of one pulse per IR cycle and the signature of the additional control is that central energy of the attosecond pulses can be tuned by changing φ. We demonstrate that already $\mathcal{R} = 15\%$ is sufficient to tune the peak of the harmonic spectrum between 23 and 29 eV. We also perform calculations to investigate the influence of higher field strengths. We find that the tunable range can be extended to $2.5U_\mathrm{p}$, U_p being the ponderomotive energy of the IR, for $\mathcal{R} = 50\%$ and by carefully choosing the conditions a narrow frequency range can be selected and further enhanced.

In figure 1(c), we plot the return energy as a function of return time for the high $\rightarrow$ low trajectories for three different values of φ together with the return energy for a one colour driving field. For a one colour driving field the highest return energy (cut-off) corresponds to an excursion time (τ) of $0.65T$ where T is the period of the IR field [16]. Trajectories with longer excursion times result in more divergent harmonic emission and can hence be strongly reduced after the generation using an aperture [17]. For the two-colour field we will continue to use $\tau = 0.65T$ to distinguish between short and long trajectories since the divergence of

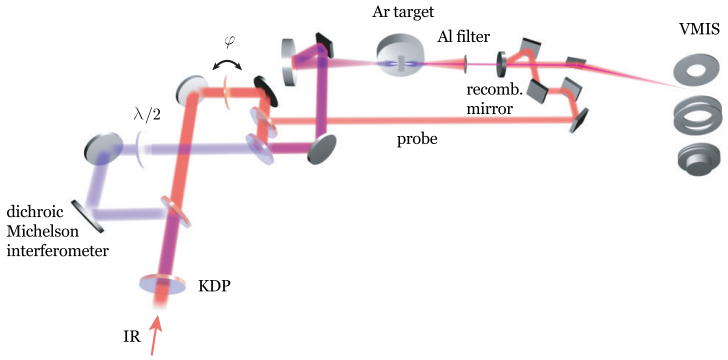

Figure 2. Experimental setup for two-colour generation and characterization of APTs.

the emission mainly depends on the time spent in the continuum. The highest energy reached during the short (high → low) trajectory depends strongly on the relative delay between the two fields, φ, figure 1(c). We find both experimentally and theoretically that we get most of the emission where the slope of the return energy curve decreases. In some cases the curve goes through a maximum at this point (figure 1(c) blue curve). By selecting only the emission from the short, high → low trajectories we thus get a pulse train with only one pulse per cycle and a central energy that can be tuned by changing the delay between the two fields. The central energies of spectra calculated within the strong field approximation (SFA) for the same parameters are marked with + in figure 1(c) and the energy difference between the two markers i.e. the tunable range is denoted ΔE.

2. Experimental method

The setup used to generate the attosecond pulses and characterize their spectral and temporal properties is schematized in figure 2. Incoming 35 fs, 800 nm, 2 mJ laser pulses are sent through a 0.6 mm KDP (potassium dihydrogen phosphate), type I crystal for second-harmonic generation. The IR and the generated second-harmonic radiation (blue) are separated in a dichroic interferometer where the phase difference between the two colours, φ, can be adjusted. Before the IR and the blue are combined at the exit of the interferometer, the polarization of the blue is made parallel with the IR and a fraction of the IR is split off as a probe. After the interferometer the two-colour field is focused into a 1 kHz pulsed Ar gas-target to generate harmonics, which are filtered spectrally and spatially. The spectral filtering is done using a 200 nm thick aluminium (Al) transmission filter that blocks the two-colour driving field and the low-order harmonics and improves the synchronization of the transmitted harmonics [18]. The filter does not significantly affect the shape of the high harmonic spectrum as the transmission

of Al is rather constant in the studied spectral region (20–40 eV)[4]. The emission is spatially filtered using a 1.5 mm aperture, located 400 mm from the laser focus, which efficiently blocks the more divergent contributions from the long trajectories [19]. The spatial filter serves the dual purpose of being a recombination mirror. The back side is a convex mirror off which the probe is reflected and made collinear with the XUV light.

The harmonic emission and the co-propagating probe are focused into an atomic Ar beam inside a velocity map imaging spectrometer (VMIS) [20]. The VMIS projects the 3D momentum distribution of the ejected photoelectrons onto a micro-channel plate detector coupled to a phosphor screen, which is read out by a CCD camera. From the measured 2D projection, the full 3D momentum distribution of the photoelectrons can be unambigously retrieved using an iterative inversion algorithm [21], and from this the photoelectron and corresponding photon spectra shown below can be easily extracted. With the probe present at the time of ionization the energy distribution of the electrons can be shifted as a function of XUV–probe delay [22]–[24]. The shift in momentum is proportional to the vector potential of the probe field, $A(t)$, at the time of ionization, $\Delta p = -eA(t_i)$. The streaking of the photoelectrons allows us to recover the duration of the attosecond pulses [25] since the pulse periodicity is matched exactly to a full IR cycle and consecutive ionization events are identical for a multi-cycle laser [26]. The strength of the probe field has to be chosen below that necessary to turn the photoelectrons around and thereby induce coherent electron scattering [26] in order not to perturb the temporal characterization. Coherent electron scattering occurs when the dimensionless parameter $\tilde{\gamma} = \sqrt{\frac{\hbar\omega_c - I_p}{2U_p}}$ is less than 1, where $\hbar\omega_c$ is the central energy of the XUV light and I_p is the ionization potential of the target atom. In the experiment $\tilde{\gamma} = 3.7$ and no electron–ion interaction is expected.

3. Results

Experimental results showing spectral shaping are presented in figures 3(a) and (c). In (a) harmonic spectra are plotted as a function of φ, for an IR intensity estimated to be $7.5 \times 10^{13}\,\mathrm{W\,cm^{-2}}$ and $\mathcal{R} = 15\%$. The odd and even harmonics have comparable strengths and oscillate with φ with a period of π. The positions of the oscillation maxima depend strongly and almost linearly on the harmonic order. As a consequence, the central frequency can easily be varied simply by changing φ. The measured tunability extends over 6 eV, limited mainly by the target gas (Ar) and the intensities used. The tunable range, ΔE, can be increased by increasing the IR intensity while keeping $\mathcal{R}$ fixed. Higher intensity might demand a target gas with higher ionization potential. For a fixed $\mathcal{R}$, ΔE is proportional to U_p and thus the intensity. For the intensity we use in the calculations and experiment presented in figures 1 and 3, $\Delta E \approx U_p$.

We also perform a temporal measurement at a phase φ marked with green in figure 3(a). The phase was chosen to be within the range where the APT consists of one pulse per IR cycle, i.e. between the ice-blue and red lines. In figure 4, the presence of the probe shifts the photoelectron distribution. The on-axis photoelectron spectra are plotted as a function of the XUV–probe delay in (a) together with an angular distribution in (b), taken at the XUV–probe delay indicated by the white line in (a), where streaking is maximized. The fact that the energy transfer in (a) is either upward or downward proves that we only have one attosecond pulse per IR cycle. The phase of the attosecond pulses can be retrieved either by considering the

[4] Center for X-Ray Optics, Lawrence Berkley National Laboratory.

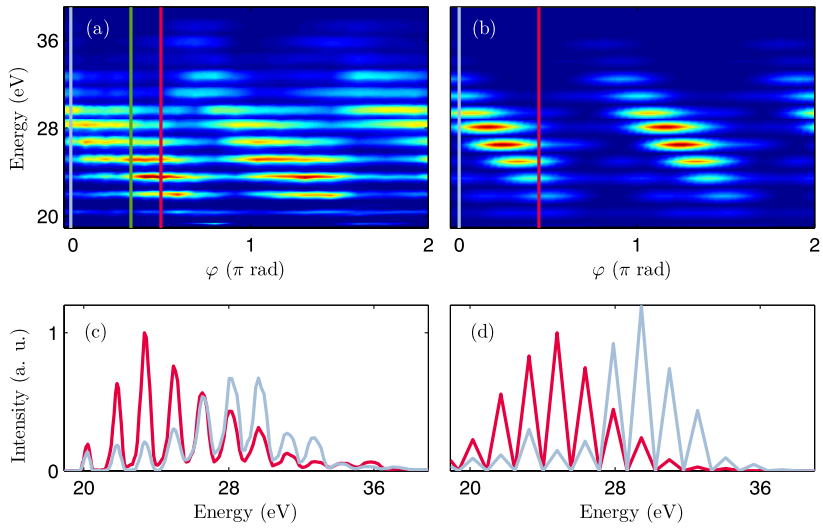

Figure 3. (a) and (b) photon energies as a function of φ, (a) an experimental scan and (b) a calculated scan where only short trajectories are included. (c) and (d) spectra for minimum and maximum energy taken at the relative phases marked with ice-blue and red lines in the scans, (c) experimental and (d) calculated. The green line in (a) indicates the relative phase for which the pulse duration was measured.

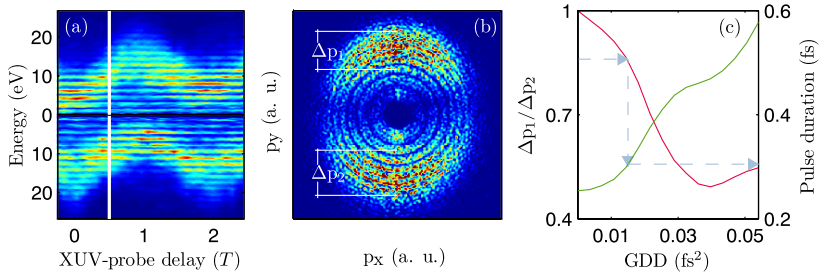

Figure 4. (a) Electron energy distribution along the polarization axis as a function of XUV–probe delay. (b) Electron momentum distribution at the XUV–probe delay when streaking is maximized. The probe-field is polarized along the y-axis. (c) Momentum asymmetry as a function of GDD, red curve and left y-axis, and pulse duration as a function of GDD, green curve and right y-axis. The ice-blue arrows point out the path starting from the measured $\Delta p_1/\Delta p_2$ to the retrieved GDD where it meets the red curve and the pulse duration where it meets the green curve.

full scan [27] (figure 4(a)) or the up/down asymmetry, $\Delta p_1/\Delta p_2$, of the angular distribution at XUV–probe delays corresponding to maximum streaking i.e. when $A(t) = 0$ at the time of ionization (figure 4(b)). We choose the latter technique which in principle can be used to measure the pulse-duration of the attosecond pulses with a single shot. Electrons leaving the atom upward and downward to the probe polarization direction are affected differently by the probe field [22]. In figure 4(b) the upward electrons get a more narrow distribution than the downward electrons ($\Delta p_1 < \Delta p_2$). For each combination of harmonic spectrum and probe intensity the ratio $\Delta p_1/\Delta p_2$ depends on the group delay dispersion (GDD) of the attosecond pulses in a unique way. The probe intensity can be extracted from the maximum momentum shift in the scan. For our measured harmonic spectrum and probe intensity we calculate, using the SFA, how the electron distributions change with GDD. This allows us to deduce $\Delta p_1/\Delta p_2$ as a function of GDD (figure 4(c) red line). The variation of the pulse duration with GDD is indicated by the green line. From our experimentally measured ratio, $\Delta p_1/\Delta p_2 = 0.85$, we obtain a GDD of 0.015 fs^2 and a pulse duration of 300 as. The negative GDD of the Al-filter compresses the pulse from 450 as towards the transform limit of 250 as.

Our theoretical calculations consist of solving the time-dependent Schrödinger equation within the SFA [28]. The atomic dipole $\langle x(\omega)\rangle$ from the calculations is converted to an intensity spectrum by taking the product $\omega^4|\langle x(\omega)\rangle|^2$. Experimentally, contributions from the short trajectories can be selected through phase matching and spatial filtering [29]. To mimic this effect in the single atom calculations we restrict the SFA integration to include only the excursion times with: $0 < \tau < 0.65T$. Comparing calculations and experiment, in figure 3, we find a good agreement between the experimental (a) and the calculated (b) spectra. Note that the calculations, based on a continuous driving field, give information about the intensity but not the shape of individual harmonics. The experimental results together with the calculations confirm the idea of sub-cycle control induced by the second-harmonic field. The probability for ionization and return of the electron wave packet is increased over a certain energy range close to the highest detected energy. This energy range can be tuned by changing the phase difference φ.

We investigate theoretically how the sub-cycle control can be improved by increasing $\mathcal{R}$ even further. The situation where $\mathcal{R} = 25\%$ and $\varphi = 0.6$ (see figure 5) stands out in particular since the electron is pulled back with an almost constant energy over an extended period of time, $\sim T/4$, i.e. there are many sub-cycle tunnelling times that lead to the same final energy (figure 5(b)). This results in a significant enhancement of the harmonic emission at that particular energy. The intensity within the enhanced energy region is well above the already strong harmonics for $\varphi = 0$ and 1.2 rad in figure 5(c).

For $\mathcal{R} > 25\%$, the electron is pulled back to the atom in a more complex way and the return energies are now highly dependent on φ. In figure 6(b), the calculated return energy is plotted as a function of τ for three phase differences. We note that the energy curve can peak twice; once for $0 < \tau < 0.65T$ and another time for $0.65T < \tau < T$. The highest obtainable energy within the short and long trajectory integration windows vary in opposite ways with φ. This results in a central photon energy that decreases with φ for the short trajectories and increases for the long trajectories, see figures 6(a) and (c). Under these conditions, 2×10^{14} W cm^{-2}, $\mathcal{R} = 50\%$, the tunable range is increased and we find that it is feasible to tune the energy over $2.5U_p$.

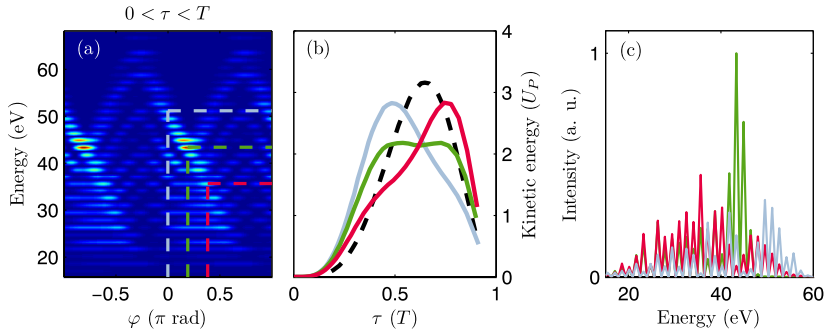

Figure 5. (a) A calculated scan of φ including the phases presented in (b) and (c). The calculations are done for an IR intensity of 2×10^{14} W cm^{-2} and $\mathcal{R} = 25\%$. (b) Kinetic energy of the returning electrons for the three φ-values shown in figure 1, $\varphi = 0$ rad (ice-blue), $\varphi = 0.6$ rad (green) and $\varphi = 1.2$ rad (red). (c) Harmonic spectra showing the enhanced emission at 42 eV corresponding to the flat region in the return energy curve (b).

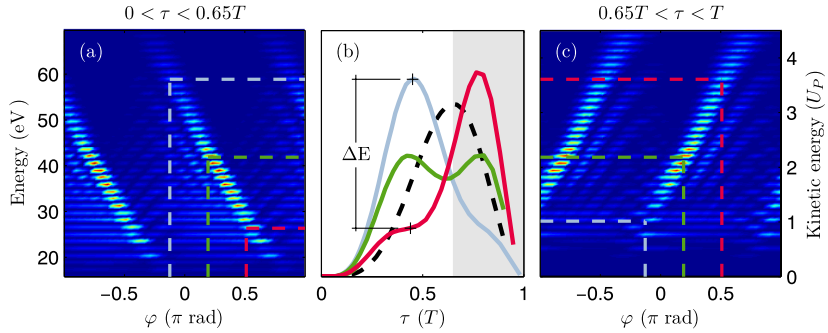

Figure 6. Calculations for an IR intensity of 2×10^{14} and $\mathcal{R} = 50\%$. (a) SFA calculations including short trajectories, $0 < \tau < 0.65T$. (b) Electron return energies for $\varphi = -0.4$ rad (ice-blue), $\varphi = 0.6$ rad (green) and $\varphi = 1.6$ rad (red). (c) SFA calculations for long trajectories, $0.65T < \tau < T$. The φ-values used to calculate the return energies are indicated in the scans by the vertical dashed lines. The horizontal dashed lines mark the peak of the spectra and connect the peak to the return energy curves.

4. Conclusion

We have shown that by altering the driving laser field on a sub-cycle level using a two-colour laser field, we can control the spectral properties of the generated APT by varying the phase difference φ between the IR and its second harmonic. With this method we have extended the spectral control beyond that of transmission filters. For applications this will be very useful as the photon energy of the emitted attosecond pulses can be tuned close to or just below the

ionization potential of a target gas to study below threshold ionization [30]. For almost all values of φ one pulse per IR cycle is generated. For a sequence of pulses the central frequency can be tuned by varying φ except for a narrow transition φ-region where two pulses per cycle are generated. In the same manner, isolated attosecond pulses generated by a two-colour field can be tuned in frequency by varying φ within the range where only one pulse is generated. By increasing the second-harmonic intensity compared to the experiment presented here, we predict that the tunable frequency range can be extended further and provide a flexible attosecond source to meet future needs.

Acknowledgments

This research was supported by the Marie Curie Early Stage Training Site (MAXLAS), the Integrated Initiative of Infrastructure LASERLAB-EUROPE (RII3-CT-2003-506350) within the 6th European Community Framework Programme, the Knut and Alice Wallenberg Foundation, the Crafoord Foundation and the Swedish Research Council.

References

[1] Paul P M, Toma E S, Breger P, Mullot G, Augé F, Balcou Ph, Muller H G and Agostini P 2001 Observation of a train of attosecond pulses from high harmonic generation *Science* **292** 1689
[2] Schafer K J, Yang B, DiMauro L F and Kulander K C 1993 Above threshold ionization beyond the high harmonic cutoff *Phys. Rev. Lett.* **70** 1599
[3] Corkum P B 1993 Plasma perspective on strong-field multiphoton ionization *Phys. Rev. Lett.* **71** 1994
[4] Baltuška A *et al* 2003 Attosecond control of electronic processes by intense light fields *Nature* **421** 611
[5] Ivanov M, Corkum P B, Zuo T and Bandrauk A 1995 Routes to control of intense-field atomic polarizability *Phys. Rev. Lett.* **74** 2933
[6] Sola I J *et al* 2006 Controlling attosecond electron dynamics by phase-stabilized polarization gating *Nat. Phys.* **2** 319
[7] Sansone G *et al* 2006 Isolated single-cycle attosecond pulses *Science* **314** 443–6
[8] Hentschel M, Kienberger R, Spielmann Ch, Reider G A, Milosevic N, Brabec T, Corkum P, Heinzmann U, Drescher M and Krausz F 2001 Attosecond metrology *Nature* **414** 509
[9] Sansone G, Benedetti E, Vozzi C, Stagira S and Nisoli M 2008 Attosecond metrology in the few-optical-cycle regime *New J. Phys.* **10** 025006
[10] Perry M D and Crane J K 1993 High-order harmonic emission from mixed fields *Phys. Rev.* A **48** R4051–4
[11] Eichmann H, Egbert A, Nolte S, Momma C, Wellegehausen B, Becker W, Long S and McIver J K 1995 Polarization-dependent high-order two-color mixing *Phys. Rev.* A **51** R3414
[12] Mauritsson J, Johnsson P, Gustafsson E, L'Huillier A, Schafer K J and Gaarde M B 2006 Attosecond pulse trains generated using two color laser fields *Phys. Rev. Lett.* **97** 013001
[13] Pfeifer T, Gallmann L, Abel M J, Neumark D M and Leone S R 2006 Single attosecond pulse generation in the multicycle-driver regime by adding a weak second-harmonic field *Opt. Lett.* **31** 975
[14] Merdji H, Auguste T, Boutu W, Caumes J P, Carr B, Pfeifer T, Jullien A, Neumark D M and Leone S R 2007 Isolated attosecond pulses using a detuned second-harmonic field *Opt. Lett.* **32** 3134–6
[15] Mashiko H, Gilbertson S, Li C, Khan S D, Shakya M M, Moon E and Chang Z 2008 Double optical gating of high-order harmonic generation with carrier-envelope phase stabilized lasers *Phys. Rev. Lett.* **100** 103906
[16] Krause J L, Schafer K J and Kulander K C 1992 High-order harmonic generation from atoms and ions in the high intensity regime *Phys. Rev. Lett.* **68** 3535
[17] Bellini M, Lyngå C, Tozzi A, Gaarde M B, Delfin C, Hänsch T W, L'Huillier A and Wahlström C-G 1998 Temporal coherence of ultrashort high-order harmonic pulses *Phys. Rev. Lett.* **81** 297

[18] López-Martens R *et al* 2005 Amplitude and phase control of attosecond light pulses *Phys. Rev. Lett.* **94** 033001
[19] Gaarde M B and Schafer K J 2006 Generating single attosecond pulses via spatial filtering *Opt. Lett.* **31** 3188
[20] Eppink A T J B and Parker D H 1997 Velocity map imaging of ions and electrons using electrostatic lenses: application in photoelectron and photofragment ion imaging of molecular oxygen *Rev. Sci. Instrum.* **68** 3477
[21] Vrakking M J J 2001 An iterative procedure for the inversion of two-dimensional ion/photoelectron imaging experiments *Rev. Sci. Instrum.* **72** 4084
[22] Kienberger R *et al* 2004 Atomic transient recorder *Nature* **427** 817
[23] Johnsson P *et al* 2005 Attosecond electron wave packet dynamics in strong laser fields *Phys. Rev. Lett.* **95** 013001
[24] Remetter T *et al* 2006 Attosecond electron wave packet interferometry *Nat. Phys.* **2** 323
[25] Itatani J, Quéré F, Yudin G L, Ivanov M Yu, Krausz F and Corkum P B 2002 Attosecond streak camera *Phys. Rev. Lett.* **88** 173903
[26] Mauritsson J, Johnsson P, Mansten E, Swoboda M, Ruchon T, L'Huillier A and Schafer K J 2008 Coherent electron scattering captured by an attosecond quantum stroboscope *Phys. Rev. Lett.* **100** 073003
[27] Mairesse Y and Quéré F 2005 Frequency-resolved optical gating for complete reconstruction of attosecond bursts *Phys. Rev.* A **71** 011401
[28] Lewenstein M, Balcou Ph, Ivanov M Yu, L'Huillier A and Corkum P B 1994 Theory of high-order harmonic generation by low-frequency laser fields *Phys. Rev.* A **49** 2117
[29] Antoine Ph, L'Huillier A and Lewenstein M 1996 Attosecond pulse trains using high-order harmonics *Phys. Rev. Lett.* **77** 1234
[30] Johnsson P, Mauritsson J, Remetter T, L'Huillier A and Schafer K J 2007 Attosecond control of ionization by wave-packet interference *Phys. Rev. Lett.* **99** 233011

Paper IV

Interference Effects in Two-Color High-Order Harmonic Generation

X. He, J. M. Dahlström, R. Rakowski, C. M. Heyl, A. Persson, J. Mauritsson, and A. L'Huillier.

Phys. Rev. A **82**, 033410 (2010).

PHYSICAL REVIEW A **82**, 033410 (2010)

Interference effects in two-color high-order harmonic generation

X. He,[1] J. M. Dahlström,[1] R. Rakowski,[1] C. M. Heyl,[1,2] A. Persson,[1] J. Mauritsson,[1] and A. L'Huillier[1]
[1]*Department of Physics, Lund University, P. O. Box 118, SE-221 00 Lund, Sweden*
[2]*Department of Physics, University of Marburg, Marburg, Germany*
(Received 5 May 2010; published 13 September 2010)

We study high-order harmonic generation in argon driven by an intense 800 nm laser field and a small fraction of its second harmonic. The intensity and divergence of the emitted even and odd harmonics are strongly modulated as a function of the relative delay between the two fields. We provide a detailed analysis of the underlying interference effects. The interference changes drastically when approaching the cutoff region due to a switch of the dominant trajectory responsible for harmonic generation.

DOI: 10.1103/PhysRevA.82.033410 PACS number(s): 32.80.Rm, 32.80.Qk, 42.65.Ky

High-order harmonic generation (HHG) from the interaction of an intense infrared (IR) laser field and a gas target provides a coherent table-top radiation source in the extreme ultraviolet (XUV) range, of interest for a number of applications, in particular the production of attosecond light pulses [1,2]. The underlying physics of HHG is well described by the so-called three-step model [3–5]: an electron wave packet is created by tunneling through the Coulomb barrier deformed by the laser field; it is subsequently accelerated by the laser field; and returns to the atom where it recombines to the ground state, leading to the production of an XUV light burst. This process is repeated every half-cycle of the IR laser field, resulting in an attosecond pulse train (APT) with a pulse separation of one-half IR period and to a spectrum of odd harmonics.

There is a growing interest to achieve even better control of the generation process [6], e.g., to obtain higher conversion efficiency or to tailor attosecond pulses or pulse trains for specific applications. Two-color HHG driven by an IR laser and its second harmonic (blue) provides subcycle control of the generating electric field, with the interesting property that two consecutive half-cycles become different, and not simply opposite in sign. This breakdown of the electric field inversion symmetry has been used for several applications, e.g., the generation of even and odd high-harmonics with increased conversion efficiency [7,8] and the production of attosecond pulse trains with one pulse per IR cycle [9,10]. In some conditions, when the intensity of the second harmonic is much weaker than that of the fundamental laser field, even harmonics can be used to provide information about the generation process [11–13].

In this article, we investigate both experimentally and theoretically high-order harmonic generation driven by a two-color laser field consisting of a 800 nm fundamental and a fraction of its second harmonic. The even and odd harmonic intensities are found to be modulated as a function of IR-blue delay, forming in some cases a rich interference pattern (Fig. 1). We investigate how these oscillations depend on harmonic energy and intensity of the blue field and how the spatial profiles of the emitted harmonics are affected. We provide an interpretation based on quasiclassical calculations.

Experiments were performed using an amplified 10 Hz titanium sapphire laser system delivering 40 fs pulses at 800 nm with energy up to 1 J. The results presented in this article are obtained with only a small fraction (less than 10 mJ) of this energy. The laser beam was sent through a 1.3 mm-thick type I KDP (potassium dihydrogen phosphate) crystal to generate the second harmonic. A Michelson interferometer was used to separate and delay the second harmonic and to make the polarizations of the two laser fields parallel to each other. The relative delay was adjusted with a 500 μm-thick glass plate. After recombination of the two colors, the beam was focused by a spherical mirror with a 2 m focal length into a cylindrical gas cell with 1 mm diameter and 15 mm length, filled with Ar gas. Variable apertures were placed in the fundamental and second harmonic beams to adjust intensities and focusing geometries. These conditions are such that phase matching is optimized and pulse energies per harmonic reaching 100 nJ have been measured. The harmonic spectra were detected by a flat-field XUV spectrometer, located 1.5 m from the source and allowing us to obtain spatial and spectral information simultaneously [14].

Figures 1(a)–1(c) presents the spectra of the 21st to 24th harmonics as a function of relative delay (τ) in units of the period of the blue field $T_B = 1.3$ fs. The color code indicates the intensity of the emitted light. When the blue intensity is less than a percent of the IR [panel (a)], the odd and even harmonics oscillate with opposite phase twice per blue cycle [11–13]. When the blue intensity is increased to a few percent [Figs. 1(b) and 1(c)], even and odd harmonics become comparable in strength and vary more strongly with the IR-blue delay.

Figure 2 compares the intensities of the 22nd (a) and 23rd (b) harmonics as a function of τ for the three different intensities of the blue field used in Fig. 1. At low intensity (thin red line), the odd and even harmonics oscillate out of phase. When the blue intensity is increased, the patterns become more complex, exhibiting multiple maxima per half blue period. The number and position of these maxima depend on the blue intensity, as well as harmonic order. These results arise from the interferometric nature of the HHG process, which will be analyzed in more detail in the following.

To understand the interference structure shown in Figs. 1 and 2, let us consider the radiation emitted every IR cycle over a certain energy range. It comprises predominantly two bursts, one each half-cycle. In absence of the blue field, they are identical except for a change of sign. We further assume that the emitted bursts are identical from one IR cycle to the next. The radiation emitted from the interaction of an intense laser field comprising n periods with an atom can be generally

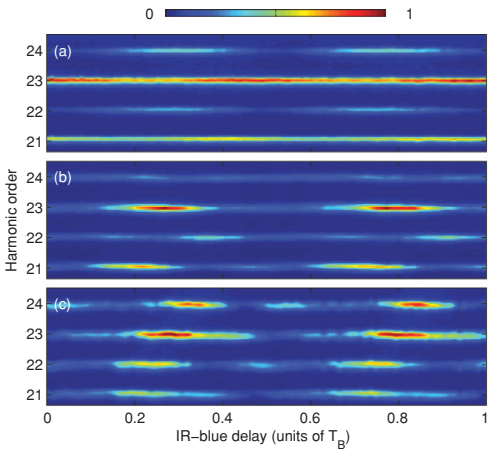

FIG. 1. (Color online) 21st to 24th harmonic spectra as a function of the relative delay between the IR and blue fields for different intensity ratios, increasing from about half a percent in (a) to a few percent in (b) and (c). The IR intensity is estimated to be 1.8×10^{14} W/cm^2, based on the cutoff position. The color code indicates the harmonic intensities in arbitrary units.

expressed as

$$s(t) = \sum_{j=1}^{j=n} a_+(t) \otimes \delta(t - jT) + a_-(t) \otimes \delta\left(t - jT - \frac{T}{2}\right), \tag{1}$$

where $a_+(t)$ and $a_-(t)$ are the fields emitted in the first and second half period, respectively, and T is the IR field period. If the blue field is weak, it mainly affects the phase of the emitted radiation. $a_\pm(t) \approx \pm a(t)\exp[\pm i\sigma(t)]$, where $a(t)$ is the pulse emitted from the first (positive) half period due to the interaction with the fundamental field only, and $\sigma(t)$ is a slow function over time. The Fourier transform of the pulse train can then be approximated as

$$S(\Omega) \approx A(\Omega) \sum_{j=1}^{j=n} e^{ij\Omega T + i\sigma(\Omega)} - e^{ij\Omega T + i\frac{\Omega T}{2} - i\sigma(\Omega)}, \tag{2}$$

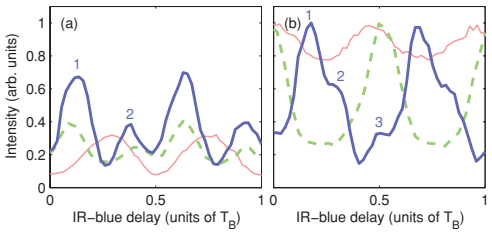

FIG. 2. (Color online) Intensities of the 22nd (a) and 23rd harmonics (b), normalized to the maximum value of the 23rd harmonic for the three cases in Fig. 1. The thin red line, green dashed line, and thick blue line correspond to (a), (b), and (c).

where $A(\Omega)$ is the Fourier transform of $a(t)$ and $\sigma(\Omega) = \sigma[t_r(\Omega)]$. $t_r(\Omega)$ represents the time at which the component at frequency Ω of the light burst is emitted, i.e., the return time of the corresponding classical electron trajectory. The Ω dependence accounts for the chirp of the emitted radiation [15]. The power spectrum reduces to the form

$$|S(\Omega)|^2 \approx 4\,|A(\Omega)|^2 \left|\frac{\sin\left(\frac{n\Omega T}{2}\right)}{\sin\left(\frac{\Omega T}{2}\right)}\right|^2 \left|\sin\left[\frac{\Omega T}{4} - \sigma(\Omega)\right]\right|^2, \tag{3}$$

which has a straightforward interpretation. The first factor is the spectrum emitted by a single attosecond pulse, the second factor modulates this broad spectrum, leading to a comb of even and odd harmonics. Finally the last factor cancels the even harmonic components when there is no second harmonic ($\sigma = 0$). When a second harmonic field is present, it modulates the amplitude of both even and odd harmonics. For the even harmonics ($\Omega = q\omega$ where ω is the IR frequency and q is an even integer), $|S(q\omega)|^2 \propto |\sin[\sigma(q\omega)]|^2$, while for the odd harmonics (q odd), $|S(q\omega)|^2 \propto |\cos[\sigma(q\omega)]|^2$.

The phase change induced by the blue field can be estimated using the classical limit, $I_p \to 0$. By treating the blue field as a perturbation, $\sigma(\Omega)$ is found to be [13]

$$\sigma(\Omega) = \frac{e}{\hbar}\int_{t_i}^{t_r} dt' x_R(t_r, t') E_B(t'), \tag{4}$$

where t_i is the ionization time and e the electron charge. x_R denotes the position at time t' of an electron that starts its motion in the IR field [$E_R(t) = E_R^0 \sin(\omega t)$] at time t_i. Finally, E_B is the second harmonic field $E_B(t) = E_B^0 \sin(2\omega t + \phi_B)$. Equation (4) can be rewritten as

$$\sigma(\Omega) = \sigma_0 \sin[\phi_B + \delta(\Omega)], \tag{5}$$

with $\sigma_0 = eE_B^0\Delta(\Omega)/\hbar$. $\Delta(\Omega)$ and $\delta(\Omega)$ are the frequency-dependent modulus and argument of the Fourier transform at 2ω of the electron trajectory in the IR field.

Figures 3(a) and 3(b) shows the calculated intensity of two consecutive harmonics (even and odd) as a function of σ_0 and delay, expressed here as $(\phi_B + \delta)/2\pi$, while (c), (d) present lineouts at three different σ_0, indicated by the corresponding lines in (a) and (b). The odd and even harmonic intensities strongly varies with delay in opposite phase with each other, so that the total intensity remains constant. The number of maxima increases with σ_0, i.e., with the blue field intensity.

When the blue field is weak ($\sigma_0 \ll 1$), the intensity of the even harmonic varies as $|\sigma_0 \sin(\phi_B + \delta)|^2$, while the odd harmonic intensity varies as $1 - |\sigma_0 \sin(\phi_B + \delta)|^2$ [thin red line in Fig. 3(d)]. At moderate blue intensity, corresponding to the conditions of Fig. 1(b), the even harmonic intensity (green dashed line) show two peaks of equal strength over a delay of $T_B/2$, while the odd harmonics show one strong and one weak peak. This behavior compares well to that observed experimentally in Fig. 2 where two (one) peaks are visible in the even (odd) harmonics. We estimate σ_0 to be just above $\pi/2$ in this case. At higher blue intensity, as in Fig. 1(c), the even harmonic intensity (thick blue line) show two peaks (1,2), while the odd harmonics presents a broad peak with two maxima (1,2) and an additional sharp peak (3). The same qualitative behavior is observed experimentally

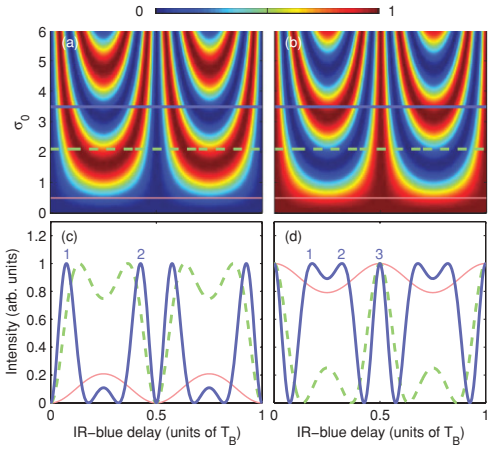

FIG. 3. (Color online) Harmonic intensity as a function of σ_0 and IR-blue delay for even (a) and odd (b) harmonics. The σ_0 corresponding to the intensities used in Figs. 1(a)–1(c) are indicated by the thick blue solid (1a), green dashed (1b), and thin red lines (1c). (c) and (d) show the corresponding lineouts.

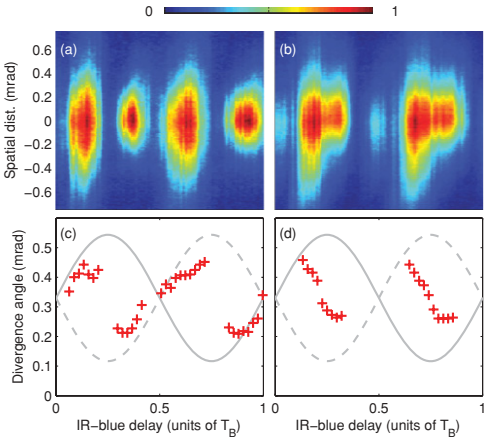

FIG. 4. (Color online) Spatial profiles for the 22nd (a) and 23rd (b) harmonics as a function of delay, in the conditions of Fig. 1(c). The experimental divergence angles (red symbols) are compared to the theoretical half-cycle divergences in (c) and (d) for the 22nd and 23rd harmonics, respectively.

(blue line in Fig. 2). σ_0 is thus estimated to be slightly above π. From this analysis, we can estimate the ratios of the blue to IR intensities to be 0.4, 5, and 20 % in Figs. 1(a), 1(b), and 1(c). The relative strength of the experimental peaks in Fig. 2 is not accurately modeled using Eq. (3) since we include neither amplitude effects nor propagation in our calculation. In addition, experimental effects, such as dephasing between the IR and the blue, could lead to decrease in contrast.

Complementary information on the generation process can be obtained by studying the spatial distribution [16]. In Figs. 4(a) and 4(b) we show the spatial distribution of the 22nd and 23rd harmonics. In the one-color case, the divergence of the qth harmonic Θ_q can be estimated using Gaussian optics by the simple expression [14],

$$\Theta_q = \frac{\lambda_q}{\pi w_q}\sqrt{1+4\alpha_q^2 I_R^2 \frac{w_q^4}{w_R^4}} \approx |\alpha_q| I_R \frac{\lambda_q w_q}{\pi w_R^2}, \qquad (6)$$

where I_R is the peak IR intensity, w_R, w_q are the radii of the IR and qth harmonic fields and λ_q the qth harmonic wavelength. $\alpha_q I_R$ is the single-atom phase, corresponding to the phase accumulated by the electron on its trajectory, often called "dipole phase". When $\alpha_q I_R$ is large, it dominates the diffraction limit in Eq. (6) and the divergence takes the simple expression shown on the right side in Eq. (6). For the short trajectory, we have $|\alpha_q| \approx 2.7 \times 10^{-14}$ cm^2/W for the 23rd harmonic [14,17].

As shown in Eq. (2), the addition of a weak blue field affects the phase of each half-cycle contribution by $\pm\sigma$. The divergence of the qth harmonic is then expected to vary between $\Theta_q(1 \pm \sigma/|\alpha_q| I_R)$, the limits being reached when one half-cycle is dominant. These limits are indicated by the grey lines in Figs. 4(c) and 4(d), calculated by using the experimentally determined one-color divergence $\Theta_q = 0.33$ mrad. The two lines (solid and dashed) show the variation of the divergence for two (positive or negative) half-cycles. Our experimental results for the 22nd and the 23rd harmonics are indicated by the red symbols. As expected, the measured divergence angles are comprised between the theoretical values for two consecutive half-cycle contributions. The variation of the measured divergence can be interpreted as follows: In (c), one half-cycle (corresponding to the dashed line) is dominant from $\tau = 0.3T_B$ to $0.7T_B$, while the other half-cycle prevails for the other delays. In contrast in (d), the measured divergence does not indicate preferential emission during one particular half cycle since it is well within the expected half-cycle values for almost all delays.

Finally, we investigate how the interference pattern depends on Ω, i.e., harmonic order, from the plateau to the cutoff region. Figure 5(a) shows the harmonic spectra as a function of delay, in the weak blue intensity case [corresponding to Fig. 1(a)]. The nodes of the oscillations of the even harmonics are indicated by the white crosses. The position of the nodes varies approximately linearly from harmonic order 22 to 28, in agreement with the prediction of the simple model presented above (see also [11,13]), for the short trajectory (see red line). In Fig. 5(b), we examine the behavior of higher-order harmonics, approaching the cutoff region. Surprisingly, the 30th harmonic hardly oscillates, while the 32nd and 34th oscillate almost out of phase with the 28th. To understand the apparent lack of oscillation of the 30th harmonic, we analyze its spatial profile. In Fig. 5(c), we present the 30th harmonic intensity obtained by integrating over the outer (central) part of the spatial profile, plotted as a thick blue (thin red) line. This allows us to unravel two different oscillations almost opposite in phase [see also $+$ and $*$ symbols in Fig. 5(a)]. The phase obtained by integrating the outer part of the spatial profile is close to that obtained for the 32nd and 34th harmonics in Fig. 5(b).

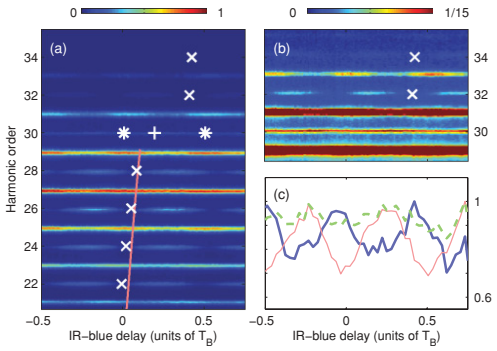

FIG. 5. (Color online) (a) Harmonic spectra as a function of delay. (b) Corresponding high energy region using a saturated color scale. The white crosses indicate the position of the nodes of the oscillations. The red curve in (a) is $\delta(\Omega)$ for the short branch. (c) 30th harmonic intensity as a function of delay, spatially integrated (green dashed), integrated over the central part (thick blue line); and over the outer part (thin red line) of the spatial profile. The + and ∗ symbols in (a) refer to the nodes of the central and outer part, respectively.

We interpret this result as due to the long trajectory which becomes more important when approaching the cutoff region. The switch between the two trajectories seems to occur at the 30th harmonic in our experiment. If this harmonic has comparable (and approximately out of phase) contributions from the two trajectories, it would only weakly oscillate with τ, which is what is observed experimentally. Phase matching calculations performed using our experimental conditions show a progressive switch from the short trajectory to the long trajectory when approaching the cutoff region and thus confirm this interpretation.

In summary, we have experimentally identified and theoretically analyzed interference effects in two-color HHG. Adding a weak blue field allows us to control the intensity and divergence of the harmonic emission. An interesting switch between the short and long trajectories of the harmonic emission has been identified when approaching the cutoff region.

This research was supported by the Marie Curie Incoming International Fellowship OHIO, the European Research Council (ALMA), the Knut and Alice Wallenberg Foundation, the Joint Research Programme ALADIN of Laserlab-Europe II, and the Swedish Research Council.

[1] P. M. Paul *et al.*, Science **292**, 1689 (2001).
[2] M. Hentschel *et al.*, Nature **414**, 509 (2001).
[3] K. J. Schafer, B. Yang, L. F. DiMauro, and K. C. Kulander, Phys. Rev. Lett. **70**, 1599 (1993).
[4] P. B. Corkum, Phys. Rev. Lett. **71**, 1994 (1993).
[5] M. Lewenstein, P. Balcou, M. Y. Ivanov, A. L'Huillier, and P. B. Corkum, Phys. Rev. A **49**, 2117 (1994).
[6] C. Winterfeldt, C. Spielmann, and G. Gerber, Rev. Mod. Phys. **80**, 117 (2008).
[7] I. J. Kim, C. M. Kim, H. T. Kim, G. H. Lee, Y. S. Lee, J. Y. Park, D. J. Cho, C. H. Nam, Phys. Rev. Lett. **94**, 243901 (2005).
[8] T. T. Liu, T. Kanai, T. Sekikawa, and S. Watanabe, Phys. Rev. A **73**, 063823 (2006).
[9] J. Mauritsson, P. Johnsson, E. Gustafsson, A. LHuillier, K. J. Schafer, M. B. Gaarde, Phys. Rev. Lett. **97**, 013001 (2006).
[10] J. Mauritsson, P. Johnsson, E. Mansten, M. Swoboda, T. Ruchon, A. LHuillier, K. J. Schafer, Phys. Rev. Lett. **100**, 073003 (2008).
[11] N. Dudovich *et al.*, Nature Phys. **2**, 781 (2006).
[12] G. Doumy, J. Wheeler, C. Roedig, R. Chirla, P. Agostini, L. F. DiMauro, Phys. Rev. Lett. **102**, 093002 (2009).
[13] J. M. Dahlstrom, T. Fordell, E. Mansten, T. Ruchon, M. Swoboda, K. Klunder, M. Gisselbrecht, A. LHuillier, J. Mauritsson, Phys. Rev. A **80**, 033836 (2009).
[14] X. He *et al.*, Phys. Rev. A **79**, 063829 (2009).
[15] We assume that there is one dominant trajectory contributing (one saddle point).
[16] N. Dudovich, J. L. Tate, Y. Mairesse, D. M. Villeneuve, P. B. Corkum, and M. B. Gaarde, Phys. Rev. A **80**, 011806(R) (2009).
[17] K. Varju *et al.*, J. Mod. Opt. **52**, 379 (2005).

Paper V

Atomic and Macroscopic Measurements of Attosecond Pulse Trains

J. M. Dahlström, T. Fordell, E. Mansten, T. Ruchon, M. Swoboda, K. Klünder, M. Gisselbrecht, A. L'Huillier, and J. Mauritsson.

Phys. Rev. A **80**, 033836 (2009).

PHYSICAL REVIEW A **80**, 033836 (2009)

Atomic and macroscopic measurements of attosecond pulse trains

J. M. Dahlström,[1] T. Fordell,[1] E. Mansten,[1] T. Ruchon,[2] M. Swoboda,[1] K. Klünder,[1] M. Gisselbrecht,[1,3] A. L'Huillier,[1] and J. Mauritsson[1]

[1]*Department of Physics, Lund University, P.O. Box 118, SE-221 00 Lund, Sweden*

[2]*DSM, Service des Photons, Atomes et Molcules, CEA-Saclay, 91191 Gif sur Yvette, France*

[3]*UMR8624, LIXAM, CNRS–Université Paris Sud, Bat. 350, 91405 Orsay, France*

(Received 12 May 2009; published 25 September 2009)

We characterize attosecond pulses in a train using both the well established "reconstruction of attosecond beating by interference of two-photon transitions" (RABITT) technique and the recently demonstrated *in situ* method, which is based on a weak perturbation of the harmonic generation process by the second harmonic of the laser field. The latter technique determines the characteristics of the single atom emission, while RABITT allows one to measure attosecond pulses "on target." By comparing the results of the two methods, the influence of propagation and filtering on the attosecond pulses can be extracted.

DOI: 10.1103/PhysRevA.80.033836 PACS number(s): 42.65.Ky, 32.80.Qk, 32.80.Rm

I. INTRODUCTION

Attosecond pulse trains (APTs) are created when intense infrared (ir) laser pulses interact with a gas of atoms or molecules [1]. The characteristics of the attosecond pulses depend both on the quantum-mechanical single atom dynamics as well as on macroscopic effects due to propagation in the nonlinear medium [2]. Under normal experimental conditions, the pulse train contains two pulses per cycle of the laser field [3–5]. The properties of these pulses can be modified by transmission through filters [6] or reflection by gratings and/or multilayer mirrors [7]. Several techniques to characterize attosecond pulse trains have been proposed, each with specific advantages and limitations. In this paper we concentrate on analyzing and comparing two of these techniques: the reconstruction of attosecond beating by interference of two-photon transitions (RABITT) [1] and a two-color *in situ* method [8], which uses a weak perturbation of the high-order harmonic generation (HHG) by the second harmonic of the fundamental laser field. Both techniques aim to characterize the average attosecond pulse structure in an APT.

Figure 1 illustrates schematically the difference between these two techniques. RABITT allows us to determine the *final* structure of the attosecond pulses after propagation in the gas cell and filtering. The attosecond pulses are characterized "on target," i.e., in the chamber where they can be used for applications. The RABITT scheme is implemented by ionizing an atomic gas with the APT in presence of a synchronized weak ir field. The perturbation due to the ir field results in sidebands in the photoelectron spectra as shown in Fig. 2(a). Information about the structure of the attosecond pulses can then be obtained by studying the intensity oscillations of these sidebands with respect to the subcycle delay between the probe field and the APT.

The *in situ* method measures the single atom emission from the individual atoms. In contrast to RABITT, the *initial* shape of the attosecond pulses, before propagation and filtering, is now measured [Fig. 1]. This is important for applications that are conducted in the generation process itself, e.g., the tomography of electronic orbitals [9]. The presence of a weak second harmonic (blue) field in the generation chamber leads to the generation of even harmonics as shown in Fig. 2(b) [10]. The harmonic generation process is nonlinear beyond the perturbative regime, which results in comparable probabilities for the processes shown in Fig. 2(b) even though the number of ir photons absorbed differs by 4. Information about the initial properties of the attosecond pulse is obtained by studying the intensity oscillations of the even harmonics with respect to the phase between the ir and the blue field.

In this paper we present a detailed theoretical and experimental comparison between the two characterization methods. Implementing both schemes allows us to measure both the initial and final shapes of the attosecond pulses. From these measurements the influence of propagation as well as

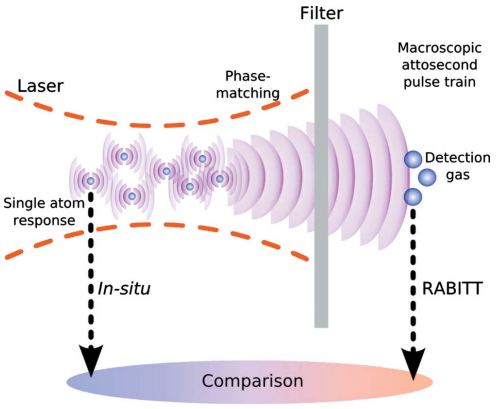

FIG. 1. (Color online) Cartoon illustrating the differences between the two characterization methods. The *in situ* method measures the single atom emission, while the RABITT scheme determines the corresponding attosecond pulses "on target." The influence of phase matching and filtering on the attosecond pulses can be deduced through the implementation of both methods on the same HHG setup.

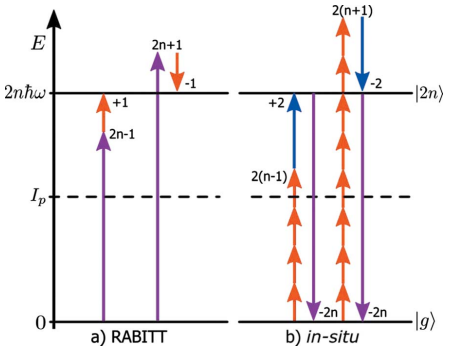

FIG. 2. (Color online) Energy diagrams associated with the two characterization methods. (a) Sidebands are created through the absorption and emission of an ir photon (ω_R) in the RABITT method. (b) Even harmonics are produced in the *in situ* method due to the presence of a weak blue field ($2\omega_R$). Attosecond pulses are characterized by studying the interferences arising from the degenerate ways of reaching the sidebands or even harmonics.

filtering can be determined. The paper is composed as follows: Sec. II reviews the theory of the two characterization methods, Sec. III gives an overview of the experimental setup, Sec. IV presents results from both methods at low gas generation pressure, Sec. V discusses the reasons for the difference observed at higher gas pressures, and Sec. VI summarizes the paper with an outlook.

II. THEORY

The electric field of an attosecond pulse can be written as $\tilde{E}(t)=\tilde{\Lambda}(t)\exp[i\tilde{\phi}(t)]$, where $\tilde{\Lambda}(t)$ and $\tilde{\phi}(t)$ represent the temporal envelope and phase, respectively. It can also be described through its Fourier transform

$$E(\omega)=\Lambda(\omega)\exp[i\phi(\omega)] \tag{1}$$

$$=\int dt\tilde{\Lambda}(t)\exp[i\tilde{\phi}(t)-i\omega t], \tag{2}$$

where $\Lambda(\omega)$ and $\phi(\omega)$ are the spectral envelope and phase. The Fourier integral in Eq. (2) can be approximated using the saddle point method when the linear part in the temporal phase cancels the Fourier component,

$$\left.\frac{d\tilde{\phi}}{dt}\right|_{t=t'(\omega)}-\omega=0, \tag{3}$$

and the quadratic part of the temporal phase is large,

$$\left.\left|\frac{d^2\tilde{\phi}}{dt^2}\right|\right|_{t=t'(\omega)}\gg 0. \tag{4}$$

Note that the temporal phase must be expanded at different times for different Fourier components, i.e., the saddle point time is a function of frequency, $t'(\omega)$. The saddle point approximation yields

$$E(\omega)\approx\left.\sqrt{\frac{2\pi}{\left|\frac{d^2\tilde{\phi}}{dt^2}\right|}}\tilde{\Lambda}(t)\exp\left[i\tilde{\phi}(t)-i\omega t\pm\frac{i\pi}{4}\right]\right|_{t=t'(\omega)}, \tag{5}$$

where the positive (negative) phase factor corresponds to a positive (negative) chirp which is the case for attosecond pulses from the short (long) branch. The spectral phase is approximately equal to

$$\phi(\omega)=\tilde{\phi}(t'(\omega))-\omega t'(\omega)\pm\frac{\pi}{4} \tag{6}$$

and its first derivative is

$$\frac{d\phi}{d\omega}=-t'(\omega), \tag{7}$$

which is obtained using the chain rule and Eq. (3). We can, therefore, interpret the group delay (GD=$-d\phi/d\omega$) as the time when the temporal phase oscillates as ω. A deeper analysis is needed if Eqs. (3) and (4) are not satisfied, which is the case of frequencies above the harmonic cutoff.

We define the relative timing of spectral components (or relative group delay) as

$$t^{(rel)}(\omega,\omega_0)=t'(\omega)-t'(\omega_0)=-\frac{d\phi}{d\omega}+\left.\frac{d\phi}{d\omega}\right|_{\omega_0}, \tag{8}$$

where $t^{(rel)}(\omega,\omega_0)$ is the time it takes for the attosecond pulse to go from oscillating at ω_0 to oscillating at ω. The reference frequency, ω_0, is arbitrarily chosen to be the lowest frequency of the pulse.

In the present work performed with relatively long (multicycle) driving pulses, the emission spectrum contains peaks at harmonic frequencies. In what follows, we use the following notation for the spectral phase $\Phi_n=\phi(n\omega_R)$, where n is the harmonic number and ω_R is the angular frequency of the ir laser field.

A. RABITT

The sidebands that appear in the RABITT method can be understood through the use of second-order perturbation theory [1]: absorption of a high-order harmonic photon followed by absorption or emission of an ir photon. Interferences occur between the different quantum paths that lead to the same sideband [Fig. 2(a)]. If we assume that the competing quantum paths have the same amplitude, then the intensity of the sideband varies as

$$I_{2n}(\varphi)\propto 1+\cos[2\varphi-\Delta\Phi_{2n}-\Delta\Phi_{2n}^{at}], \tag{9}$$

where φ is the phase of the probe field oscillations relative to the attosecond pulses, $\Delta\Phi_{2n}=\Phi_{2n+1}-\Phi_{2n-1}$ is the difference between the phases of the corresponding harmonics, and $\Delta\Phi_{2n}^{at}$ is the difference in atomic phase for the corresponding energies [11]. The atomic phase is neglected in the following because it only has a small effect on the final result in the spectral region that we consider. The first derivative of the

spectral phase can then be determined using the approximate relation

$$\left.\frac{d\phi}{d\omega}\right|_{2n\omega_R} \approx \frac{\Delta\Phi_{2n}}{2\omega_R}. \tag{10}$$

The final shape of an average attosecond pulse in the APT can be reconstructed using Eq. (10) combined with a measurement of the spectrum [12]. The aim of this paper is, however, not to reconstruct attosecond pulses but rather to study how the corresponding relative timing is affected by macroscopic dispersion in the generation cell. Using Eqs. (8)–(10), the relative timing can be written as a function of experimental observables as

$$t_{final}^{(rel)}(\omega,\omega_0) \approx -\frac{1}{\omega_R}[\varphi_{min}(\omega)-\varphi_{min}(\omega_0)], \tag{11}$$

where $\varphi_{min}(\omega)$ is the relative phase between the probe and the APT that minimizes the sideband intensity, $I_{2n}[\varphi_{min}(\omega)]=0$, for $\omega=2n\omega_R$. The subscript final is used to indicate that this is the final state of the pulse as it is detected on target.

B. *In situ*

We will now derive an analog to Eq. (11) for the *in situ* method, where the relative timing of the initial attosecond pulses is determined from the oscillation of the induced even harmonics. Using the strong field approximation (SFA), the Fourier components of the HHG dipole can be approximated as [13]

$$\vec{x}_n \propto \int dt d\tau d^3\vec{p}\, \exp\left[\frac{iS(\vec{p},t,\tau)}{\hbar} - in\omega_R t\right], \tag{12}$$

where $\vec{p}$ is the canonical (drift) momentum, τ is the time between tunneling and recombination, S is the quasiclassical action, and n is the harmonic order. Finding the stationary points of the quasiclassical action and then applying the saddle point approximation five times reduce the integrals in Eq. (12) to a sum of discrete contributions, each corresponding to a quasiclassical trajectory [5,14]. In the limit of a vanishing ionization potential, the quasiclassical trajectories become classical and the quasiclassical action becomes the classical action,

$$S[x(t,t')] = \int_{t-\tau(t)}^{t} dt' \left\{\frac{mv(t,t')^2}{2} + qx(t,t')E(t')\right\}, \tag{13}$$

where x, v, m, and q are the position, velocity, mass, and charge of the electron, respectively. We label the electron trajectories as $x=x(t,t')$, where t is the return time and t' is the integration variable for the action. The electron is released from the atom at time $t-\tau$ and accelerated by the laser field, E, until it returns and recombines with the atom at time t. In the one-color HHG, where $E=E_R=E_{R0}\sin(\omega_R t)$, the process is repeated with an alternating sign every half period, $x_R(t,t')=-x_R(t+T_R/2,t'+T_R/2)$, since $E_R(t')=-E_R(t'+T_R/2)$. The action is, however, the same, $S_R(t)=S_R(t+T_R/2)$.

Adding a weak blue field, $E=E_R+E_B$, $E_B=E_{B0}\sin(2\omega_R t+\varphi)$, induces a small change in the trajectories and the accumulated action. We treat the blue field as a perturbation and expand the trajectory,

$$m\frac{d^2}{dt^2}\sum_{n=0}^{\infty}\lambda^n x^{(n)} = qE_R + \lambda qE_B, \tag{14}$$

where λ is the usual perturbation parameter. The zeroth-order solution is the same as in the one-color case, $x^{(0)}=x_R$, and the first-order solution is purely given by the blue field, $x^{(1)}=x_B$. Higher orders, $n>1$, are equal to zero. We expand the action as $S=S^{(0)}+\lambda S^{(1)}+\lambda^2 S^{(2)}$. The zeroth-order action is the same as in the one-color case, $S^{(0)}=S_R$. The first-order action, $S^{(1)}=\sigma$, is composed of three cross terms that can be rewritten using a few partial integrations,

$$\sigma = \int_{t-\tau}^{t} dt'\{mv_R v_B + qx_R E_B + qx_B E_R\} \tag{15}$$

$$= q\int_{t-\tau}^{t} dt' x_R E_B, \tag{16}$$

where the following boundary conditions are used: $x_R(t,t)=x_R(t,t-\tau)=v_R(t,t-\tau)=x_B(t,t)=0$. It is interesting to note that σ can be written as an integral over the unperturbed trajectory, x_R, and the blue field (or as an integral over the trajectory perturbation, x_B, and the red field). Unlike S_R, the first-order action changes sign between opposite half cycles of the ir field, $\sigma(t)=-\sigma(t+T_R/2)$, which reflects the fact that the electron is now moving differently in the two half cycles, $x(t,t')\neq -x(t+T_R/2,t'+T_R/2)$. The second order action is given purely by the blue field, $S^{(2)}=S_B$, and it has, therefore, the same sign in opposite half cycles of the ir. The sum of the contributions from the zeroth and the second order is labeled as $\Sigma=S^{(0)}+S^{(2)}$.

The integrals of Eq. (12) are evaluated for the two-color case using the saddle point solutions for the ir field only, i.e., we assume that σ and S_B are slowly varying compared to S_R. Only the two stationary points corresponding to the short branch of trajectories in two neighboring half cycles of the fundamental are used, in accordance with the experiment where the long branch has been removed using spatial filtering in a narrow aperture. The contributions from the first-order action can be combined using Euler's formula. The HHG dipole takes the following form for the odd harmonics:

$$\vec{x}_{n=2N+1} \propto \cos\left[\frac{\sigma_n}{\hbar}\right]\exp\left[\frac{i\Sigma_n}{\hbar} - in\omega_R t_n\right], \tag{17}$$

where the first-order change in action, σ_n, leads to a change in dipole amplitude. In the limit of a vanishing blue field, we recover the one-color case: $\cos(\sigma_n/\hbar)\to 1$ and $\Sigma_n \to S_{Rn}$. The HHG dipole for the even harmonics takes the following form:

$$\vec{x}_{n=2N} \propto \sin\left[\frac{\sigma_n}{\hbar}\right]\exp\left[\frac{i\Sigma_n}{\hbar} - in\omega_R t_n\right], \tag{18}$$

where the amplitude again is dependent on the change in action. The even harmonics vanish if there is no blue field since $\sin(\sigma_n/\hbar)\to 0$. The intensities of the odd and even har-

monics vary out of phase: the odd harmonics decrease when the even harmonics increase. A weak blue field implies that $\sin(\sigma_n/\hbar) \approx \sigma_n/\hbar$. In this regime the even harmonic amplitudes grow linearly with the applied blue field and oscillate with the relative phase, φ. It is in this regime that an *in situ* measurement can be carried out.

Using Eq. (16), we seek the relative phase, $\varphi_{min}(t)$, that induces no even harmonic amplitude,

$$\sigma(t, \varphi_{min}(t)) = q \int_{t-\tau(t)}^{t} dt' x_R(t,t') E_B(t', \varphi_{min}(t)) = 0, \tag{19}$$

where the return time, $t=t(\omega)$, is a saddle point solution to Eq. (12) and, therefore, a function of frequency [in close analogy with Eqs. (3) and (4)]. We find excellent agreement with the pioneering work of Dudovich *et al.* [8] using unperturbed classical trajectories in Eq. (19). The solution, $\varphi_{min}(t)$, is expanded to first order around the central return time, $t_c = 0.35T_R$,

$$\varphi_{min}(t) - \varphi_{min}(t_c) \approx -(1+\xi)\omega_R(t-t_c), \tag{20}$$

where $\xi \approx -0.06$ is the "systematic scaling difference" between φ_{min} and $\omega_R t$. Our numerical linearization of $\varphi_{min}(t)$ in Eq. (20) depends on the choice of t_c: ξ varies from 0.1 (in the shortest return) to 0 (in the cutoff regime). It is, however, the scaling around the central return time (central frequency) that is most appropriate for calculating the initial properties of the entire attosecond pulse. Using Eqs. (8) and (20), we find the following simple relation between the oscillations in the even harmonics and the relative emission time from the atom:

$$t_{initial}^{(rel)}(\omega, \omega_c) \approx -\frac{\gamma}{\omega_R}[\varphi_{min}(t(\omega)) - \varphi_{min}(t(\omega_c))], \tag{21}$$

where $\gamma = 1/(1+\xi) \approx 1.06$ is a correction factor. Equation (21) resembles Eq. (11) from the RABITT section in both form and interpretation. The even harmonic oscillations are mapping out the relative emission times from the atom much like the sidebands in a RABITT scan map out the relative arrival times on target. In contrast to RABITT, the *in situ* method needs a correction factor, γ, which is slightly larger than one for the short branch of trajectories. The validity of Eq. (21) is limited to the high-order harmonic plateau where the constant amplitude approximation [Eq. (12)] and the linearization of $\varphi_{min}(t)$ [Eq. (20)] are sound. The *in situ* method can also be applied to the second (long) branch of trajectories. The correction factor for the long branch is $\gamma \approx 0.88$ for $t_c = 0.55T_R$.

We want to stress that the *in situ* method is *not* a direct measure of the emission time (or the group delay) because $\varphi_{min}(t)$ is not related to the return time in a trivial way [Eq. (19)]. In fact, one could also interpret the *in situ* method as a measurement of the continuum time which is an equally good parameter of the process.

All technical details aside, we have found that the *in situ* method produces traces of oscillating even harmonics which, to reasonable agreement, can be treated as RABITT scans. In the following, we will present data which are uncorrected,

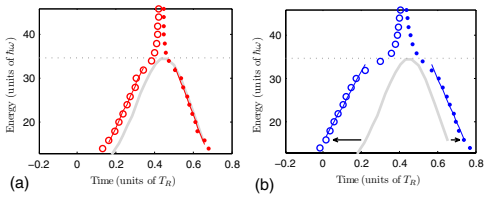

FIG. 3. (Color online) (a) The single atom response of the short (○) and the long (●) branches are calculated using SFA for a typical ir intensity, $I_R = 2\times10^{14}$ W/cm^2. The group delays, $-d\phi/d\omega$, of both branches are in good agreement with the simple classical model (gray line). The group delay branches merge beyond the cutoff (dotted line). (b) The numerical *in situ* scans generated using SFA with a weak blue field, $I_B/I_R = 0.1\%$, show qualitative agreement for both the short (○) and the long (●) branches with the simple classical model (gray line).

$\gamma = 1$, verifying numerically and experimentally the validity of $\gamma \approx 1$ for harmonics in the plateau. Unlike RABITT, the *in situ* method is not limited to sampling the relative timing at only even harmonic energies. The oscillations in the odd harmonic energies [Eq. (17)] can be treated in a similar way, thus doubling the number of sampling points for the relative timing compared to RABITT.

C. Numerical SFA calculation

We perform a numerical experiment using SFA to verify the analytical work presented in Sec. II B for an ir intensity of $I_R = 2\times10^{14}$ W/cm^2. Our numerical calculations are based on Eq. (13) in [5] where the saddle point approximation is done only over $\vec{p}$ space. The integration over continuum time, τ, and actual time, t, is done numerically. This allows us, in a simple way, to access either branch of trajectories by numerically restricting the integral over the continuum time, τ. We calculate the single atom response for the short branch of trajectories by restricting the continuum time integral to $0 < \tau < 0.65T_R$. Then we calculate the response from the long branch of trajectories by restricting the continuum time integral to $0.65T_R < \tau < T_R$. The corresponding group delays are calculated numerically from the first derivative of the spectral phase of the short branch dipole [Fig. 3(a), ○] and the long branch dipole [Fig. 3(a), ●]. The time-energy curves are compared to a simple classical model [Fig. 3(a), gray line], consisting in finding the classical kinetic return energy for a classical electron in a sinusoidal electric field, $E(t) = E_0 \sin \omega t$, which starts and returns to the origin, and then adding the ionization energy.

Next, we perform the numerical *in situ* measurement by calculating the single atom response from the same ir field plus a weak blue field with a relative intensity of $I_B/I_R = 0.1\%$. The phase of the blue field, φ, is then shifted relative to the ir and the atomic response is calculated again. As expected, we obtain weak oscillations in the even harmonics which vary with respect to φ. The relative phases, φ_{min}, that minimize the even harmonic signal are extracted from the short branch [Fig. 3(b), ○] and the long branch [Fig. 3(b),

●]. We find that the *in situ* method produces time-energy slopes [lines in Fig. 3(b)] that are in qualitative agreement with the simple classical model [Fig. 3(b), gray line] for harmonics below the cutoff [Fig. 3(b), dotted line]. There is, however, an absolute time difference between $-\varphi_{min}/\omega_R$, and the (unshifted) simple classical model [Fig. 3(b), gray line]. A careful study of the numerical experiment indicates that the *in situ* measurement suffers from a small systematic deviations from the group delay which can be attributed to the correction factor, γ. We stress that all data presented in Fig. 3(b) are uncorrected, i.e., $\gamma=1$.

A larger and possibly more interesting systematic deviation between the group delay and the *in situ* method arises for harmonics close to and beyond the cutoff [Figs. 3(a) and 3(b), dotted line]. This deviation occurs in a spectral region where Eqs. (3) and (4) are questionable and it is, therefore, more difficult to interpret the deviation. It is clear, however, that the *in situ* measurement is not a direct measurement of the group delay (or the relative timing) of the attosecond pulses and that a deeper analysis is needed for understanding the behavior beyond the cutoff.

The numerical experiment is repeated at progressively higher relative intensities to investigate the robustness of the *in situ* method. We observe the depletion of the odd harmonics, as expected from Eq. (17). The information retrieved from the even harmonics is intact as long as $I_B/I_R<1\%$ for $I_R=2\times10^{14}$ W/cm^2. Increasing the relative intensity further results in an invalid *in situ* measurement.

III. EXPERIMENTAL SETUP

The experimental work is carried out at the Lund Laser Center (LLC) using a kHz Ti-sapphire chirped pulse amplified laser operating at a wavelength of 800 nm (ir). The pulseenergy is 2 mJ and the pulse length is 35 fs. The APTs are generated by focusing the ir laser pulses into a synchronized pulsed argon gas cell [15]. Having a pulsed gas cell allows us to maintain a low average background pressure in the generation chamber while the effective gas pressure in the gas cell is high. We do not measure the instantaneous generation pressure in the gas cell but it is reasonable to assume that it scales with the average background pressure in the generation chamber.

We use aluminum filters after the HHG to

(i) remove the remaining ir and the low-order harmonics in the pump line and

(ii) compress the pulses in the APT.

Eliminating the intense ir beam after the generation cell is important since neither of the characterization schemes work if there is a strong ir field present in the detection process. The individual filters are 200 nm thick and the number of filters used can be changed using a motorized filter holder [6]. Being able to change the number of filters is important in order to access the effect of filters on the attosecond pulses [3]. The attosecond pulses are finally detected using a magnetic bottle electron spectrometer (MBES). The detection gas is argon which allows us to study the high-order harmonics from the plateau and cutoff regions.

In the RABITT method the ionization step in the MBES is perturbed by a synchronized weak ir probe field, which is coupled into the MBES using a Mach-Zehnder interferometer [Fig. 4(a)]. The relative phase, φ, between the APT and the ir is controlled using a piezoelectric translation stage in the interferometer. A typical RABITT scan is shown in Fig. 4(b).

In the *in situ* method the ir pulse is used to generate a second harmonic field (blue) with a 1.3-mm-thick potassium dideuterium phosphate (KDP) type-I crystal. The ir and the blue field are synchronized before the generation chamber using a three-dimensional dichroic interferometer [Fig. 4(c)]. A glass plate in the interferometer enables control of the relative phase, φ, between the ir and the blue fields. The interferometer is engineered so that the polarizations of the recombined red and blue fields are parallel [16]. A typical *in situ* scan is shown in Fig. 4(d). Using Eqs. (11) and (21), we know that the information about the attosecond pulses is derived in the same way from both methods, while the physical interpretation of the two measurements differs.

IV. PROOF OF PRINCIPLE FOR *IN SITU* MEASUREMENTS

In this section, we study the properties of an APT using both the RABITT and the *in situ* method. A direct comparison of the two measurements is not meaningful since attosecond pulses are probed at different times. Two main effects influence the properties of the attosecond pulses:

(i) dispersion from the Al filters;

(ii) phase matching in the generation cell.

To avoid effects due to phase matching as much as possible [2,17], we perform the measurement at the lowest possible pressure, corresponding to a background pressure of $P_G\approx1.5$ μbar. At this pressure, the high-order harmonic signal is weak but still stable enough for both characterization methods to work. The results from the RABITT method are shown in Fig. 5(a) and the results from the *in situ* method are shown in Fig. 5(b).

The change in relative timing induced to an attosecond pulse propagating through one aluminum filter, $\Delta t_{\mathrm{Al}}^{(rel)}(\omega,\omega_0)$, can be determined using two RABITT measurements,

$$\Delta t_{\mathrm{Al}}^{(rel)}(\omega)=t_{final_2}^{(rel)}(\omega)-t_{final_1}^{(rel)}(\omega), \tag{22}$$

where $t_{final_1}^{(rel)}$ is the relative timing of the attosecond pulse having passed one filter and $t_{final_2}^{(rel)}$ is the relative timing after passing two filters. Note that we now drop the notation for the reference frequency since it is $\omega_0=14\omega_R$ for all experimental data. We have verified that $\Delta t_{\mathrm{Al}}^{(rel)}(\omega)$ agrees with the GD deduced from the refractive index of aluminum [18]. Assuming that the two filters are identical we can calculate the relative timing of the attosecond pulse before passing the filter(s),

$$t_{final_0}^{(rel)}(\omega)=t_{final_1}^{(rel)}(\omega)-\Delta t_{\mathrm{Al}}^{(rel)}(\omega). \tag{23}$$

The "unfiltered" relative timing of attosecond pulses [Fig. 5(a), ○] is in good agreement with the simple classical model (gray line) for an effective intensity of $I_R\approx1$

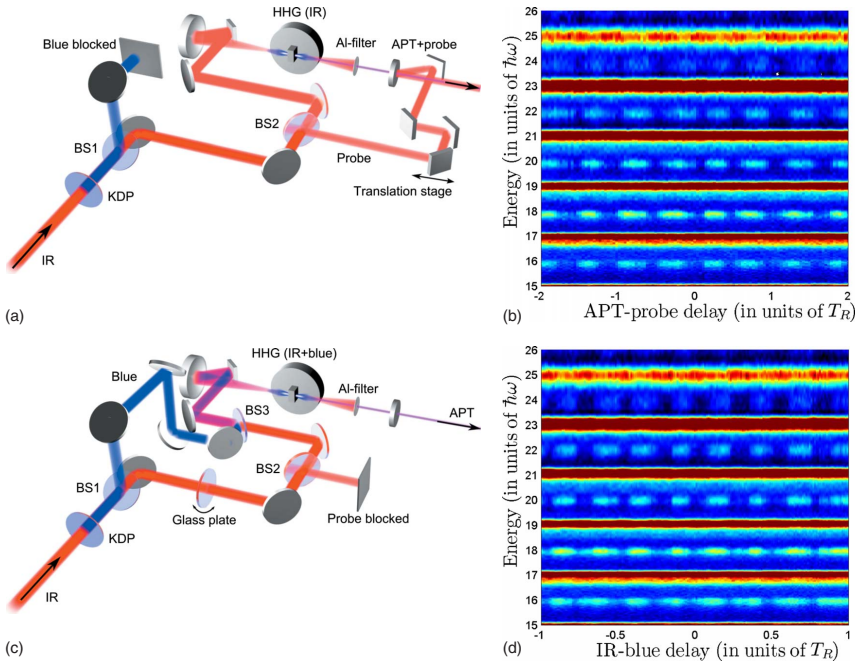

FIG. 4. (Color online) (a) In RABITT mode the blue field (from KPD) is split off (BS1) and blocked. A weak ir probe field is created (BS2) and delayed on the subcycle scale using a translation stage. The APT is generated from the intense ir pulses [HHG (ir)] in a synchronized pulsed gas cell. The intense ir field is eliminated using aluminum filter(s). The APT and the probe are recombined (APT +probe) using a mirror with a narrow aperture. The APT passes through the aperture while the probe is reflected on the mirror. The temporally overlapping APT and probe field are then focused using a toroidal mirror and detected using an electron spectrometer (not shown). (b) The RABITT scan is recorded using an electron spectrometer with subcycle synchronization of the APT and the probe in the detection chamber. (c) In *in situ* mode the ir and the blue field (from KDP) are separated (BS1) into a dichroic interferometer. The ir field is delayed on the subcycle scale using a glass plate (which can be tilted) before it is recombined with the blue field (BS3). The probe is blocked (after BS2). The APT is generated from intense ir pulses in the presence of a weak blue field [HHG (ir+blue)] in a synchronized pulsed gas cell. The ir and blue fields are eliminated using aluminum filter(s). The APT is detected using an electron spectrometer (not shown) after passing a narrow aperture. (d) The *in situ* scan is recorded using an electron spectrometer with subcycle synchronization of the ir and the blue fields in the generation cell [HHG (ir+blue)]. The color scale in (b) and (d) is saturated so that the interferometric beating is more clearly seen.

$\times 10^{14}$ W/cm^2. This intensity corresponds to a cutoff at harmonic (23), which agrees well with spectral measurements taken without the probe field present.

Having estimated the initial state of the attosecond pulses using the RABITT method, we now proceed with the *in situ* scheme. One important advantage of the *in situ* scheme is that all information is imprinted spectrally, which makes it possible to analyze attosecond processes with great accuracy using a photon spectrometer rather than an electron spectrometer. In this paper, however, we use the same MBES as for the RABITT so that a straightforward comparison of the two schemes is made.

The *in situ* measurements are taken immediately after their respective RABITT measurements for one and two aluminum filters [Fig. 5(b)]. The HHG conditions, therefore, have little time to evolve when changing schemes (a few seconds). The filters should not influence the *in situ* measurement because the information is imprinted spectrally already in the HHG process. Using the *in situ* scheme, we should ideally obtain identical information regardless of the number of filters. The measurements again nicely follow the classical model for $I=1\times10^{14}$ W/cm^2 (gray curve). We determine the initial relative timing, $t^{(rel)}_{initial}(\omega)$, and compare it to the relative timing obtained with the RABITT method, $t^{(rel)}_{final_0}(\omega)$, in Fig. 5(c). The corresponding group delay dispersion (GDD) is calculated by fitting a line to the relative timing using sidebands and even harmonics (14)–(22),

$$-\left.\frac{d^2\phi}{d\omega^2}\right|_{18\omega_R} \approx \begin{cases} 2.31\times10^4 \text{ as}^2/\text{rad} & \text{(RABITT)} \\ \gamma\times 2.24\times10^4 \text{ as}^2/\text{rad} & (\textit{in situ}), \end{cases} \tag{24}$$

with a root mean square deviation of approximately 23 as for

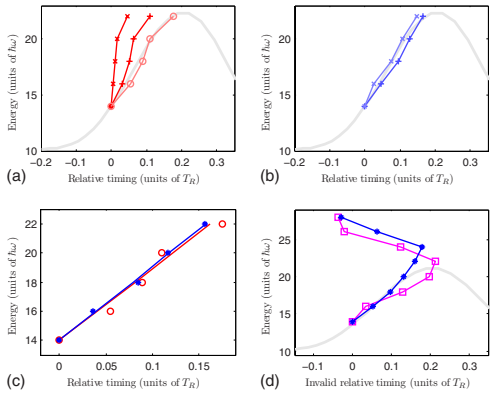

FIG. 5. (Color online) (a) RABITT measurements with one (+) and two (×) aluminum filters are used to determine the relative timing of the unfiltered attosecond pulses (○). All temporal measurements are presented as relative timings with reference to harmonic (14). (b) *In situ* measurements with one (+) and two (×) aluminum filters. The data are uncorrected, $\gamma=1$. The simple classical model ($I_R=1\times10^{14}$ W/cm^2) [(a) and (b) gray curve] is plotted for reference. (c) Unfiltered RABITT measurement (red, ○) compared to the average *in situ* measurement (blue, *). (d) A slight increase in the blue intensity (blue, *) has a small effect on the measurement in the harmonic plateau [harmonics (14)–(24). Increasing the blue intensity further (pink, □) results in an invalid measurement. The simple classical model ($I_R=0.9\times10^{14}$ W/cm^2) (gray line) is plotted for reference.

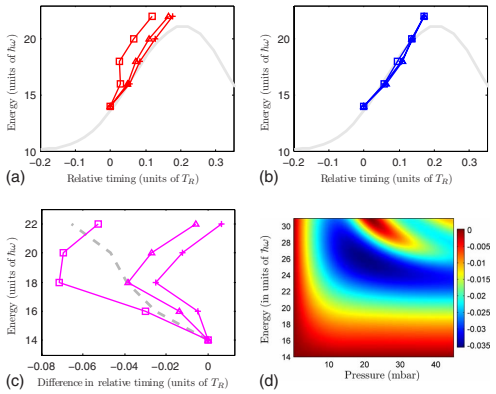

FIG. 6. (Color online) (a) Relative timing measurements from RABITT for a variety of high background pressures in the generation chamber: 5×10^{-3} (×), 6×10^{-3} (△), and 7×10^{-3} (□) mbar (the exact instantaneous pressure in the gas cell is unknown). The effect of the Al filter has been subtracted. At high pressures there is an increased deviation from the simple classical model ($I_R=0.9\times10^{14}$ W/cm^2) (gray curve). (b) The corresponding *in situ* measurements are mostly unaffected by the increased pressure. The data are not corrected, $\gamma=1$. (c) The difference in relative timing, $\Delta t_{macro}^{(rel)}(\omega,P_G)$ (pink ×, △, and □), is interpreted as the macroscopic delay due to phase matching in the gas cell. The symbols correspond to the same pressures as in the figures above. The delay from phase matching has approximately the same magnitude as an aluminum filter (gray dashed curve). (d) The relative timing due to phase matching (false color in units of T_R) is calculated using a one-dimensional model [17] for pressures ranging from 0 to 100 mbar. The intensity used in the model is 1.25×10^{14} W/cm^2 and the duration of the pulse is 35 fs. The length of the cell is modeled as 5 mm.

the corresponding difference in relative timing. We treat the *in situ* data as a RABITT scan, and the numerical value of the GDD must, therefore, be multiplied by the correction factor, γ. The experiment shows that the correction factor is close to unity for the short branch, as expected from the theory section. The good agreement between these measurements shows that either the RABITT or the *in situ* method can be used to characterize the APTs at low generation pressures for energies in the central and upper regions of the harmonic plateau.

It is tempting to increase the intensity of the blue field so that the even harmonics become stronger and more visible. We use an adjustable aperture in the blue arm of the three-dimensional dichroic interferometer so that the intensity of the blue field can be increased while all other experimental parameters are constant. It has been demonstrated that an increased blue intensity will alter the quasiclassical trajectories in the HHG process [19,20], but a systematic study of how the *in situ* method breaks down has not yet been reported. Even harmonic oscillations appear *beyond the cutoff* for a slight increase in the blue intensity. The information extracted from these oscillations show strong deviations with the expected group delays, while the information from the plateau region remains rather accurate [Fig. 5(d), *]. Even harmonic oscillation beyond the cutoff regime should, therefore, not be included in our simple interpretation [Eq. (21)] of the *in situ* method. The experimental results at high photon energy are in qualitative agreement with the numerical calculations of the long branch shown in Fig. 3(b) shifted by half their period. At moderately higher blue intensities we observe a shift of the modulations in the plateau [Fig. 5(d), □]. This shows that the *in situ* method now predicts the wrong relative timing for the initial attosecond pulses also in the plateau region and that the relative intensity must be reduced.

V. COMPARISON OF RABITT AND *IN SITU* MEASUREMENTS AT HIGHER PRESSURE

We now study how the phase of the attosecond pulses is modified due to a higher gas pressure in the generation chamber. It has recently been shown that in some conditions an increasing gas pressure can lead to a compression of the attosecond pulses [17]. The effect predicted theoretically was, however, small and difficult to demonstrate experimentally. Here, combined measurements using the RABITT and the *in situ* method allow us to unambiguously extract the contribution of phase matching to the temporal structure of attosecond pulses.

RABITT results obtained at different pressures are shown in Fig. 6(a). The data are collected with one aluminum filter,

but the effect of this filter is removed using Eq. (23). The corresponding *in situ* measurements are shown in Fig. 6(b). The *in situ* measurements are mostly insensitive to the increased gas pressure, while the RABITT measurements are deformed in a nontrivial way. Deviations in relative timing for attosecond pulses due to the macroscopic propagation through the gas cell can be extracted by subtracting the final and initial relative timings,

$$\Delta t^{(rel)}_{macro}(\omega, P_G) = t^{(rel)}_{final_0}(\omega, P_G) - t^{(rel)}_{initial}(\omega, P_G), \quad (25)$$

where we have explicitly written P_G to indicate that the macroscopic effects depend on the gas pressure. In $t^{(rel)}_{initial}(\omega, P_G)$, the P_G dependence refers to a possible change in the fundamental field in the nonlinear medium that could affect the single atom response. The results are shown in Fig. 6(c), together with the effect of a 200 nm Al filter (gray). Macroscopic effects introduce a (nontrivial) negative relative timing, first decreasing then increasing with frequency. The corresponding induced GDD might help to compensate for the single atom GDD for low orders, but for higher orders the GDD is increased. These results agree well with those presented in [17].

To understand the origin of the macroscopic group delay, we perform a simple model calculation [17,21]. We consider for simplicity a one-dimensional approximation along the propagation axis z, a homogeneous medium of length L, and a collimated geometry. In this simple case, the contribution of the single atom response and of propagation can be separated and the effect of propagation both on the phase (or more exactly phase variation) and amplitude of the nth harmonic can be described by

$$F_n = \frac{1 - \exp[(-i\Delta k_n - \kappa_n)L]}{i\Delta k_n + \kappa_n} = |F_n| \exp[i\phi_n^{mac}]. \quad (26)$$

The phase mismatch Δk_n is equal to $k_n - nk_1$, where k_n and k_1 denote the wave vector of harmonic n and the fundamental, respectively. Absorption at the nth harmonic frequency is described by κ_n. The macroscopic phase can be written as

$$\phi_n^{mac} = -\arctan\left[\frac{\sin[\Delta k_n L]}{\cos[\Delta k_n L] - \exp[\kappa_n L]}\right] - \arctan\left[\frac{\Delta k_n}{\kappa_n}\right]. \quad (27)$$

Figure 6(d) presents in color its derivative as a function of harmonic order and pressure. These results show a variation in the phase derivative that qualitatively agrees with the measured one. For a given pressure >20 mbar, the induced GD is negative, showing a decrease at low orders, a minimum around the 23rd harmonic, followed by an increase. We stress that this satisfactory agreement is obtained with a simple model, not including the geometric phase due to focusing or two-dimensional effects. Combined RABITT and *in situ* measurements provide a way to really unravel the effect of propagation in the generation of attosecond pulses.

VI. CONCLUSIONS

We have performed a proof of principle experiment for the *in situ* scheme by comparing it to the well established RABITT method. We have found excellent agreement between the methods at low generation gas pressures when the macroscopic phase matching plays a negligible role.

We have found that it is not possible to use the *in situ* scheme to predict the final relative timing of the average attosecond pulses if the generation pressure is high or if it passes through some unknown dispersive material. It is equally important to realize that accurate single atom measurements cannot be conducted at high generation gas pressures with the RABITT scheme. In a RABITT measurement there will always be a trade off between the number of harmonic photons generated and their phase perturbation from propagation through the generation cell.

The advantages and disadvantages of the two schemes become quite clear when the generation pressure is high and one could argue that *both* schemes are needed for a more complete understanding of the attosecond pulse production and propagation.

ACKNOWLEDGMENTS

We thank Lou DiMauro for valuable comments on this work. This research was supported by the Marie Curie programmes (MAXLAS, ATTOCO) of the European Union, the European and Swedish Reseach Councils and the Kunt and Alice Wallenberg Foundation.

[1] P. M. Paul *et al.*, Science **292**, 1689 (2001).
[2] M. B. Gaarde, J. L. Tate, and K. J. Schafer, J. Phys. B **41**, 132001 (2008).
[3] R. López-Martens *et al.*, Phys. Rev. Lett. **94**, 033001 (2005).
[4] Y. Mairesse *et al.*, Science **302**, 1540 (2003).
[5] M. Lewenstein, P. Balcou, M. Y. Ivanov, A. LHuillier, and P. B. Corkum, Phys. Rev. A **49**, 2117 (1994).
[6] E. Gustafsson *et al.*, Opt. Lett. **32**, 1353 (2007).
[7] A.-S. Morlens *et al.*, Opt. Lett. **31**, 1558 (2006).
[8] N. Dudovich *et al.*, Nat. Phys. **2**, 781 (2006).
[9] J. Itatani *et al.*, Nature (London) **432**, 867 (2004).
[10] Even harmonics are not generated if there is no blue field present due to parity conservation.
[11] J. Mauritsson, M. B. Gaarde, and K. J. Schafer, Phys. Rev. A **72**, 013401 (2005).
[12] Except for the carrier envelope phase of the attosecond pulse.
[13] M. Lewenstein, P. Salières, and A. L'Huillier, Phys. Rev. A **52**, 4747 (1995).
[14] P. Salières *et al.*, Science **292**, 902 (2001).
[15] D. Proch and T. Trickl, Rev. Sci. Instrum. **60**, 713 (1989).
[16] J. Mauritsson, J. M. Dahlström, and T. Fordell, J. Phys. B **42**, 134003 (2009).
[17] T. Ruchon *et al.*, New J. Phys. **10**, 025027 (2008).

[18] O. E. Martinez, J. P. Gordon, and R. L. Fork, J. Opt. Soc. Am. B **1**, 1003 (1984).

[19] J. Mauritsson, P. Johnsson, E. Gustafsson, A. LHuillier, K. J. Schafer, and M. B. Gaarde, Phys. Rev. Lett. **97**, 013001 (2006).

[20] E. Mansten *et al.*, New J. Phys. **10**, 083041 (2008).

[21] E. Constant, D. Garzella, P. Breger, E. Mevel, C. Dorrer, C. Le Blanc, F. Salin, and P. Agostini, Phys. Rev. Lett. **82**, 1668 (1999).

Paper VI

Quantum Mechanical Approach to Probing the Birth of Attosecond Pulses using a Two-Color Field

J. M. Dahlström, A. L'Huillier and J. Mauritsson.

J. Phys. B: At. Mol. Opt. Phys. **44**, 095602 (2011).

IOP PUBLISHING JOURNAL OF PHYSICS B: ATOMIC, MOLECULAR AND OPTICAL PHYSICS

J. Phys. B: At. Mol. Opt. Phys. **44** (2011) 095602 (7pp) doi:10.1088/0953-4075/44/9/095602

Quantum mechanical approach to probing the birth of attosecond pulses using a two-colour field

J M Dahlström, A L'Huillier and J Mauritsson

Department of Physics, Lund University, PO Box 118, SE-221 00 Lund, Sweden

E-mail: Anne.LHuillier@fysik.lth.se

Received 9 February 2011, in final form 15 March 2011
Published 21 April 2011
Online at stacks.iop.org/JPhysB/44/095602

Abstract

We investigate the generation of even and odd harmonics using an intense laser and a weak second harmonic field. Our theoretical approach is based on solving the saddle-point equations within the strong field approximation. The phase of the even harmonic oscillation as a function of the delay between the fundamental and second harmonic field is calculated and its variation with energy is found to be in good agreement with recent experimental results. We also find that the relationship between this phase variation and the group delay of the attosecond pulses depends on the intensity and wavelength of the fundamental field as well as the ionization potential of the atom.

(Some figures in this article are in colour only in the electronic version)

1. Introduction

Attosecond pulses [1, 2] are created through the interaction between intense infrared (IR) laser fields and atoms or molecules in a process known as high-order harmonic generation (HHG). This process is initiated by the creation of an electron wave packet through tunnelling ionization, followed by acceleration in the laser field and recombination with the ion core resulting in extreme ultraviolet (XUV) emission confined to a fraction of the laser cycle. The generation process can be controlled by shaping the driving laser field, e.g. by coherently adding laser fields of different wavelengths to the fundamental laser field [3–6]. Most investigations have been carried out by adding the second harmonic generated in a doubling crystal [7–14], with various goals ranging from optimization of the conversion efficiency, characterization of the emitted attosecond pulses and production of attosecond pulse trains with one pulse per cycle of the fundamental field. Several parameters can be varied in these experiments: the intensity ratio, the phase difference and the relative polarization direction.

When the second harmonic field is a weak perturbation to the fundamental, the generation of odd harmonics is barely changed, but the induced symmetry breaking leads to the appearance of weak even harmonics. High-order harmonic spectra recorded as a function of delay between the two fields show that the intensity of the even harmonics is modulated and that this modulation has an offset depending on the harmonic order, as shown in figure 1(a) [13]. These photon spectrograms are at a first glance similar to the photoelectron spectrograms of the RABITT (reconstruction of attosecond beating by interference of two-photon transitions) method [1] used to characterize attosecond pulses. Dudovich *et al* [16] suggested that the two-colour HHG spectrograms could be used to determine the emission times of the attosecond pulses *in situ*, thus 'probing the birth of attosecond pulses'. This method was then applied by Doumy *et al* [17], using laser systems of different wavelengths, and by us [18], in a direct experimental comparison with the RABITT method.

In this paper we investigate HHG by a laser field and its second harmonic by solving the Schrödinger equation within the strong field approximation (SFA), using the saddle-point equation method [20]. We assume throughout that the second harmonic is weak and can be considered as a small perturbation to the fundamental field. We calculate the phase variation of the even harmonic oscillation and compare it with the harmonic emission times. Our model also allows us to interpret the rapid variation of this phase at high energy, observed in several experiments [13, 18], as a change of the dominant quasiclassical trajectory from the short to the long

J. Phys. B: At. Mol. Opt. Phys. **44** (2011) 095602 J M Dahlström *et al*

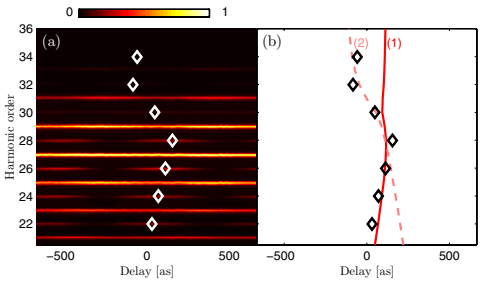

Figure 1. (a) Experimental two-colour high-order harmonic spectrogram over relative delay [13]. The diamonds (⋄) indicate the experimental delays corresponding to maxima of the modulation in the even harmonic orders. (b) Calculated delays corresponding to maxima of the even orders for an effective intensity of 1.4×10^{14} W cm^{-2}. The full (dashed) curve is calculated for the short (long) branch labelled 1 (2). Below (above) harmonic order 28, the short (long) branch fits the experimental data (⋄).

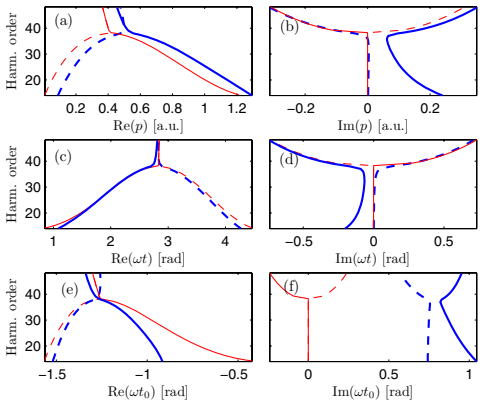

Figure 2. Real and imaginary parts of the stationary points, $[p, t, t_0]$. Ionization potentials: argon $I_p^{(Ar)} = 15.76$ eV (thick blue) and classical $I_p^{(0)} = 0$ eV (thin red). The classical case is shifted by $1.3I_p$ to match the quantum mechanical cutoff. The short branch is a line; while the long branch is a dashed line. The intensity is 2×10^{14} W cm^{-2} and the wavelength is 800 nm.

one (figure 1(b)). The paper is organized as follows. In section 2 we review and compare classical and quasiclassical electron trajectories for one-colour (section 2.1) and two-colour HHG (section 2.2). In section 3 we study the generation of even harmonics close to the cutoff (section 3.1) and we relate the phase of the even harmonic oscillation to the emission times of the attosecond pulses (section 3.2). In section 4 we summarize our results by presenting a more general relationship between the phase of the even harmonic oscillation and the emission times.

2. Quasiclassical trajectories

Our method is based on the stationary phase method (also referred to as the saddle-point method) to solve the Schrödinger equation for an atom exposed to a strong laser field using the SFA [19]. In particular, we consider the interaction of an atom with a strong IR laser field (frequency ω) and a weak second harmonic (frequency 2ω). In the SFA, the electron will (i) tunnel into the continuum, (ii) accelerate in the strong laser field and then (iii) return to the atom and emit a harmonic photon (frequency Ω). The phase of the harmonic radiation is related to the quasiclassical action of the electron

$$S(\vec{p}, t, t_0) = \int_{t_0}^{t} \mathrm{d}t' \left(\frac{(\vec{p} - e\vec{A}(t'))^2}{2m} + I_p \right), \tag{1}$$

where $\vec{A}(t)$ is the vector potential of the laser field, I_p is the ionization potential of the atom, and $\vec{p}$, t_0, t, m and e are the drift momentum, tunnelling time, return time, mass and charge of the electron, respectively. The high-order harmonic emission will mainly originate from the stationary points of S–$\hbar\Omega t$, with respect to all variables $[\vec{p}, t, t_0]$, which satisfy the following three equations [19]:

$$\int_{t_0}^{t} \mathrm{d}t' e\vec{A}(t') = (t - t_0)\vec{p}, \tag{2}$$

$$\frac{(\vec{p} - e\vec{A}(t_0))^2}{2m} = -I_p, \tag{3}$$

$$\frac{(\vec{p} - e\vec{A}(t))^2}{2m} = \hbar\Omega - I_p. \tag{4}$$

The electron is thus required to return to the atom at time t (equation (2)), to undergo complex tunnelling at time t_0 (equation (3)) and to satisfy energy conservation (equation (4)). For any realistic atom, we have $I_p > 0$ which implies that the electron must tunnel into the continuum. The tunnelling process results in damping of the electron trajectories, i.e. complex stationary points in the harmonic plateau [20]. The electron trajectories beyond the cutoff are always strongly damped (also for $I_p = 0$), because they are always classically forbidden, corresponding to large imaginary components of the stationary points. The physical emission time of a given harmonic is given by the real part of the complex emission time [15, 21, 22].

2.1. One-colour case

We first consider the one-colour case with a vector potential, $\vec{A}(t) = \vec{A}_1 \sin(\omega t)$, where ω is the angular frequency of the fundamental laser light. The complex stationary points $\left[\vec{p}^{(n)}, t^{(n)}, t_0^{(n)}\right]$ are calculated as a function of the high-order harmonic photon angular frequency, Ω. The index n is used to separate different sets of solutions, where $n = 1$ corresponds to the short branch and $n = 2$ corresponds to the long branch. A direct comparison between the stationary points for $I_p = 15.76$ eV (Ar) and $I_p = 0$ eV (referred to as the classical case) is shown in figure 2. The detailed behaviour of these stationary points will prove to be important not only for the generation of attosecond pulses

from one-colour HHG but also in the quantitative analysis of two-colour HHG. The classical case corresponds to solving equations (2)–(4) for $I_p = 0$. The stationary points are first real, describing classical trajectories in the continuum. Using classical trajectories to explain the HHG process leads to the approximate cutoff law: $\hbar\Omega_{\max} \approx 3.2U_p + I_p$ [23, 24]. Harmonics above this cutoff cannot be generated because there are no electrons returning with sufficient kinetic energy. Quantum mechanically, we see that the stationary points quickly develop large imaginary components above the cutoff, which result in an exponential damping of the harmonic yield. Solving equations (2)–(4) for $I_p \neq 0$, the exact cutoff law is found to be $\hbar\Omega_{\max} = 1.3I_p + 3.2U_p$ [19]. In figure 2 we have, therefore, shifted the classical solutions by $1.3I_p$ so that the cutoff harmonic of the classical case coincides with the quantum mechanical case of argon for a more meaningful comparison. The similarities and differences between the classical case (red line) and the quantum case (blue line) are clearly observed. The real parts of the drift momenta (figure 2(a)) are almost the same in the two cases, apart from a small systematic shift. The real parts of the return times (figure 2(c)) overlap almost perfectly in the main part of the plateau for both the short (line) and long (dashed) branches. This demonstrates the usefulness of the classical model for understanding the intrinsic chirp of the returning electron wave packet and the resulting chirp of the attosecond light pulses. The real parts of the tunnelling times (figure 2(e)) are, however, quite different. In the lower part of the plateau there is a discrepancy of a factor of 2 for the short branch. The short branch trajectories tunnel at earlier times compared to the classical case due to the ionization potential. This implies longer times in the continuum and an increased amount of phase acquired, as the path of integration extends in equation (1). For the long branch the trend is opposite and smaller. The imaginary parts of the stationary points (figures 2(b), (d), (f)) lead to exponential damping of the electron amplitudes. This is especially clear for the imaginary part of the tunnelling time (figure 2(f)) where the complex part is zero in the classical case where no tunnelling is required; while, in the complex case, the short branch will suffer more damping than the long branch due to a lower instantaneous electric field strength at the time of tunnelling.

The high-order harmonic dipole from one-*half* period of the laser field can be approximated as a sum of stationary contributions

$$\vec{x}_\Omega = \int \mathrm{d}^3p \int_0^{T/2} \mathrm{d}t \int_{-\infty}^{t} \mathrm{d}t_0 \Lambda \exp[\mathrm{i}S(\vec{p}, t, t_0)/\hbar - \mathrm{i}\Omega t] \approx \sum_{n=1,2} \vec{x}_\Omega^{(n)}. \quad (5)$$

These discrete contributions correspond to different sets of stationary phase solutions

$$\vec{x}_\Omega^{(n)} = \Lambda^{(n)} \left(\frac{\mathrm{i}h^5}{\det\left[M_{ij}^{(n)}\right]} \right)^{1/2} J \exp[\mathrm{i}S^{(n)}/\hbar - \mathrm{i}\Omega t^{(n)}], \quad (6)$$

where $S^{(n)} = S\left(\vec{p}^{(n)}, t^{(n)}, t_0^{(n)}\right)$ and where

$$M_{ij} = \frac{\partial^2}{\partial i \partial j}[S(\vec{p}, t, t_0) - \hbar\Omega t] \quad (7)$$

is the Hessian matrix of second-order derivatives of the Legendre transformed action with i and j being any of our variables $[\vec{p}, t, t_0]$. The Hessian matrix is complex symmetric and we have assumed that it can be diagonalized so that the one-dimensional stationary phase approximation can be applied to all five integrals independently. The prefactor $\Lambda = d(\vec{p} - e\vec{A}(t))^* E(t_0) d(\vec{p} - e\vec{A}(t_0))$ describes the dipole transitions to the continuum at time t_0, and the subsequent recombination to the ground state at time t. In the following, we will assume that Λ is slowly varying and that it, therefore, does not affect the stationary points. A more exact analysis could, however, also include the effect of the energy-dependent atomic scattering phases, η_l, in the stationary phase equations (equations (2)–(4)) (from the recombination matrix element $d(\vec{p} - e\vec{A}(t))^* \propto \exp[-\mathrm{i}\eta_l]$). This would lead to a small change in the stationary points, which would be especially interesting to study in argon due to an unusually strong variation of the scattering phase in the present energy region [25, 26].

Assuming the process to be periodic, the total dipole response, $\vec{X}_\Omega$, is found by summing the stationary points from one *whole* period of the fundamental laser field, $0 < t < T$, i.e. two adjacent half-periods. There are thus two contributions from each branch,

$$\vec{x}_\Omega^{(n)}(t + T/2, t_0 + T/2) = -\vec{x}_\Omega^{(n)}(t, t_0) \exp[-\mathrm{i}\Omega T/2], \quad (8)$$

separated by a half-period, $T/2$. The overall minus sign comes from the change of sign of $E(t)$, while the phase factor originates from the Fourier component in the Legendre transformed action. The total dipole response becomes

$$\vec{X}_\Omega \approx \sum_n \vec{x}_\Omega^{(n)} \{1 - \exp[-\mathrm{i}\Omega T/2]\} = 2\sum_n \vec{x}_\Omega^{(n)} \begin{cases} 1, & \Omega/\omega \text{ is odd} \\ 0, & \Omega/\omega \text{ is even,} \end{cases} \quad (9)$$

where the two contributions add constructively for odd orders and destructively cancel for even orders.

2.2. Two-colour case

We now consider a two-colour laser field composed of a fundamental laser field and a weak second harmonic with the same polarization, $\vec{A}(t) = \vec{A}_1 \sin(\omega t) + \lambda \vec{A}_2 \sin(2\omega t + \phi)$, where λ is a perturbation parameter. It is possible to solve the two-colour high-order harmonic emission using the stationary phase equations (equations (2)–(4)) directly, but this requires evaluation of the system at all values of ϕ. We will follow a different route where the second harmonic is treated as a perturbation and only the stationary points of one-colour HHG need to be calculated. The two-colour action is expanded in λ as

$$S \approx \underbrace{\int_{t_0}^{t} \mathrm{d}t' \left(\frac{[\vec{p} - e\vec{A}_1(t')]^2}{2m} + I_p \right)}_{S_1} \times \underbrace{-\lambda \int_{t_0}^{t} \mathrm{d}t' \frac{[\vec{p} - e\vec{A}_1(t')][e\vec{A}_2(t', \phi)]}{m}}_{\lambda\sigma}. \quad (10)$$

The first term in equation (10) corresponds to the action in the one-colour case, S_1 and the second term is the correction term due to the interaction with the second harmonic field, $\sigma = \sigma(\phi)$. The correction term can be calculated as

$$\sigma = \frac{e}{m}\left[\vec{p}\vec{A}_2\frac{\cos(2\omega t'+\phi)}{2\omega} + e\vec{A}_1\vec{A}_2\left(\frac{\sin(3\omega t'+\phi)}{6\omega} - \frac{\sin(\omega t'+\phi)}{2\omega}\right)\right]_{t_0}^{t}, \tag{11}$$

where σ depends on the ionization potential through the stationary points. Note that the derivation of equation (11) using the quantum mechanical stationary points differs from those presented previously [16, 18], because it includes the effect of the ionization potential within the SFA.

The two-colour high-order harmonic dipole can be calculated by using equation (6) and by adding an additional slow factor due to the second harmonic. In analogy with equation (9), the dipole from one period of the fundamental field contains one discrete contribution for each branch and half-period:

$$\vec{X}_\Omega \approx \sum_n \vec{x}_\Omega^{(n)}\left\{\exp[\mathrm{i}\sigma^{(n)}] - \exp\left[-\mathrm{i}\sigma^{(n)} - \frac{\mathrm{i}\Omega T}{2\hbar}\right]\right\} = 2\sum_n \vec{x}_\Omega^{(n)} \times \begin{cases}\cos[\sigma^{(n)}/\hbar], & \Omega/\omega \text{ is odd}\\ \mathrm{i}\sin[\sigma^{(n)}/\hbar], & \Omega/\omega \text{ is even}\end{cases} \tag{12}$$

where $\vec{x}_\Omega^{(n)}$ is the half-period contribution in the one-colour field, and where the property

$$\sigma^{(n)}(t+T/2, t_0+T/2) = -\sigma^{(n)}(t, t_0) \tag{13}$$

relating the two-colour phase between adjacent half-periods for a given branch n is used. The intensity of the even order harmonic emission from a single atom can be approximated by

$$I_\Omega \propto |\vec{X}_\Omega|^2 \approx \left|2\sum_n \vec{x}_\Omega^{(n)}\mathrm{i}\sigma^{(n)}/\hbar\right|^2, \tag{14}$$

which is valid for $|\sigma^{(n)}| \ll \pi$. We define the intensity from a specific branch, n, as

$$I_\Omega^{(n)}(\phi) \propto |\sigma^{(n)}(\phi)|^2. \tag{15}$$

This (artificial) separation of the branches can be realized in a macroscopic medium either by phase matching in a long gas cell [13] or by spatial separation in the far field [11, 16].

3. Subcycle delay dependence of even harmonics

One fascinating aspect of two-colour HHG is that it depends on the subcycle delay (or relative phase ϕ) between the laser fields. Dudovich *et al* [16] have proposed to use the ϕ-dependence of even-order harmonics in order to estimate the emission times of the attosecond pulses *in situ*. We will refer to the relative phases that maximize the intensity of the even harmonics as the *in situ phases*: $\phi_0^{(1)}(\Omega)$ and $\phi_0^{(2)}(\Omega)$, for the short and long branch, respectively. The *in situ* phases are plotted in figures 3(a) and (d) as a function of harmonic order for argon at two different IR intensities. The corresponding emission times of the high-order harmonics, $\mathrm{Re}\{t^{(n)}(\Omega)\} = t_R^{(n)}(\Omega)$, are shown in figures 3(b) and (e).

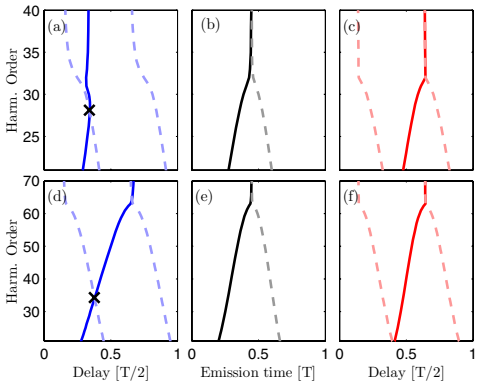

Figure 3. Quantum mechanical *in situ* phases, $\phi_0^{(n)}$, between the fundamental and weak second harmonic field that maximize the even harmonic emission in argon ($I_p^{(Ar)} = 15.75$ eV) for intensities of (a) 1.5×10^{14} W cm^{-2} and (d) $I = 4 \times 10^{14}$ W cm^{-2}. The *in situ* phases are presented as delays $\tau_0^{(n)} = -\phi_0^{(n)}/2\omega$ in units of $T/2$. The corresponding high-order harmonic emission times are shown in (b) and (e), in units of T. Classical *in situ* phases ($I_p^{(0)} = 0$) for intensities of (c) 1.5×10^{14} W cm^{-2} and (f) $I = 4 \times 10^{14}$ W cm^{-2}. The short (long) branch is a full (dashed) curve. $T = 2\pi/\omega$ is the period of the fundamental laser field.

The intensity in (a), (b) is realistic for typical laser pulses of 30 fs in argon, while the intensity in (d), (e) is greater than the saturation intensity and, therefore, not experimentally feasible for multicycle laser pulses. The aim of our analysis is to distinguish between what can be measured experimentally, $\phi_0^{(n)}(\Omega)$, and the desired emission times, $t_R^{(n)}(\Omega)$. The *in situ* phases from the classical model ($I_p = 0$) are plotted in figures 3(c) and (f) for comparison.

3.1. Behaviour close to cutoff

The similarity between the *in situ* phases and the emission times is striking, especially for the high intensity (figures 3(d), (e), (f)) where the short and long branch merge in the cutoff at harmonic 63. At lower intensity (figure 3(a)) the *in situ* phases do not merge in the cutoff. Intuitively, one might think that the short and long branch should merge in the cutoff, but this is not necessary in the quantum mechanical case. The stationary points of the short and long branch do *not* merge on the imaginary axis in the cutoff (figures 2(b), (d), (f)). The different behaviour of the *in situ* phases for the short and long branch in the cutoff is, hence, an amplitude effect rather than a pure phase effect. This is verified by inserting only the real part of the stationary points into equation (15) which does indeed yield coincidental cutoff behaviour of both branches, as expected for pure phase effects. Furthermore, it is the long branch that remains physical beyond the cutoff, while the strange behaviour of the short branch arises from

a set of stationary points that become unphysical beyond the cutoff [27]. In the classical model (figures 3(c), (f)), the *in situ* phases always merge in the cutoff since there are no amplitude effects (damping) in the plateau (figures 2(b), (d), (f)).

It is also worth noting that the *in situ* phases of the two branches intersect at lower harmonic orders than the cutoff. This 'intra-plateau crossing' is marked with a cross (×) in figures 3(a), (d) and it should *not* be confused as the position of the cutoff. At high intensities it is easy to distinguish between the intra-plateau crossing and the cutoff, while at low intensities they may be separated by a few harmonic orders only. In figure 1 we present an experimental result where ϕ_0 is linear from harmonic 22 to harmonic 28. At higher harmonic orders, a dramatic bend is observed [13, 18]. Using our quantum mechanical model we identify the lower orders as part of the short branch, $n = 1$ (full curve), while the higher orders are identified as the long branch, $n = 2$ (dashed curve). We stress that the dominance of the long branch close to the cutoff is a new result which already appears at the single-atom level when the short branch becomes unphysical. This new finding illustrates the usefulness of quantitative probing of HHG using a perturbative field. This effect would be very difficult to observe with the RABITT method because the corresponding emission times always merge in the cutoff, see figures 3(b), (e). The classical model fails to reproduce the bend (figure 3(c)) because the corresponding intra-plateau crossing occurs at much lower harmonic orders (not shown). Having discussed the details of the behaviour close to the cutoff, we now turn our attention to the central part of the harmonic plateau.

3.2. Ratio of in situ phases and emission times

In the following, we consider the first spectral derivative of the *in situ* phase, $\partial\phi_0^{(n)}/\partial\Omega$, which we wish to compare with the group delay dispersion (GDD), $\partial t_R^{(n)}/\partial\Omega$. Both quantities are evaluated in the central 50% of the harmonic plateau, i.e. in a region set by $1.3I_p + (1.6 \pm 0.8)U_p$, where both $\phi_0^{(n)}(\Omega)$ and $t_R^{(n)}$ are linear to a very good approximation. We avoid fast and nonlinear variations both close to the ionization potential ($\hbar\Omega = I_p$) and close to the cutoff ($\hbar\Omega = 1.3I_p + 3.2U_p$) using this central region. We define the ratio between the two quantities as

$$\gamma^{(n)} = -\omega \frac{\partial t_R^{(n)}}{\partial\Omega} \Big/ \frac{\partial\phi_0^{(n)}}{\partial\Omega} = -\omega \frac{\partial t_R^{(n)}}{\partial\phi_0^{(n)}}. \tag{16}$$

The GDD can in principle be obtained from the ϕ-dependence of the even-order harmonics as $\partial t_R^{(n)}/\partial\omega = -\gamma^{(n)}\partial\phi_0^{(n)}/\partial\omega/\omega$. This relation would be very useful if $\gamma^{(n)}$ was a constant (or at least a constant for each branch n). Unfortunately we show that $\gamma^{(n)}$ depends on the ionization potential of the atom, as well as the laser intensity and wavelength.

3.2.1. Role of ionization potential. In this subsection we study how $\gamma^{(n)}$ varies with laser intensity for a given laser wavelength (800 nm) and different atomic species (helium, argon, sodium and the classical case). In our model of $\gamma^{(n)}$, atom-specific properties enter only through the value of the ionization potential, I_p. In figure 4, we plot $\gamma^{(n)}$ for the short branch (a) and the long branch (b). In the classical case ($I_p = 0$) we find constant ratios: $\gamma^{(1)} \approx 1.1$ for the short branch and $\gamma^{(2)} \approx 0.84$ for the long branch, while in all realistic cases, where $I_p > 0$, there is a significant change in $\gamma^{(n)}$ as a function of the fundamental intensity. In the case of argon there is an especially strong variation of the ratio: from 1.6 to 0.5 for the short branch over the given intensity range. This strong intensity dependence is problematic for the experimental determination of two-colour HHG since the exact effective intensity is often unknown in experiments. The variation of the ratios is smaller for the long branch, because the stationary points are more similar to the corresponding classical case, as seen in figure 2. The variation of the ratios is smaller for sodium than for helium because of the smaller ionization potential. Sodium is chosen as an example to show that there is a significant difference between the classical and quantum mechanical cases even for a relatively small ionization potential. Using the two-colour HHG approach for characterization of attosecond pulses would require an accurate determination of the laser intensity, as well as a quantum mechanical calculation of $\gamma^{(n)}$.

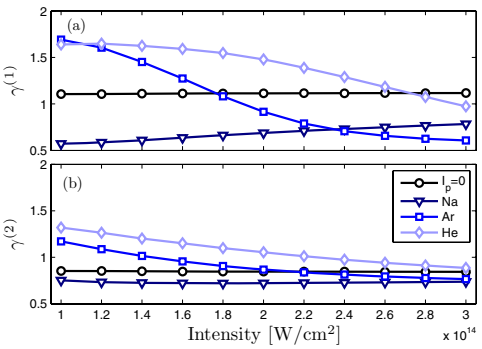

Figure 4. Ratios for different ionization potentials as a function of fundamental intensity for (a) the short branch and (b) the long branch. Symbols are ⋄ helium $I_p^{(\mathrm{He})} = 24.58$ eV, □ argon $I_p^{(\mathrm{Ar})} = 15.76$ eV, ▽ sodium $I_p^{(\mathrm{Na})} = 5.14$ eV and ○ classical $I_p^{(0)} = 0$ eV.

Next we comment on our previous work [18] where we compared the *in situ* method and the RABITT method for GDD of attosecond pulses. An explanation for the good agreement we found between the two methods may come from the crossing of $\gamma^{(1)}$ for argon occurring at 1.8×10^{14} W cm^{-2} with the classical limit, see figure 4(a). It would be interesting to see more experimental results, carried out on different atoms.

3.2.2. Role of laser wavelength. Finally, we study the dependence of the ratios, $\gamma^{(n)}$, with laser wavelength. The ratios are calculated for 800 nm, 1.3 μm and 2 μm, corresponding to a titanium–sapphire laser system and two mid-IR laser sources. We use the ionization potential of argon.

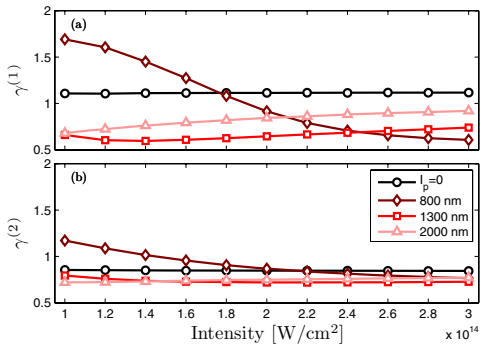

Figure 5. Ratios for different laser wavelengths as a function of fundamental intensity for (a) the short branch and (b) the long branch. Symbols are $\diamond$ $\lambda = 800$ nm, $\square$ $\lambda = 1.3$ μm, $\triangle$ $\lambda = 2$ μm for argon $I_p^{(Ar)} = 15.6$ eV, while symbol $\circ$ is the classical case $I_p^{(0)} = 0$ eV, which is independent of λ.

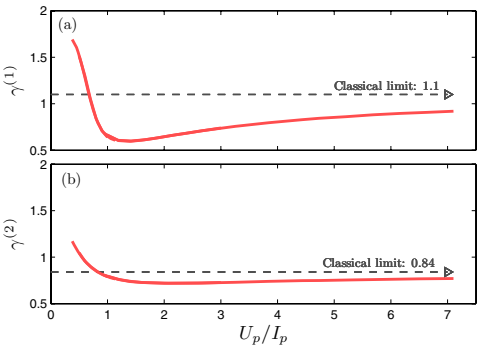

Figure 6. Universal ratio between the group delay dispersion and the derivative of the *in situ* phases as a function of the ratio of ponderomotive energy and ionization potential for (a) the short branch and (b) the long branch. The classical limit, $I_p^{(0)} = 0$, is reached very slowly, see the grey arrows.

Similar to figure 4, all ratios look different when they are plotted as a function of laser intensity, see figure 5(a) for the short branch and (b) for the long branch. The ratios of the short branch show larger variations than those of the long branch. Furthermore, it is seen that the longer wavelengths lead to less variation of the ratios over intensity. The recent experiments of Doumy *et al* [17] were carried out at these wavelengths. Applying our method improves the scaling law for the GDD from $\lambda^{-0.77}$ to $\lambda^{-1.05}$, which is closer to the expected λ^{-1} scaling of the harmonic chirp times intensity. We stress that in order to use the calculated ratios to determine the GDD, the experimental intensity must first be measured as accurately as possible independent of the two-colour HHG scheme.

4. Discussion and conclusions

In our quantum mechanical derivation of two-colour HHG we find that both amplitude and phase effects are important. The ratio of the ponderomotive energy and the ionization potential, U_p/I_p, serves as a measure on how 'classical' or 'quantum' the electron trajectories are. Choosing this ratio as our x-axis for the data in figures (4) and (5), we find that all individual ratios $\gamma^{(n)}$ follow a universal curve, as shown in figure 6. Photoelectron emission ranging from the photon picture to the tunnelling picture is described in the theory of Keldysh [28] where the ratio $\sqrt{I_p/2U_p} \ll 1$ (corresponding to $U_p/I_p \gg 1$) implies efficient tunnel ionization. In this limit we find that $\gamma^{(n)}$ slowly converges towards the classical limit, $I_p = 0$. One should look at figure 6 with some caution since the SFA is derived for the long wavelength limit requiring $I_p \gg \hbar\omega$ and $U_p/I_p > 1/2$. It is clear that the behaviour of the HHG process changes dramatically around $U_p/I_p \approx 1$, i.e. when the kinetic energy of the electron is close to the potential energy of the atom.

In conclusion, we have studied the HHG process perturbed by a weak second harmonic field within the SFA. We find that the dependence of the even harmonics on the subcycle delay between the two fields, cannot be understood using classical theory. Our calculations show good agreement with experimental results [13, 18] showing the change of behaviour at high energy, explained as a change of dominant quasiclassical branch of trajectories. We stress that there is an intra-plateau crossing between the short and the long branch which does not coincide with the true cutoff. Furthermore, we calculate the ratio between the GDD of the attosecond pulses and the phase variation of the even-order harmonics, $\gamma^{(n)}$, as a function of intensity, wavelength and ionization potential. The analysis method called *in situ* probing of the birth of attosecond pulses [16] must be improved by considering the influence of the atomic properties and laser parameters, before it can be applied for quantitative experimental studies. Using the classical analysis will only lead to a qualitative prediction for the GDD of the attosecond pulses with the correct sign. It will be interesting to compare the results of our quantum mechanical approach to probing the birth of attosecond pulses using a two-colour field with more refined calculations.

Acknowledgments

The authors would like to thank K Varjú and K J Schafer for helpful discussions. This research was supported by the Marie Curie program ATTOFEL (ITN), the European Research Council (ALMA), the Swedish Foundation for Strategic Research, the Swedish Research Council and the Knut and Alice Wallenberg Foundation.

References

[1] Paul P M, Toma E S, Breger P, Mullot G, Augé F, Balcou Ph, Muller H G and Agostini P 2001 Observation of a train of tttosecond pulses from high harmonic generation *Science* **292** 1689

[2] Hentschel M, Kienberger R, Spielmann C, Reider G A, Milosevic N, Brabec T, Corkum P, Heinzmannß U, Drescher M and Krausz F 2001 Attosecond metrology *Nature* **414** 509

[3] Long S, Becker W and McIver J K 1995 Model calculations of polarization-dependent two-color high-harmonic generation *Phys. Rev.* A **52** 2262–78

[4] Gaarde M B, L'Huillier A and Lewenstein M 1996 Theory of high-order sum and difference frequency mixing in a strong bichromatic laser field *Phys. Rev.* A **54** 4236–48

[5] Radnor S B P, Chipperfield L E, Kinsler P and New G H C 2008 Carrier-wave steepened pulses and gradient-gated high-order harmonic generation *Phys. Rev.* A **77** 033806

[6] Chipperfield L E, Robinson J S, Tisch J W G and Marangos J P 2009 Ideal waveform to generate the maximum possible electron recollision energy for any given oscillation period *Phys. Rev. Lett.* **102** 063003

[7] de Morisson Faria C F, Milošević D B and Paulus G G 2000 Phase-dependent effects in bichromatic high-order harmonic generation *Phys. Rev.* A **61** 063415

[8] Mauritsson J, Johnsson P, Gustafsson E, L'Huillier A, Schafer K J and Gaarde M B 2006 Attosecond pulse trains generated using two-color laser fields *Phys. Rev. Lett.* **97** 013001

[9] Mansten E, Dahlström J M, Johnsson P, Swoboda M, L'Huillier A and Mauritsson J 2008 Spectral shaping of attosecond pulses using two-colour laser fields *New J. Phys.* **10** 083041

[10] Ishii N, Kosuge A, Hayashi T, Kanai T, Itatani J, Adachi S and Watanabe S 2008 Quantum path selection in high-harmonic generation by a phase-locked two-color field *Opt. Express* **16** 20876–83

[11] Dudovich N, Tate J L, Mairesse Y, Villeneuve D M, Corkum P B and Gaarde M B 2009 Subcycle spatial mapping of recollision dynamics *Phys. Rev.* A **80** 011806

[12] Frolov M V, Manakov N L, Silaev A A and Vvedenskii N V 2010 Analytic description of high-order harmonic generation by atoms in a two-color laser field *Phys. Rev.* A **81** 063407

[13] He X, Dahlström J M, Rakowski R, Heyl C M, Persson A, Mauritsson J and L'Huillier A Interference effects in two-color high-order harmonic generation *Phys. Rev.* A **82** 033410

[14] Eilanlou A A, Nabekawa Y, Ishikawa K L, Takahashi H, Takahashi E J and Midorikawa K 2010 Frequency modulation of high-order harmonic fields with synthesis of two-color laser fields *Opt. Express* **18** 24619–31

[15] Muller H G 2002 Reconstruction of attosecond harmonic beating by interference of two-photon transitions *Appl. Phys. B: Lasers and Optics* **74** S17–21

[16] Dudovich N, Smirnova O, Levesque J, Mairesse Y, Ivanov M Y, Villeneuve D M and Corkum P B 2006 Measuring and controlling the birth of attosecond XUV pulses *Nat. Phys.* **2** 781

[17] Doumy G, Wheeler J, Roedig C, Chirla R, Agostini P and DiMauro L F 2009 Attosecond synchronization of high-order harmonics from mid-infrared drivers *Phys. Rev. Lett.* **102** 093002

[18] Dahlström J M, Fordell T, Mansten E, Ruchon T, Gisselbrecht M, Klünder K, Swoboda M, L'Huillier A and Mauritsson J 2009 Atomic- and macroscopic measurements of attosecond pulse trains *Phys. Rev.* A **80** 033836

[19] Lewenstein M, Balcou Ph, Ivanov M Yu, L'Huillier A and Corkum P B 1994 Theory of high-order harmonic generation by low-frequency laser fields *Phys. Rev.* A **49** 2117

[20] Becker W, Grasbon F, Kopold R, Milosević D B, Paulus G G and Walter H 2002 Above-threshold ionization: from classical features to quantum effects *Adv. At. Mol. Opt. Phys.* **48** 35

[21] Chirilă C C, Dreissigacker I, van der Zwan E V and Lein M 2010 Emission times in high-order harmonic generation *Phys. Rev.* A **81** 033412

[22] Varju K *et al* 2005 Frequency chirp of harmonic and attosecond pulses *J. Mod. Opt.* **52** 379

[23] Krause J L, Schafer K J and Kulander K C 1992 High-order harmonic generation from atoms and ions in the high intensity regime *Phys. Rev. Lett.* **68** 3535

[24] Corkum P B 1993 Plasma perspective on strong-field multiphoton ionization *Phys. Rev. Lett.* **71** 1994

[25] Kennedy D J and Manson S T 1972 Photoionization of the noble gases: cross sections and angular distributions *Phys. Rev.* A **5** 227

[26] Klünder K, Dahlström J M, Gisselbrecht M, Fordell T, Swoboda M, Guénot D, Johnsson P, Caillat J, Mauritsson J, Maquet A, Taïeb R and L'Huillier A 2011 Probing Single-Photon Ionization on the Attosecond Time Scale *Phys. Rev. Lett.* **106** 143002

[27] Lewenstein M, Salières P and L'Huillier A 1995 Phase of the atomic polarization in high-order harmonic generation *Phys. Rev.* A **52** 4747

[28] Keldysh L V 1965 Ionization in the field of a strong electromagnetic wave *Sov. Phys.—JETP* **20** 1307

Paper VII

Intensity Dependence of Laser-Assisted Attosecond Photoionization Spectra

M. Swoboda, J. M. Dahlström, T. Ruchon, P. Johnsson,
J. Mauritsson, A. L'Huillier and K. J. Schafer.

Laser Physics **19**, 1591 (2009).

ISSN 1054-660X, Laser Physics, 2009, Vol. 19, No. 8, pp. 1591–1599.

Intensity Dependence of Laser-Assisted Attosecond Photoionization Spectra[1]

M. Swoboda[a, *], J. M. Dahlström[a], T. Ruchon[a, c], P. Johnsson[a], J. Mauritsson[a], A. L'Huillier[a, **], and K. J. Schafer[b]

[a] *Department of Physics, Lund University, P.O. Box 118, Lund, 22100 Sweden*
[b] *Department of Physics and Astronomy, Louisiana State University, Baton Rouge, Louisiana 70803-4001, USA*
[c] *CEA-Saclay, DSM, Service des Photons, Atomes et Molécules, Gif sur Yvette, 91191 France*
*e-mail: marko.swoboda@fysik.lth.se
**e-mail: anne.Lhuillier@fysik.lth.se
Received March 20, 2009; in final form, March 24, 2009

Abstract—We study experimentally the influence of the intensity of the infrared (IR) probe field on attosecond pulse train (APT) phase measurements performed with the RABITT method (Reconstruction of Attosecond Beating by Interference in Two-Photon Transitions). We find that if a strong IR field is applied, the attosecond pulses will appear to have lower-than-actual chirp rates. We also observe the onset of the streaking regime in the breakdown of the weak-field RABITT conditions. We perform a Fourier-analysis of harmonic and sideband continuum states and show that the mutual phase relation of the harmonics can be extracted from higher Fourier components.

PACS numbers: 32.80.Fb, 32.80.Rm, 33.20.Xx, 33.60.+q, 42.65.Ky

DOI: 10.1134/S1054660X09150390

I. INTRODUCTION

Laser-assisted ionization processes provide an elegant tool to study dynamics and details of atomic and molecular systems [1–3]. For time-dependent measurements, the assisting laser needs to be synchronous to the ionization event on a time scale shorter than that of the process to be resolved. A number of experiments in the past years have shown that the attosecond (as) time scale is routinely accessible and laser-assisted ionization processes have become the chief tool for experiments in the field of attosecond science [1–6].

The emission of a comb of high-order harmonics when an atomic medium is exposed to a driving intense laser field is well understood. The resulting attosecond pulse trains (APT) [7, 8] provide a premier tool to controllably ionize atomic media [5, 9] and it is important to determine their characteristics, both amplitude and phase. This can be done by cross-correlation with an IR probing field under stable interferometric conditions. Using weak infrared (IR) fields, this is often done with the Reconstruction of Attosecond Beating by Interference of Two-Photon Transition (RABITT) method [7], while the AC-Streak camera method [10, 11], using stronger IR fields, has mainly been applied to the characterization of isolated attosecond pulses. A special case is the full characterization method FROG-CRAB (Frequency-Resolved Optical Gating-Complete Reconstruction of Attosecond Bursts), which is based on an iterative deconvolution of a time-frequency spectrogram [12, 13]. In this paper, we study the transition from the weak to the strong field regime, and the effect of the probe field strength on the validity of the characterization.

In Section 2, the experimental setup and performed experiments will be presented. We perform in Section 3 a conventional analysis of the data in the RABITT regime, studying specifically the probe intensity dependence of the phase measurement. A Fourier-series approach (Section 4) allows us to see the fingerprints of processes with more than one contributing IR photons and provides a more general description of our delay-dependent laser-assisted photoionization spectra.

2. EXPERIMENT

2.1. Setup

The experiments were performed at the High Power Laser Facility of the Lund Laser Centre. We use a 1 kHz chirped-pulse-amplification (CPA) titanium-sapphire based laser system, providing 2 mJ 30 fs pulses centered around 800 nm. The pulses are focused into an Ar gas cell, pulsed at 1 kHz, to generate high-order harmonics, which then propagate through silica plates and a thin Al-foil to filter the harmonics to form a well-defined APT (cf. Fig. 1). The APT is then recombined with an IR probe beam in a Mach–Zehnder-type interferometer. In the last step of the interferometer, the APT is passed through a drilled mirror while the IR is reflected on the back side of the

[1] The article is published in the original.

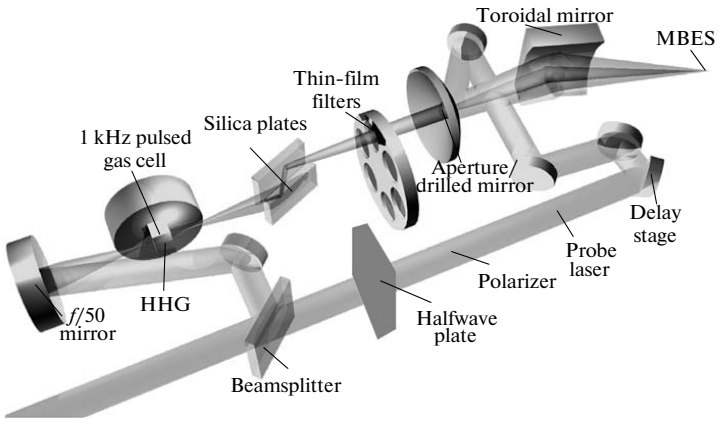

Fig. 1. Setup for the experiment: a 2 mJ, 30 fs laser pulse is split into a probe and a pump arm. The larger part is used in high-order harmonic generation while a fraction travels through a delay stage to serve as probe pulse. The generated harmonics are filtered spectrally and spatially by silica plates, a thin-film metallic filter and an aperture, before recombining with the probe using a drilled mirror and being focused into the detection gas of a magnetic bottle electron spectrometer.

mirror. Both beams are focused into the detection gas of a magnetic-bottle electron spectrometer (MBES) with the help of a toroidal mirror. Using a combination of half-wave plate and polarizer in the probe beam, the pulse energy of the IR can be varied continuously between 5 and 100 μJ. As all focusing parameters are kept constant, any change in the probe pulse energy will directly result in a proportional change of the IR intensity in the detection region of the MBES. The MBES has a 2π acceptance angle and a maximum energy resolution of about 100 meV.

The relative delay of IR probe and APT can be adjusted on two time scales. Using a motorized translation stage in the probe arm we can vary the delay in the range of one femtosecond to several picoseconds. To accurately resolve attosecond processes, a delay stage with a piezoelectric crystal is used to change the relative phase of the two beams with a precision of a few tens of as. This stability allows us to perform interferometry of two-photon pathways as in the RABITT characterization scheme, as shown below. It is also crucial for the use of the AC streak camera method, where the relative phase of the two beams has to be stable with similar precision.

2.2. Delay-Dependent Two-Color Photoionization Spectra

In the experiments presented here, the resulting photoelectron spectra from an IR probe and XUV field were recorded. A shift in the relative delay of the two fields induces a change in the observed spectrum, and recording the spectra at different subcycle delays allows us, in some conditions, to determine the temporal structure of the XUV emission.

Figure 2 shows the seven scans that constitute our experimental results. From left to right, the probe pulse energy changes by a factor of 20, ranging from 5 to 100 μJ. At the lowest intensity, the presence of a weak IR field leads to weak sidebands between the odd harmonic orders. These sidebands originate from $\omega_n + \omega_R$ and $\omega_n - \omega_R$ two-photon transitions [14], where ω_R is the IR photon frequency and $\omega_n = n\omega_R$, with n being an odd integer, see Fig. 3a. The two possible pathways to each final state lead to the observed interference pattern. This pattern is repeated every IR half-cycle, $T_R/2$, reproducing the frequency of the attosecond pulse periodicity. This probe intensity regime is commonly referred to as the RABITT regime.

With increasing IR intensity, the amplitude of the sidebands becomes comparable to direct photoionization by the harmonics (see, e.g. sideband 22 in Figs. 2d–2g). These two-photon processes induce a depletion of the peaks at odd harmonic energies, at the delays where the sidebands are maximum. The cutoff region is first affected by depletion since the strength of continuum-continuum transitions rapidly increases with the energy of the initial state (Figs. 2b and 2c at harmonic 25 and above). For a probe pulse energy of 40 μJ (Fig. 2d), depletion effects become visible even in the low energy region (see harmonic 19 to 23 in Figs. 2d–2g).

At the higher probe intensities (Figs. 2d–2g), processes involving more than one IR photon become significant. This is the so-called streaking regime, where the AC-streak camera becomes the preferred charac-

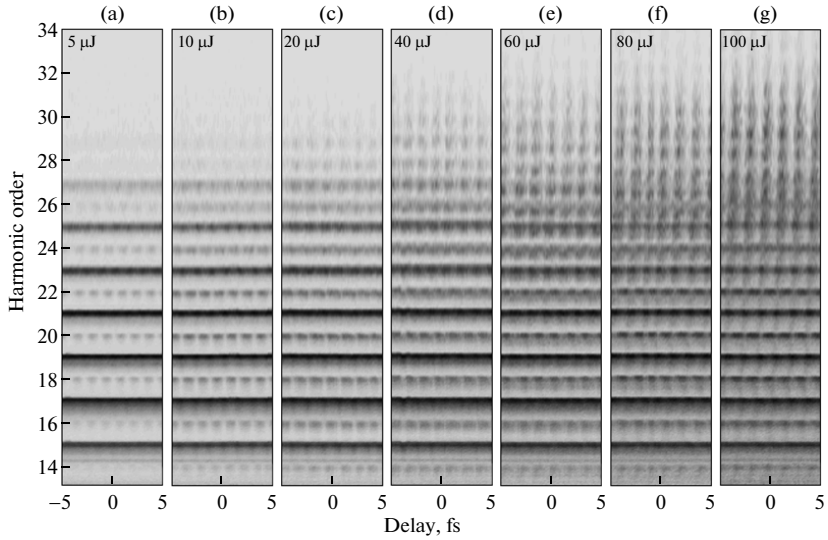

Fig. 2. XUV photoionization spectra, recorded for varying sub-cycle delay between IR and XUV field. The corresponding probe pulse energies are written in the upper part of the figures. A change of this energy translates proportionally to a change of the probe intensity. The zero delay indicates the delay at which the maxima of the IR pulse and the APT coincide.

terization method [10, 11, 13]. The streaking regime is clearly entered in the last two of the scans in Fig. 2, the cutoff being increased by as much as seven IR photons (from harmonic 27 and above). Note that the electron signal is still showing discrete IR photon energy spacing because of the periodicity of photoionization from the sequence of attosecond pulses.

3. ANALYSIS OF THE EXPERIMENT

3.1. Reconstruction of Attosecond Beating by Interference in Two-Photon Transitions (RABITT)

We now analyze the results in Fig. 4 (same as Fig. 2a) within a perturbation theory framework. Here, we will consider the photoionization of the detection gas by the APT as a first-order perturbation and the onset of the sidebands and the RABITT modulation as a perturbation of the second order. This is a good description of two-color photoionization at low IR intensities.

Contributions to the final state probability amplitudes of order N can be obtained from those of order $(N-1)$ through the following equation [15, 16]:

$$a_m^{(N)}(t) = \frac{1}{i\hbar}\sum_f \sum_l \int_0^t dt' \mu_{m,l} E(\omega_f) a_l^{(N-1)}(t') e^{i(\omega_{ml}-\omega_f)t'}, \quad (1)$$

where l is the index of the respective contributing states, ω_f are the frequencies acting on the atom and m denotes the final state. The effect of the IR on the ground state is negligible. The population of continuum states after perturbing the system with a harmonic frequency can be approximated by

$$a_n^{(1)}(t) = \frac{\mu_{n,g} E(\omega_n)}{i\hbar} t, \quad (2)$$

where $\mu_{n,g}$ is the transition dipole matrix element from the ground to the continuum state, and t the interaction time, approximately a measure of the pulse duration. The population of the sideband state $(n-1)$ can be expressed as

$$\begin{aligned} a_{n-1}^{(2)}(t) &= \frac{1}{(i\hbar)^2}\frac{t^2}{2}[\mu_{n-1,n-2}\mu_{n-2,g}E(\omega_R)E(\omega_{n-2}) \\ &\quad + \mu_{n-1,n}\mu_{n,g}E(-\omega_R)E(\omega_n)] \\ &\approx M\frac{E_{R0}E_{X0}t^2}{(i\hbar)^2}\frac{1}{2}[e^{i(\phi_R+\phi_{n-2})} + e^{i(-\phi_R+\phi_n)}], \end{aligned} \quad (3)$$

where the factor M represents a combination of the various transition dipole moments, which we approximate as equal for both quantum paths, and E_{R0}, E_{X0} are the amplitudes of the IR and XUV fields. The sideband intensity will finally oscillate

$$I_{n-1}^{(2\omega)}(\varphi) \propto \cos(2\phi_R + \Delta\phi_{n-2,n}), \quad (4)$$

with $\phi_R = \omega_R\tau$, τ being the delay between the XUV and the IR fields. $\Delta\phi_{n-2,n}$ is the phase difference between the harmonic spectral phases ϕ_{n-2} and ϕ_n. This allows

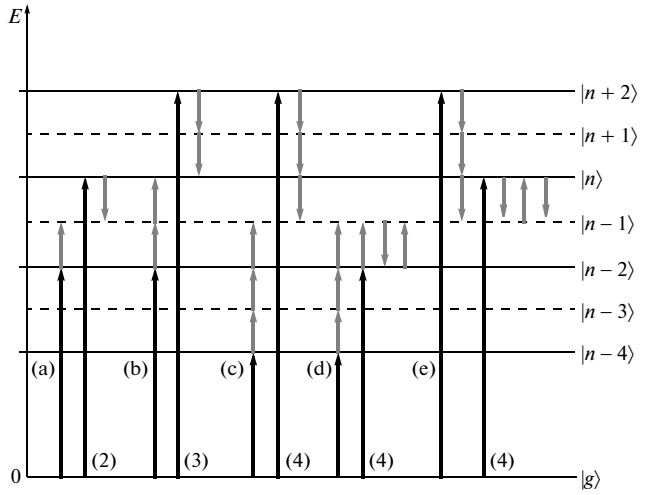

Fig. 3. Sketch over possible transitions involving single harmonic- and multiple IR photons. (a) Shows the RABITT transition, which couples two harmonic photons with an energy difference of $2\omega_R$ to a final state with energy $(n-1)\omega_R$. (b) Shows that the absorption/emission of two IR photons leads to a similar coupling with odd final energy $n\omega_R$. (c) Illustrates that yet another IR photon can be used to couple harmonic photons that are $6\omega_R$ apart in an even final energy $(n-1)\omega_R$. (d, e) Shows that three IR photons will also couple new harmonics that are $2\omega_R$ apart in even final energy $(n-1)\omega_R$, which will distort the information from the RABITT signal in (a).

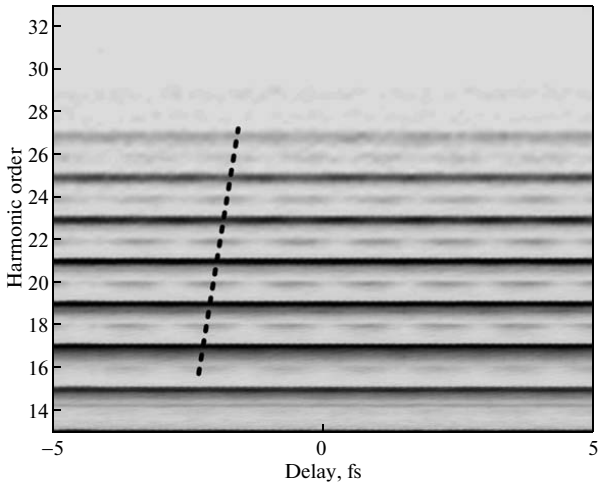

Fig. 4. Delay-dependent photoionization spectrum in the RABITT regime, measured at 5 μJ probe pulse energy. The dashed line indicates the sideband maxima.

us to obtain the phase difference $\Delta\phi_{n-2,n}$ from a Fourier transform of the spectrum over delay.

Using the obtained phase, we can reconstruct a pulse shape as in Fig. 5. The Fourier limit for our spectrum is 160 as. Due to the chirp rate of 18400 as^2 we obtain an average pulse duration of 440 as FWHM. This method of measuring APTs has been successfully employed in a number of experiments [7, 8, 17]. The

high chirp rate and asymmetric pulses come as no surprise as only one thin aluminum filter was employed to counter the intrinsic chirp of the HHG process. The addition of more filters would help to approach the Fourier limit and further compress the pulses [17, 18]. The RABITT method provides access to the relative phase difference of presumably monochromatic harmonics [7, 14]. The measured phase difference is equal to the group delay (GD) over the spectrum of the APT, and an integration allows us to reconstruct an average attosecond pulse in the train. Such a retrieved pulse represents a good approximation for pulses within the FWHM of the APT, accounting for about 90% of the signal from experiments with such trains. There are extensions and implementations of the method that yield more information on the full structure of the APT [19, 20].

3.2. Intensity Dependence of RABITT Signal

The influence of an intense probe field on the measured spectral phase was studied by progressively increasing the IR intensity and recording the delay-dependent photoionization spectra. Figure 6 shows the phase differences $\Delta\phi_{n-2,n}$ evaluated according to the method outlined above, for varying probe intensities. It is clear that the slope is decreasing with increasing intensity, as if the chirp rate was lower, even though the actual APT remained the same.

As a consequence of the phase variation with intensity shown in Fig. 6, the reconstructed pulses will appear more compressed at higher probe intensities, which is a pure artifact of the increased IR intensity. The RABITT analysis relies heavily on the presence of a single IR photon contributing to the final state as to allow only the phase difference of the neighboring harmonics to be measured. Higher-order processes perturb the RABITT signal, as will be discussed in more detail in Section 4.

3.3. Streaking

We now consider briefly the regime of high probing intensities (Fig. 7, same as Fig. 2g) where the interaction between photoelectrons and probing laser field can be understood by simple classical arguments. In this regime, an electron is released into the continuum at a given ionization time t_i due to photoionization by an attosecond pulse. It will gain an additional momentum proportional to the IR vector potential $\mathbf{A}(t_i)$ at the time of ionization. This momentum shift imparted by the IR probe is therefore dependent on the relative delay between the two fields. With APTs generated by two-color fields, or with single attosecond pulses, the pulse properties (duration and chirp) can be extracted from analyzing the streaking trace and the pulse(s) can be reconstructed [10, 11, 13]. In the case of an APT with two pulses per cycle, the situation is more complex and a reconstruction of the attosecond pulses

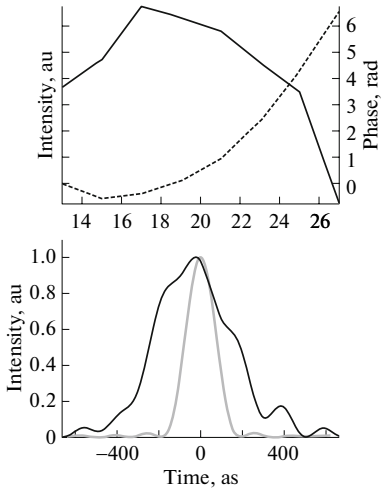

Fig. 5. Reconstruction of average pulse in the pulse train, measured by the RABITT method. The upper panel shows the harmonic intensities (solid line) and integrated spectral phase (dashed line). Using these intensities and phase, one can reconstruct the pulse shape as in the lower panel. The Fourier limited pulse shape is shown as dashed.

from the experimental data is more difficult, since the sign of the probe field reverses for consecutive pulses. Without going further with the analysis of our experimental data, we note that the chirp of our attosecond pulses, however, is clearly visible in the high energy region of the spectrum (see dashed line in Fig. 7). The onset of the streaking regime also explains the observed phase shift of the sideband orders close to the cutoff in Fig. 6. In the perturbative regime and, for simplicity, in absence of attosecond chirp, the maxima of the sidebands occur at the maxima of the probe laser electric field. At moderate probe intensity, depletion of the harmonic states will lead to maxima of the harmonics shifted by $\pi/2$ with respect to the sidebands, thus corresponding to the zeros of the electric field. At high energy, electron peaks, coming from direct electrons being streaked by the probe field, will therefore be maxima at the zeros of the electric field, thus shifted by a factor $\pi/2$ from the sidebands.

4. FOURIER DECOMPOSITION OF THE PHOTOELECTRON SPECTRA

4.1. Perturbation Theory Analyzis

To better understand the influence of a high IR intensity on a RABITT measurement, we extend the analyzis performed in the previous section, based on perturbation theory to the next orders. The third order of perturbation includes components coupling the

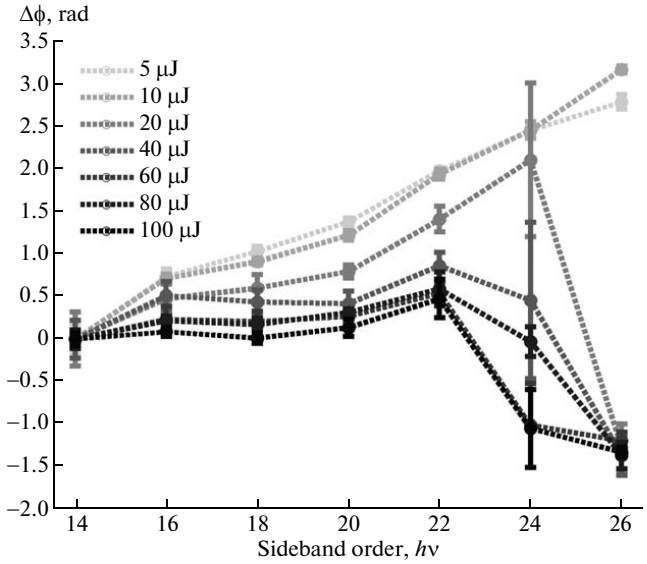

Fig. 6. Phase differences Δϕ measured over the harmonic spectrum, for different probe pulse energies. Higher probe intensities result in a flatter measured spectral phase in the plateau region (order 14–22).

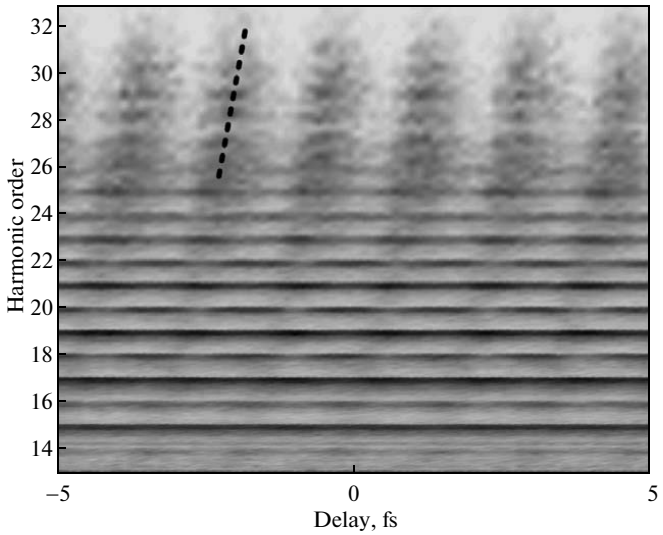

Fig. 7. Delay-dependent photoionization spectrum in the streaking regime, measured at 100 μJ probe pulse energy.

states $(n + 2)$ and $(n - 2)$ to the harmonic (n) state by two IR photon absorption or emission (Fig. 3b):

$$a_n^{(3)} = \frac{1}{(i\hbar)^3}\frac{t^3}{6} \times [\mu_{n,n-1}\mu_{n-1,n-2}\mu_{n-2,g}E(\omega_R)E(\omega_R)E(\omega_{n-2}) + \mu_{n,n-1}\mu_{n-1,n}\mu_{n,g}E(\omega_R)E(-\omega_R)E(\omega_n) + \mu_{n,n+1}\mu_{n+1,n}\mu_{n,g}E(-\omega_R)E(\omega_R)E(\omega_n) + \mu_{n,n+1}\mu_{n+1,n+2}\mu_{n+2,g}E(-\omega_R)E(-\omega_R)E(\omega_{n+2})] \approx M\frac{E_{R0}^2 E_{X0} t^3}{(i\hbar)^3}\frac{1}{6}[e^{i(2\phi_R+\phi_{n-2})} + 2e^{i\phi_n} + e^{i(-2\phi_R+\phi_{n+2})}]. \quad (5)$$

This term gives rise to oscillations at frequencies $4\omega_R$, $2\omega_R$, and to a constant term. The intensity of the $4\omega_R$ modulation at the harmonic energy $n\omega_R$ is

$$I_n^{(4\omega)}(\phi_R) \propto \cos(4\phi_R + \Delta\phi_{n-2,n+2}) \quad (6)$$

which is similar to Eq. (4). The next order of perturbation leads to a $6\omega_R$ component in the sideband states and the next to an $8\omega_R$ component in the harmonic states. Higher IR intensities lead to new couplings of states lying further apart and thus higher modulation frequencies.

Figure 3 illustrates how the number of pathways that lead to a given modulation frequency is unique only under certain restrictions. Even numbers of contributing IR photons couple to harmonic states while odd numbers couple to sideband states. The $4\omega_R$ frequency is meaningful only in the harmonic final states, as shown in Eq. (5) and the phase difference that can be determined is that between harmonic states $(n - 2)$ and $(n + 2)$. A Fourier transform that isolates this component will allow us to access to the spectral phase in the same way as with the conventional RABITT, looking at the $2\omega_R$ modulation in the sideband states. Experimentally, due to the resolution of our scans, the $6\omega_R$ component is the highest resolvable. It is already close to the Nyqvist limit, with only three to four data points per period.

Figure 8 shows a comparison of the group delay obtained over the spectrum for three different modulation frequencies. The usual RABITT is based on the 5 μJ-scan, the phases of the $4\omega_R$-modulation were obtained at 20 μJ, and the $6\omega_R$-modulation was present for the central harmonics in the 80 μJ-scan. Excellent agreement was found between the chirp rates obtained with the different methods. Our results are also consistent with previous experiments [8, 17]. From the $2\omega_R$-measurement we obtain a chirp rate of 18400 as^2 or—in terms of a group delay—an emission time difference $\Delta t_e = \Delta\phi/(2\omega_R) = 87$ as. This is very similar to 16800 as^2 ($\Delta t_e = 79$ as) obtained from the $4\omega_R$-component in the harmonics. The slope of the phase difference in the $6\omega_R$-component is also in good agreement with 16900 as^2 chirp rate or a Δt_e of 80 as.

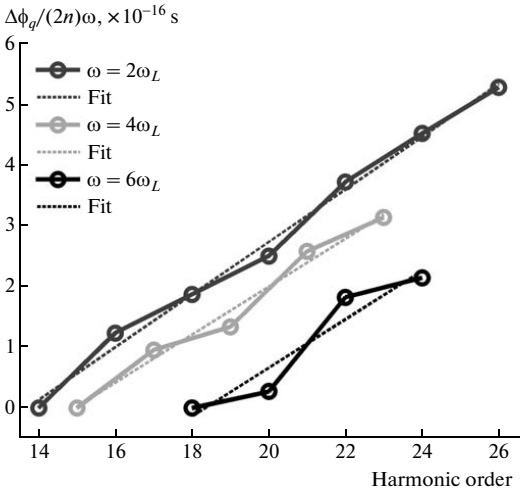

Fig. 8. Comparaison of the obtained phase differences for three different frequency components present in the experimental electron signal. The conventional RABITT includes contribution from sidebands 14 to 26. The $4\omega_R$-component has been extracted from harmonics 15 to 23 and the $6\omega_R$-modulation was obtained from sidebands 18 to 24. The curves have been shifted for better comparison.

4.2. Generalization

Because of the analogy between the conventional RABITT and the possibility to extract the same information from higher components we will now introduce a more general expression for the delay dependence of our photoelectron spectrum. This expression will hold beyond the breakdown of the perturbation picture. The amplitude of any photoelectron peak in the spectrum is periodic with delay ϕ_R between the IR and XUV fields. It can therefore be expressed as a discrete Fourier series:

$$S(\phi_R, I_R) = \sum_{k=-\infty}^{\infty} \tilde{S}_k(I_R)e^{i\phi_R 2k} = \sum_{k=0}^{\infty} S_k(\phi_R, I_R) \quad (7)$$

with $\tilde{S}_k^* = \tilde{S}_{-k}$. Considering only the $k = \pm 1$ contributions we have

$$S_1(\phi_R, I_R) = \tilde{S}_1(I_R)e^{i\phi} + \tilde{S}_1^*(I_R)e^{-i\phi} = 2\left|\tilde{S}_1(I_R)\right|\cos(2\phi_R + \arg(\tilde{S}_1(I_R))), \quad (8)$$

which is the common RABITT case, for low IR intensity, with $\arg(\tilde{S}_1(I_R)) = \Delta\phi_{n-1}$. For higher IR intensi-

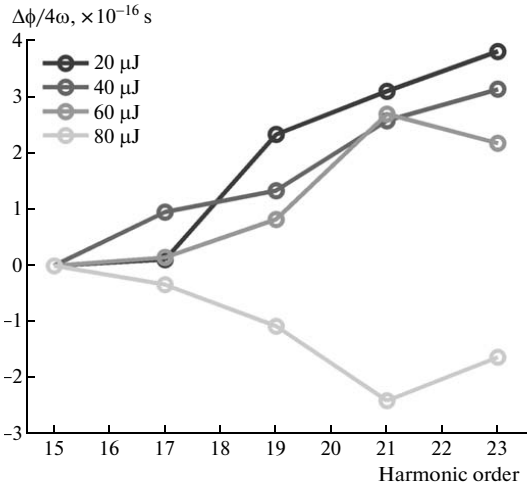

Fig. 9. Intensity dependence of the measured phase from the $4\omega_R$ component in the harmonics. The measured chirp rate over the spectrum shows good agreement at 40 μJ with the $2\omega_R$-measurement from the sidebands. It breaks down at higher probe energy.

ties, higher order terms contribute, the argument will change and higher order terms of the sum $\tilde{S}_k(I_R)$ will grow revealing higher contributing frequencies. In the case of $k = 2$,

$$S_2(\phi_R, I_R) = 2\left|\tilde{S}_2(I_R)\right|\cos(4\phi_R + \arg(\tilde{S}_2(I_R))), \quad (9)$$

which can readily be identified as the $4\omega_R$ component with an argument of $\Delta\phi_{n-2,n+2}$ for a suitable probe intensity. Figures 3d–3e show the effect of the participation of three IR photons, and how two non-surrounding harmonics contribute their phase difference to sideband $n - 1$, destroying the unique source of the $2\omega_R$ modulation. Thus $\arg(\tilde{S}_1(I_R))$ changes and the phase observed in the RABITT analysis varies with IR intensity.

At the same order of perturbation, a $6\omega_R$ modulation can be constructed with three IR photons coupling harmonic $n - 4$ and $n + 2$ to sideband $n - 1$ (cf. Fig. 3d). For sufficiently high intensity, the number of contributing IR photons is $\gg 1$, resulting in a great number of frequencies added to form the delay-dependent signal in the sideband. More and more harmonics contribute to the phase, which becomes flat. The oscillation does not uniquely depend on the adjacent orders anymore—the requirement for RABITT. This is the streaking regime, where the classical limit is reached.

As we previously studied the effect of the IR intensity on the phase measurement in the conventional RABITT method, we perform a similar analysis for our measurements with the $4\omega_R$ component. Figure 9 shows the intensity dependence of the harmonic phase measured in this component. We find that at 20 to 60 μJ the phase is meaningful compared with the conventional measurement. The measurement at 80 μJ is showing a similar characteristic flattening of the phase as the conventional RABITT. The $4\omega_R$ breakdown occurs for much higher probe intensities. In this case the number of contributing photons becomes so high that $\arg(\tilde{S}_2(I_R))$ is affected by ambiguous coupling of states. The analyzis of this $4\omega_R$ component provides an additional check on the measured phase from conventional RABITT method. This allows us to assess whether the probe intensities in any experiment have been too high by comparing the $2\omega_R$ with the $4\omega_R$ components and possibly even higher orders.

5. CONCLUSIONS

We have studied the influence of IR probe intensity in two-color XUV photoionization experiments. In the laser-assisted ionization process that is at the heart of the RABITT method for characterizing APTs, the probe intensity needs to be maintained at levels which only perturb the process very slightly. A high probe intensity will greatly alter the measured phase relation of the individual high-order harmonics, making it appear flat over the spectrum, as if the pulses were compressed. RABITT is only valid in the limit of weak IR intensity.

In a next step, the increasing number of contributing IR photons was tracked down by Fourier-analysis of sideband and harmonic states. As an increasing number of photons allows to couple states further and further away, higher modulation frequencies occur. The $4\omega_R$ component of the harmonic states allows us to obtain their mutual phase relation. Also in this case an increasing IR intensity started to affect the phase measurement making the pulses appear artificially compressed. We believe these experiments will allow the scientific community to gain a better understanding of the IR intensity dependence of laser-assisted ionization of a gas using high-order harmonics.

ACKNOWLEDGMENTS

This paper is dedicated to the memory of N.B. Delone, who was a father of this exciting field of research "atoms in strong laser fields," with the first "multiphoton ionization" (1965) and "multielectron multiphoton ionization" (1975) experimental results. This research was supported by the Marie Curie Intra-European Fellowship (Attotech), the Marie Curie Early Stage Training Site (MAXLAS), the Knut and Alice Wallenberg Foundation, the Swedish Research Council, and the National Science Foundation (Grant no. PHY-0701372).

REFERENCES

1. A. L. Cavalieri, N. Mller, T. Uphues, V. S. Yakovlev, A. B. Caronka, B. Horvath, B. Schmidt, L. Blmel, R. Holzwarth, S. Hendel, M. Drescher, U. Kleineberg, P. M. Echenique, R. Kienberger, F. Krausz, and U. Heinzmann, "Attosecond Spectroscopy in Condensed Matter," Nature **449**, 1029–1032 (2007).
2. M. Drescher, M. Hentschel, R. Kienberger, M. Uiberacker, V. Yakovlev, A. Scrinzi, T. Westerwalbesloh, U. Kleineberg, U. Heinzmann, and F. Krausz, "Time-Resolved Atomic Inner-Shell Spectroscopy," Nature **419**, 803 (2002).
3. J. Mauritsson, P. Johnsson, E. Mansten, M. Swoboda, T. Ruchon, A. L'Huillier, and K. J. Schafer, "Coherent Electron Scattering Captured by an Attosecond Quantum Stroboscope," Phys. Rev. Lett. **100**, 073003 (2008).
4. E. Goulielmakis, M. Uiberacker, R. Kienberger, A. Baltuska, V. Yakovlev, A. Scrinzi, T. West- erwalbesloh, U. Kleineberg, U. Heinzmann, M. Drescher, and F. Krausz, "Direct Measurement of Light Waves," Science **305**, 1267 (2004).
5. P. Johnsson, J. Mauritsson, T. Remetter, A. L'Huillier, and K. J. Schafer, "Attosecond Control of Ionization by Wave-Packet Interference," Phys. Rev. Lett. **99**, 233011 (2007).
6. T. Remetter, P. Johnsson, J. Mauritsson, K. Varjú, Y. Ni, F. Lépine, E. Gustafsson, M. Kling, J. Khan, R. López-Martens, K. J. Schafer, M. J. J. Vrakking, and A. L'Huillier, "Attosecond Electron Wave Packet Interferometry," Nature Phys. **2**, 323 (2006).
7. P. M. Paul, E. S. Toma, P. Breger, G. Mullot, F. Augé, P. Balcou, H. G. Muller, and P. Agostini, "Observation of a Train of Attosecond Pulses from High Harmonic Generation," Science **292**, 1689 (2001).
8. Y. Mairesse, A. de Bohan, L. J. Frasinski, H. Merdji, L. C. Dinu, P. Monchicourt, P. Breger, M. Kovacev, R. Tai'eb, B. Carré, H. G. Muller, P. Agostini, and P. Salieres, "Attosecond Synchronization of High-Harmonic Soft X-rays," Science **302**, 1540 (2003).
9. O. Guyiétand, M. Gisselbrecht, A. Huetz, P. Agostini, R. Taieb, A. Maquet, B. Carre, P. Breger, O. Gobert, D. Garzella, J.-F. Hergott, O. Tcherbakoff, H. Merdji, M. Bougeard, H. Rottke, M. Bottcher, Z. Ansari, and P. Antoine, "Evolution of Angular Distributions in Two-Colour, Few-Photon Ionization of Helium," J. Phys. B: At. Molec. Opt. Phys. **41**, 051002 (2008).
10. J. Itatani, F. Quéré, G. L. Yudin, M. Y. Ivanov, F. Krausz, and P. B. Corkum, "Attosecond Streak Camera," Phys. Rev. Lett. **88**, 173903 (2002).
11. R. Kienberger, M. Hentschel, M. Uiberacker, C. Spielmann, M. Kitzler, A. Scrinzi, M. Wieland, T. Westerwalbesloh, U. Kleineberg, U. Heinzmann, M. Drescher, and F. Krausz, "Steering Attosecond Electron Wave Packets with Light," Science **297**, 1144 (2002).
12. Y. Mairesse and F. Quéré, "Frequency-Resolved Optical Gating for Complete Reconstruction of Attosecond Bursts," Phys. Rev. A **71**, 011401(R) (2005).
13. G. Sansone, E. Benedetti, F. Calegari, C. Vozzi, L. Avaldi, R. Flammini, L. Poletto, P. Villoresi, C. Altucci, R. Velotta, S. Stagira, S. D. Silvestri, and M. Nisoli, "Isolated Single-Cycle Attosecond Pulses," Science **314**, 443–446 (2006).
14. V. Véniard, R. Taieb, and A. Maquet, "Phase Dependence of $(N + 1)$-Color $(N > 1)$ IR-UV Photoionization of Atoms with Higher Harmonics," Phys. Rev. A **54**, 721 (1996).
15. J. J. Sakurai, *Modern Quantum Mechanics* (Addison-Wesley, New York, 1994).
16. R. W. Boyd, *Nonlinear Optics* (Academic, New York, 2003).
17. R. López-Martens, K. Varjú, P. Johnsson, J. Mauritsson, Y. Mairesse, P. Salières, M. B. Gaarde, K. J. Schafer, A. Persson, S. Svanberg, C.-G. Wahlström, and A. L'Huillier, "Amplitude and Phase Control of Attosecond Light Pulses," Phys. Rev. Lett. **94**, 033001 (2005).
18. K. Varjú, P. Johnsson, R. López-Martens, T. Remetter, E. Gustafsson, J. Mauritsson, M. B. Gaarde, K. J. Schafer, C. Erny, I. Sola, A. Zaïr, E. Constant, E. Cormier, E. Mével, and A. L'Huillier, "Experimental Studies of Attosecond Pulse Trains," Laser Phys. **15**, 888–898 (2005).
19. K. Varjú, Y. Mairesse, P. Agostini, P. Breger, B. Carré, L. J. Frasinski, E. Gustafsson, P. Johnsson, J. Mauritsson, H. Merdji, P. Monchicourt, A. L'Huillier, and P. Salières, "Reconstruction of Attosecond Pulse Trains Using an Adiabatic Phase Expansion," Phys. Rev. Lett. **95**, 243901 (2005).
20. J. Mauritsson, P. Johnsson, R. López-Martens, K. Varjú, A. L'Huillier, M. B. Gaarde, and K. J. Schafer, "Probing Temporal Aspects of High-Order Harmonic Pulses via Multi-Colour, Multi-Photon Ionization Processes," J. Phys. B **38**, 2265 (2005).

Paper VIII

Sub-cycle Control of Attosecond Pulse Generation using Two-Colour Laser Fields

J. Mauritsson, J. M. Dahlström, E. Mansten and T. Fordell.

J. Phys. B: At. Mol. Opt. Phys. **42**, 134003 (2009).

IOP PUBLISHING JOURNAL OF PHYSICS B: ATOMIC, MOLECULAR AND OPTICAL PHYSICS

J. Phys. B: At. Mol. Opt. Phys. **42** (2009) 134003 (6pp) doi:10.1088/0953-4075/42/13/134003

Sub-cycle control of attosecond pulse generation using two-colour laser fields

J Mauritsson, J M Dahlström, E Mansten and T Fordell

Department of Physics, Lund University, PO Box 118, SE-221 00 Lund, Sweden

E-mail: johan.mauritsson@fysik.lth.se

Received 19 December 2008, in final form 12 February 2009
Published 12 June 2009
Online at stacks.iop.org/JPhysB/42/134003

Abstract

Strong field laser–matter interaction is intrinsically a sub-cycle phenomenon, which is clearly illustrated by the generation of attosecond pulses through the high-order harmonic process. Therefore, to control strong field processes the structure of the field driving the generation has to be controlled on a sub-cycle level. One approach is to use phase stabilized few-cycle driving pulses and vary the carrier-envelope phase of these pulses; an alternative method is to use longer pulses and include the second harmonic to tailor the field structure.

(Some figures in this article are in colour only in the electronic version)

1. Introduction

Strong field processes start with the creation of temporally localized electron wave packets (EWPs) through ionization when atoms or molecules are exposed to strong laser fields. These subfemtosecond EWPs are produced twice per optical cycle and may be driven back to the ion for further interaction. This basic sequence of events, commonly known as the three-step model [1, 2], is the essence of strong field laser physics and leads to many different phenomena [3–7]. One method to control these processes is to tailor the sub-cycle structure of the driving field. The strength and shape of the half-cycle during which the electron is ionized determines the timing and amount of ionization whereas the next half-cycle sets the energy of the electron when it returns to the ion.

The sub-cycle field structure can be controlled if the fundamental infrared (IR) field is mixed with its second harmonic. The combined field can be written as: $E(t) = E_\omega[\sin(\omega t) + \sqrt{\mathcal{R}}\sin(2\omega t + \varphi)]$, where $\sqrt{\mathcal{R}} = E_{2\omega}/E_\omega$ is the ratio between the two field amplitudes, ω is the IR frequency and φ a tunable phase difference between the two fields. This method to control multiphoton ionization of atoms attracted both experimental [8, 9] and theoretical [10, 11] interest at the time when the three-step model was put forward. It was demonstrated that the first step in this model, the ionization, can be controlled using a two-colour laser field. Both the amount of ionization and the direction of the ejected electron are affected when the relative phase between the two fields is changed. It was soon demonstrated that also the second and third steps are controllable [12–14]. At this time the metrology to characterize attosecond pulses was not yet developed and only spectral measurements were possible.

An alternative method to break the inversion symmetry is through the use of few-cycle pulses where consecutive half-cycles are different due to the very short envelopes of the pulses. With these pulses asymmetries have been observed in multiphoton ionization experiments [15, 16] and high-order harmonic generation [17]. The ability to control strong field processes using few-cycle pulses significantly improved when it became possible to stabilize the carrier-envelope phase (CEP) of femtosecond optical pulses in the visible and near infrared wavelength regions. This technique has lead to a variety of new applications, ranging from precision spectroscopy to attophysics [17–21]. The effect of changing the CEP of few-cycle pulses is similar to that obtained when changing the relative phase, φ, between the two fields in a bichromatic laser field (figure 1).

Attophysics is among the most celebrated offspring of strong field laser physics. It is the short-timescale frontier of physics and replaces femtochemistry in this regard. Attosecond pulses have most likely been generated since the process of high-order harmonic generation was discovered, but the metrology to characterize these pulses was not developed until 2001. At that time two groups independently generated and characterized attosecond pulses using very different schemes [22, 23]. Both schemes are based on high-order harmonic generation from IR laser pulses; however, while the first method uses multi-cycle pulses to generate

J. Phys. B: At. Mol. Opt. Phys. **42** (2009) 134003 J Mauritsson *et al*

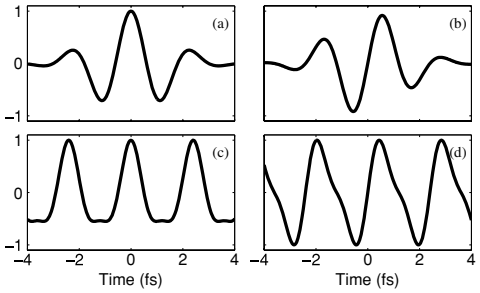

Figure 1. Comparison between the asymmetry and control of few-cycle pulses and two-colour fields. In (a) and (b) few-cycle (3.3 fs) cosine and sine pulses are plotted and compared to two-colour fields with $\mathcal{R} = 9\%$ for two different values on φ (c) and (d). The role of the relative phase, φ, between the two fields is very similar to that of the CEP for a few-cycle laser pulse. Just as the relation between consecutive half-cycles changes when the CEP is varied for a few-cycle pulse, so does the shape of consecutive half-cycles in a multi-cycle two-colour field change when φ is varied.

trains of attosecond pulses [22] the second method use few-cycle pulses, which may result in the generation of isolated attosecond pulses [23, 24].

In this paper we focus on the effect of symmetry breaking on attosecond pulse generation, and in particular how the use of bichromatic driving field complements and bridges the two schemes presented above. The half-cycle to half-cycle symmetry of the two-colour driving field is broken which opens up for sub-cycle control of the generation process, also with multi-cycle driving pulses [25–27]. Experimentally a multi-cycle two-colour field is less demanding than CEP controlled few-cycle pulses, but the two techniques still have a lot in common.

2. Experimental two-colour setup

With the experimental setup in Lund we are able to generate the second harmonic and control the relative intensity, polarization and phase between the two fields. We do this in a two-colour interferometer with one colour in each arm, which means that we, as opposed to collinear setups, can manipulate the two colours independently. Incoming 35 fs, 2–3 mJ, 800 nm laser pulses are first frequency doubled in a 1.3 mm thick KDP (potassium dihydrogen phosphate), type I crystal. After the frequency doubling the polarizations of the IR and blue pulses are orthogonal, which is usually not desirable for attosecond pulse generation. The relative polarization can be controlled simply by placing a half-wave plate in one arm of the interferometer, but this will increase the amount of material the pulses have to pass through and also limit the bandwidth, in particular when the setup is used with short pulses [28]. Therefore, it is preferable to use a design where the blue arm of the interferometer contains a periscope, which rotates the polarization 90°, see figure 2.

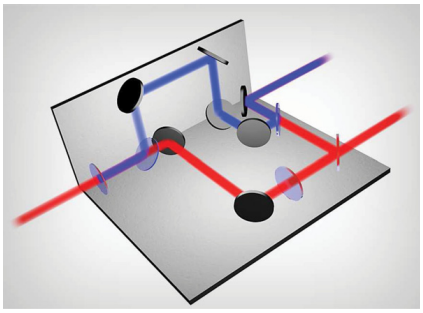

Figure 2. Versatile experimental setup to generate a two-colour laser field. The setup can be made very compact and stable, but still be versatile and useful in different types of two-colour experiments. The incoming IR pulses are frequency doubled before the two-colour interferometer. The polarization of the blue beam is rotated without the use of a half-wave plate so that the setup can be used with short pulses.

Another advantage of having one of the arms partly in a vertical plane is that the two beam splitters in the interferometer can be used in a better configuration. To maximize the bandwidth of both the IR and blue the beam splitters should transmit P-polarized IR and reflect S-polarized blue light. This is the case for the first beam splitter, but the beam splitter used for recombination of the arms transmits S-polarized IR with some energy losses as a result, the bandwidth is, however, not significantly reduced. Before the recombination of the two colours a fraction of the IR beam is split off to be used as a probe to characterize the temporal structure of the generated attosecond pulses [26, 29]. The amount of light sent to the probe beam is also a way to control the relative strength of the two frequency components when a high ratio of blue is required. For experiments that require a weak blue component [30] a variable aperture can be added to the blue interferometer arm. This will reduce the blue intensity relative to the IR without affecting the bandwidth or pulse duration. The focus size of the blue beam will increase with decreasing aperture and ensure that the blue intensity is almost constant across the red focus.

The relative phase between the two colours is controlled by a translation stage in the blue interferometer arm and a thin plate in the IR interferometer arm. The overlap between the pulses is set by the delay stage, while the relative phase is fine tuned by rotating the delay plate, thereby delaying the IR pulses with respect to the blue. The delay between the IR pulses and the probe, however, is not affected by the delay plate since they are separated after this plate.

The two-colour field exiting the interferometer is focused into a pulsed Ar gas target for harmonic generation. To form attosecond pulses the harmonic emission is spectrally filtered by a metallic filter and spatially filtered by an aperture [32]. The back side of the aperture is a convex mirror on which the probe beam is combined with the attosecond pulses. The combined beam is finally focused into the sensitive region of an electron spectrometer. Two types of electron spectrometers are

used; a magnetic bottle time-of-flight spectrometer (MBES) or a velocity map imaging spectrometer (VMIS). The probe can be delayed with respect to the harmonic beam with a high precision piezo translation stage to perform pump-probe measurements.

The two-colour setup can be used not only to control, but also to characterize the generation process [30]. When the relative strength of the second harmonic is very weak compared to the IR field it will induce a small shift in the electron phase without significantly perturbing the trajectory itself. In the case of argon, the blue field intensity should be approximately 0.1% of the IR intensity for typical generation conditions where the IR intensity is 1×10^{14} W cm^{-2}. The sign of the induced phase is opposite for adjacent half-cycles of the IR, which breaks the half-cycle periodicity and results in the emission of weak even high-order harmonics. The phase difference between consecutive harmonics can be deduced by measuring the even harmonic strengths as a function of the relative phase between the red and the blue pulses. In combination with the harmonic amplitudes this provides sufficient information to reconstruct the average temporal structure of the attosecond pulse as it is being generated [30]. An experimental proof of principle for the two-colour characterization method using the well-established RABITT method as a reference is soon to be published [31].

3. Control of attosecond pulse generation using two-colour fields

For multi-cycle, one-colour laser pulses the sequence of ionization, acceleration and recombination is repeated every half-cycle. The only difference between consecutive half-cycles is the sign change of the field. This means that the attosecond pulses are generated with a half-cycle periodicity, and that there is a phase shift of π from one pulse to the next. The periodicity leads, in the frequency domain, to a comb of harmonics spaced by two times the driving laser frequency. These harmonics are odd multiples of the driving frequency due to the phase shift of π from pulse to pulse (figure 1(a)).

With few-cycle pulses the short envelope gives half-cycle to half-cycle variations of the carrier. By changing the phase of the carrier wave with respect to the envelop the relative strength of consecutive half-cycles is varied. The phase variation between consecutive attosecond pulses may, therefore, differ from the simple π-shift observed for longer pulses, which consequently leads to a shift of the spectral peaks [17, 28].

For two-colour laser fields the shape and strength of consecutive half-cycles are controlled by varying the relative phase, φ, and/or the relative intensity, $\mathcal{R}$, of the two fields. The half-cycle periodicity is then replaced by a full-cycle periodicity and both odd and even harmonics are generated (figures 3(b) and (c)). If the blue field is sufficiently strong, odd and even harmonics are generated for almost all relative phases, but their relative strengths varies with φ (figures 3(b) and (c)). The ionization, and hence the harmonic yield, is also affected when φ is changed (figure 4). We find that odd and even harmonics have comparable strengths for the value of φ that corresponds to the maximum generation efficiency.

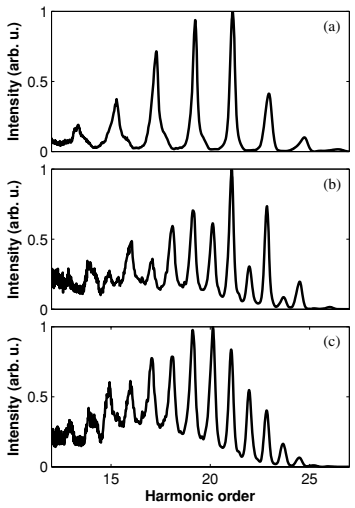

Figure 3. (a) Experimental harmonic spectrum generated in argon with a 35 fs, 800 nm pulse focused to an intensity of approximately $I = 2 \times 10^{14}$ W cm^{-2}. When the second harmonic ($\mathcal{R} \approx 10\%$) is added to the generation process the inversion symmetry is broken and the spectral signature of this is the appearance of even harmonics (b). By changing the relative phase between the two fields the total field structure is altered and the strength of the harmonics can be tailored.

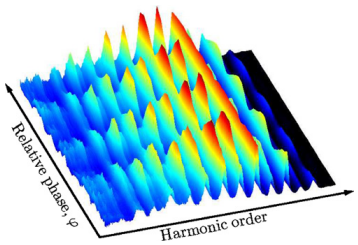

Figure 4. Experimental harmonic spectra generated in argon with a two-colour laser field, ($\mathcal{R} \approx 10\%$) as a function of the relative phase, φ, between the fields. The total yield is strongly modulated and odd and even harmonics have comparable strengths for the same values on φ that maximizes the yield. The spectra in figures 3(a) and (b) are line-outs from this scan when the yield is minimized and maximized, respectively.

When the symmetry of the driving field is broken, the strength of the field driving the electron back to the ion is also different between consecutive half-cycles. For few-cycle pulses *each* half-cycle has a unique cut-off energy that can be estimated by calculating the highest return energy for an electron driven back during that half-cycle. This means that there will be one effective cut-off for every contributing half-cycle [33]. The symmetry breaking using a two-colour field results in *two* different cut-offs that depends on φ. For some φ these cut-offs can differ by many harmonic orders as seen in

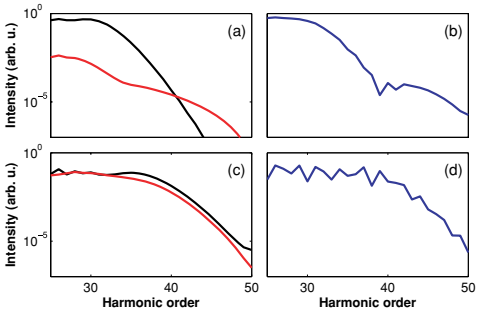

Figure 5. Harmonic spectra calculated for an IR intensity of $I = 2 \times 10^{14}$ W cm^{-2}, $\mathcal{R} = 10\%$ and two different values on φ. In (a) and (c) the harmonic generation from different half-cycles is separated and calculated for ionization when the field is positive or negative. In (b) and (d) the total harmonic spectra are presented. The values on φ are selected to maximize ((a) and (b)) or minimize ((c) and (d)) the difference in the spectral shape from consecutive half-cycles. When the strength from consecutive half-cycles is comparable the contributions interfere, which is clearly seen for all energies in (d), but only around harmonic order 40 in (b).

figure 5(a) while other relative phases result in similar energies for both cut-offs (figure 5(b)). The lowest energy cut-off is produced when the field driving the electrons back to the ion is rather weak; these electrons are, however, ionized during the strongest half-cycle with a resulting high harmonic yield. This leads to a very efficient suppression of the harmonic generation every second half-cycle and enhancement for the other half-cycles, which in the time domain corresponds to a strong APT with only one pulse per IR cycle [26, 27].

For a particular value of φ consecutive half-cycles share almost the same spectral signature (figure 5(c)), which suggest that two nearly identical pulses are generated by the different half-cycles. The pulses are, however, generated by different driving fields and their temporal structure may still differ dramatically. The phase of the attosecond pulses depends on the time the electron spends in the continuum between the ionization and the recombination. In a two-colour field the electron trajectories that have the same return energy for consecutive half-cycles may have spent different times in the continuum. The two cut-off trajectories in figure 5(c) correspond to electron continuum times of $0.45T$ and $0.65T$, where T is the period of the IR field, i.e., the electrons are pulled back with maximal energy much faster in one half-cycle compared to the other. The difference in temporal structure results in an interference in the total spectra when different half-cycles have amplitudes of comparable strengths as seen in figures 5(d) and 3(b). This interference diminishes when the harmonic yield from one half-cycles clearly dominates over the other by several orders of magnitude as seen in figures 5(b) and 3(c).

Any effect of the symmetry breaking will be enhanced by increasing the asymmetry between consecutive half-cycles. For a few-cycle pulse the asymmetry is increased by reducing the pulse duration, while for the two-colour field the intensity of the second harmonic is simply to be increased compared to the IR field. The shortest IR pulses generated, as of today, are 3.3 fs with a carrier wavelength of 720 nm [34], which leads to a maximum amplitude asymmetry of 0.71:1. To obtain a similar asymmetry with the two-colour field the intensity of the second harmonic has only to be approximately 2.5% of the IR intensity.

A stronger second harmonic field, $\mathcal{R} \geqslant 15\%$, induce dramatic changes to the sub-cycle field structure [29]. The cut-off energy and the continuum time for the cut-off electrons strongly depend on φ. Phase matching in a generation target in combination with an aperture removing divergent harmonic emission can act as a temporal filter that efficiently suppresses emission from electrons with a continuum time longer than $0.65T$. Within this time window the maximum electron energy varies when φ is changed. As the ionization probability increases for electrons returning with higher energy the net result is attosecond pulses with tunable central energy. Another example of temporal control using a two-colour field can be obtained when $\mathcal{R} \approx 25\%$. For this particular value of $\mathcal{R}$ the right choice of φ results in many electron trajectories that have the same return energy for a large part of the half-cycle. This leads to a dramatic increase in harmonic intensity for this particular energy while the other energies are suppressed (see [29]).

4. Attosecond pulse CEP

The role of the CEP has so far mainly been studied for optical pulses in the visible and near IR wavelength regions. Attosecond pulses have a central frequency in the XUV wavelength region and can therefore be very short and still consist of multiple cycles. As the duration of the attosecond pulses gets shorter, approaching the single cycle limit [32, 35], it gets meaningful to talk also about their CEP.

The addition of the second harmonic to the driving field provides the possibility not only to control the periodicity of the pulses in the generated APT but also the CEP of the pulses [26]. An APT generated by a single colour driving field consists of a train of attosecond pulses with a periodicity equal to half that of the driving field and a π shift between consecutive pulses; see figure 6. The addition of a small amount of second harmonic to the driving field enables control of the CEP. By carefully selecting $\mathcal{R}$ and φ, consecutive attosecond pulses can be made to accumulate an additional phase of π, which results in an APT that still has a half-cycle periodicity, but with the same CEP from pulse to pulse (figures 6(c) and (d)). In the frequency domain this corresponds to a comb of even harmonics [30]. The spectral range over which a comb of even harmonics can be obtained is limited by the intrinsic chirp rate of the attosecond pulses, but can be extended by increasing the IR intensity or using longer wavelength drivers [36, 37]. As the blue intensity is increased the attosecond pulse generation will rapidly decrease for every second half-cycle, and a pulse train with only one pulse per cycle is effectively generated for almost all values of φ once $\mathcal{R} \approx 10\%$. In the generated APT with one pulse per cycle the CEP will also be the same from pulse to pulse (figures 6(e) and (f)). Furthermore, the

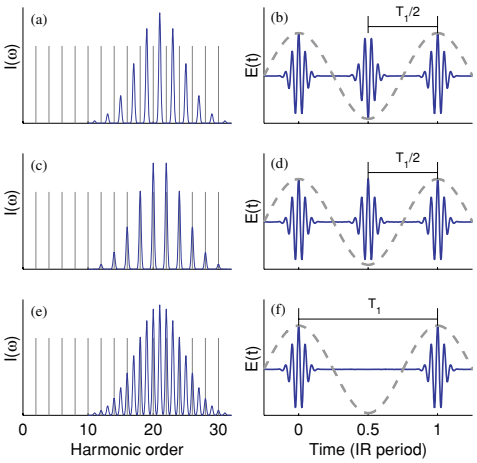

Figure 6. (a) A one colour driving field results in a comb of odd harmonics. (b) Phase locking produces an APT with periodicity equal to half that of the driving field and a π phase shift from pulse to pulse. (c) With a small amount of second harmonic added to the generation process a comb of even harmonics can be produced, which in the time domain (d) corresponds to an APT with periodicity equal to half that of the driving field and no phase shift from pulse to pulse. (e) A stronger blue field results in equally strong odd and even harmonics and (f) an APT with a full IR cycle periodicity and stable CEP.

increased amount of blue helps to stabilize the CEP of the attosecond pulses across the pulse train [26].

5. Towards XUV–XUV pump-probe experiments

Dynamics of various systems are frequently studied using pump-probe techniques where the sample is excited by a pump pulse and the time evolution recorded by a probe pulse after a variable delay. This can be generalized to situations where the object is to control the dynamics, e.g., by using additional, intermediate control pulses or by initiating the dynamics at specific times when the outcome is known to be favourable. Such pump-probe and control experiments of electron dynamics call for flexible attosecond pulse sources where the number of pulses, the delay between them and their relative CEP can be tailored.

The number of attosecond pulses can be varied by changing the CEP of a few-cycle pulse driving the high-harmonic generation process. If more than a few pulses are desired, a longer driving IR pulse combined with suitable phase matching [38, 39] or polarization gating [40, 41, 35] can be used, or combinations thereof [42]. In order to control the delay between pulses, one needs to vary the period, i.e. the wavelength, of the driving IR field. Continuous tuning over limited intervals is available with parametric sources; however, if discrete tunability is sufficient, then it is enough to add the second harmonic blue field to the generation process. This will allow the user to choose between half-cycle and full-cycle intervals with the additional freedom of selecting the relative carrier-envelope phase between consecutive pulses, thus open the door for the possibility of observing CEP effects with attosecond pulses.

Combining a two-colour driving field with few-cycle pulses and/or polarization gating can provide a flexible source to be used in XUV–XUV pump-probe and control experiments, especially if combined with a tunable parametric chirped pulse amplifier system. Indeed, such a double optical gate has been shown to produce isolated attosecond pulses starting with 10 fs driving IR fields [43, 44]. By adding the second harmonic to the driving field cleaner isolated pulses, with weaker pre- and/or post-pulses can be produced. The extended continuous spectral bandwidth opens for even shorter isolated attosecond pulses, provided that the right material can be found to compensate the phase variation across the pulses [45].

6. Conclusion

In this paper we have compared the effect of symmetry breaking using a two-colour field with that obtained with few-cycle pulses. The two techniques have many things in common and complement each other very well. With two-colour fields the induced asymmetries can easily be made very large and we have demonstrated that this allows us to control the periodicity, the CEP and the central frequency of the generated attosecond pulses. If combined with polarization gating and/or few-cycle pulses this enables the generation of controlled sequences of attosecond pulses. The ability to tailor attosecond pulse sequences in terms of number of pulses, periodicity and CEP will be important when attosecond physics move towards XUV–XUV pump-probe experiments.

Acknowledgments

We acknowledge useful discussions with K J Schafer, M B Gaarde and A L'Huillier. This research was supported by the Swedish Science Council, the Marie Curie intra European fellowship (PIEF-2008-221217), the Integrated Initiative of Infrastructure LASERLAB-EUROPE within the 6th European Community Framework Programme, and the Knut and Alice Wallenberg Foundation.

References

[1] Schafer K J, Yang B, DiMauro L F and Kulander K C 1993 *Phys. Rev. Lett.* **70** 1599
[2] Corkum P B 1993 *Phys. Rev. Lett.* **71** 1994
[3] Agostini P, Fabre F, Mainfray G, Petite G and Rahman N K 1979 *Phys. Rev. Lett.* **42** 1127
[4] Ferray M, L'Huillier A, Li X F, Mainfray G and Manus C 1988 *J. Phys. B: At. Mol. Opt. Phys.* **21** L31
[5] Yang B R, Schafer K J, Walker B, Kulander K C, Agostini P and DiMauro L F 1993 *Phys. Rev. Lett.* **71** 3770
[6] Walker B 1994 *Phys. Rev. Lett.* **73** 1227
[7] Paulus G G, Nicklich W, XU H L, Lambropoulos P and Walther H 1994 *Phys. Rev. Lett.* **72** 2851

[8] Muller H G, Bucksbaum P H, Schumacher D W and Zavriyev A 1990 *J. Phys. B: At. Mol. Opt. Phys.* **23** 2761
[9] Yin Y, Chen C, Elliott D S and Smith A V 1992 *Phys. Rev. Lett.* **69** 2353
[10] Schafer K J and Kulander K C 1992 *Phys. Rev.* A **45** 8026
[11] Schumacher D W, Weihe F, Muller H G and Bucksbaum P H 1994 *Phys. Rev. Lett.* **73** 1344
[12] Perry M D and Crane J K 1993 *Phys. Rev.* A **48**
[13] Eichmann H *et al* 1995 *Phys. Rev.* A **51** R3414
[14] Paulus G G, Becker W and Walther H 1995 *Phys. Rev.* A **52** 4043
[15] Paulus G G, Grasbon F, Walther H, Villoresi P, Nisoli M, Stagira S, Priori E and De Silvestri S 2001 *Nature* **414** 182
[16] Eckle P *et al* 2008 *Nature Phys.* **4** 565
[17] Baltuška A *et al* 2003 *Nature* **421** 611
[18] Reichert J, Holzwarth R, Udem T and Hänsch T W 1999 *Opt. Commun.* **172** 59
[19] Udem T, Holzwarth R and Hänsch T W 2002 *Nature* **416** 233
[20] Goulielmakis E *et al* 2004 *Science* **305** 1267
[21] Brabec T and Krausz F 2000 *Rev. Mod. Phys.* **72** 545
[22] Paul P M, Toma E S, Breger P, Mullot G, Augé F, Balcou P, Muller H G and Agostini P 2001 *Science* **292** 1689
[23] Hentschel M *et al* 2001 *Nature* **414** 509
[24] Gaarde M B and Schafer K J 2006 *Opt. Lett.* **31** 3188
[25] Kim I J, Kim C M, Kim H T, Lee G H, Lee Y S, Park J Y, Cho D J and Nam C H 2005 *Phys. Rev. Lett.* **94** 243901
[26] Mauritsson J, Johnsson P, Gustafsson E, L'Huillier A, Schafer K J and Gaarde M B 2006 *Phys. Rev. Lett.* **97** 013001
[27] Mauritsson J, Johnsson P, Mansten E, Swoboda M, Ruchon T, L'Huillier A and Schafer K J 2008 *Phys. Rev. Lett.* **100** 073003
[28] Mansten E *et al* 2008 arXiv:0811.3550v1
[29] Mansten E, Dahlström J M, Johnsson P, Swoboda M, L'Huillier A and Mauritsson J 2008 *New. J. Phys.* **10** 083041
[30] Dudovich N *et al* 2006 *Nature Phys.* **2** 781
[31] Dahlström J M *et al* 2009 in preperation
[32] López-Martens R *et al* 2005 *Phys. Rev. Lett.* **94** 033001
[33] Haworth C A, Chipperfield L E, Robinson J S, Knight P L, Marangos J P and Tisch J W G 2007 *Nature Phys.* **3** 52
[34] Goulielmakis E *et al* 2008 *Science* **320** 1614
[35] Sansone G *et al* 2006 *Science* **314** 443
[36] Tate J, Auguste T, Muller H G, Salieres P, Agostini P and DiMauro L F 2007 *Phys. Rev. Lett.* **98** 013901
[37] Colosimo P *et al* 2008 *Nature Phys.* **4** 386
[38] Jullien A, Pfeifer T, Abel M, Nagel P, Bell M, Neumark D and Leone S 2008 *Appl. Phys.* B **93** 433
[39] Strelkov V, Mével E and Constant E 2008 *New J. Phys.* **10** 083040
[40] Corkum P B, Burnett N H and Ivanov M Y 1994 *Opt. Lett.* **19** 1870
[41] Sola I J *et al* 2006 *Nature Phys.* **2** 319
[42] Altucci C, Esposito R, Tosa V and Velotta R 2008 *Opt. Lett.* **33** 2943
[43] Mashiko H, Gilbertson S, Li C, Khan S D, Shakya M M, Moon E and Chang Z 2008 *Phys. Rev. Lett.* **100** 103906
[44] Gilbertson S, Mashiko H, Li C, Khan S, Shakya M, Moon E and Chang Z 2008 *Appl. Phys. Lett.* **92** 071109
[45] Gustafsson E, Ruchon T, Swoboda M, Martens R L, Balcou P and L'Huillier A 2007 *Opt. Lett.* **32** 1353

Paper IX

Spectral Signature of Short Attosecond Pulse Trains

E. Mansten, J. M. Dahlström, J. Mauritsson, T. Ruchon, A. L'Huillier, J. Tate, M. B. Gaarde, P. Eckle, A. Guandalini, M. Holler, F. Schapper, L. Gallmann, and U. Keller.

Phys. Rev. Lett. **102**, 083002 (2009).

PRL **102,** 083002 (2009) PHYSICAL REVIEW LETTERS week ending 27 FEBRUARY 2009

Spectral Signature of Short Attosecond Pulse Trains

E. Mansten, J. M. Dahlström, J. Mauritsson, T. Ruchon,* and A. L'Huillier
Department of Physics, Lund University, P. O. Box 118, SE-221 00 Lund, Sweden

J. Tate and M. B. Gaarde
Department of Physics and Astronomy, Louisiana State University, Baton Rouge, Louisiana 70803-4001, USA

P. Eckle, A. Guandalini, M. Holler, F. Schapper, L. Gallmann, and U. Keller
Physics Department, ETH Zurich, CH-8093, Switzerland
(Received 6 August 2008; published 26 February 2009)

We report experimental measurements of high-order harmonic spectra generated in Ar using a carrier-envelope-offset (CEO) stabilized 12 fs, 800 nm laser field and a fraction (less than 10%) of its second harmonic. Additional spectral peaks are observed between the harmonic peaks, which are due to interferences between multiple pulses in the train. The position of these peaks varies with the CEO and their number is directly related to the number of pulses in the train. An analytical model, as well as numerical simulations, support our interpretation.

DOI: 10.1103/PhysRevLett.102.083002 PACS numbers: 32.80.Rm, 32.80.Qk, 42.65.Ky

The availability of one, two or a few attosecond light pulses will enable physicists to pump and probe, and possibly to coherently control electronic processes at an unprecedented time scale. While attosecond pulse trains (APT), comprising many pulses, are easily produced by harmonic generation in gases [1,2], the generation of single attosecond pulses (SAP) requires state-of-the-art laser systems and advanced characterization techniques, which to date, have been achieved by only two groups [3,4]. Today, many laboratories in the world are working towards this goal. Different methods are being explored including generation with ultrashort laser pulses [3], polarization gating [4–6], two-color frequency mixing [6,7] and spatial filtering [8,9]. A common denominator to all of these methods is the requirement of stabilization of the laser CEO [10–12], which allows for the optimization of the electric field waveform required to generate one or two pulses [13].

This Letter presents spectral measurements in conditions where the harmonic emission consists of only a few pulses. When the CEO is stabilized, we observe *additional frequency components* between the harmonics, the number of which decreases from low to high photon energies, as shown in Fig. 1. We provide a simple and straightforward interpretation of the origin of these components, in terms of interferences between all of the emitted pulses in the train. We discuss how the number of these extra peaks gives information about the number of pulses in the train depending on the frequency region considered. This is a general result that will be encountered when a small number of attosecond pulses are generated with phase-stabilized laser systems. The additional frequency components can be used to get immediate information on the number of pulses in the train as well as on the CEO value needed for the production of a given number of pulses. The position of the frequency components varies with the CEO, in a way that depends on which trajectory (long or short) contributes to the harmonic emission [14].

Our work is closely related to two previous experimental results obtained in quite different conditions. Sansone and co-workers [15] studied interferences between the long trajectories contributions of two consecutive harmonics and pointed out that these could also be interpreted as interferences between multiple pulses in the train. Pfeifer *et al.* [16] used ultrashort laser pulses and observed harmonic spectra containing harmonics and a continuous cutoff. By Fourier filtering they were able to remove the harmonic oscillation, thus revealing an additional modulation due to interferences between at least three pulses. In

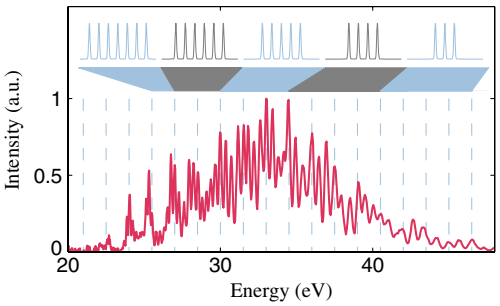

FIG. 1 (color online). Experimental harmonic spectrum. The dashed light blue lines indicate the position of the harmonics, starting from the 14th. The top pictures illustrate the composition of the pulse train corresponding to a selection of an approximately 3 eV spectral bandwith. The relative amplitude of the pulses is not known.

the present paper, multiple pulse interferences are observed *directly* and over the whole emitted spectrum, thus allowing us to get an immediate diagnostic of the status of the pulse train.

For our experimental studies we use a Ti:sapphire laser system delivering 30 fs CEO-stabilized 800 nm pulses at a repetition rate of 1 kHz with a maximum pulse energy of 0.8 mJ. The pulses are temporally compressed in a filament followed by chirped mirrors [17]. The compressed 12 fs laser pulses are sent through a 80 μm type I BBO crystal for second harmonic generation. The IR and the generated second harmonic radiation (blue) are separated in a dichroic interferometer where the relative phase, φ, between the IR and the blue can be finely controlled [18]. The two-color laser beam enters a vacuum chamber and is focused by a 50 cm radius of curvature spherical mirror into a pulsed argon jet. The Ar gas jet is positioned just after the laser focus for maximum efficiency as well as for phase-matching preferentially the short trajectory [19]. The high harmonic emission, generated in the jet, enters an XUV-spectrometer composed of a platinum grating and a backside-illuminated CCD. The acquisition of each harmonic spectrum is performed over a few thousand laser shots.

Figure 1 presents the key result of this work: The harmonic spectrum generated by the few-cycle two-color driving pulse exhibits spectral peaks in addition to the even and odd harmonics. The number of extra peaks decreases as the harmonic frequency increases, while their amplitude relative to the harmonic peaks increases. Their origin can be understood through a *time domain* description of harmonic generation. Let us first consider for simplicity n identical attosecond pulses, separated by a constant time interval ($T = 2.7$ fs in the experiment), with the same complex amplitude [$a(t)$]. Their sum can be expressed as a convolution,

$$s(t) = a(t) * \sum_{j=0}^{j=n-1} \delta(t - jT), \tag{1}$$

and the Fourier transform of Eq. (1) gives

$$S(\Omega) = A(\Omega) \sum_{j=0}^{j=n-1} e^{ij\Omega T}, \tag{2}$$

where $A(\Omega)$ is the spectral amplitude of each of the pulses which is equal to the Fourier transform of $a(t)$. The power spectrum is thus equal to

$$|S(\Omega)|^2 = |A(\Omega)|^2 \left| \frac{\sin(n\Omega T/2)}{\sin(\Omega T/2)} \right|^2, \tag{3}$$

and consists of main peaks when the denominator in Eq. (3) is zero, positioned at frequencies $\Omega = q\omega$, where q is an integer and ω the laser carrier frequency. These are the harmonic peaks which, in the simple case where the periodicity is assumed to be a full laser cycle, can be odd or even. The spectrum in Eq. (3) exhibits smaller peaks when the numerator is maximized, at the positions $(q + k/n + 1/2n)\omega$ where k is an integer between one and n-2 [20]. The number of additional peaks between two harmonics is equal to n-2 and their intensity is of course reduced compared to the harmonics. Our model can be generalized to describe attosecond pulses with pulse-to-pulse varying amplitude and phase, formally expressed as

$$S(\Omega) = \sum_j A_j(\Omega) e^{ij\Omega T}, \tag{4}$$

where the number of pulses contributing is now included in the distribution of (complex) spectral components $A_j(\Omega)$. Based on this simple model, our interpretation of the results presented in Fig. 1 is the following: The spectral structure is the result of the coherent sum of a few attosecond pulses. By simply counting the number of fringes, we can determine the number of pulses in the train for a given energy range. As shown by the insets in Fig. 1, and as expected since the highest energy region requires the highest field amplitude, this number decreases with increasing energy. The importance of the additional frequency components relative to the main harmonic peaks reflects the intensity distribution of the pulses, their phase difference and the number of contributing pulses.

The physics discussed here is quite general and by no means specific to a two-color field. Calculations performed with a one-color field and for realistic amplitude and phase variations between consecutive attosecond pulses also show additional frequency components for short enough APTs. The relationship between the number of these components and the number of pulses in the train is found to be remarkably robust. In our experiment, the addition of the blue field helps to observe the fringe structure simply because it reduces the number of pulses which interfere by half.

To verify our interpretation, we have also performed numerical calculations based on the coupled solutions of the time-dependent Schrödinger equation and the Maxwell wave equation [21]. Results shown in Fig. 2 represent the contribution from the short trajectory only, which is selected by limiting the available return times in the single atom part of the calculation. The top of the figure indicates the structure of the pulse train at certain energies. The number of generated attosecond pulses increases towards lower energies and agrees reasonably well with the number of additional spectral components plus two. It confirms our interpretation that the frequency structure between the main harmonic peaks gives information on the time-frequency structure of the pulse train and more specifically on the number of pulses in the train contributing to a certain frequency range. This simple and direct method, which can be implemented ''on line'', is complementary to more advanced characterization techniques like Reconstruction of attosecond bursts by interference of

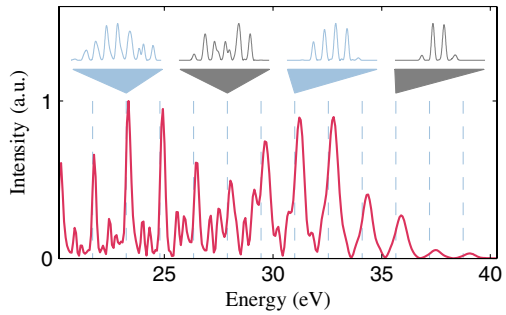

FIG. 2 (color online). Calculated harmonic spectrum and structure of the pulse train at different energies. The position of the harmonics 14 to 25 is indicated by the dashed light blue lines.

two-photon transition (RABITT) [1] or Frequency-resolved optical gating- Complete reconstruction of attosecond burst (FROG-CRAB) [22].

The behavior of the measured harmonic spectra strongly depends on the relative IR-blue phase φ as shown in Fig. 3(a). In general, the additional frequency components are best observed when φ is such that even harmonics are as strong as odd harmonics [see gray curve in Fig. 3(b), corresponding to the delay outlined in gray in (a)], which leads in the time domain to a train of pulses with one pulse per cycle [18]. When two pulses per IR-cycle are generated, the harmonic signal is weaker and the high energy part of the experimental spectrum is dominated by the beating of two pulses separated by half an IR-cycle [see the green curve in Fig. 3(b)]. Finally, for the delay outlined by the red line, a continuum above 37 eV is observed. This is the spectrum of a short APT where one pulse is more intense and reaches higher photon energy than the others. Spectral filtering of this energy region (above 37 eV) is expected to yield a single attosecond pulse. The two-color scheme [7] proposed in the present experiment is of interest for single attosecond pulse generation since it does not require ultrashort laser pulses [3] and since it should be more efficient than schemes based on polarization gating [4–6].

In Fig. 4(a), we study the variation of the spectra as a function of the CEO phase (ϕ_0). The position of the spectral structures changes with CEO, with a tilt increasing with energy. Indeed, when the CEO is not stable, the fringe structure is smeared out. Some of the fringes split or merge together as the CEO is changed. Finally, after a 2π change of ϕ_0 the fringes come back to their original position. This periodicity can be understood with simple arguments. The spectral component $A_j(\Omega)$ corresponding to each attosecond pulse, which includes an amplitude and a phase reflecting the electron trajectory, depends on the value of the laser intensity (I_j) at which the attosecond pulse is created. When ϕ_0 changes by 2π, $I_j \rightarrow I_{j+1}$ and $A_j \rightarrow A_{j+1}$, so that

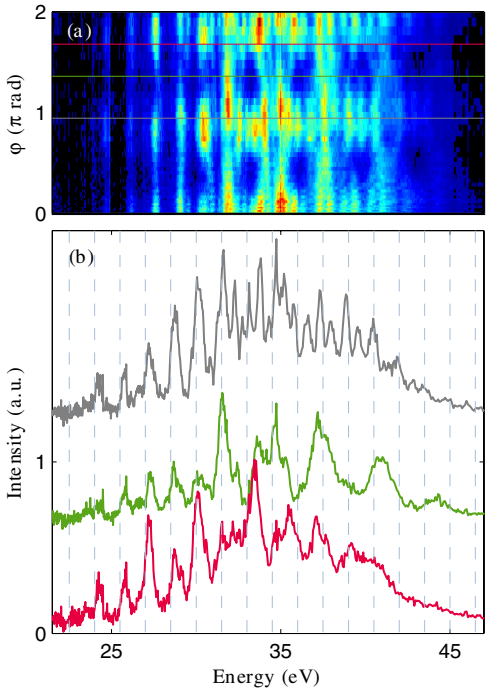

FIG. 3 (color online). (a) Experimental harmonic spectrum as a function of the phase difference between the infrared and blue fields, φ. (b) Spectra taken at the three phases marked in (a); the green and gray curves are shifted 0.6 and 1.2 intensity units, respectively. The dashed light blue lines indicate approximately the positions of harmonics 15 to 31.

$S(\Omega, \phi_0) = S(\Omega, \phi_0 + 2\pi)\exp(-i\Omega T)$. Consequently, the fringe pattern (proportional to $|S(\Omega, \phi_0)|^2$) varies periodically with ϕ_0. The phase of $A_j(\Omega)$ can be approximated by $\alpha(\Omega)I_j$, where α depends on the spectral region as well as on the electron trajectory causing the emission [14]. The phase variation with intensity leads to a tilt of the interference fringes. For small phase variation, the position of the fringes can be shown to vary linearly with the CEO, with a slope proportional to $\alpha(\Omega)$ [23]. The observed tilt of the bimaxima is thus a signature of the dipole phase variation during the laser pulse. How rapidly the fringes move depends on whether the harmonic emission is predominantly from the short or the long trajectory. A similar effect was observed by Sansone and co-workers and attributed, in their experimental conditions, to the long trajectory [15]. Finally, the variation of the amplitude $|A_j(\Omega)|$ affects the intensity distribution of the attosecond pulses, and even sometimes the number of pulses effectively contributing to the radiation, thereby changing the number of

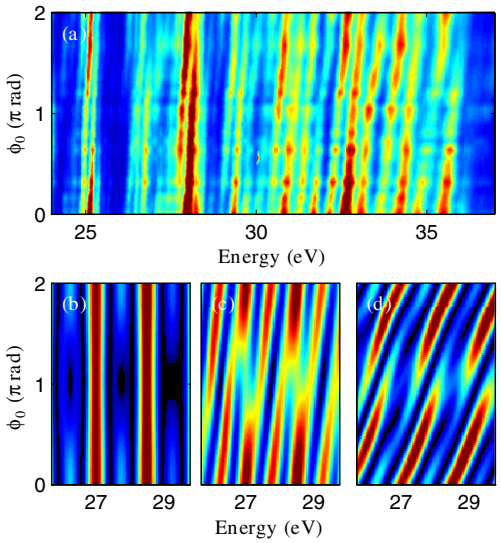

FIG. 4 (color online). (a) Experimental harmonic spectrum as a function of ϕ_0. (b) Calculated harmonic spectra as a function of ϕ_0 including amplitude effects. (c) Phase variations for the short trajectories added to the calculation in (b). (d) Phase effects corresponding to the long trajectories added to the calculation in (b).

additional peaks. This effect can be seen experimentally as fringes splitting and merging as the number of pulses contributing changes with the CEO. To illustrate the different effects discussed above, we present in Figs. 4(b)–4(d) the results of simple calculations based on Eq. (4). Figure 4(b) shows the effect of the amplitude variation for a Gaussian 10 fs-long fundamental pulse, neglecting phase variation. The number of extra peaks oscillates between one and two as a function of the CEO. The effect of both phase and amplitude variation is shown in (c),(d) for α values corresponding to the short and long trajectories, respectively, in the spectral region considered. Our experimental observation is consistent with the (rather slow) variation of the short trajectory.

In conclusion, we have studied high-order harmonic generation by short laser pulses, so that the attosecond pulse train comprises only a few pulses. In these conditions, the spectra do not include only harmonics of the laser frequency, but also extra peaks whose number decreases as a function of photon energy. These additional spectral peaks are due to multiple interferences between the pulses in the train. The number of additional peaks allows us to determine the structure of the attosecond pulse train as a function of energy. In addition the tilt of the fringes with carrier envelope phase gives us information on the dipole phase variation as a function of intensity, with a clear distinction between the short and the long trajectories.

This research was supported by the Marie Curie Early Stage Training Site (MAXLAS), the Integrated Initiative of Infrastructure LASERLAB-EUROPE within the 6th European Community Framework Programme, the Swedish foundation for international cooperation in research and high education (STINT), the Swedish Research Council, the National Science Foundation through grant no. PHY-0449235, the Center for Computation and Technology at Louisiana State University, NCCR Quantum Photonics (NCCR QP) and a research instrument of the Swiss National Science Foundation (SNSF).

*Present address: CEA-Saclay, DSM, Service des Photons, Atomes et Molcules, 91191 Gif sur Yvette, France.

[1] P. M. Paul *et al.*, Science **292**, 1689 (2001).
[2] R. López-Martens *et al.*, Phys. Rev. Lett. **94**, 033001 (2005).
[3] R. Kienberger *et al.*, Nature (London) **427**, 817 (2004).
[4] G. Sansone *et al.*, Science **314**, 443 (2006).
[5] I. J. Sola *et al.*, Nature Phys. **2**, 319 (2006).
[6] H. Mashiko *et al.*, Phys. Rev. Lett. **100**, 103906 (2008).
[7] T. Pfeifer *et al.*, Phys. Rev. Lett. **97**, 163901 (2006).
[8] M. B. Gaarde and K. J. Schafer, Opt. Lett. **31**, 3188 (2006).
[9] C. Haworth *et al.*, Nature Phys. **3**, 52 (2007).
[10] H. Telle *et al.*, Appl. Phys. B **69**, 327 (1999).
[11] D. J. Jones *et al.*, Science **288**, 635 (2000).
[12] A. Apolonski *et al.*, Phys. Rev. Lett. **85**, 740 (2000).
[13] A. Baltuška *et al.*, Nature (London) **421**, 611 (2003).
[14] M. Lewenstein, P. Salières, and A. L'Huillier, Phys. Rev. A **52**, 4747 (1995).
[15] G. Sansone *et al.*, Phys. Rev. Lett. **92**, 113904 (2004).
[16] T. Pfeifer *et al.*, Opt. Express **15**, 17 120 (2007).
[17] C. Hauri *et al.*, Appl. Phys. B **79**, 673 (2004).
[18] J. Mauritsson *et al.*, Phys. Rev. Lett. **97**, 013001 (2006).
[19] P. Salières, A. L'Huillier, and M. Lewenstein, Phys. Rev. Lett. **74**, 3776 (1995).
[20] The positions $k = 0$ and $k = n - 1$ do not lead to maxima, since they are not separated from the main peaks by a zero.
[21] M. B. Gaarde, J. L. Tate, and K. J. Schafer, J. Phys. B **41**, 132001 (2008).
[22] Y. Mairesse and F. Quéré, Phys. Rev. A **71**, 011401(R) (2005).
[23] This can be formally shown by making a Taylor expansion of the fundamental laser intensity at the time where pulse j is generated as a function of the CEO, and by inserting the expansion in Eq. (4).